Université catholique de Louvain
Ecole polytechnique de Louvain
Unité d'Ingénierie des Matériaux et des Procédés

In situ monitoring of the internal stress evolution during titanium thin film anodising

These présentée le 8 janvier 2009
par Jean-François Vanhumbeeck
en vue de l'obtention du grade de
Docteur en Sciences Appliques.

Composition du jury:

Prof. Joris Proost (promoteur)	Université catholique de Louvain, Belgique
Prof. Jean-Luc Delplancke	Université libre de Bruxelles, Belgique
Prof. Francesco Di Quarto	Università di Palermo, Italie
Prof. Luc Piraux	Université catholique de Louvain, Belgique
Prof. Patrik Schmuki	University of Erlangen-Nürnberg, Allemagne
Prof. Christian Bailly (President)	Université catholique de Louvain, Belgique

Louvain-la-Neuve, Dcembre 2008

Acknowledgements

Bien que mon seul nom figure sur la couverture de cette thèse, celle-ci n'a pu être réalisée qu'avec l'aide précieuse de nombreuses personnes qui, toutes, ont contribué, que ce soit sur le plan pratique, scientifique ou humain, à faire de ces quatre années de doctorat une expérience si positive. Je souhaite les remercier toutes très chaleureusement.

Merci tout d'abord au Professeur Francis Delannay pour avoir eu la bonne idée de me recruter pour entamer une thèse. Merci ensuite au FRIA qui a financé ma recherche pendant ces quatre années. Merci également à tous les Professeurs de l'UCL qui m'ont donné de précieux coups de mains ponctuels. Je pense notamment à Thomas Pardoen pour nos discussions sur l'électrostriction, à Pascal Jacques pour son aide pour le SEM, à Denis Flandre pour les discussions sur la caractérisation électrique de mes couches d'oxyde et à Bernard Nysten pour les mesures AFM. Un immense merci au Professeur Stéphane Lucas et à toute l'équipe du LARN pour leur accueil chaleureux et généreux pour mes analyses RBS.

Je voudrais remercier également tous les membres du secrétariat IMAP, Albert, Micheline, Suzy et Viviane qui m'ont aidé à réduire le poids des formalités administratives et des soucis pratiques qui jalonnent le quotidien d'une thèse. Merci à toute l'équipe du laboratoire d'analyses, Françoise, Ghislaine, Luc, Monique, Nadine, Ronny et Yvette pour leur aide généreuse et efficace. Merci à l'équipe technique IMAP, Emile, Luc et Marc pour leur support technique sans faille, en particulier pour la réalisation de mon dispositif expérimental, et à toute l'équipe des chambres propres.

Un immense merci à Laurence Ryelandt grâce à qui j'ai découvert avec beaucoup de plaisir le monde fascinant de la microscopie en transmission. Un merci tout particulier au Professeur Nick Schrijvers et au Docteur He Tian du labo EMAT pour les splendides images TEM en coupe de mes échantillons. Un grand merci également au Docteur Dominik Kramer, au Professeur Joerg Weissmüller, à Maxim Smetanin et à toute leur équipe pour leur invitation

au FZ Karlsruhe, pour leur accueil chaleureux et pour toutes nos discussions scientifiques. Merci à Vincent Mairiaux pour le travail exploratoire accompli dans le cadre de son travail de fin d'étude.

Je tiens à remercier également tous les membres de mon jury pour leur enthousiasme et leur lecture attentive de ma thèse. Merci en particulier au Professeur Jean-Luc Delplancke pour les discussions scientifiques que nous avons eues et pour ses conseils avisés. Un tout grand merci également aux Professeurs Francesco Di Quarto et Patrik Schmuki pour avoir pris le temps de traverser l'Europe à deux reprises pour assister à mes deux défenses de thèse.

Je voudrais remercier aussi mes deux excellents voisins de bureau Mathieu et Quentin dont j'ai beaucoup apprécié la compagnie et qui m'ont supporté pendant ces quatre ans. Merci à tous les chercheurs d'IMAP pour l'ambiance inégalable. Les tartes, drinks, soupers de labo, séminaires du vendredi et autres barbecues vont vraiment me manquer.

Merci Julien et Paul-Emile pour leurs fichiers LaTeXmodèles qui m'ont été bien utiles. Merci à Evelyne pour la courageuse tentative de relecture. Merci à toute ma famille pour son support à 200%!

Enfin, last but not least, un immense merci à mon promoteur le Professeur Joris Proost pour son soutien enthousiaste et sa disponibilité exceptionnelle. Merci, Joris, pour tes encouragements constants qui m'ont maintenu sur les rails dans les moments de doute, pour nos moments d'émerveillement devant de nouveaux résultats et nos discussions animées pour leur interprétation. Merci pour toutes ces choses que j'ai apprises grâce à toi.

Contents

General introduction

Anodisation has been studied for almost eighty years, primarily in the field of corrosion science, as a simple and efficient way of producing thick protective oxide coatings on Al, Fe, Ti or Zr alloys. Anodisation is very specific oxidation process in that it relies on the migration of ions across solid films over rather large distances typically up to several hundreds of nanometers, the migration being promoted by very high electric fields of the order of 10^7 V/cm. From the fundamental point of view, many aspects regarding the growth of anodic films have been studied extensively. However, so far, little interest has been devoted to the mechanical aspects involved in the growth process. It has been known for long that large internal stresses develop in anodic films during their growth. Internal stresses are therefore often cited in the literature as a possible origin for film crystallisation or for various growth instabilities although, paradoxically, very little experimental evidence is available on the magnitude of such stresses and their evolution during the growth. Especially in the case of Ti, the stress development in anodic oxide films is poorly known as the few experimental studies unravelling this field report apparently contradictory observations, from which the only conclusion seems to be that the mechanical behaviour of such films is complex.

The evolution of the internal stresses accompanying the growth is however important from the perspective of applications as well as from the fundamental point of view. A good control of the internal stresses is indeed crucial in order to guarantee the durability of anodic coatings, their structural and functional properties. In addition, the stress evolution directly reflects the motion of the ions in the film and therefore provides a unique means to investigate in-situ the mechanisms of growth of anodic films.

Within this framework, this thesis was devoted to the investigation of the stress evolution in anodic TiO_2 films, as obtained from high-resolution in situ stress measurements. This project combined mechanical and electrochemical aspects in a materials science approach towards a better understanding of the mechanisms of growth of anodic TiO_2 films. The stress measurements have

been performed in situ using a multi-beam sensor, derived from the classical beam deflection technique. To the best of our knowledge, this study is the first report on the use of the multi-beam sensor for the monitoring of processes in liquid environments.

To our opinion, the main contributions of this theses are threefold:

- demonstrating the capability of the multi-beam sensor for monitoring processes in liquids, and developing an adequate experimental set-up allowing for in situ stress measurements in anodic films
- providing experimental data on the stress evolution in anodic TiO_2 films, with specific emphasis put on establishing correlations between the evolution of the mechanical and electrochemical variables
- deriving a novel constitutive equation for predicting the magnitude of electrostriction stresses in anodic oxide films and providing quantitative measurements of the electrostriction stresses in TiO_2 films, supporting the model

This manuscript has been divided into 5 chapters. In the first chapter, the reader is introduced to anodisation processes. A comprehensive review of the literature on Ti anodising is presented, with a special interest in studies dealing with the stress behaviour of anodic TiO_2 films. The second chapter is presented in a textbook style and aims at providing the necessary background to readers wanting to start-up with in situ stress measurements. Our experimental set-up is described in details, the calibration equations are derived and their domain of validity is discussed. Experimental results on the stress evolution in anodic TiO_2 films are presented and discussed in the third and fourth chapters. The third one focuses on general observations on the stress evolution and their correlations with the cell voltage evolution. The fourth chapter is devoted more specifically to the reversible contribution of electrostriction stresses during the growth of anodic oxide films. Finally, the last chapter deals with efficiency changes affecting the growth of anodic TiO_2 films. The influence of such efficiency changes on the cell voltage evolution is discussed in the first part. In the second part, the origin of the efficiency changes is discussed based on in-plane TEM observations.

Scientific Production

The results presented in this thesis have been published in the following scientific journals and presented on the international scientific meetings listed below.

Publications in peer-reviewed journals and conference proceedings:

- J.-F. Vanhumbeeck and J. Proost, "On the origin of the local voltage decrease during galvanostatic Ti anodising", in preparation.
- J.-F. Vanhumbeeck and J. Proost, "On the relation between growth instabilities and internal stress evolution during galvanostatic Ti thin film anodisation", J. Electrochem. Soc. 155 (2008) C506.
- J.-F. Vanhumbeeck and J. Proost, "On the contribution of electrostriction to charge-induced stresses in anodic oxide films", Electrochim. Acta 53 (2008) 6165.
- J.-F. Vanhumbeeck and J. Proost, "In-situ monitoring of the dielectric and electrostrictive properties of anodised thin films for biochip applications", Colloids and Surfaces B: Biointerfaces, 56 (2007) 163.
- J. Proost, J.-F. Vanhumbeeck and Q. Van Overmeere, "In-Situ Monitoring of the Internal Stress Evolution during Thin Film Anodising" Electrochemical Society Transactions 11 (2008) 35.
- J.-F. Vanhumbeeck and J. Proost, "Electrochemical processing of ultrathin metallic oxides featuring in-situ monitoring of growth stress transitions", Electrochemical Society Transactions 2 (2007) 281.

Presentations on international scientific meetings:

- Q. Van Overmeere, J.-F. Vanhumbeeck and J. Proost, "In-situ investigation of the relationship between electrical and mechanical properties during the growth of anodic oxide films." 59th Meeting of the International Society of Electrochemistry, Seville, September 2008.
- J.-F. Vanhumbeeck and J. Proost, "Influence of the applied current density on the growth stress evolution in anodic TiO2 films." 59th Meeting of the International Society of Electrochemistry, Seville, September 2008.
- J.-F. Vanhumbeeck, Q. Van Overmeere, and J. Proost, "Instability of anodically formed TiO2 layers: revisited". 4th Gerischer Symposium, Berlin, June 2008.
- Q. Van Overmeere, J.-F. Vanhumbeeck and J. Proost, "In-situ Monitoring of the Growth Stress Evolution during Galvanostatic Anodizing of Aluminum Thin Films". 213th Meeting of the Electrochemical Society, Phoenix, May 2008.
- J.-F. Vanhumbeeck, Q. Van Overmeere, and J. Proost, "On the origin of local cell voltage maxima during galvanostatic Ti anodising". 213th Meeting of the Electrochemical Society, Phoenix, May 2008.
- J. Proost, J.-F. Vanhumbeeck and Q. Van Overmeere, "In-situ monitoring of the internal stress evolution during thin film anodising", Invited presentation, 212th Meeting of the Electrochemical Society, Washington DC , October 2007.
- J.-F. Vanhumbeeck and J. Proost, "In situ monitoring of surface reactions using high-resolution curvature measurements: application to Ti anodising". 58th Meeting of the International Society of Electrochemistry, Banff, September 2007.
- J.-F. Vanhumbeeck and J. Proost, "Application of high-resolution curvature measurements to the investigation of charging effects at metal oxide/electrolyte interfaces". 11th International Conference on Electrified Interfaces, Sahoro, June 2007.
- J.-F. Vanhumbeeck and J. Proost, "In-situ diagnostics for monitoring the processing and properties of anodised metallic oxide thin films". Electroceramics X, Toledo, June 2006.
- J.-F. Vanhumbeeck and J. Proost, "Electrochemical processing of ultrathin metallic oxides featuring in-situ monitoring of growth stress transitions". 209th Meeting of the Electrochemical Society, Denver, May 2006.

Chapter 1

State-of-the-art on Ti anodisation

Contents

This first chapter is divided into four sections. The first one provides a general introduction to anodisation processes. The second deals more specifically with the anodisation of Ti. Owing to their central importance in this work, the third section is devoted to stress measurements in anodic oxide films. Finally, the fourth section gives an overview of the various techniques available for the characterisation of anodic oxide films.

1.1 General introduction to anodisation

The first sub-section aims at introducing the main concepts and notions in relation to anodisation which will be used throughout the subsequent sections and chapters. Theoretical models for the growth kinetics and the breakdown are presented in, respectively, the second and third sub-sections.

1.1.1 Definitions and concepts

Definition: Anodisation can be defined as the well-desired electrochemical growth of a solid (oxide) film on a metal (or a semi-metal) substrate, obtained by polarising the metal anodically in an electrochemical cell. During the anodisation, electrons flow from the metal to be anodised to the cathode through the external circuit. This results in the ionisation of metal atoms at the anode surface. The latter then react with oxygen-containing anions from the electrolyte, which leads to the formation of a solid film, usually an oxide. Once the first monolayer of oxide is formed on the substrate, further growth of the oxide film requires that the metal cations, produced at the metal/film interface, can react with the oxygen-containing anions, injected in the film at the film/electrolyte interface. Hence, the growth of the oxide film relies on the transport of the metal cations and/or O^{2-} anions across the film. In order to have such ions to migrate, very large electric fields must be sustained in the oxide film. Typically, the field in a growing anodic oxide film is of the order of 0.1 to $1{\cdot}10^9$ V/m [139]. It should be noted that not all metals can be anodised. The conditions for a metal to be suitable for anodisation are the following [102]:

- That the anode metal is susceptible to forming an oxide compound with oxy-anions from the solution. In the case of Pt, for instance, no compounds are formed in most electrolytic solutions.

- That the corresponding metal-oxide, produced by the reaction of metal cations with oxygen-containing species from the electrolyte, is essentially insoluble in the used electrolyte. If it is not, only anodic dissolution will be observed, like in the case of Cu for instance, as anodic polarisation of a copper electrode in acidic electrolytes results in the dissolution of the metal electrode in the form of Cu^{2+} ions.

1 **H** Hydrogen 1.00794																	2 **He** Helium 4.003
3 **Li** Lithium 6.941	4 **Be** Beryllium 9.012182											5 **B** Boron 10.811	6 **C** Carbon 12.0107	7 **N** Nitrogen 14.00674	8 **O** Oxygen 15.9994	9 **F** Fluorine 18.9984032	10 **Ne** Neon 20.1797
11 **Na** Sodium 22.989770	12 **Mg** Magnesium 24.3050											13 **Al** Aluminium 26.981538	14 **Si** Silicon 28.0855	15 **P** Phosphorus 30.973761	16 **S** Sulfur 32.066	17 **Cl** Chlorine 35.4527	18 **Ar** Argon 39.948
19 **K** Potassium 39.0983	20 **Ca** Calcium 40.078	21 **Sc** Scandium 44.955910	22 **Ti** Titanium 47.867	23 **V** Vanadium 50.9415	24 **Cr** Chromium 51.9961	25 **Mn** Manganese 54.938049	26 **Fe** Iron 55.845	27 **Co** Cobalt 58.933200	28 **Ni** Nickel 58.6934	29 **Cu** Copper 63.546	30 **Zn** Zinc 65.39	31 **Ga** Gallium 69.723	32 **Ge** Germanium 72.61	33 **As** Arsenic 74.92160	34 **Se** Selenium 78.96	35 **Br** Bromine 79.904	36 **Kr** Krypton 83.80
37 **Rb** Rubidium 85.4678	38 **Sr** Strontium 87.62	39 **Y** Yttrium 88.90585	40 **Zr** Zirconium 91.224	41 **Nb** Niobium 92.90638	42 **Mo** Molybdenum 95.94	43 **Tc** Technetium (98)	44 **Ru** Ruthenium 101.07	45 **Rh** Rhodium 102.90550	46 **Pd** Palladium 106.42	47 **Ag** Silver 107.8682	48 **Cd** Cadmium 112.411	49 **In** Indium 114.818	50 **Sn** Tin 118.710	51 **Sb** Antimony 121.760	52 **Te** Tellurium 127.60	53 **I** Iodine 126.90447	54 **Xe** Xenon 131.29
55 **Cs** Cesium 132.90545	56 **Ba** Barium 137.327	57 **La** Lanthanum 138.9055	72 **Hf** Hafnium 178.49	73 **Ta** Tantalum 180.9479	74 **W** Tungsten 183.84	75 **Re** Rhenium 186.207	76 **Os** Osmium 190.23	77 **Ir** Iridium 192.217	78 **Pt** Platinum 195.078	79 **Au** Gold 196.96655	80 **Hg** Mercury 200.59	81 **Tl** Thallium 204.3833	82 **Pb** Lead 207.2	83 **Bi** Bismuth 208.98038	84 **Po** Polonium (209)	85 **At** Astatine (210)	86 **Rn** Radon (222)
87 **Fr** Francium (223)	88 **Ra** Radium (226)	89 **Ac** Actinium (227)	104 **Rf** Rutherfordium (261)	105 **Db** Dubnium (262)	106 **Sg** Seaborgium (263)	107 **Bh** Bohrium (262)	108 **Hs** Hassium (265)	109 **Mt** Meitnerium (266)	110 (269)	111 (272)	112 (277)	113	114				

Figure 1.1: Localisation of the metals suitable for anodisation in the periodic chart. The elements shaded in dark grey are the so-called valve-metals. Other metals, shaded in light grey can be anodised as well under specific conditions.

- That the corresponding metal-oxide is a poor electronic conductor. If the oxide exhibits a high electronic conductivity, only a thin passivating oxide film of molecular thickness will be formed on the anode surface, after which other electrochemical oxidation reactions will take place on the surface of the passivation film and further oxidation of the metal will no longer occur. This is the case for instance for Fe in dilute aqueous sulphuric acid.

The metals which can be anodised are mainly the so-called 'valve metals': Al, Ta, Ti, Nb, Zr, Hf and W. The latter metals form stable solid oxide films which are good ionic conductors and, generally speaking, poor electronic conductors. Other metals and semi-metals such as V, Mn, Fe, Ni, Co, Bi or Sb can be anodised as well under specific conditions. As illustrated on Fig.1.1, all the valve metals are transitional metals, with the exception of aluminium which belongs to the IIIA family of the periodic table. One of the main advantages of anodisation is the extreme simplicity of the process. In order to carry out anodisation, only the metal electrode to be anodised, a counter-electrode, a power source and an electrically conductive electrolytic solution are required. A schematic representation of an anodisation cell is shown on Fig.1.2. A supplementary reference electrode can be used in order to provide for a more accurate control of the anode potential. The influence of the characteristics of the anode and of the electrolyte will be discussed in the specific case of Ti in section 1.2.

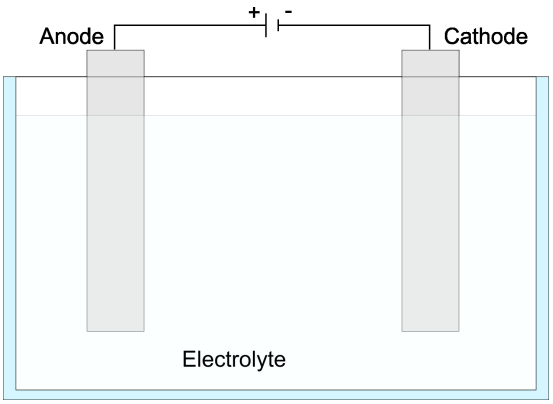

Figure 1.2: Schematic representation of an anodisation cell.

Growth mode: As mentioned in the previous paragraphs, anodisation is carried out by forcing a current to flow from the cathode to the anode, using an external power source. Typical potentiostats and programmable power sources can be used in different control modes, leading to different growth modes of the oxide films. The anodisation can be conducted by applying a given constant potential difference between anode and cathode (potentiostatic mode), by imposing a constant cell current (galvanostatic mode), or by sweeping the anode potential at a given rate (potentiodynamic mode). Galvanostatic of potentiodynamic growth is sometimes followed by a potentiostatic aging at the final voltage. Under potentiostatic conditions, the oxide film grows rapidly during the first seconds of the anodisation. As a result, a very high cell current flows through the cell at the beginning of the experiment, then decays exponentially. Chronocoulometry provides a way of following potentiostatic anodisation, as illustrated on Fig.1.3. Under galvanostatic conditions, in the ideal case when the film grows with 100% efficiency (no side-reactions) and without any structural transformation throughout the growth, the oxide film grows at a constant rate, proportional to the imposed current density, according to the Faraday law. Under such conditions, a constant field is required through the film in order for the constant current to flow through the cell [260]. Hence, the cell voltage increases proportionally with the thickness of the oxide film on the anode. Therefore, chronopotentiometric curves provide a simple tool allowing to follow the thickness evolution during the growth. This is illustrated on Fig.1.3. The potentiodynamic growth is very similar to galvanostatic conditions in the ideal case. Indeed, as evident from Fig.1.3, scanning the cell voltage at a given constant rate will cause a constant current to flow through the cell.

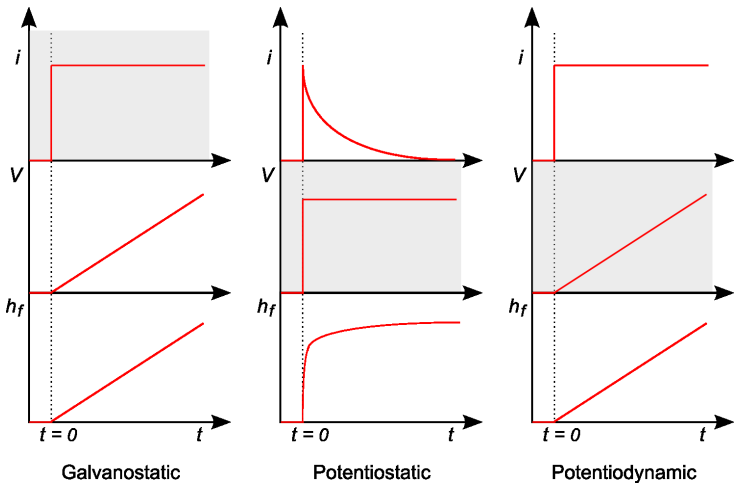

Figure 1.3: Schematic representation of the evolution of the cell current (i), the cell voltage (V) and the film thickness (h_f) for a galvanostatic, a potentiostatic and a potentiodynamic anodisation process. For each growth mode, the shaded figure represents the control variable.

Anodising ratio: As mentioned in the previous paragraph, under galvanostatic or potentiodynamic conditions, the measured cell voltage is usually observed to be proportional to the thickness of the oxide film on the anode. The proportionality coefficient is called '**anodising ratio**' (AR) or sometimes 'formation coefficient'. Under ideal conditions, the anodising ratio usually keeps a constant value throughout the growth. Its value is primarily a function of the nature of the metal but also varies slightly with the process parameters (growth rate, T°). It should be noted that, owing to its definition, the anodising ratio is in fact equal to the inverse of the electric field E applied to the film $AR = 1/E$. A smaller AR-value means that a larger field is required to grow the film. Under potentiostatic conditions, a similar linear relationship exists between the formation voltage and the thickness of the oxide film, for a constant anodisation time.

Ionic migration: After an initial step during which a first monolayer of oxide is formed on the metal surface, the oxide film grows further by migration of ions through the existing film. The mobile ionic species are the metal cations M^{x+} and the oxygen-containing anions, mainly O^{2-} with some possible contribution of OH^- ions as well [190, 76]. The relative contribution of anions and cations can vary widely from one metal oxide to another, and depends on the process conditions as well. One direct consequence of one or the

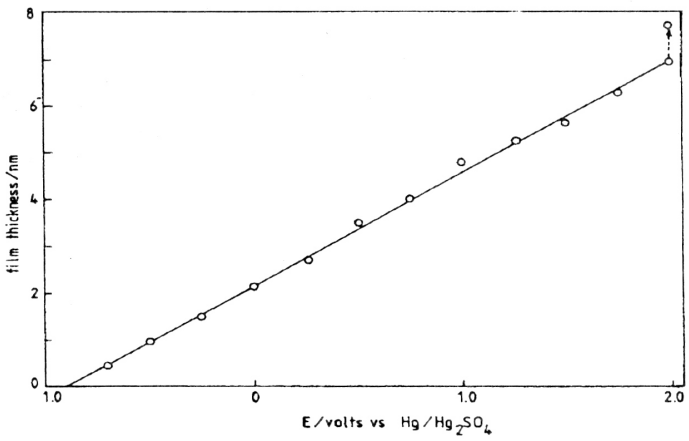

Figure 1.4: Illustration of the evolution of the film thickness with the anode potential for a galvanostatic anodisation experiment. This figure is reproduced from Blackwood et al. [23].

other type of ion dominating the ionic transport is the location of new film growth. Indeed, as illustrated on Fig.1.5, if the film grows by migration of cations from the metal/oxide interface outwards, new oxide will be formed at the oxide electrolyte interface. In contrast, the oxide film will grow mainly at the metal/oxide interface if inwards anionic transport is dominant. In the case of anodic ZrO_2 films for instance, the Zr^{4+} ions are almost immobile and the film grows only at the metal/oxide interface by inward migration of O^{2-} ions into the Zr lattice [45]. However, in most cases, both types of ions contribute to the ionic current and new oxide is formed at both interfaces [110, 133]. The proportion of the ionic current carried by anions and cations is referred to as, respectively, the **anionic transport number** t_a and the **cationic transport number** t_c. Obviously, $t_c = 1 - t_a$. The transport numbers t_a and t_c thus reflect the proportion of the oxide film formed, respectively, at the metal/oxide and oxide/electrolyte interfaces. As will be discussed later on in this thesis, the location where new oxide is formed can have a significant influence on the anodisation process.

Barrier and porous oxide: Anodic oxide films can be formed either as a dense material, referred to as barrier oxide, or present a nanoporous morphology. At the beginning of anodisation, anodic oxide films usually grow on all valve metals in the form of barrier layers. Under specific conditions, a porous layer develops on top of the barrier oxide, characterised by a more-or-less regular arrangement of cylindrical pores oriented with their principal axe normal to the sample

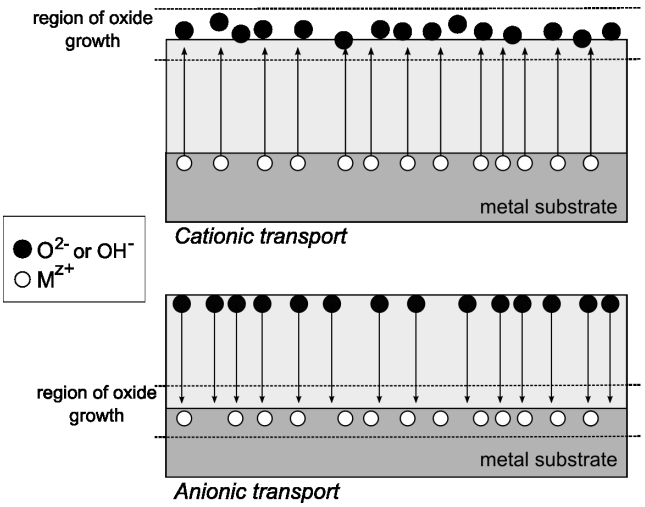

Figure 1.5: Illustration of the influence of the type of ionic transport on the location of new film growth.

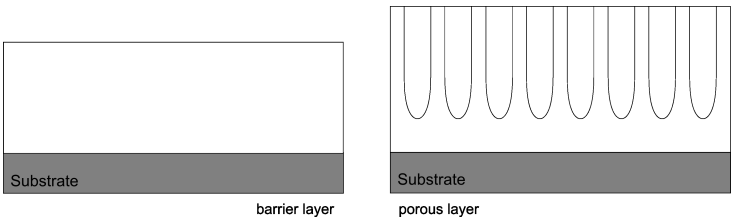

Figure 1.6: Representation of a barrier and porous oxide films.

surface [147]. This is illustrated on Fig.1.6. The tendency to adopt a porous morphology depends on the metal oxide and the electrolyte. For instance, the formation of such porous layers is observed for Al in the most acidic electrolytes while, in contrast, it is observed only in fluorine-containing solutions in the case of Ti [141]. The formation of porous oxide has not been studied in the present work. Therefore, all discussions in this thesis focus mainly on the growth of barrier films.

Amorphous and crystalline oxide: Regarding the structure of anodic oxide films, there is no general trend among the different metal oxides. On some metals, the anodic oxide films are observed mainly as an amorphous phase. This is the case of Al and Nb, for instance. On other metals, mainly Hf and Zr, the opposite trend is observed, with the oxide films being generally fully crys-

talline, even at low formation voltages [133]. Finally, in the case of Ti, the oxide films are usually observed to be initially amorphous but partial crystallisation of the film can take place during the growth, depending on the experimental conditions.

Breakdown: Homogeneous anodic oxide films cannot grow infinitely. Their growth is always limited by the breakdown of the film. The latter consists of a local increase of the electronic conductivity of the film, which strongly perturbs the growth process and leads to the formation of oxide films having a specific morphology. Breakdown can have many different origins, which are discussed more extensively in section 1.1.3.

At this point, the main concepts which will be used throughout this manuscript have been introduced. In the following section, the growth kinetics of anodic oxide films are discussed.

1.1.2 Growth kinetics of anodic oxide films

One of the most fundamental cornerstones of general kinetics theory is that, the overall kinetics of a given process consisting of a series of successive steps is determined by the rate of the slowest step. As illustrated on Fig.1.7, typical electrochemical processes involve:

- the transport of reactants to both the cathode and the anode
- a couple of electrochemical reactions, involving charge transfer reactions
- the transport of the reaction products away from both electrodes

Each of those steps can be the rate-limiting step. As compared to such classical electrochemical processes, anodisation involves one supplementary step as a result of the solid oxide film covering the anode and through which charge and mass must be transported. It is generally agreed that, under usual experimental conditions, the rate of the anodisation process i.e. the rate of growth of the anodic film, is limited by this supplementary solid-state mass-transport step. Therefore, specific kinetic models apply to anodisation, which differ in some respect from the classical ones for homogeneous electrochemical processes.

There are two main classes of models describing the kinetics of anodisation, corresponding to a **high-field** and a **low-field** treatment of the migration kinetics. According to high-field theories, the ionic current density associated with the migration of one type of ion, for instance metal cations, through the film varies exponentially with the electric field within the film according to [241, 10, 139]:

$$i_c = i_o exp\left(\beta \cdot E\right) \tag{1.1}$$

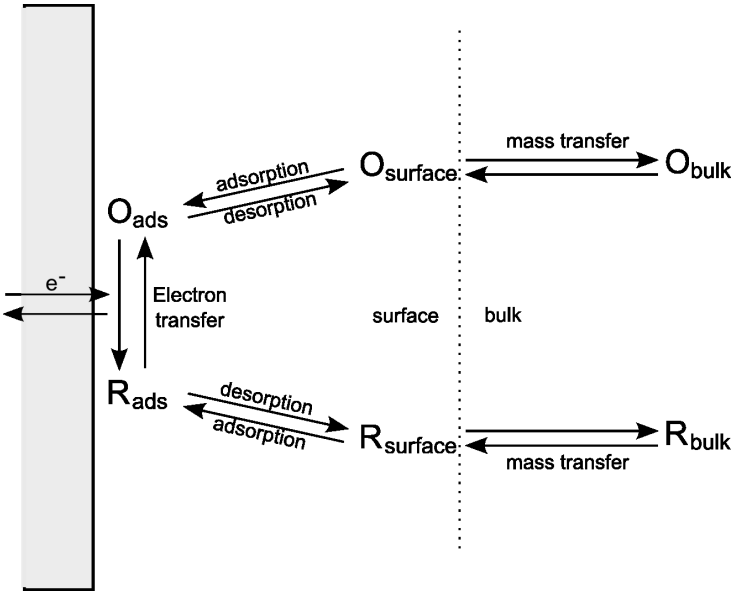

Figure 1.7: Schematic representation of the sequence of steps typically involved in an electrochemical reaction. 'O' and 'R' represent the oxidised and reduced form of a redox couple.

The contribution of diffusion to the ion transport is postulated to be negligible as compared to the migration. In contrast, low-field models consider that the effective electric field in the film is low, due to shielding effects at the interfaces, so that the classical Fick and Nernst-Einstein equations apply to the transport of ions through the film. As a result, the current density associated with the migration of metal cations is given by:

$$i_c = -zFD_c\frac{dc_c}{dx} - zF\mu c_c\frac{d\Phi}{dx} \tag{1.2}$$

where z is the charge of the metal cations, F is Faraday's constant, D is the diffusion coefficient, μ is the electrochemical mobility and c stands for concentrations. The subscript 'c' refers to cationic transport. In Eq.1.2, the first term represents the contribution from diffusion and the second term the contribution from low-field migration [37].

So far, there is no general agreement as to which approach should be used. Both high-field and low-field approaches have been reported to be coherent with some series of experimental data. In the following paragraphs, the high-field and low-field theories are presented in more details.

The low-field approach

The main model based on the low-field approach is the point-defects model (PDM) presented by Macdonald and co-workers in 1981 [37] and further developed in more recent publications of this group [142]. The PDM, originally developed for Fe passivation, was based on the following hypotheses:

1. The oxide film contains a significant concentration of points-defects, namely oxygen and metal vacancies. The ionic current through the film is carried by such vacancies.

2. The oxide film grows at the metal/oxide interface only, by migration of anions inwards. Cationic transport leads to the ejection of metal cations into the electrolyte, which, depending on the electrolyte, can lead to the formation of a porous precipitated oxide layer on top of the barrier one. However, the formation of the porous layer is not taken into account by the PDM.

3. The rate-limiting step of the process is the diffusion of the anions through the film.

4. Adopting the Kroger-Vink notations, the reactions taking place at the metal/oxide and oxide/electrolyte interface and responsible for the creation and annihilation of the point defects can be written as :

$$m \Leftrightarrow M_M + \frac{\chi}{2}V_{O^{\cdot\cdot}} + \chi e^- \tag{1.3}$$

$$m + V_{M^{\chi\prime}} \Leftrightarrow M_M + \chi e^- \tag{1.4}$$

$$V_{O^{\cdot\cdot}} + H_2O \Leftrightarrow 2H^+(aq) + O_O \tag{1.5}$$

$$M_M \Leftrightarrow V_{M^{\chi\prime}} + M^{\chi+}(aq) \tag{1.6}$$

5. The electric field in the film is buffered by electron/hole pair generation at the film/electrolyte interface, so that the field strength (E) within the film is independent of the applied voltage and oxide thickness (h_f). Only the potential drop $\phi_{f/e}$ across the oxide/electrolyte interface varies with the applied potential while the metal/film interface is considered to be in equilibrium (hence being characterised by a constant potential drop $\Phi_{m/f}$).
$$V_{ext} = \phi_{m/f} + \phi_f + \phi_{f/e} = \phi_{m/f} + E \cdot h_f + \phi_{f/e} \tag{1.7}$$

6. The potential drop $\phi_{f/e}$ at the film/electrolyte interface is assumed to vary linearly with pH and external applied voltage, as expected for a polarisable interface:
$$\phi_{f/e} = \phi^o_{f/e} + \alpha V + \beta pH \tag{1.8}$$

The constitutive equations of the PDM linking the thickness of the oxide film to the experimental conditions were derived in the following way. According to the PDM, the rate of increase of the thickness of the oxide film is proportional to the flux of oxygen vacancies crossing the film $J_{V_{O''}}$(see Hyp. 2).

$$\frac{dh_f}{dt} = \frac{\omega}{N_{AV}} J_{V_{O''}} \tag{1.9}$$

where ω is the thickness of oxide formed per unit area and corresponding to 1 mole of oxygen. The flux of oxygen vacancies crossing the film obeys the generalised Fick's first law, describing diffusion in the presence of both a concentration and a potential gradient.

$$J_{V_{O''}} = -D_{V_{O''}} \frac{dc_{V_{O''}}}{dx} - D_{V_{O''}} \frac{c_{V_{O''}}}{RT} 2F \frac{d\phi}{dx} \tag{1.10}$$

$D_{V_{O''}}$ is the electrochemical diffusivity of oxygen vacancies. In order to calculate $J_{V_{O''}}$ from the differential equation Eq.1.10, one must know the boundary conditions, i.e. the concentration of oxygen vacancies at both interfaces. The latter concentrations are calculated from the potential difference at the metal/film and film/electrolyte interfaces and the ΔG° values associated with the reactions consuming and producing vacancies (Eq.1.3 to Eq.1.6). Following this procedure, Macdonald et al. arrive at the following equation for the evolution of the film thickness:

$$\frac{dh_f}{dt} = \frac{A(B-1)}{\exp(2Eh_f) - 1} \tag{1.11}$$

where A and B are functions of the external applied potential V_{ext}, the solution pH, the constant field E in the film and the ΔG° of reactions Eq.1.3 to 1.6. Under potentiostatic conditions, Eq.1.11 can be further expressed as [37]:

$$h_f(t) = \frac{1}{2E}\left[\ln\left(2EA\left(B-1\right)\right) + \ln t\right] \tag{1.12}$$

The latter equation predicts a logarithmic growth, as indeed experimentally observed. Under galvanostatic conditions, Eq.1.11 can be transformed into:

$$i = \frac{A \cdot (B-1) \cdot 2FN_{AV}}{\Omega exp(2Eh_f)} \tag{1.13}$$

hence providing a relationship between current density, electric field and oxide thickness. The PDM equations are obviously much more complicated than the one for the high-field model (Eq.1.1) and analytical predictions of the influence of the various parameters is not straightforward.

It is worth mentioning other models based on the PDM, for instance the one by Pyun and Hong [193], Krishnamurthy [121, 122, 123] or Bojinov [28]. Pyun and Hong transposed the PDM to the growth of anodic films at the oxide/electrolyte interface by cationic migration (instead of the purely anionic transport postulated in the PDM). These authors logically obtain constitutive equations which are formally very similar to those of the original PDM. The formalism adopted by Krishnamurthy et al. is interesting in that it allows describing the film formation as a moving-boundary problem. Krishnamurthy et al. also introduce dimensionless formulation of the kinetic equations. Bojinov has adopted the same interfacial reactions and constant field hypothesis as in the PDM but relaxes the PDM hypotheses relative to the low-field motion of the ions, which is no longer described by the Nernst-Planck equation but in a more general way [28]. In those models, however, mixed transport cannot be taken easily into account. The model proposed by Battaglia and Newmann [18] is based on a similar low-field approach and is a priori adapted to situations when multiple charge carriers contribute to the current, although this renders the derivation of the constitutive kinetic equations very complex.

The high-field model

The following derivation of the high-field equation is essentially reproduced from the review paper by Lohrengel on the high-field model [139]. Let us consider two successive atomic planes of the oxide film located at positions x

and $x + a$ along the X-axis normal to the metal/film interface. [1] These planes contain, respectively, a number n_x and n_{x+a} of charge carriers (for instance interstitial metal cations or oxygen vacancies) per unit area. The latter charge carriers can jump to an adequate site on an adjacent atomic plane, with an activation barrier W being associated with this movement. Accordingly, the probability p for one mole of charge carriers to jump from a position x to a position $x + a$ is given by:

$$p = \nu \exp\left(\frac{-W}{RT}\right) \tag{1.14}$$

where ν is the attempt frequency. In the absence of an applied electric field, the activation barrier is symmetric and the probability for a charge carrier to jump in the opposite direction from $x + a$ to x is also given by Eq.1.14. Hence the molar flux of atoms between x and $x + a$ is given by:

$$\frac{dn}{dt} = n_x \nu \exp\frac{-W}{RT} - n_{x+a}\nu \exp\frac{-W}{RT} \tag{1.15}$$

Now, when an electric field E is applied, the activation barrier is lowered for the jump in the direction of the field and increased in the opposite direction, as illustrated on Fig.1.8. As a result,

$$\frac{dn}{dt} = n_x \nu \exp\frac{-(W - \alpha azFE)}{RT} - n_{x+a}\nu \exp\frac{-(W + (1-\alpha)azFE)}{RT} \tag{1.16}$$

where α is a coefficient describing the symmetry of the activation barrier, so that $\alpha \cdot a$ defines the position of the maximum of the activation barrier. If we express Eq.1.16 in terms of concentrations instead of number of moles per unit area (using $c_x = n_x/a$) and calculate the concentration of charge carriers at $x + a$ considering a linear concentration gradient according to:

$$c_{x+a} = c_x + a\frac{dc}{dx} \tag{1.17}$$

it yields :

$$\frac{dn}{dt} = a\nu \exp\frac{-W}{RT}\left[c_x exp\left(\frac{\alpha azFE}{RT}\right) - \left(c_x + a\frac{dc}{dx}\right) exp\left(\frac{-(1-\alpha)azFE}{RT}\right)\right] \tag{1.18}$$

The high-field approach then postulates that, due to the strong electric field, the contribution from diffusion is negligible as compared to that of migration (i.e. $dc/dx \approx 0$) and that migration in the reverse direction, against the field, is negligible as well. According to Van Rysselberghe, this should be the case for

[1] It should be noted that, while the notion of 'atomic planes' tacitly assumes that the oxide film is crystalline, the conclusions remain valid in the case of amorphous films as well.

large enough current densities ($>5\mu A/cm^2$) [241]. Under these assumptions, Eq.1.18 simplifies to:

$$\frac{dn}{dt} = \nu a c_x \exp\left(\frac{-W}{RT}\right) \exp\left(\frac{\alpha a z F E}{RT}\right) \tag{1.19}$$

In the case of an electrochemical environment, the current density is proportional to the flux of the charge carriers so that:

$$i = zF\frac{dn}{dt} \tag{1.20}$$

If we define two parameters i_o (primary ionic current) and β (field factor) as, respectively:

$$i_o = zF\nu a c_x exp\left(\frac{-W}{RT}\right) \tag{1.21}$$

and

$$\beta = \frac{\alpha a z F}{RT} \tag{1.22}$$

equation Eq.1.20 can be written as:

$$i = i_o \exp\left(\beta \cdot E\right) \tag{1.23}$$

This is the usual form of the classical equation for high-field models.

As pointed out by Lohrengel, the general model described above does not require any assumption as to the position of the activation barrier. According to Verwey, the rate-limiting step is the transfer of charge-carriers through the bulk of the film according to the high-field migration. Mott and Cabrera [35], in contrast, consider that the rate-limiting step is the injection of cations from the metal into the oxide film. Within this framework, the activation barrier associated with the high-field model would be located at the metal/film interface, but the growth kinetics would obey the same equation. The high-field model does not either make any a priori assumption as to the type of charge carrier. While, in the very first description of the high-field model by Guntherschultze and Betz, both anions and cations were assumed to contribute to the ionic current, Mott and Cabrera [35], Verwey and Bean [19] later postulate that the current is carried by interstitials metal cations only, while Fehlner and Mott make the converse assumption and postulate anion migration-induced growth [139]. From studies on the transport coefficients in anodic oxide films, it is now well established that, for most valve metals (Ta, Al, Nb, Ti), both anions and cations are mobile and contribute to the growth of the oxide film, while anionic transport is largely dominating in the case of the anodic films grown on Hf and Zr [45]. Therefore, rigorously, in the case when both anions and cations

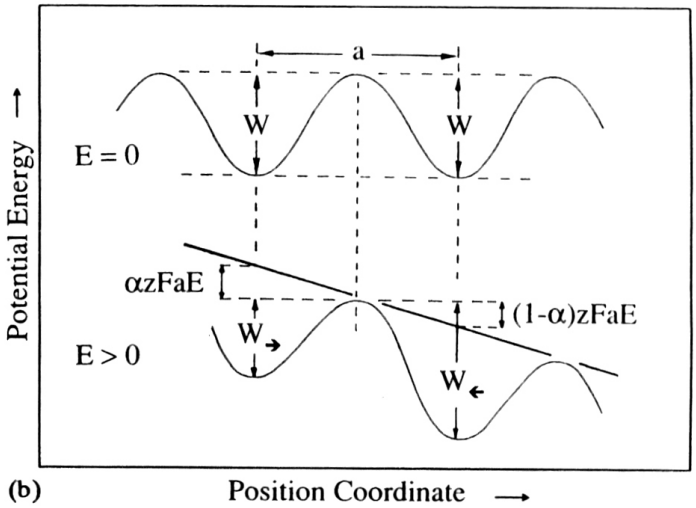

Figure 1.8: Schematic representation of the energy barrier associated with the transfer of a charge carrier between two adjacent planes, respectively in the absence and in the presence of an applied electric field (reproduced from Lohrengel [139]).

contribute to the ionic current density, both the anionic and cationic current densities are described by a high-field equation, with adequate coefficients $i_{o,a}$, $i_{o,c}$, β_a and β_c. The total ionic current density would be given by:

$$i_i = i_{o,a} \exp(\beta_a \cdot E) + i_{o,c} \exp(\beta_c \cdot E). \tag{1.24}$$

The latter expression is less straightforward than the classical high-field equation Eq.1.23 and contains four unknown parameters $i_{o,a}$, $i_{o,c}$, β_a and β_c instead of two. However, in the literature, Eq.1.23 is generally used and it is postulated that one type of charge carriers is largely dominating [92]. Finally, it should be noted that the high-field model doesn't involve any assumption as to whether ions move through the oxide films as interstitials or through a vacancy migration mechanism.

Finally, it is worth mentioning the contributions of Bean [19], Young [264], Kirchheim [114, 115] or Davenport [44] to further refine the high-field model. According to Bean et al., the i_o factor of the high-field model is field dependent in the low-field range. This effect arises from a field-dependence of the activation barrier associated with the production of interstitial metal cations. According to Young, the 'a' parameter from the high-field equation, characterising the length of the jump between two adjacent positions is not constant but

field-dependent due to the electrostriction effect which induces a change in the density of the film. Therefore, he proposes that the current-field relationship should be corrected as:

$$i = i_o \exp\left(\beta \cdot E - \gamma \cdot E^2\right) \tag{1.25}$$

In the case of oxides in which electrostriction strains are large (TiO_2, for instance, as will be demonstrated in chapter 4), this could be an important effect to take into account. Kirchheim has proposed an improved version of the high-field model. In contrast to the models derived by Cabrera and Mott or Verwey in which the potential drops at the interfaces are supposed to be constant (equilibrium conditions), Kirchheim takes into account the possibility of having overpotentials (ϕ_η) at the film/electrolyte interface, which vary with the current density:

$$V_{ext} = \phi_{m/o} + \phi_f + \phi^o_{o/e} + \phi_\eta \tag{1.26}$$

He also integrates in his model the step of production of the charge carriers. This allows accounting for the observations from current and voltage transient experiments. Davenport et al. followed the approach of Kirchheim and showed that the external applied potential can be separated into the potential difference ϕ_f across the film and a potential difference ϕ_{inter} at the interfaces. The latter was demonstrated to follow a Tafel relationship. It should be noted that, for constant current conditions, the overpotentials are expected to keep a constant value, so that neglecting this contribution leads to a slight overestimation of the field ΔV_f applied to the film. Correcting the cell voltage values for the contribution from the overpotentials is mainly important in the case of galvanostatic transient experiments and leads to a limited error in the case of galvanostatic anodisation.

Both the low-field and high-field models have been presented in this section in order to give a general overview of the main models describing the growth kinetics of anodic oxide films. However, in the following sections and chapters, the kinetics of anodisation will always be discussed in reference to the high-field model. This choice is justified mainly by the fact that the high-field theory is more widely accepted for valve-metal anodising while the coherence of the PDM-based models has been demonstrated mainly for the passivation of iron and nickel. The simplicity of the high-field equation, as compared to the PDM one, further provides a considerable advantage. It should be noted that recent tracer experiments have demonstrated that, besides diffusion and migration, stress-induced material flow (creep) contributes as well to the mass transport in thick porous anodic oxide films [65, 134]. Transport models taking into account the contribution of viscous flow have recently been developed by the group of Kurt Hebert [90]. Whether creep contributes as well to material transport in barrier films is so far open question. In the following paragraph, the high-field

equations are discussed in the specific case of galvanostatic, potentiostatic and potentiodynamic anodisation.

Discussion of the kinetic equations

Galvanostatic conditions: Under galvanostatic conditions, the electric field in the oxide film is related to the constant applied current density according to

$$E = \frac{(\ln i - \ln i_o)}{\beta} \tag{1.27}$$

Provided that no modification of the experimental conditions (the temperature, for instance) or of the characteristics of the growing oxide film (e.g. its density) take place, i_o and β keep constant values, so that the growth of an anodic oxide film under galvanostatic conditions proceeds under constant field conditions as well. A direct consequence of this is that the potential drop across the anodic film ϕ_f increases linearly with its thickness. Furthermore, in the ideal case when the growth efficiency remains constant throughout the growth process, the thickness of the oxide film increases linearly with time, according to the Faraday law:

$$h_f = \Omega i t \tag{1.28}$$

where Ω is the effective thickness of oxide film formed per unit charge. If ϕ_f is assimilated to the cell voltage V (hence neglecting the potential drops at the interfaces),

$$E = \frac{V}{h_f} \tag{1.29}$$

Combining equations 1.27, 1.28 and 1.29, the cell voltage is predicted to increase with time at a constant rate:

$$V = \left(\frac{\Omega i \, (\ln i - \ln i_o)}{\beta} \right) t \tag{1.30}$$

Fig.1.9 shows a typical V-t curve for the growth of an anodic oxide film on an Al-Nb alloy, in the ideal case described above.

Potentiodynamic conditions: Under potentiodynamic conditions, the anode potential is swept at a rate v from the open circuit potential to a formation voltage. Starting from the high-field equation as expressed on Eq.1.27 and assimilating again ϕ_f to the cell voltage yields:

$$\frac{v \cdot t}{h_f} = \frac{(\ln i - \ln i_o)}{\beta} \tag{1.31}$$

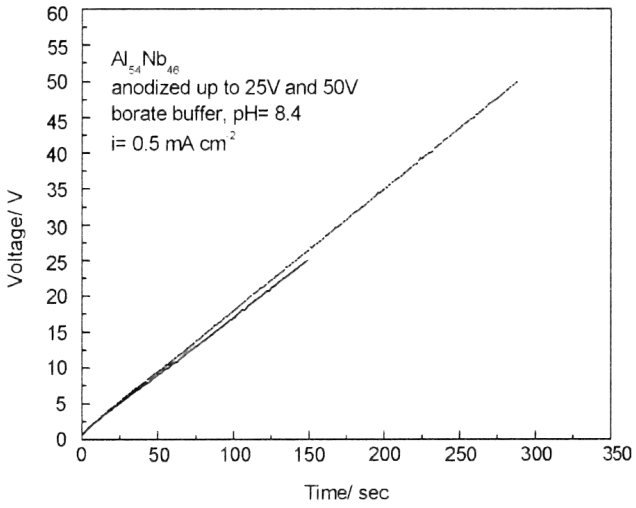

Figure 1.9: Typical time-evolution of the cell-voltage during an anodisation experiment carried out under galvanostatic conditions and exhibiting ideal behaviour. This figure is reproduced from Janik-Czachor et al. [101].

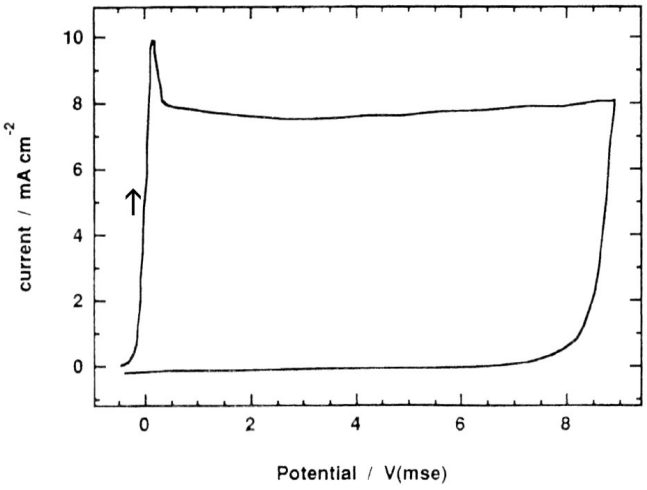

Figure 1.10: Typical cyclic voltammogram corresponding to the potentiodynamic growth of an anodic oxide film, reproduced from Di Quarto et al. [53].

Considering again the ideal case of constant growth efficiency and thus expressing h_f as in Eq.1.28, rearranging Eq.1.31 yields :

$$i\,(\ln i - \ln i_o) = \frac{\beta v}{\Omega} \tag{1.32}$$

According to the previous equation, scanning the potential at a constant rate is expected to give a constant current. Fig.1.10 shows a typical cyclic voltammogram for the potentiodynamic growth of an anodic oxide film on Ti, reproduced from Di Quarto et al. [53]. After the initial current increase at 0V, the current is observed to keep a constant value in the range of 0.5 to 8.5V, as predicted by Eq.1.32. According to equation Eq.1.27, we can conclude that, under these conditions, the oxide film grows under constant field conditions, as in the case of the galvanostatic experiment.
Any deviation from the linear V-t behaviour under galvanostatic conditions, or of the constant current plateau for potentiodynamic growth is interpreted as a perturbation in the growth of the oxide film. Typical perturbations may include:

- a change in the effective growth efficiency due to the onset of a side-reaction, which may lead to a change in the electric field in the film, or associated with a change in the dissolution rate of the oxide film

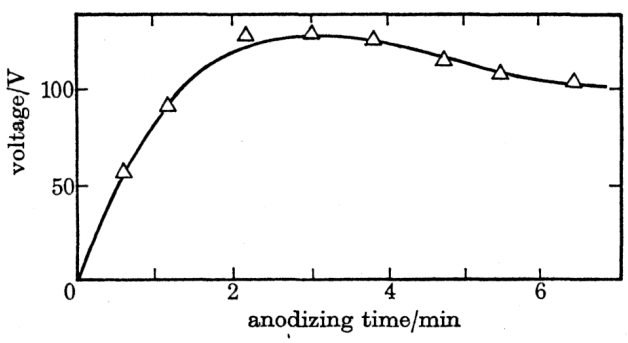

Figure 1.11: V-t curve for the anodisation of Al under galvanostatic conditions in 0.4 M H_3PO_4 electrolyte. A marked transition is observed in the evolution of the cell voltage, corresponding to the transition from the growth of a barrier film to the growth of a porous film. This figure is reproduced from O'Sullivan and Wood [181].

- A change in the structure of the oxide film associated for instance with crystallisation or with the development of a porous or cracked layer

This is illustrated on Fig.1.11, which shows a typical example of V-t curve for galvanostatic anodisation of Al in phosphoric acid with a current density of 5 mA/cm^2. The observed transition from a linear V-t evolution to a V-plateau is associated with the transition from a barrier film growth to a porous film growth [181].

Potentiostatic conditions: Under potentiostatic conditions, the prediction of the growth kinetics is less straightforward than in the previous two cases. The electric field in the film will decrease rapidly as the thickness of the anodic oxide film increases and, therefore, the growth rate also. Equation 1.31 can be presented in the following way:

$$\ln \frac{i(t)}{i_o} h_f(t) = \beta \cdot V \tag{1.33}$$

In the ideal case described above, h_f can be calculated as

$$h_f = \int \Omega \cdot i dt \tag{1.34}$$

Combining the equations 1.33 and 1.34 yields the general time-evolution of the cell current as a function of the applied voltage.

1.1.3 Breakdown of anodic oxide films

Homogeneous growth of anodic oxide films is usually limited by the breakdown of the film. At some stage during the growth process, the oxide film does no longer withstand the high electric field to which it is submitted and a local increase of its conductivity, usually by many decades, is observed, accompanied by a partial destruction of the oxide film [211]. Breakdown can have different origins, depending on the metal oxide and on the processing conditions. The most studied type of breakdown is the dielectric breakdown which, in many respects, is analogous to the breakdown of (dry) dielectrics in metal/insulator/metal structures but also exhibits some specific features which arise from the presence of the electrolyte and from the fact that the film is growing. It has been for long a matter of debate whether dielectric breakdown takes place as a bulk phenomenon or locally, at flaws in the oxide film and whether it originates is electron avalanching or thermal effects. Indeed, some authors proposed that breakdown could be caused by a bulk Joule heating of the oxide film. However, Ikonopisov [99] convincingly showed that this scenario was incompatible with the observation that the breakdown voltage V_b was not modified when the anodisation was interrupted just below V_b, allowing for the film to cool down before pursuing the anodisation process. So, it seems unlikely that the initial triggering mechanism would be a bulk Joule heating. As to the bulk or local nature of the breakdown, evidence in favour of this second possibility has been provided by several authors, for instance Shimizu et al. [216] who demonstrated the role of flaws as breakdown sites on Al_2O_3 films. Young proposed that breakdown could be initiated by a local heating due to the preferential conduction through cracks and flaws [216]. Although such local heating at the breakdown sites is well-established, it is unclear whether the temperature increase triggers breakdown or, conversely, comes as a consequence of it. A correlation between crystallisation and breakdown was established by Yahalom et al. and crystallisation was therefore proposed as another possible cause of breakdown [260]. However, more recent studies have provided evidence that crystallisation results from breakdown rather than causing it [106, 216]. In analogy with the breakdown of dielectrics, Ikonopisov proposed that an electron avalanching could be at the origin of dielectric breakdown in anodic films, with the primary electrons being injected from electrochemical reactions at the oxide/electrolyte interface. He derived a semi-quantitative model accounting for the dependence of V_b on the main experimental parameters. Albella et al. [158, 8] adopted the electron avalanching model from Ikonopisov but claimed that direct injection of electrons from the electrolyte is unlikely and that the primary electron current is rather provided by electrolyte species incorporated in the oxide film. The strong correlation observed by Albella et al. between the primary electronic current and the concentration of incorporated species in the case of Ta anodising (See Fig.1.12) is evidence in favour of their theory. Ac-

cording to their model, the breakdown process would thus require the following steps:

- incorporation of electrolyte species in the film
- ionisation, under the action of the electric field, of the incorporated species. The latter act as donor or acceptor levels in the bandgap of the oxide film depending on the valence of the metal cations and incorporated electrolyte species, which leads to the injection of electrons in the conduction band of the oxide film.
- electrons multiplication due to avalanching
- breakdown when the avalanche current reaches a critical value, as illustrated on Fig.1.13.

Besides dielectric breakdown, other types of breakdown have been reported. Some authors have demonstrated that anodic films can break down as a consequence of mechanical effects. Indeed, cracks in the film constitutes preferential breakdown sites, where the underlying metal is exposed to the electrolyte. Sato [205] derived a model linking the mechanical stress experienced by the oxide film to the electric field and the surface energy of the film at the film/electrolyte interface. He concludes that the compressive electrostriction stresses can be high enough to induce local cracking of the film. Mechanical breakdown was indeed reported by Di Quarto et al. in the case of ZrO_2 films [52]. These authors also demonstrated that this type of breakdown is distinct from the "classical" dielectric breakdown discussed above which, in their experiment, takes place after the mechanical breakdown, at a higher V. Finally, film breakdown can also arise from a corrosion process, associated with the presence of aggressive ions or from anodic corrosion of the film at weak sites.

Growth of oxide films in the breakdown regime

It is worth noting that dielectric breakdown does not impede further growth of the anodic oxide films but leads to the formation of oxide films exhibiting specific morphological and functional characteristics. The growth of anodic oxide films in the breakdown regime has been studied quite extensively during the last decade. This process, usually referred to as 'spark-anodising' or 'plasma electrochemical oxidation' (PEO), allows producing microporous oxide films having a very hard surface and very good self-lubricating properties, hence being of interest for tribological applications. The microporous morphology can also favour osseointegration and PEO anodic oxide coatings are therefore studied as well for biomedical applications. The growth of anodic films on the breakdown regime has not been investigated in this work and will therefore not been further described. More information can be found for instance in references [262] and [153].

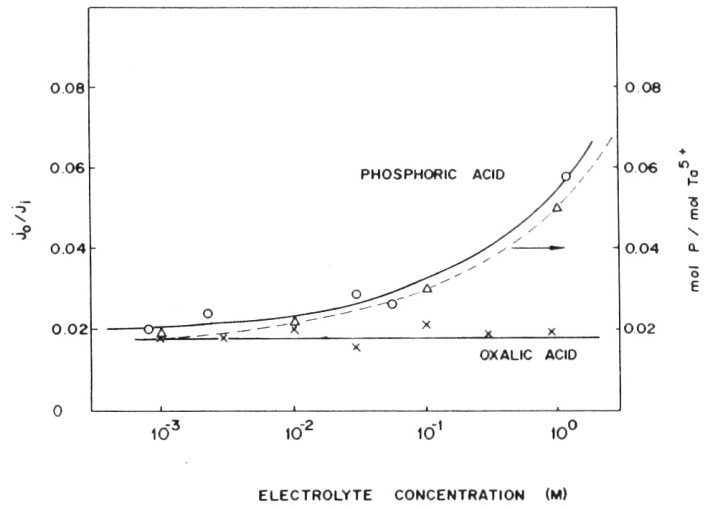

Figure 1.12: Evolution of the primary electronic current j_o (expressed in relative form, j_i being the ionic current) and of the concentration of incorporated species with the electrolyte concentration, reproduced from Montero et al. [158]. The cases of an incorporating (H_3PO_4) and non incorporating (oxalic acid) electrolyte are compared.

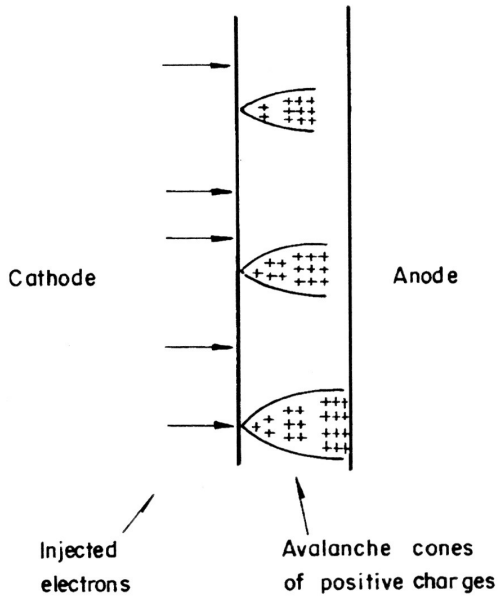

Figure 1.13: Schematic representation of the electron avalanching phenomenon, reproduced from Albella et al. [9].

1.2 The specific features of Ti anodisation

With respect to the anodising behaviour, the main specific feature of Ti as compared to other typical valve metals is the semiconducting character of its anodic oxide. As pointed out in the introduction of this chapter, one requirement for a metal to be suitable for anodisation is that its oxide is a poor electronic conductor. In fact, TiO_2 exhibits a marked n-type semiconducting character and Ti is therefore a priori not the best candidate for anodisation. A direct consequence of the significant e^- conductivity of the growing anodic TiO_2 films is that, besides the ionic current responsible for film growth, an electronic current, associated with side-reactions taking place at the surface of the oxide film, can flow through the film. Therefore, under galvanostatic conditions, there is a competition between oxide growth and other electrochemical oxidation side-reactions (mainly the oxygen evolution reaction (OER)). A significant fraction of the imposed current can be consumed in side-reactions, hence directly decreasing the efficiency for film formation and slowing down the growth process. In the case of potentiostatic or potentiodynamic processes, the growth process is not slowed down by the side-reactions but the coulombic efficiency is decreased due to a large supplementary current being consumed in side-reactions. In addition, as will be discussed extensively in this work, the side-reactions can profoundly influence the growth process as well.

1.2.1 Influence of the semiconducting character of anodic TiO_2

Electronic properties of anodic TiO_2 films

The e^- conductivity of metal oxides ranges from that of insulators to semiconductors and even conductors. Their conductivity depends on the width of the oxide bandgap and on the position of the Fermi level within the bandgap [206]. Crystalline metal oxides present a band structure of e^- energy levels typical for ionic crystals, with a valence band formed from the 2p orbitals of oxygen while the conduction band is composed of the outer orbitals of the metal ions [211]. Al, which belongs to the family IIIA of the periodic table, is a typical example of such metal oxides, as illustrated on Fig.1.14. The valence band of alumina is formed from the 2p orbitals of oxygen atoms while the conduction band is formed from the 3s and 3p orbitals of Al. The valence and conduction bands are separated by a wide bandgap of 7 eV, responsible for the marked insulator behaviour of Al_2O_3. In the case of transitional metal oxides (such as TiO_2), the supplementary contribution from the d-orbitals of the metal to the conduction band of the oxide results in a reduction of the bandgap [206].

In the case of TiO_2, the valence and conduction bands are separated by a

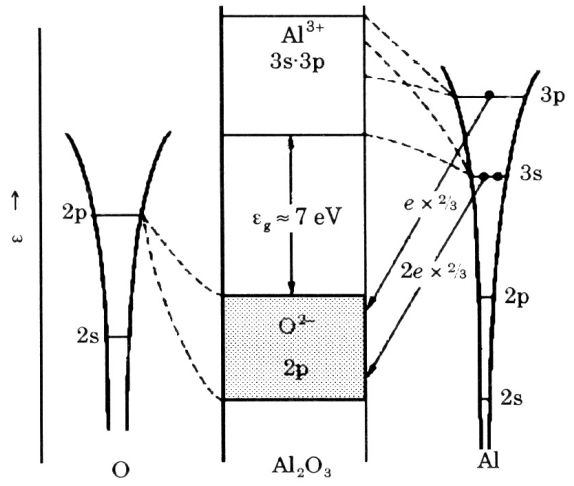

Figure 1.14: Illustration of the formation of the electronic bands of Al_2O_3 from the atomic orbitals of Al and O, reproduced from Sato et al. [206].

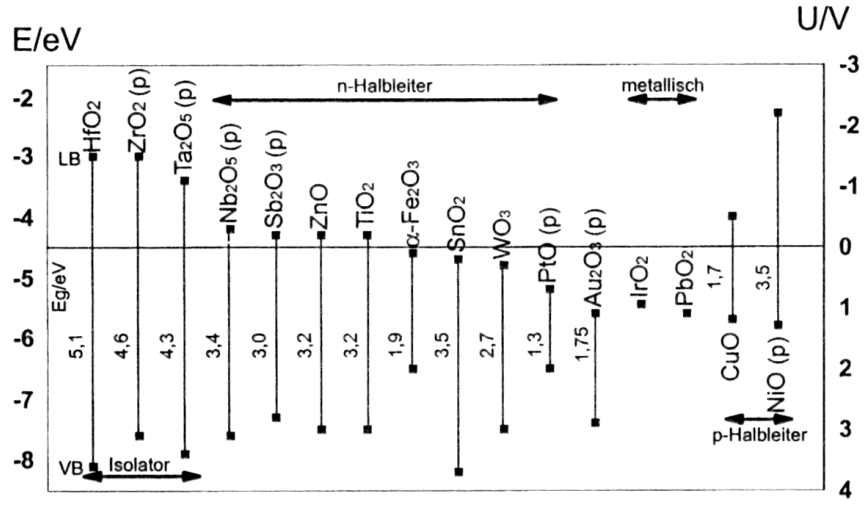

Figure 1.15: Comparison of the bandgap values of typical metal oxides, reproduced from Schultze et al. [211]. TiO_2 is observed to belong to the semiconductor oxides.

gap of 3.2 eV (TiO_2 anatase) or 3.06 eV (TiO_2 rutile) [67]. As compared to other metal-oxides, TiO_2 has a quite narrow bandgap, as illustrated on Fig.1.15, reproduced from Ref.[211]. Owing to its low bandgap, TiO_2 is expected to have a more pronounced semiconductor behaviour than, for instance, HfO_2 or Al_2O_3, which is indeed experimentally observed. The bandgap of ionic metal oxides is a function of the bond energy [206] and has been shown to be proportional to the difference of the Pauling electronegativity of the oxygen anion and metal cation (χ_M and χ_O) [54]. The following semi-empirical equation has been proposed by Di Quarto et al. for assessing the bandgap of transitional d-metals [54]:

$$E_g[eV] = 1.35\left(\chi_M - \chi_O\right)^2 - 1.49 \tag{1.35}$$

The two numerical constants apply to oxides of d-transitional metals and take other values in the case of sp metals (Al for instance). The Pauling electronegativity of oxygen is around 3.44 eV, while that of Ti is around 1.66 eV [202].

With respect to the ideal structure of a perfect ionic crystal described above, anodic oxide films present supplementary energy states within the bandgap associated with the various types of structural defects:

- 1D defects: all punctual defects in the oxide film like oxygen or Ti vacancies, Ti interstitials and interstitial or substitutional heteroatoms introduce energy levels in the bandgap. In the case of TiO_2, oxygen vacancies would be the main type of defects, giving rise to donor levels close to the conduction band [197].

- 2D defects: the presence of dangling bonds at the film surface or at interfaces (grain- or phase boundaries) provide a second type of electronic defects of considerable importance [206].

- amorphous films: although the long range order characteristic for crystalline materials is not present in amorphous materials, the short range order is sufficient to give rise to a band-like structure of e^- energy states. However, the edges of the bands become indistinct owing to local variations of the bond distances and bond energies [206]. The concept of bandgap is replaced by that of a 'mobility gap' with a trail of localised states within the bandgap (See Fig.1.16). The mobility gap is slightly larger than the corresponding bandgap for the crystalline oxide. According to Di Quarto et al., Eq. 1.35 for the bandgap of crystalline d-transitional metal oxides can be adapted to amorphous materials as follows:

  $$E_g^{opt} - \Delta E_{g,am} = 1.35\left(\chi_M - \chi_O\right)^2 - 1.49 \tag{1.36}$$

  where $\Delta E_{g,am}$ corresponds to a enlargement of the effective gap associated with the amorphous structure. Typical values for the latter contribution amount to 0.1 to 0.5 eV, depending on the degree of order of the

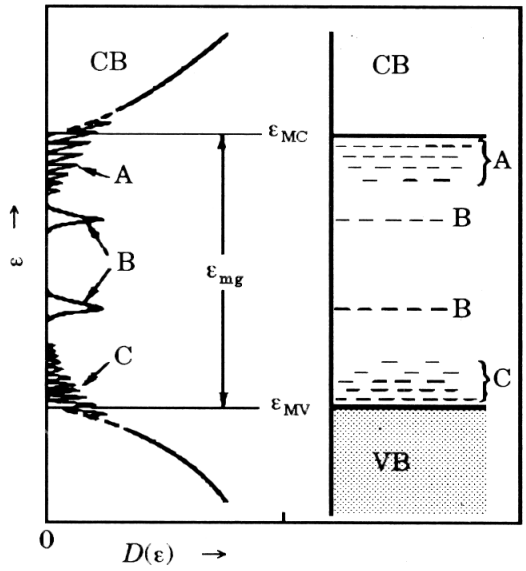

Figure 1.16: Illustration of the concept of 'mobility gap' of amorphous oxide films, reproduced from Sato [206].

material [202]. Therefore, direct injection of electrons from the valence band to the conduction band is expected to be more difficult in amorphous films as a consequence of the enlarged bandgap. However, other conduction modes can contribute to e^- transport in amorphous films. According to Leiva [138], if a sufficient concentration of defects is present in the oxide film, electronic conduction is possible by a hopping mechanism from one defect to another (percolation).

The electronic properties of anodic TiO_2 films evolve in the course of the growth process, as evident from impedance or photoelectrochemical studies [137, 146]. Typically, TiO_2 films exhibit semiconducting properties only above a given voltage (under galvanostatic conditions) or after a given anodisation time (under potentiostatic conditions). Changes in the electronic properties are likely to result from progressive changes in the film stoichiometry (hence a variation in the donor density) and in the degree of order of the film (hence inducing a progressive decrease of the $\Delta E_{g,am}$ in Eq.1.36). These transformations of the oxide film, which are associated with oxide crystallisation will be discussed in subsection 1.2.2.

Side-reactions accompanying anodisation

Owing to the semiconducting character of TiO_2, large electronic currents can flow through anodic TiO_2 films, arising from side-reactions taking place on the oxide surface. Delplancke et al. [49] have studied the current efficiency associated with oxide growth and with the various side-reactions during galvanostatic anodisation of Ti in sulphuric medium. He found that, besides oxygen evolution which is by far the main side-reaction, a fraction of the total current is also consumed for peroxide formation. The overall fraction of the current which was effectively used for oxide growth amounts to about 10% [49]. Other authors [242] report efficiency values slightly larger but still well-below 100% for Ti anodisation in the voltage region where oxygen evolution takes place.

To the best of our knowledge the exact mechanism of oxygen evolution on anodic TiO_2 films has not yet been identified. Boddy [27] has carried out studies on the OER on TiO_2 monocrystal electrodes. He concludes that surface states play a major role in the OER. According to his proposed mechanism, e^- would be injected from surface states into the conduction band of the oxide film and the resulting hole would be rapidly annihilated by an electrochemical reaction taking place on the surface of the oxide film. Recently, this scenario has been cited by Roh et al. [197] as well but has not been confirmed so far. The bulk TiO_2 crystals used by Boddy for his experiments are likely to have a smaller defect concentration than anodic TiO_2 films, which might be the reason for the dominant role of surface states. It is not unlikely that the conduction mechanisms would be different in the case of anodic films. Schultze et al. [210] proposed that the rate-determining step for the oxygen evolution reaction on metals covered with semiconducting oxide films with high donor densities is the electron transfer between an adsorbed species and the oxide film or the metal. The OER might involve a partial dissolution of the anodic film, as suggested by Delplancke et al. [49] and Vergé et al [242]. The latter authors indeed observed a mass loss of their Ti anode, measured using an electrochemical quartz microbalance (EQCM), correlated with the voltage at which the oxygen evolution sets off.

Evidence has been provided by Habazaki et al. [76] that oxygen evolution can take place as well within anodic TiO_2 films, with fine oxygen bubbles being formed around anatase nanocrystals (see Fig.1.17). According to Zhuravlyova [265], the oxygen gas would be produced as a solid-state oxidation of O^{2-} ions from the film material at flaws, where impurity levels are locally increased. Matykina et al. [154] have provided supplementary evidence that oxygen gas evolved within anodic TiO_2 films can form high-pressure gas-filled cavities which grow, coalesce and finally lead to local rupture of the films, allowing for release of the gas. According to their observations, the oxygen evolution

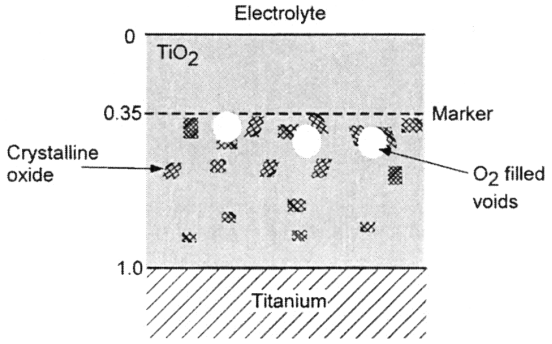

Figure 1.17: Schematic illustration of oxygen evolution within anodic TiO_2 films, reproduced from Habazaki et al. [76]. Oxygen bubbles are formed around anatase nanocrystals.

within the film would be associated with the formation of rutile nanocrystals, which would be facilitated at the metal/oxide interface on basal-like Ti grains. Hence, in addition to decreasing the growth efficiency, the side-reactions can have a more profound impact on the growth process and the characteristics of the film.

1.2.2 Crystallisation of TiO_2 films

Anodic TiO_2 films are usually reported to be initially amorphous, then to crystallise progressively in the course of the growth process[2]. First, isolated crystallites with an average size of 10 nm form in an amorphous matrix. Their size and number then increase with increasing anodisation time or voltage, to yield a polycrystalline microstructure. This was shown in TEM studies carried out by Jouve et al. [106] Shibata et al. [215] and Marsh et al. [146]. Usually, amorphous TiO_2 is observed to crystallise mainly to anatase at first. Transformation of anatase to rutile, the high-temperature allotropic form of TiO_2, is usually observed to accompany the breakdown of the oxide film, as a result of the high temperatures attained locally [186, 70]. However, evidence of the presence of rutile crystallites before breakdown has been shown as well in some studies [48, 253, 154]. Both crystalline phases are tetragonal, but have very different cell parameters. The crystalline cell for anatase and rutile are represented on Fig.1.18.

[2]Only a few studies [253, 259], in which the oxide films are grown at a particularly low rate (0.1 mV/s) report the formation of crystalline TiO_2 from the beginning on the anodisation

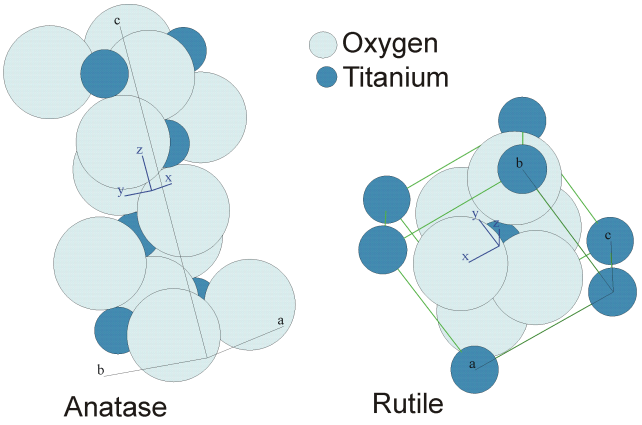

Figure 1.18: Representation of the cell of anatase and rutile TiO_2, reproduced from the CaRIne 3.0 software database.

Even before crystallites are clearly observable by TEM, re-arrangements of the atoms towards a more ordered structure take place. Marsh et al. [146] report that their samples anodised below 10V do not yet show clear evidence of crystallisation when observed in TEM. In contrast, they observe a significant modification of the photoelectrochemical behaviour of their oxide films between 5V and 10V, characterised by a marked decrease of the sub-bandgap activity, which suggests evolution towards a more ordered film. Habazaki et al. [76] also conclude that nanocrystals of anatase grow from zones of relatively ordered oxide of sub-nm size. X-ray absorption (XAS) studies carried out by da Fonseca et al. confirm the fact that a short range order exists in the oxide film before crystallisation can be detected by X-ray diffraction under grazing incidence conditions (GXRD) [43]. These authors observed a short-range structure consisting of clusters of 11 atoms, involving a first Ti-shell surrounded by an O-shell and a second Ti-shell.

Most experimental observations point out to the conclusion that crystallisation is a slow thermally-activated process. Indeed, crystallisation is promoted by low growth rates [253, 259], by long anodisation times, by potentiostatic aging [16, 43, 127] and elevated temperatures [215]. In contrast, crystallisation is delayed at low T°, high growth rates and is also complicated when the short range order of the oxide film is reduced, for instance in the case of Ti alloys or when anodisation is carried out in an electrolyte which migrates inwards in the oxide film and becomes therefore incorporated into the inner part of the oxide film (see section 1.2.4).

According to the TEM studies carried out by Habazaki et al. [76], only the inner part of TiO_2 films, the one formed at the metal/oxide interface by anion migration inwards, crystallises, while the outer part of the oxide film remains amorphous. In the case of anodic oxide films grown on Ti alloys, the first crystallites are formed in the region adjacent to the plane separating the inner and outer part of the oxide film. Habazaki et al. also observe that aging the Ti alloy in air for several weeks prior to the anodisation favours crystallisation. Based on this observation, they propose that crystallisation would be initiated from crystalline nuclei already present in the native air-formed oxide film.

The presence of specific ions in the electrolyte can influence directly the crystallisation process. In a recent study by Kunze et al. [127], it was shown that the presence of F^- ions in the electrolyte favours the crystallisation of the film to rutile while, in F^--free electrolytes, the TiO_2 films crystallise to anatase. The atomistic origin of this phenomenon has not yet been identified. A relationship might exist as well between internal stresses and crystallisation. Indeed, some authors [260, 133, 214] have proposed that crystallisation could be triggered by large compressive stresses developing in the film. Other authors [243, 244, 100] conversely propose that crystallisation could induce local tensile stresses, finally leading to local cracking of the film. These questions are discussed in more details in the section devoted to growth stresses.

According to Habazaki et al. [76] there is a direct relationship between the film crystallisation and the increase of the electronic conductivity of the film, leading to oxygen evolution and the resulting decrease of the growth efficiency. The photoelectrochemical studies carried out by Santamaria et al. [202] suggest that the transition from an insulator to a semiconductor behaviour of the film could indeed be the result of a crystallisation-induced decrease of the bandgap of the oxide film.

It is on purpose that, in this sub-section, no values for the voltage at which crystallisation takes place were mentioned. Indeed, reported literature values are scattered over a very wide range for different experimental conditions and even for apparently identical ones. This is likely to be due to both a high sensitivity of the crystallisation voltage towards slight differences in the characteristics of the Ti substrate (purity, crystallographic texture, surface condition) and to a different sensitivity of the experimental techniques used to detect the onset of crystallisation.

1.2.3 Discussion of the validity of the breakdown models

Especially in the case of Ti, many different sources of breakdown can be observed depending on the processing conditions. Dielectric breakdown is ob-

served in electrolytes free from aggressive ions and at high current densities. There is a good agreement on the features of dielectric breakdown :

- Breakdown is accompanied by visible sparks moving across the sample surface, audible cracking, copious gas evolution [9], local overgrowth of the film [216] and current or voltage oscillations (see Fig.1.19) [99].
- Breakdown corresponds to a short-circuit of a capacitor. The energy stored on the capacitor heats the breakdown channel, eventually up to temperatures where metal vaporisation or plasma formation occurs [211].
- Prolonged anodisation at or above the breakdown voltage yields films with a very characteristic microporous structure, as illustrated on Fig.1.20 [106].
- Breakdown is observed to take place when the cell voltage reaches a given value V_b. Wood [255] observed a proportionality between V_b and $\log(\rho)$ where ρ is the electrolyte conductivity. The latter observation was confirmed by several authors [106, 52, 2]. In contrast, the breakdown voltage appears to be virtually unaffected by the history of the sample [99].

At low current density, electrical breakdown is usually observed, owing to the semiconducting character of anodic TiO_2. In that case, the loss of the insulating character of the film is attributable to changes in the bandgap of the film induced by atomic rearrangements. Mechanical breakdown has never been explicitly demonstrated so far in anodic TiO_2. However, Di Quarto et al. [51] have provided undirect evidence that cracks may form in anodic TiO_2 films. Furthermore, considering the model derived by Sato for the field-induced stress in anodic films, the resulting stress in TiO_2 is expected to be particularly large owing to the large dielectric constant of TiO_2 as compared to other valve-metal oxides. Hence, it is not unlikely that mechanical breakdown could take place under given conditions. Anodic corrosion of TiO_2 films has been observed in the work of Delplancke et al. [48] on films films anodised galvanostatically at low current density after long anodisation times. This kind of breakdown was reported to lead to the formation of a very characteristic cone structure of the oxide films, the cones being formed as a result of the deposition of corrosion products around the corrosion pit.

1.2.4 Discussion of the influence of the processing conditions on the anodisation behaviour of Ti

Influence of the metal substrate

Influence of alloying elements: Systematic studies on the anodisation behaviour of binary alloys of valve metals have been carried out by the groups of

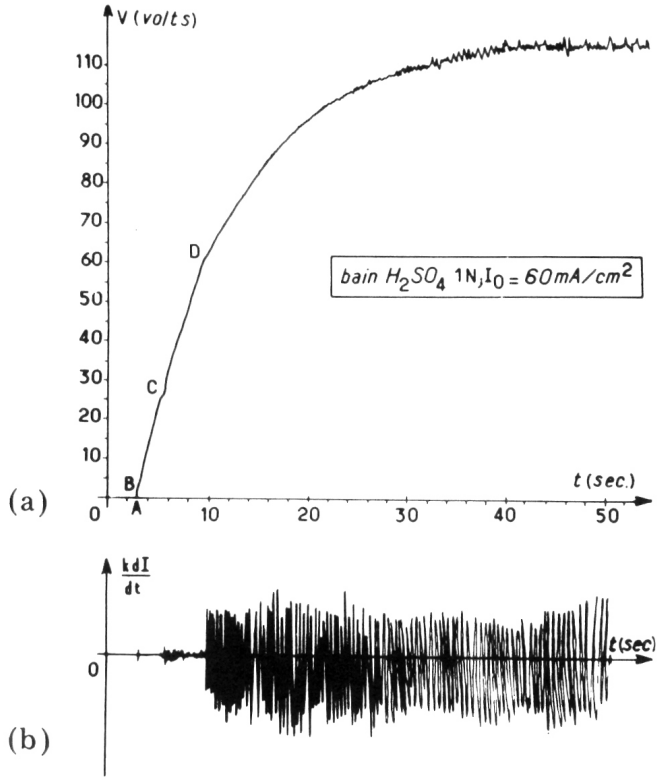

Figure 1.19: Illustration of the current and voltage oscillations accompanying the breakdown of a TiO_2 film under supposedly galvanostatic conditions, as reproduced from Jouve et al. [106].

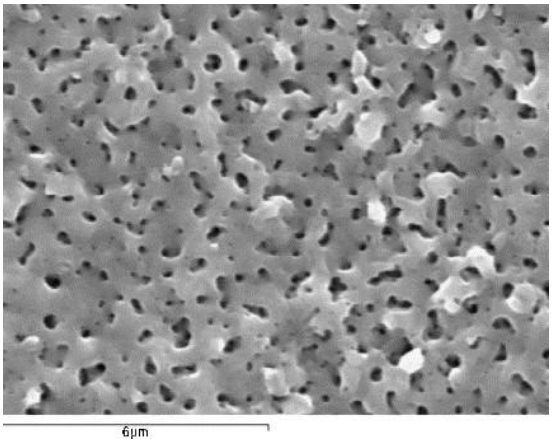

Figure 1.20: Characteristic microporous morphology of anodic oxide films obtained upon anodisation in the breakdown regime. This figure is reproduced from Diamanti et al. [55].

G. Thompson and K. Shimizu. Among many others, the alloys of Ti with Zr [78, 81], Al [71, 76], Si [76, 232], Mo [75, 77] and W [72, 79] have been investigated. Supplementary experimental observations devoted mainly to the electronic properties of anodic oxide films grown on Ti alloys have been provided by the group of F. Di Quarto [185, 174, 202]. According to these authors, the presence of alloying elements in the titanium substrate affects the growth of the oxide film mainly in three ways. Firstly, the anodisation of alloys usually leads to a multi-layered structure. Secondly, the presence of alloying elements tends to delay the crystallisation of the TiO_2 films, which directly affects the growth efficiency. Finally, it modifies the dielectric constant and electronic properties of the oxide film.

Firstly, generally speaking, anodic oxide films formed on alloys will present an inhomogeneous composition profile, characterised by a multi-layered structure, as a result of different migration rates of the different elements composing the alloy [78]. Indeed, the outer region of the anodic oxide film will contain essentially the most mobile species from the alloy while the inner region of the anodic film will be enriched in the less mobile species. On Ti-Mo alloys, for instance, the anodic oxide film comprises an outer TiO_2 layer, free of Mo, due to the larger migration rate of Ti as compared to this metal. This phenomenon is illustrated in Fig.1.21 , taken from the work of Habazaki [77], which shows the composition depth profile of an anodic oxide film grown on a Ti-28.5 at% Mo alloy, as obtained by GD-OES. The depletion of Mo at the surface of the film is

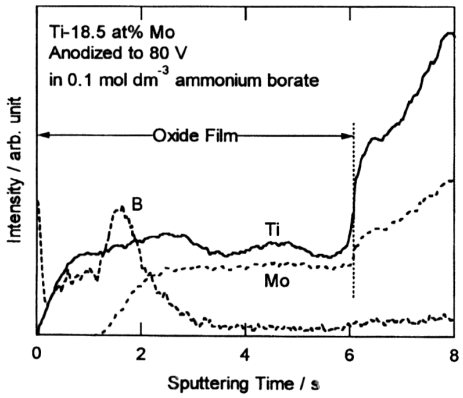

Figure 1.21: GDOES composition depth profile for an anodic film grown on a Ti-Mo alloy, reproduced from Habazaki et al. [77]. The outer region of the film (corresponding to the low values on the time-scale) is observed to be depleted in Mo, hence indicating a lower mobility of the latter specied as compared to Ti ions.

clearly visible. Similar observations have been reported for other Ti alloys, the most alloying elements exhibiting a lower mobility than Ti. The mobility of a specific alloying element in the oxide film has been proposed to be correlated with the energy ξ_{M-O} of the corresponding M^{x+}-O bond. For a species M, forming an oxide M_xO_y, the energy of the M^{x+}-O bond is calculated as the energy for atomisation of M_xO_y divided by the coordination number (C) and by the stoichiometric coefficient x [72].

$$\xi_{M-O} = \frac{\xi_{atomisation}}{xC} \tag{1.37}$$

The energy of the Ti^{4+}-O bond is between 319 and 323 kJ/mol, which is the lowest reported value for typical valve-metals [74]. For comparison, the bond energy for the M^{z+}-O bond for the valve-metal oxides are presented in Table 1.1. The energy of Si^{4+}-O bonds in SiO_2 has been included as well, owing to the importance of Si as an alloying element. As a consequence of the low value of the Ti^{4+}-O bond, Ti is expected to exhibit a large mobility in anodic oxide films. In contrast, the very high energy associated with the Si^{4+}-O bond is believed to be the reason why Si species are observed to be almost immobile in oxide films grown on Ti-Si alloys, so that, at the end of the anodisation, they are found in the portion of the oxide film which has been formed at the M/Ox interface by inward migration of anions. As a result Si has proved very successful as a marker species for the investigation of transport coefficients in

	Si	Ti	Mo	W	Zr
Bond energy [kJ/mol]	465	319-323	360-385	407-413	368
Source	[74]	[74]	[249]	[79]	[78]

Table 1.1: Typical values for the M^{z+}-O bonds in valve-metal oxides and SiO_2.

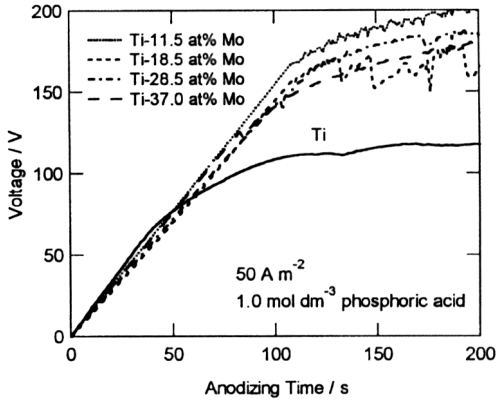

Figure 1.22: Illustration of the influence of the presence of Mo as an alloying element in Ti on its anodisation behaviour. Additions of Mo are observed to delay the onset of the oxygen evolution reaction to higher voltages (reproduced from Habazaki et al. [77]).

thin anodic TiO_2 films.

Secondly, the presence of alloying elements usually renders crystallisation of the film more difficult, as a result of a decrease in the short-range order in the film. With that respect, Si-additions are particularly efficient as 6 at% Si have been demonstrated to be sufficient for increasing the crystallisation voltage of TiO_2 films from about 10 V to more than 100 V. Similarly, 11 at% Mo (see Fig.1.22) or 26 at% Al in Ti have been reported to increase the crystallisation voltage above 160 V in ammonium pentaborate buffer, while 23% Zr hinders the crystallisation up to 200 V [78]. Again, some evidence suggests that the efficiency of a given alloying element for delaying the crystallisation would be related to its mobility in the growing film [76]. A direct consequence of the delayed crystallisation is that films can be grown with a high efficiency to larger thicknesses on Ti alloys than on pure Ti.

Finally, the presence of alloying elements obviously modifies the chemistry

of the anodic oxide film and, therefore, influences the functional properties of the anodic films. If we consider the case of the anodisation of Ti-Zr alloys, for instance, the dielectric constant of the film has been reported to decrease progressively with increasing Zr-content, up to about 42 at% Zr, because of a decreased quantity of anatase being formed in the film (see Fig.1.23). Above that threshold, the dielectric constant of the film increases again with increasing Zr-content because crystalline ZrO_2 is formed at the metal/oxide interface [78]. Incorporated alloying elements also modify the bandgap of the oxide film, as shown by Santamaria et al. for Ti-Zr alloys as well [202]. The oxide bandgap E_g increases with increasing Zr content and, as a result, the behaviour of anodic oxide films grown on Ti-Zr alloys is shifted from semiconducting to insulating with increasing Zr-content (See Fig.1.24). This observation can be rationalised based on the model derived by Di Quarto et al. for the optical bandgap of amorphous oxides (Eq.1.36): Indeed, for a mixed oxide $A_aB_bO_y$, the effective metal electronegativity is given by:

$$\chi_M = x_A\chi_A + x_B\chi_B \tag{1.38}$$

where x_A and x_B are the molar fractions of A and B. In the specific case of Ti-Zr alloys, the Pauling electronegativity of Ti in the oxide is 1.656 while that of Zr is 1.4. Therefore, increasing the proportion of Zr in the alloy decreases the effective electronegativity χ_M in Eq.1.36, so that an increased value of the optical bandgap is expected [202].

Influence of oxygen in the metal substrate: Bulk metal substrates usually contain negligible amounts of oxygen. Therefore, the influence of incorporated oxygen on the growth of anodic films has been given so far little attention. However, in recent years, more and more studies deal with the anodisation of metal thin films prepared by PVD techniques. Such films, and especially Ti films can incorporate significant quantities of oxygen during deposition, the influence of which is poorly known. From the Ti-O phase diagram, it can be seen that the Ti substrates can dissolve large amounts of oxygen, up to 30 at% [213]. To the best of our knowledge, the influence of incorporated oxygen on the anodisation process has never been studied so far in the case of Ti but was investigated by Habazaki et al. for the case of Nb [80]. We decided to include the results on niobium as a basis for the discussion. Nb films containing up to 52 at% oxygen have been prepared by magnetron sputtering and anodised galvanostatically in phosphoric acid electrolyte. Habazaki et al. report the following observations:

- The V-t curves for the anodisation of Nb are not modified qualitatively when O is incorporated. However, films grow at a higher rate (larger dV/dt) with increasing content of oxygen (see Fig.1.25).
- The anodic films contain essentially Nb_2O_5, independent of the initial

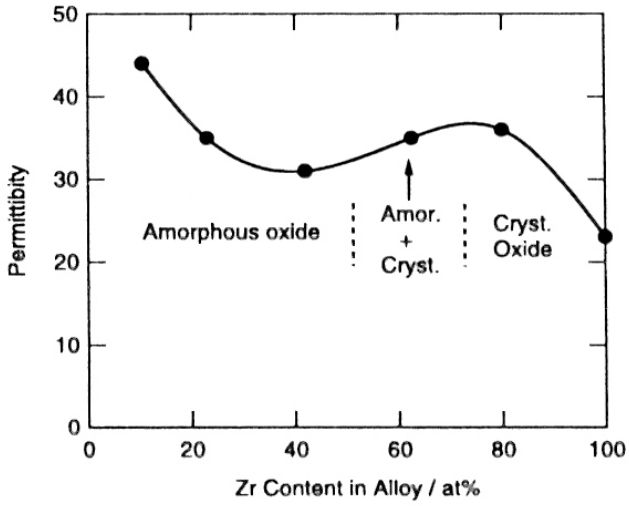

Figure 1.23: Influence of the proportion of Zr on the dielectric constant of anodic oxide films grown on Ti-Zr alloys, reproduced from Habazaki et al. [78].

> oxygen content of the metal substrate. The field strength, ionic transport numbers and mobility of phosphate species in the film seem to be unaffected by the initial O-content.

These authors conclude that the oxygen species are present in the metal essentially in the form of O^{2-} ions and contribute to the growth of the oxide film, in addition to those from the electrolyte. These results should of course be validated for Ti as well before final conclusions can be drawn. However, if observations made on Nb extend to other valve-metals as well, the incorporation of O-species in the metal substrate is not expected to influence strongly the growth process but could lead to errors in the quantification of the growth efficiency calculated from the slope of the V-t curves.

Influence of the micro-texture: The influence of the microtexture of the Ti substrate on the growth of anodic oxide films has been known for long [126]. Jouve [106] or Delplancke [48] for instance reported that after anodisation of a polycrystalline Ti sample, the initial microstructure of the Ti substrate is still clearly visible under an optical microscope and that the oxide film shows different interference colours on the different Ti grains. Both authors conclude that the thickness of oxide films formed up to a given forming voltage (and hence the anodising ratio) is dependent on the orientation of the underlying Ti grain. Jouve et al. [106] also showed that the breakdown voltage depends on

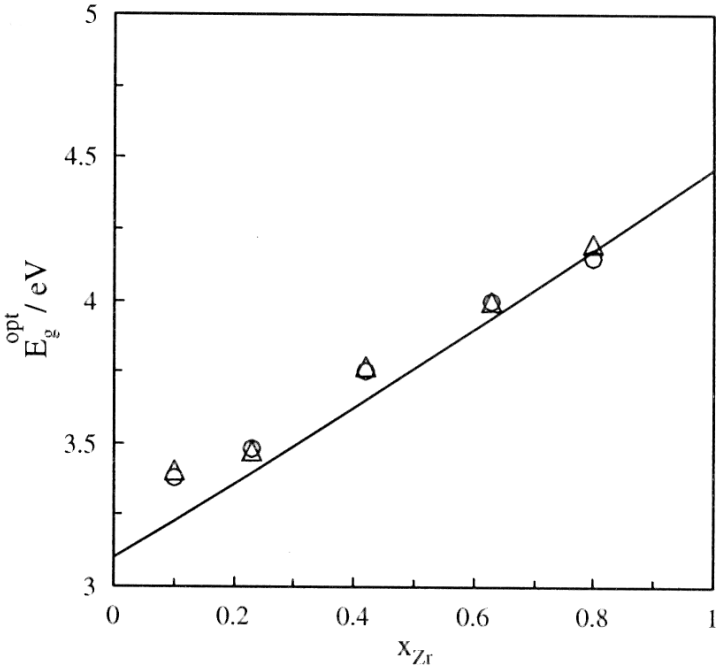

Figure 1.24: Influence of the proportion of Zr on the bandgap value of anodic oxide films grown on Ti-Zr alloys, reproduced from Santamaria et al. [202]. The black solid line corresponds to the expected value for a crystalline oxide, calculated from Eq.1.35.

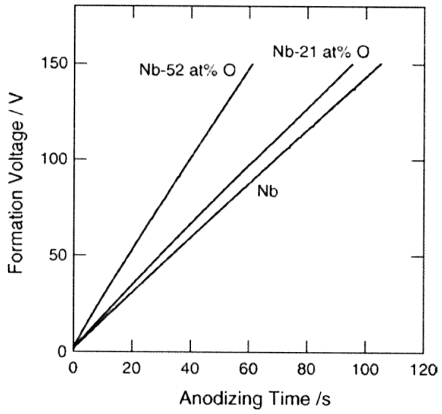

Figure 1.25: Illustration of the influence of the oxygen content on the anodisation V-t curve of sputtered Nb films, reproduced from Habazaki et al. [80].

the microtexture of the Ti substrate.

Further insight into this phenomenon was gained a few years later by the use of electrochemical characterisation techniques with high spatial resolution. Indeed, techniques like scanning electrochemical microscopy (SECM), photoelectrochemical microscopy and Raman microprobe spectroscopy allow for local investigation of the properties of anodic oxide films grown on a specific Ti grain. Kozlowski et al. [119] carried out photoelectrochemical mapping of anodised polycrystalline Ti samples and showed that the photoresponse of the anodic oxide film was homogeneous throughout a given Ti grain but varied largely from one grain to another, as illustrated on Fig.1.26. In parallel, Fushimi et al. [64] showed, using SECM mappings, that the electronic conductivity of the oxide film depends on the orientation of the Ti substrate. The papers by Kozlowski and Fushimi however disagree with one another as to the origin of the heterogeneity in the (photo)electrochemical properties of the oxide films. Indeed, Fushimi et al. claim that their observed differences in the electronic conductivity of the oxide film reflect only the grain-to-grain differences in the thickness of the oxide film. In contrast, based on independent local oxide thickness measurements by Auger depth profiling, Kozlowski et al. conclude that the variations in the thickness of the oxide film from one grain to another are too small to result in the large observed variations in photoresponse and that the latter must be attributed to differences in the defects concentration in the film. Although the observations reported by Kudelka et al. [124] seem to con-

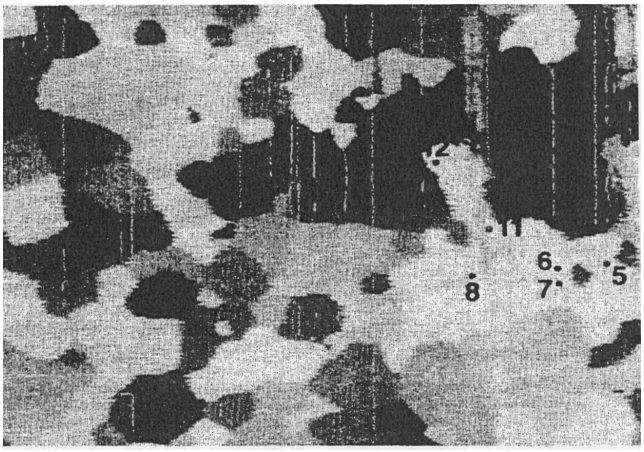

Figure 1.26: Photoelectrochemical mapping of the anodic oxide film grown on a polycristalline Ti substrate, reproduced from Kozlowski et al. [119]. The brighter regions correspond to Ti grains on which the anodic oxide film exhibits a larger photocurrent.

firm the latter conclusion that the donor concentration in anodic TiO_2 films is indeed dependent of the substrate orientation, this point remains so far a matter of debate.

The group of J. Schultze provided a significant supplementary contribution to this field by correlating the actual orientation of the Ti grains (determined by anisotropy micro-ellipsometry) with the properties of the oxide film (characterised using photoelectrochemistry, impedance spectroscopy and electron transfer reaction) [124]. For this purpose, they designed a specific electrochemical droplet cell, allowing for electrochemical measurements on single Ti grains. They showed that oxide films grown on the dense-packed (0001) planes of the Ti substrates exhibit the lowest density, the highest electrochemical activity and donor density and that the anodising ratio is voltage-dependent in the voltage range of 0 to 10V. In contrast, the TiO_2 films grown on the loose-packed (xxx0) planes exhibit the largest density, a more insulating behaviour, with a low donor density, and a constant anodising ratio. Films grown on other Ti planes exhibit properties intermediate between those of films grown on the dense-packed and loose-packed planes. They also showed that the influence of the texture of the Ti substrate is much more marked in the case of slowly grown oxide films than in the case of rapidly grown ones. In particular, they showed that anodic oxide films grown potentiostatically on (0001) planes behave similar to oxide films grown slowly on (xxx0) planes, as illustrated on Fig.1.27. This confirms the

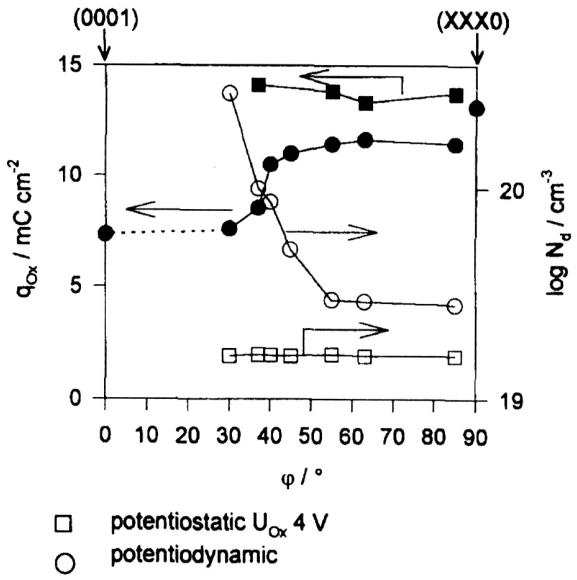

Figure 1.27: Evolution of the electronic properties of TiO_2 films, as a function of the orientation of the Ti grain on which they are grown, for both potentiostatic and potentiodynamic growth, reproduced from Kudelka et al. [124].

observation reported by Delplancke et al. that the differences in the electronic properties of anodic TiO_2 films as a function on the orientation of the substrate grains vanished in the case of potentiostatic growth while they are clearly observable for galvanostatically grown films [50].

Kudelka et al. [124] have also mentioned a direct influence of the orientation of the Ti substrate on the oxygen evolution reaction, with a much more extensive oxygen evolution being observed on oxide films grown on (0001) planes (see Fig.1.28). Recently, these results were confirmed in a study by Matykina et al. [154] devoted to the influence of the substrate microtexture on the oxygen evolution reaction on TiO_2 films. They observe that the oxide films grown galvanostatically to high cell voltages (but below the breakdown voltage) exhibit a very different morphology depending on the orientation of the underlying Ti grain. A relatively smooth and featureless oxide is formed on the loose-packed (xxx0) planes while the oxide formed on the dense-packed (0001) planes is very rough, as illustrated on Fig.1.29. They show that the orientation-dependence of the film morphology is due to different rates of oxygen evolution within TiO_2 films formed on different Ti grains. Oxygen is evolved inside the oxide

film and forms high-pressure gas-filled cavities, which progressively coalesce and lead to a roughening of the film, blistering and eventually rupture when the gas is released. The oxide formed on the dense-packed planes of the Ti substrate is characterised by a higher rate of oxygen evolution than the oxide formed on loose-packed Ti-surfaces. From electron diffraction patterns, they also confirmed that the oxide film of the 'smooth regions' is amorphous while, in the 'rough regions', where oxygen evolution is abundant, rutile peaks are clearly visible. They conclude that the amorphous-to-crystalline transition is facilitated at the metal/film interface on the dense-packed Ti grains.

Influence of the electrolyte

The influence of a given electrolytic solution on the anodisation process is essentially determined by a series of 'abilities' and 'tendencies':

- the ability to conduct the current through the cell
- the ability to provide the oxygen species which will be used for oxide formation
- the tendency to dissolve the oxide film
- the tendency to become incorporated to the oxide films
- the tendency to induce side-reactions

In this sub-section, these different abilities and tendencies are discussed in reference to their impact on the anodisation process.

conductivity: It is the primary role of an electrolytic solution to conduct the current through the electrochemical cell and the latter must therefore be sufficiently conductive. In aqueous electrolytes, conductivity is usually not a concern. In contrast, it can be an issue when anodisation is performed in organic environments. When the electrolyte is too resistive, besides increasing the power consumption of the process because of large ohmic potential drops through the electrolyte, it can lead to inhomogeneous growth of the oxide film (non-uniform thickness) as a consequence of localised current lines between the two electrodes. This kind of problem can be avoided by using a well controlled cell geometry with parallel electrodes and a cathode with a surface at least as large (or preferably larger) as that of the anode.

dissolution: Each electrolyte has the ability to dissolve (chemically) the oxide film at a given rate (usually very low) which depends on the pH and on the presence of specific aggressive anions (Cl^-, F^-). Information on the typical dissolution rates of anodic TiO_2 films in usual acidic and alkaline electrolytes can

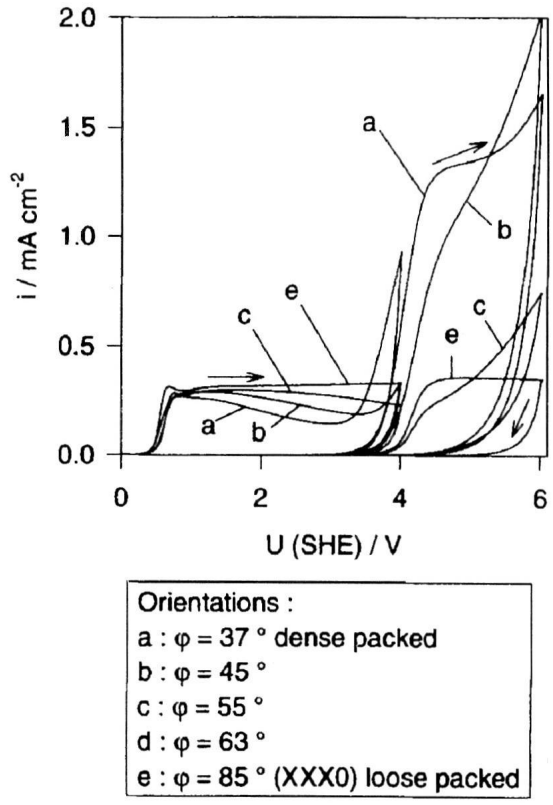

Figure 1.28: Cyclic voltammograms obtained on Ti grains exhibiting different crystallographic orientations, reproduced from Kudelka et al. [124].The large current peak associated with the onset of the oxygen evolution reaction is observed to be more marked on dense packed (a) grains than on the loose-packed ones (e).

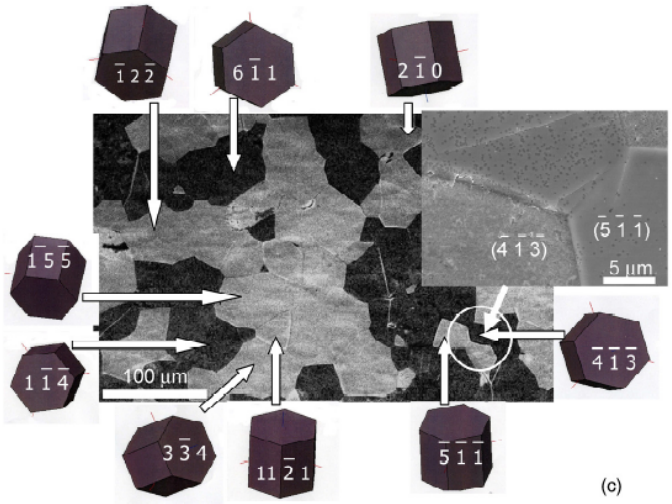

Figure 1.29: Illustration of the different morphologies of TiO_2 films grown on Ti grains having different orientations, reproduced from Matykina et al. [154].

be found in the work of Blackwood et al. [22]. Generally speaking, TiO_2 is very stable in neutral electrolytes and its dissolution rate increases slightly with decreasing pH. Blackwood et al. report a dissolution rate of the order of 2.5 nm/h in 3.0 M H_2SO_4 electrolyte. The most straightforward impact of the chemical dissolution is to reduce the effective growth rate of the oxide film. According to Sibert [219], the dissolving character can also be beneficial to the stability of the oxide films. He reports that the 'best' electrolytes for anodisation (allowing for growing thick films exhibiting good adherence and mechanical stability) are those which are capable of slightly dissolving the oxide film, thus allowing for some reordering of the film at the oxide/electrolyte interface. However, to the best of our knowledge, his observation has never been confirmed so far. The presence of specific aggressive anions in the electrolyte, mainly F^- ions modifies considerably the growth process of TiO_2 films [12, 13, 233, 82, 127]. Indeed, F^- ions are known to attack locally TiO_2 films and have also been reported to migrate rapidly through the film, at a rate equal to twice that of O^{2-} ions [82]. As a consequence, they tend to accumulate at the metal/film interface. Anodisation of Ti in F^--containing electrolytes under given conditions leads to the formation of nanoporous oxide films, similar to those produced on Al upon anodisation in acidic electrolytes. The growth of such nanoporous anodic films has not been investigated in this work, and the rest of the discussion in the present chapter focuses on the growth of barrier oxide films only. Extensive

information on the growth of nanoporous Ti can be found in the work of the group of P. Schmuki [233, 234, 141, 127]. Additional contributions to this field have been provided by C. Grimes et al. [160, 161] The presence of fluorine ions in the electrolyte has also been reported to impede the growth of the oxide film at the film/electrolyte interface [82], to favour crystallisation to rutile [127] and to modify profoundly the stress evolution associated with the growth of the film, leading to a more tensile behaviour [12, 13]. To the best of our knowledge, no other electrolyte anions have a specific dissolving action on TiO_2 films.

side-reactions: The main side-reaction accompanying anodisation in aqueous electrolytes is the oxygen evolution reaction (water oxidation reaction). The latter reaction can be avoided by working in a medium having a larger domain of electrochemical stability than water, for instance some organic electrolytes. Besides the oxygen evolution reaction and the oxide dissolution, other side-reactions have been reported as well, mainly the formation of peroxides. Information on the main side-reactions accompanying anodisation in sulphuric media and the relative proportion of the current consumed associated with those reactions has been provided by Delplancke et al [49].

incorporation: incorporation of electrolyte anions in the growing film has been known for long [7]. As a consequence of the positive charge on the anode, negatively-charged species show a larger tendency to be incorporated. Neutral species, like water molecules, can also be incorporated [169, 213], and some authors even report incorporation of small cations like Na^+ upon anodisation in NaOH or NaCl [92]. With this respect, the choice of the electrolyte has a strong influence. For instance, the counteranions of organic acids are much less incorporated in the film owing to the larger size of the alkyl chain as compared to typical inorganic anions. In contrast, significant amounts of phosphate species (typically a few atomic %) are incorporated in the growing film during anodisation in phosphate-based electrolytes.

Wood [256] has proposed a theoretical model describing the incorporation of anions from the electrolyte in the growing film and their subsequent migration within the film. Although his model was developed for anodic alumina films, the same principles should hold as well in the case of other valve metal oxides like TiO_2. The main hypothesis of his model, based on that proposed by Leach and Pearson [132], is that, when a monolayer of oxide is formed, all the molecules adsorbed in the double layer are consumed for forming the oxide film and the double layer must be renewed. As a consequence, the amount of electrolyte species which are incorporated in the film directly depends on their concentration at the surface of the film in the double layer. The surface concentration in turn depends on the bulk concentration, the surface pH (i.e. on the concentration of adsorbed OH^- species) and the current density. According to

Wood, as a first step, the anions are incorporated in the oxide films as such. No breaking of oxygen bonds takes place at that stage. Wood points out that the anions which are incorporated might be different from the main species present in the bulk of the electrolyte. Indeed, the stability of the various ions is determined by the local pH, as illustrated on Pourbaix diagrams. As the surface pH might differ from the bulk pH, the stable species at the surface might be different from those in the bulk. It should be noted that, in contrast to acidic electrolytes, alkaline electrolytes such as NaOH or KOH are expected to yield much cleaner anodic films, due to the absence of electrolyte anions other than OH^- that could be incorporated. Incorporation of electrolyte ions is favoured by a small ionic radius of the anions, a large concentration of the electrolytic solution, a lower pH (because of a decreased concentration of adsorbed OH^- on the oxide surface) and higher temperatures. The influence of the current density is not very clear so far.

Once incorporated, the electrolyte species can migrate within the film, inwards or outwards depending on their charge and at a rate which depends on their bond energy [256]. Therefore, the bond breaking appears to be a key-step of the ionic transport in amorphous films. If a given species is immobile it will be found in the whole region of the oxide film formed at the oxide/electrolyte interface. If it migrates inwards, it will eventually contaminate a region of the film larger than that formed at the oxide/electrolyte interface. In contrast, if the species migrates outwards, it will be found only near the oxide/electrolyte interface. The model of Wood is illustrated on Fig.1.30. Habazaki et al. have studied the mobility of various electrolyte species in anodic TiO_2 films. Phosphates, for instance, migrate inwards at a significant rate and are typically found in the outer 62% of TiO_2 films (while only 42% has been formed at the oxide/electrolyte interface) [74]. Based on that observation, Habazaki estimates the relative migration rate of PO_4^{3-} ions in TiO_2 films to be approximately 34% of that of O^{2-} species. In contrast, B, W and Mo species incorporated in anodic TiO_2 are observed to migrate outwards at a rate equal to, respectively, 50, 67 and 44% of that of Ti^{4+} [73]. When anodisation is carried out in chromates-containing electrolytes, chromium is incorporated as well but migrates outwards at a rate very close to that of Ti (about 92%). Therefore, it is found only in the very surface of the anodic film. This confirms an observation reported earlier by Zwilling [267] for the anodisation of Ti and TA6V alloy in chromic acid.

The question may arise as to the influence of the incorporated species on the morphology and properties of the film. The TEM studies carried out by Habazaki et al. [76] reveal that the region of the oxide film grown at the oxide/electrolyte interface is systematically amorphous, independent of the depth of penetration of the electrolyte species into the film. In contrast, in the case when electrolyte species migrate inwards (P for instance) and are incorporated

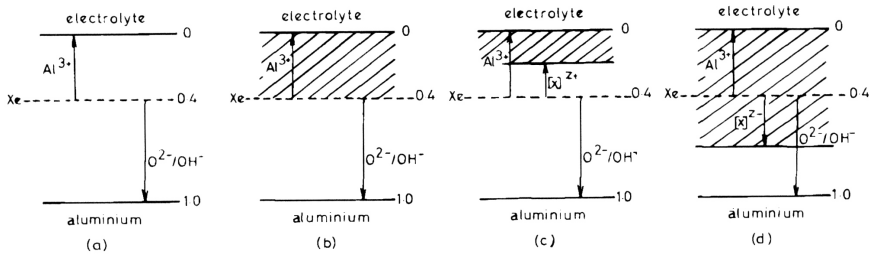

Figure 1.30: Illustration of the localisation of incorporated electrolyte species in anodic oxide films (shaded regions), as a function of their tendency to migrate, respectively outwards (c), inwards (d) or to remain immobile (b). This figure is reproduced from Wood et al. [256].

into the inner region of the film, formed at the metal/oxide interface, these species are observed to have an inhibiting effect on crystallisation. This is in agreement with the general observation that amorphous TiO_2 films can be grown to larger thicknesses in H_3PO_4 than in H_2SO_4. From these observations, they conclude that, although the 'disorder' associated with the incorporated species is likely to have a delaying effect on crystallisation, similar to what is observed for alloying elements from the substrate, this effect in not the only cause of the amorphous character of the outer region of the film.

To the best of our knowledge, besides their influence on the crystallisation behaviour, the influence of incorporated species on the functional properties of the anodic oxide film has never been studied. The incorporated quantities are relatively low (up to a few at%) but this might however be sufficient to modify the conduction properties of the oxide film through the introduction of energy levels in the bandgap of the semiconducting TiO_2 films. Furthermore, as discussed in the section 1.1.3 devoted to breakdown, the incorporated anions would also have a direct effect on the breakdown of the anodic films by providing the primary electronic current which, due to avalanching effect, leads to breakdown. As a result, more concentrated electrolytic solutions are observed to lead to a decrease of the breakdown voltage [2].

Hydration: Evidence has been provided by several authors that anodic oxide films, and especially anodic TiO_2, contain incorporated water. Only a few experimental techniques, mainly XPS, RBS, elastic recoil analysis (ERA) and neutron reflectometry (NR), allow for direct (in the case of ERA) or indirect (in the case of RBS and NR) observation of the presence of H atoms (and hence of water molecules). XPS provides supplementary information by allowing identification of the specific bonds involving the H atoms. Most of the investigations

carried out on anodic TiO_2 films using one of those techniques point out to the presence of hydroxylated compounds in the film. It is therefore likely that anodic TiO_2 films typically contain some bound water. Hydration of TiO_2 films has been extensively discussed in papers by Ohtsuka and collaborators. In a first paper [169], Ohtsuka et al., using ellipsometry, measured overfaradaic thickness-to-charge ratios and attribute this observation to water being incorporated in the oxide film. In a more recent paper, they report that anodic TiO_2 film grown faster exhibit a lower refractive index, a higher dielectric constant and a lower density than films grown slowly [170, 171]. They interpret these combined observations as an indication that films grown at a high rate are more hydrated than slowly grown ones. Ohtsuka et al. go as far as to conclude that anodic oxide films would initially grow as an hydrated oxide [172]:

$$Ti_{ox}^{4+} + 4H_2O \Rightarrow Ti(OH)_{4,ox} \tag{1.39}$$

then dehydrate progressively in the course of the growth, under the action of the electric field :

$$Ti(OH)_{4,ox} \Rightarrow TiO_{(2-x)}(OH)_x + (2-x)H_2O \tag{1.40}$$

Supplementary indirect evidence that anodic oxide films grown on Ti are hydrated has been provided by Serruys et al. [213], who have investigated anodic TiO_2 films grown at 12 mA/cm^2 in 1.0 M H_2SO_4 using RBS and ERA. RBS analysis revealed a marked oxygen overstoichiometry in the film, which could not be accounted for by the incorporation of SO_4^{2-} anions. Using ERA, they established the presence of hydrogen in their films and concluded that hydroxy-compounds must be present in the oxide, in the form of either hydroxides or hydrated oxide. Tun et al. [236, 237] have performed neutron reflectivity studies on TiO_2 films formed potentiostatically in a NaCl electrolyte. They observe a bi-layered structure of the films, with an outer region being characterised by a low scattering length density which they ascribe to the presence of significant amounts of hydrogen in the film. Finally, direct evidence of the presence of O-H bonds in the anodic TiO_2 films has been provided by XPS studies by Shibata et al. [215], Huang et al. [91], Kunze et al. [126] and Xia et al. [259]. An estimation of the amount of bound water, calculated from XPS data, can be found in the work of Shibata et al, for films grown potentiostatically for 1h at 1.5V in 0.5 M H_2SO_4. These authors report that the ratio of the amount of oxygen atoms involved in O-H bonds to that involved in M-O bonds ($N_{O(O-H)}/N_{O(Ti-O)}$) increases from about 10% for films grown at 303K to about 25% for films grown at 333K. Above that temperature, the amount of OH bonds increases dramatically and reaches 80% for films grown at 350K, as illustrated on Fig.1.31. For comparison, Ohtsuka et al. [169] report an estimated stoichiometry of their anodic films corresponding to $TiO_2 \cdot 1.4H_2O$ (i.e. $N_{O(O-H)}/N_{O(Ti-O)}$=0.7) while Serruys et al. [213] estimate the stoichiometry

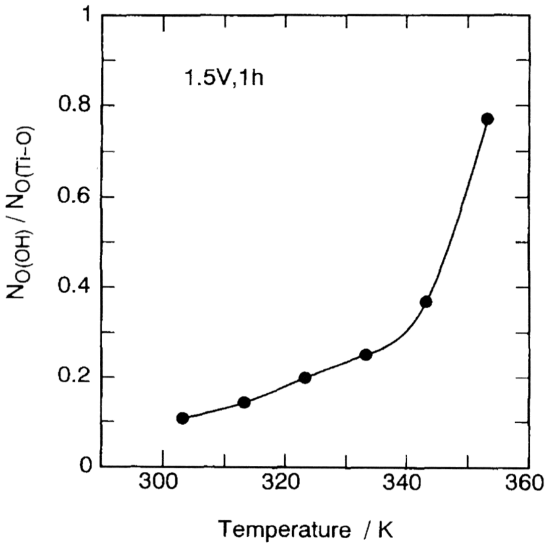

Figure 1.31: Influence of the electrolyte temperature on the amount of water incorporated in anodic TiO_2 films, as reported by Shibata et al. [215].

of their oxide films as $TiO_2 \cdot 0.6H_2O$ (i.e. $N_{O(O-H)}/N_{O(Ti-O)}$=0.3). It should be noted that the observations reported by Kunze et al. [126] for angle-resolved XPS tend to demonstrate that hydration is mostly localised at the very surface of the film. Not much is known as to the influence of the bound water on the characteristics of the oxide films. Generally, it is well accepted that water is a source of disorder in the film, delaying the crystallisation process. According to Ohtsuka et al. [171], bound water would increase the dielectric constant of the film owing to the high polarisability of the O-H bonds.

Influence of the temperature

The influence of the temperature on the growth of anodic TiO_2 films has been investigated under different growth conditions, characterised by different growth modes, growth rates and electrolytes. All reported studies agree on the following two trends. The first general observation is that the anodising ratio increases (i.e. the electric field across the film is reduced) with increasing temperature . The second observed trend is that films grown at higher temperature are more ordered and therefore crystallise more easily.

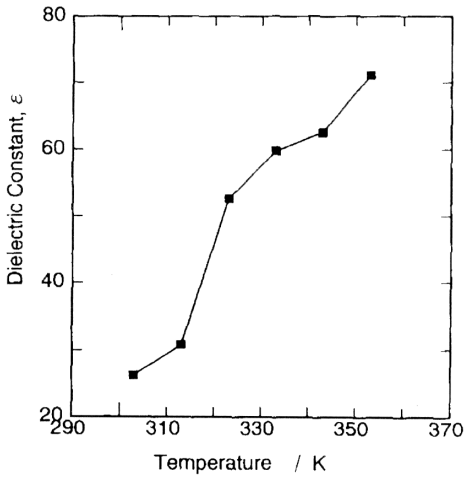

Figure 1.32: Influence of the electrolyte temperature on the dielectric constant of anodic TiO_2 films, reproduced from Shibata et al. [214].

Larger AR (and larger thickness-to-voltage ratios in the case of potentiostatic experiments) are observed with increasing temperatures [215, 231, 192]. Sul et al. report an increase of the anodising ratio by 6% when increasing the temperature from 17°C to 42°C for galvanostatic anodisation both in 0.1 M acetic acid and in 0.1 M NaOH. Similarly, Prusi et al. report increases of the thickness-to-voltage coefficient by 7 to 18% when increasing the temperature from 0°C to 20°C and by 4 to 7% from 20°C to 40°C for potentiostatic anodisation in KOH solutions with different concentrations. This observation can be rationalised based on kinetic arguments. Indeed, a larger anodising ratio means that the electric field required for transporting a given current through an oxide film of given thickness decreases as the temperature increases. This is not surprising since the mobility of ions is expected to increase with increasing temperature. According to Shibata et al., this observations could also be attributable to a larger amount of water being incorporated in films grown at a higher temperature, as suggested by their XPS results (see Fig.1.31).

A second observation by Blackwood et al. is that oxide films grown at a higher temperature are more stable, which they attribute to a more ordered structure of the film [22]. These authors therefore suggest that the growth process involves a specific, thermally activated, transformation which 'consumes' defects. This re-ordering could be a preliminary step for crystallisation. Observations by Shibata and Zhu [215] on the influence of the temperature on

the crystallisation of the films seem to confirm this scenario. After 1 hour polarisation at 1.5V at 20°C, they obtain oxide films with low dielectric constant (ϵ =26), typical for amorphous TiO_2, while after a similar potentiostatic growth at 60°C, permittivity values typical for anatase (ϵ =50-60) are measured (See Fig.1.32). The onset of the oxygen evolution is also reported to take place at lower voltages at higher temperatures, as a result of a facilitated crystallisation of the film [214]. Delplancke et al. report a marked influence of the electrolyte temperature on the overall growth behaviour [48]. They observed two different growth-behaviours associated with, respectively, low-current density and high current density and leading to oxide films showing different morphologies. Delplancke observed that the current threshold between low and high current density is temperature-dependent, with higher temperatures leading to increased threshold currents. They suggest that this transition might be due to the capacity to dissipate the heat produced in the film during growth. Below the critical current density/temperature, all the heat produced in the film would be dissipated to the electrolyte, so that the film does not heat up. In contrast, above the threshold current or temperature, the heat dissipation in no longer sufficient so that the film rapidly heats up which eventually leads to breakdown.

Influence of the growth mode and growth rate

The growth mode: As mentioned in section 1.1.1, there are mainly three anodisation modes. Anodic oxide films can be grown either by polarising the anode at a given potential for a given duration, by imposing a given cell current or by sweeping the anode potential up to the formation voltage at a given rate. Selecting one ore the other growth mode influences the anodisation process as well as the properties of the anodic oxide film. As will be developed further in this paragraph, the main difference between the three growth modes is their respective associated growth rates. Therefore, it was decided to address in the same paragraph the influence of the growth mode and growth rate. In the case of potentiostatic growth, the current density in the very first instants of anodisation is very large, usually limited only by the performances of the power source. Kudelka et al. [124], for instance, report current density peaks of more than 100 A/cm^2 at the beginning of their potentiostatic anodisation at 4V. As a result of this high current, the whole oxide film is formed in a few milliseconds. If the polarisation is maintained over a longer time-period, the very fast growth of the anodic film is followed by an aging step. In the case of galvanostatic experiments, the oxide film grows at a given, imposed, rate given by the Faraday law. The growth rate is constant as long as the structure of the film is not modified (mainly its density) and as long as no side-reaction takes place and decrease the growth efficiency. The potentiodynamic mode is in fact very similar to galvanostatic conditions, with the oxide film growing at an imposed

rate given by the sweeping rate. The effective growth rate is constant as long as the density of the oxide film is not modified and as long as the anodising ratio is constant. In contrast to galvanostatic conditions, the potentiodynamic mode allows keeping a constant growth rate even when side-reactions reduce the growth efficiency.

A discussion of the influence of the growth mode on the characteristics of the oxide film can be found in the studies carried out by Delplancke [50], Wiesler [253], Kudelka [124] or Bourdet [30]. From their studies, it comes out that oxide films grown potentiostatically are slightly thicker and more insulating than oxide films grown galvanostatically or potentiodynamically, and that their properties are less-dependent of the orientation of the underlying Ti substrate. Typically, galvanostatic anodisation is carried out with current densities in the range of 0.1 to 100 mA/cm^2. If galvanostatic anodisation would be carried out at a current density comparable to those measured for potentiostatic growth, it is likely that the differences between the two growth modes would vanish.

Before discussing the influence of the growth rate on the characteristics of the oxide film, it is worth mentioning a supplementary growth mode, proposed recently by Poznyak et al. [189]. These authors have grown anodic oxide films with thicknesses in the range of a few nm to 200 nm by using repeated pulse discharges. Pulses of more than 1000 V and a few μs were obtained from the discharge of a capacitor. The voltage pulses produce plasma conditions at the anode surface. Owing to the plasma regime, the film grows with overfaradaic efficiency. Tuning the value of the capacitance allows modifying the thickness of the oxide film which grows during the pulse, although there does not seem to be a straightforward relationship between the pulse power and the thickness increment. A comparison between the films grown by pulsed discharges and films of comparable thicknesses grown galvanostatically in H_2SO_4 reveals that the pulse discharge growth mode yields more stoichiometric oxides, exhibiting a more homogeneous composition throughout the oxide thickness (reduced concentration gradients, as measured by AES depth profiling). Pulse discharge grown oxides also appear to incorporate more species from the electrolyte than the galvanostatically grown ones. Mott-Schottky analysis also shows that the donor density in the pulse discharge oxides is up to 2 orders of magnitude smaller than in the galvanostatic oxides. As to the crystallisation behaviour, both type of oxides exhibit a similar behaviour, with the films being amorphous up to a certain thickness, then progressively crystallising to anatase.

The growth rate: During potentiodynamic or galvanostatic anodisation, the rate of growth of the oxide film can be controlled (almost) directly via, respectively, the potential scan rate or the applied current density and can be

typically varied over a wide range. This paragraph provides a discussion of the influence of the growth rate on the characteristics of the oxide film. As will be further discussed, a faster growth process yields less-dense and less-ordered films than a slow growth, while the influence of the growth rate on the functional properties of the film, remains so far controversial.

Michaelis et al. [156] and Ohtsuka et al. [170] both observed that the refractive index of anodic TiO_2 films decreases with increasing growth rate. In parallel, both authors report that the anodising ratio increases with increasing growth rate. According to Michaelis et al., these two observations are likely to be correlated. Indeed, according to the Drude model, the refractive index of the film is related to the electron density in the material. Postulating that the latter is in turn proportional to the density of the oxide film itself, variations in the oxide density are anticipated to result in variations of the refractive index. Hence, the increase of the anodising ratio and the decrease of the refractive index with increasing growth rate are indications that films grown faster are less dense than slowly grown ones. The latter conclusion is in agreement with the observation reported by Wiesler that films formed under potentiostatic conditions are 10% less dense than films grown slowly under potentiodynamic conditions [253]. However, this trend contradicts with what would be expected considering only the high-field model. Indeed, according to the high-field equations Eq.1.23, larger fields (i.e. lower AR-values) are required to allow for larger currents to flow through the film [167], as will be further discussed in chapter 5. This latter effect is readily observed in experiments during which the current density is decreased in the course of anodisation. This kind of experiment was carried out for instance by Di Quarto et al. [51]. Upon each stepwise decrease of the current density, these authors observe a downward V-step, which provides direct evidence that the electrical field in a given film decreases with decreasing current density. However, it is likely that other factors come into play when the growth rate of the film is modified, due to a direct influence of the growth rate on the oxide density [156], on its degree of hydration [170] (see subsection 1.2.4) or on the amount of incorporated electrolyte species [132]. The latter effects can overcome the natural influence of the current density on the field in the growing film.

Besides the influence of the growth rate on the final thickness of the film, there is significant evidence that slowly grown oxide films are more ordered. According to Blackwood [22], this more ordered character accounts for the improved stability (lower dissolution rates) of oxide films grown at a slower rate. It could also account for the smoother surface of galvanostatically-grown films as compared to the potentiostatically grown ones, as observed by Bourdet et al. A fast growth, as in the case of potentiostatic anodisation, also appears to suppress the possibility of preferential crystallisation of TiO_2 on Ti grains

of specific orientations. Both Delplancke [50] and Kudelka [124] report that the strong influence of the Ti-microtexture on the growth of anodic films observed under galvanostatic or potentiodynamic conditions vanishes in the case of potentiostatic growth. Indeed, under potentiostatic conditions, oxide films having the same thickness and electrochemical properties grow on all Ti grains, independent of their orientation (see Fig.1.27).

The main point on which there is no general agreement in the literature is the influence of the growth rate on the dielectric properties of the oxide film. While Blackwood et al. [24] report a decreasing ϵ-value and an increasing donor density with increasing growth rate, Ohtsuka et al. [171] report the opposite trend, with rapidly grown oxide films having a larger dielectric constant and a lower donor density. The observations reported by the two groups on the dependence of ϵ on the growth rate are reproduced on Fig.1.33. Kudelka et al. [124] compared GS and PS films and observed that rapidly grown oxide films were more insulating. The latter results are more in agreement with the trend reported by Ohtsuka.

In addition to modifying some of the characteristics of the growing film, the growth rate also has a considerable influence on the growth process itself, with oxide films grown at different rates exhibiting different morphologies. This is particularly obvious in the work of Delplancke et al. [48] who report the existence of two distinct growth regimes corresponding to low- and high-current density conditions. In the case of the high-current density regime, the cell voltage increases continuously up to the breakdown region, in which a microporous oxide is formed. (cf. section devoted to breakdown) In contrast, at low current density, a V-plateau is rapidly observed, which corresponds to the onset of oxygen evolution. Under such conditions, after some time, a very particular cone structure develops. So, the growth rate (in this case the current density) can influence the morphology of the film as well.

Finally, it should be noted that the potential values at which transitions in the growth process take place (onset of the OER, breakdown) are generally observed to increase with increasing growth rates. Dyer [57] or Ohtsuka [171], for instance, report that the onset of the OER is shifted to higher voltages when the growth rate increases (see Fig.1.34). Jouve [106] observed a proportionality between $\log i$ and both the voltage marking the onset of the OER and the dielectric breakdown. Finally, McAleer et al. [148] demonstrated that the growth instabilities observed during the growth of their films could apparently be avoided by growing the film at a high-enough rate (see Fig.1.35).

Post-anodisation treatments: After a galvanostatic or potentiostatic growth, different post-anodisation treatments can be carried out, usually in the form

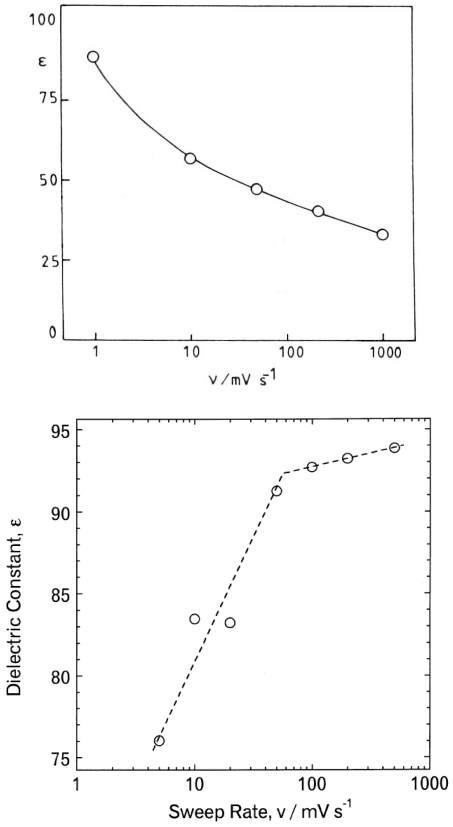

Figure 1.33: Influence of the growth rate on the dielectric constant of potentiodynamically grown TiO_2 films, as reported by a) Blackwood et al. [24] and b) Ohtsuka et al. [171].

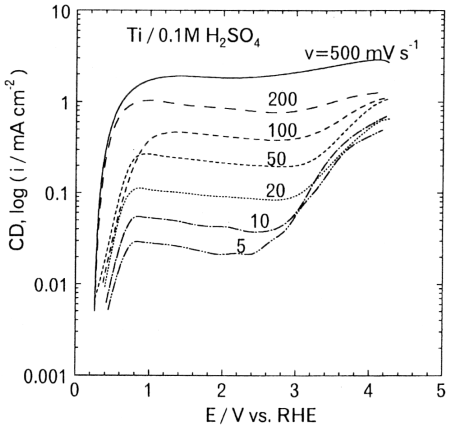

Figure 1.34: Cyclic voltammograms measured on Ti for different sweep rates, reproduced from Ohtsuka et al. [171]. The characteristic increase of the cell current at the end of the plateau region and corresponding to the onset of the OER is observed to be shifted to lower V for films grown more slowly.

of potentiostatic aging or potentiodynamic cycling, at the same temperature as for the growth or at a higher T°. As to the potentiostatic aging, all experimental evidence point out to the conclusion that they result in an increased degree of order. As to potentiodynamic cycling, only little experimental data is available and the influence of the cycling is not yet clear.

Blackwood et al. [22] report that potentiostatic aging, at a higher temperature than the growth temperature, improves the stability of their oxide films, which is manifested as a decrease of the rate of chemical dissolution of the films under open-circuit conditions. They attribute this effect to progressive changes in the film structure, leading to a more ordered structure. Similarly, Marsh and Gorse [146] attribute to a progressive ordering of the films the significant decrease of the sub-bandgap photocurrent that they observe on their anodic oxide films with increasing time of potentiostatic aging at the formation potential. According to Ohtsuka et al. [172], this re-ordering of the film structure is associated with a progressive dehydration of the film. The latter authors have studied the influence of potentiostatic aging using in-situ ellipsometry. According to their observations, potentiostatic aging results in an increase of the refractive index of the film, as well as a decrease of the film thickness when the film is aged below its formation potential (see Fig.1.36). These two combined observations suggest a densification of the film which, according to Ohtsuka, is

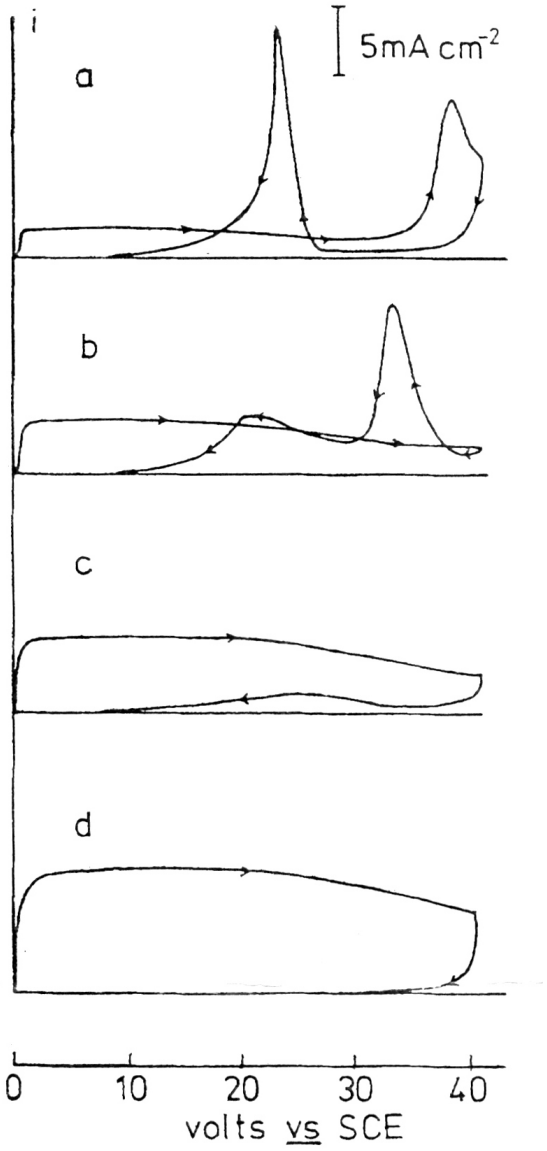

Figure 1.35: Cyclic voltammograms obtained on Ti electrodes, with sweep rates of, respectively a) 1V/s, b) 2.1V/s, c) 3V/s and d) 5 V/s. This figure is reproduced from McAleer et al. [148].

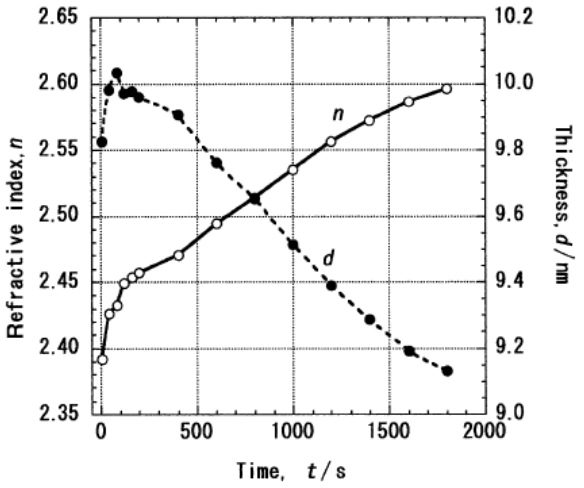

Figure 1.36: Time-evolution of the refractive index and thickness of an anodic oxide film submitted to a potentiostatic aging at a potential lower than its formation voltage, as reported by Ohtsuka et al. [172].

attributable to a dehydration process.

Eventually, potentiostatic aging can lead to the crystallisation of the oxide film. This has been demonstrated by da Fonseca et al. [43], who detected crystalline anatase by grazing-angle XRD in initially amorphous TiO_2 films after an aging step under potentiostatic conditions. A similar observation has been reported by Arsov [16] who used in-situ Raman spectroscopy. Aging at lower potentials lead to longer incubation times before the Raman signal characteristic for Anatase was observed.

The influence of potential cycling on the properties of the oxide films are not well understood yet. Two main studies deal with this question. Oliveira et al. [173] have studied the effect of potential cycling on the oxygen evolution reaction on potentiodynamically grown TiO_2 films. They observe a progressive increase of the OER current with increasing number of cycles (between 0.5 and 10 V) on an initially amorphous TiO_2 film. This observation indicates an increasing electronic conductivity of the film. When the potential scan range is extended to a more cathodic value of -1.1 V, Oliveira et al. observe a very marked increase of the current peak associated with the oxygen evolution. These authors propose this behaviour to be due to an increased electronic conductivity of the film and/or an increase of the effective surface of a

porous TiO_2 layer on the surface during cathodic polarisation. Azumi and Seo [17] have carried out impedance measurements on TiO_2 films during repeated potential cycles. They report a very complex behaviour, which they attribute to a reversible field-induced water dissociation inside the oxide film. According to these authors, above 3V, water in the film would be dissociated which leads to the formation of TiO_3 peroxide and to the annihilation of donor species. As a result, the outer part of the film would become more insulating. During the reverse scan, the reverse transformation would take place below 0.5V. From the very limited number of studies available on the influnce of potential cycling and the very complex nature of the reported phenomena, it is obvious that supplementary experimental evidence would be necessary to better understand the influence of potential cycling of anodic oxide films on their properties.

1.2.5 Stability of anodic TiO_2 films

Dissolution of anodic films under open-circuit conditions

The group of L. Peter [22, 23] provided very insightful data on the dissolution of anodic TiO_2 films in moderate acidic and alkaline environment. Using an electrochemical dissolution-regrowth method, they demonstrated that, in electrolytes free of aggressive (F^-) ions, the dissolution of the anodic TiO_2 films takes place uniformly all over the oxide surface, and not as a localised attack. The dissolution was also shown to be essentially chemical (not electrochemical), with a dissolution rate exhibiting a first-order dependence towards the protons concentration at low pH. These authors therefore propose the following reaction to be the main one responsible for the dissolution of the TiO_2 films in acidic electrolytes:

$$TiO_2 + H^+ + H_2O \Rightarrow Ti(OH)_3 \tag{1.41}$$

the hydroxide compound being rapidly dissolved in acidic electrolytes. Dissolution experiments carried out at different temperatures in the range of 2°C to 65°C suggest that the dissolution process is thermally activated, with an associated activation energy of 63 kJ/mol (measured in 3.0 M H_2SO_4 for a TiO_2 film grown potentiodynamically at 1 V/s up to 2V). Peter et al. also investigated the dissolution behaviour in different chemical environments and report typical dissolution rates in the range of 0.07 nm/h (potassium oxalate 1.0 M) to 2.23 nm/h (H_2SO_4 3.0 M). However, the previous values should only be taken as indicative for the order of magnitude of typical dissolution rate as the effective dissolution rate was also shown to be widely influenced by the rate of growth of the film. This is illustrated on Fig.1.37, showing the thinning rate as a function of the growth rate. Films grown slowly are observed to dissolve more slowly as well, which, according to these authors, is attributable to their more ordered structure. The stability of rapidly grown films can also be improved by aging

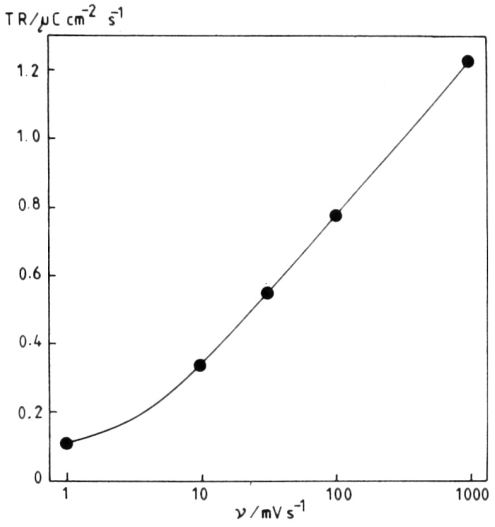

Figure 1.37: Evolution of the dissolution rate of anodic TiO_2 films (expressed in terms of the charge consumed for re-growing the dissolved fraction of the film) as a function of their rate of growth. This figure is reproduced from Blackwood et al. [22].

the film under potentiostatic conditions at the formation potential, preferably at a higher temperature.

Using the same dissolution-regrowth approach, Marino et al. [152] investigated the influence of two other parameters of oxide growth on the dissolution behaviour of anodic TiO_2 films, namely the pH of the electrolyte used for growing the oxide film and the formation voltage of the film. All their anodic TiO_2 films were grown potentiodynamically at the same rate up to forming voltages in the range of 1 to 5 V, in buffered phosphate electrolytes with pH in the range of 1 to 5. According to their observations, the charge consumed for re-growing the dissolved fraction of the oxide film is almost independent of the formation voltage and pH. The dissolution behaviour therefore seems to be unaffected by the latter parameters (at least in the range of values investigated by Marino et al).

Dissolution of anodic films under cathodic polarisation

The dissolution of TiO_2 films is accelerated when the Ti electrode is polarised cathodically but remains uniform, according to Blackwood et al. [22]. According to Arsov [15], the rate of electrochemical dissolution is maximum when the electrode is polarised at -0.6V. For more cathodic potentials, hydrogen evolution accompanies the TiO_2 reduction, as well as the formation of Ti hydrides TiH_2. Even thick TiO_2 films, formed over 80V, were reported to be completely dissolvable electrochemically upon cathodic polarisation.

1.3 Growth stresses in anodic oxide films

1.3.1 Stress measurements in anodic oxide films

The very first study

A pioneering study on the internal growth stresses in anodic films has been carried out by Vermilyea in 1963 [245]. He measured the deflection of cantilevered foils of the main valve metals during anodisation using a telescope. Although this author reports a poor reproducibility of the results, he clearly evidenced that significant internal stresses are generated in anodic oxide films during their growth and he already identified most of the main parameters influencing the stress evolution in valve metal oxides. In particular, he reports that the stresses are always more compressive under applied field conditions than at open-circuit and ascribes this to an electrostatic effect (hence, he already identified the reversible contribution from electrostriction, which will be discussed extensively in chapter 4). Vermilyea also reports an effect of the growth rate and of the presence of specific ions in solution on the stresses. Finally, he reports that more compressive stresses are generated when gas is evolved.

Stresses, crystallisation and breakdown

After the study reported by Vermilyea, internal stresses were frequently cited in the literature as a possible source of crystallisation, breakdown or growth instabilities. Leach and Pearson, for instance, suggest that a relationship exists between stresses, ionic transport numbers and crystallisation [133]. They base their reasoning on the observation that ZrO_2 and HfO_2 are the only valve metal oxides which grow almost exclusively by anionic transport and are also the only ones which are always observed in the crystallised state. Leach and Pearson conclude that anionic transport favours crystallisation. Considering the observation that the growth of anodic oxide films on Hf and Zr is also accompanied by large compressive stresses, they propose that the favourable influence of anionic transport on crystallisation could, at least partly, be due to the compressive stresses which are associated with this type of growth. Intuitively, the

fact that compressive stresses would be favourable to crystallisation can indeed be rationalised by considering that crystallisation leads to a densification of the oxide film. Yahalom and Zahavi [261] also suggest that compressive stresses can be high enough to promote direct crystallisation by pressure, at least to some extent. According to them, the amorphous-to-crystalline transition could lead to cracking of the film, thus leading to breakdown as well. This was confirmed by Vermilyea [243, 244] and Jackson [100] who observed local cracking of their Ta_2O_5 films at sites of field-crystallisation. Internal stresses can also be large enough to directly result in cracking of the oxide film (without necessarily involving crystallisation) if the stress exceeds a critical level [261]. Such a 'mechanical breakdown' was indeed observed by Di Quarto et al. and by Archibald on ZrO_2 films [52, 12]. The mechanical breakdown is manifested by the appearance of small cracks in the oxide surface and a change in the growth kinetics of the film. McAleer et al. [148] also provide indirect electrochemical evidence that, at some stage during the growth process, cracks would form in the outer part of the anodic oxide film, which would be induced by large internal stresses. Sato proposes that the stress contribution arising from electrostriction and surface stress effects (associated with the absorption of molecules on the oxide surface) can reach sufficiently high values to lead to mechanical breakdown. Shibata and Zhu [215] have studied the evolution of crystallisation as a function of the temperature and observe that crystalline films are formed after 1h potentiostatic anodisation at 1V from 323°C on. They evaluate the stresses in their oxide film as a function of the temperature according to the model of Sato and conclude that the stresses are shifted from tensile to compressive with increasing temperature, as illustrated on Fig.1.38. Therefore, they suggest that their observed crystallisation at 323°C can be attributed to the fact that the stress in the film has exceeded a compressive critical value. It should be noted that all these predictions on the relationships between internal stresses and crystallisation or cracking are rather speculative, considering the very limited amount of experimental evidence available. This is due to the fact that studies devoted to the development of internal stresses in anodic oxide films are not numerous and that they show poor quantitative and even qualitative agreement with one another. The main experimental results on the development of stresses in anodic oxide films are presented in the next paragraph, together with the different theories proposed for accounting for those stress evolutions.

Theories on the origin of stresses in anodic oxide films

The most obvious source of internal stresses arising during the transformation of a metal into his oxide by anodisation is the difference between the molar volumes of the two materials. The ratio of the respective molar volumes of the metal and metal oxide, usually referred to as the Pilling-Bedworth ratio (PBR), is typically between 1.4 and 2.4 for valve-metal oxides. Based on this

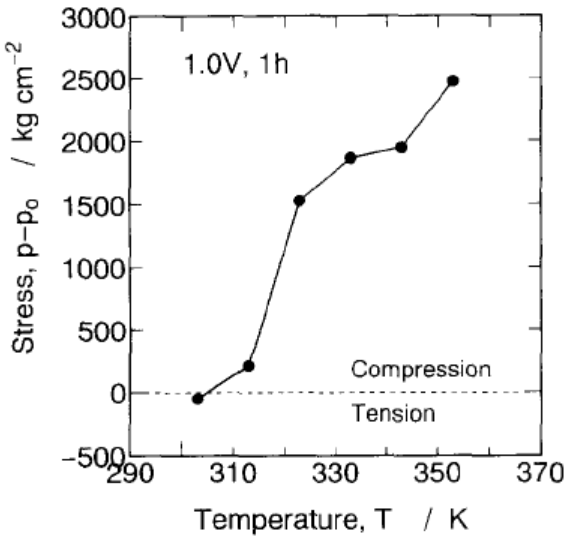

Figure 1.38: Influence of the electrolyte temperature on the estimated growth stress in anodic TiO_2 films, reproduced from Shibata et al. [215].

well-established criterion, anodic oxide films are anticipated to grow with large compressive stresses. This was however found to be in contradiction with the observation of Vermilyea that tensile stresses develop on most anodic oxide films grown on Ta, Ti, Nb, Al and W. Therefore, different scenarios were proposed to account for the origin of tensile stresses, none of them being so far completely convincing. Vermilyea [245] suggests that tensile stresses could result from a progressive dehydration of the oxide film which would be initially formed as an hydrated oxide. The latter explanation was also proposed by Wüthrich [258] and Sahu [199] for accounting for their observed tensile growth stresses on, respectively Al_2O_3 and TiO_2 films. Wüthrich ascribes the more tensile stress observed at higher current density to a higher degree of hydration. Other scenarios are based on the hypothesis that tensile stresses are the result of vacancy build-up at the metal/oxide interface. After the study by Vermilyea, described in the previous sub-section, supplementary studies were carried out by Bradhurst and Leach (on Al_2O_3 films) [31] and by Archibald (on ZrO_2 and TiO_2) [12, 13]. The former authors observed tensile stresses in alumina films grown at high current density and compression in films grown at low current density, with a transition between the two stress conditions taking place for an intermediate current density (see Fig.1.40). This characteristic transition on Al_2O_3 film was later observed by Nelson et al. [164] as well but not by Wüthrich [258]. As pointed out by Bradhurst and Leach [31], the observation of a transition from compressive to tensile stresses for a given current density is further evidence that predicting the sign and magnitude of stresses based only on the value of the PBR of the metal/metal oxide system of consideration is an oversimplification and that other factors must be taken into account. They suggest that the dependence of the average stress on the current density could be related to the variations of the cationic transport number with i previously evidenced by Davies [45]. Bradhurst and Leach consider that the oxide formed at the oxide/electrolyte interface grows relatively free of stresses while, in contrast, the fraction of the film formed at the metal/oxide interface experiences large compressive stresses. Within this framework, the relative values of anionic and cationic transport numbers have a direct influence on the average stress in the film, with an increase of the cationic transport number being expected to lead to less-compressive stresses. Archibald studied the stress development in anodic ZrO_2 films grown galvanostatically up to 200V. He observed a dependence of the average stress on the current density which also agrees with the evolution of the cationic transport number with i described by Davies, with less-compressive stresses observed at high current density due to a larger contribution of the cationic transport (see Fig.1.41). However, it should be noted that, although this model seems to provide fairly good qualitative predictions of the influence of the current density on the stress evolution, only 'more-compressive' or 'less-compressive' stresses can be accounted for. This scenario does not rationalize the development of truly tensile stresses. With

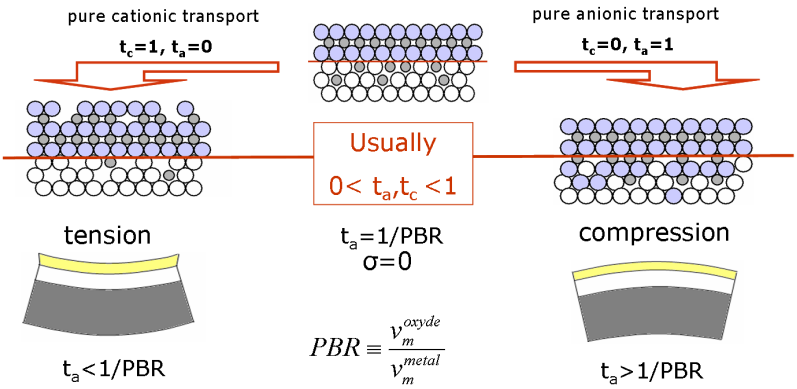

Figure 1.39: Illustration of the influence of the transport numbers on the intrinsic growth stresses in the film, according to the model of Nelson and Oriani [164].

this respect, the comprehensive model derived by Nelson and Oriani [164] is more satisfactory. These authors base their model on the observation that the stress in their anodic oxide films grown on Ti and Al appear to be independent of oxide thickness over the potential range investigated (up to 2V only). They conclude that this observation is indicative for the stress being essentially localised at the metal/oxide interface, the oxide/electrolyte interface being in contrast essentially free of stresses, as postulated by Bradhurst et al. Then, they propose that tensile stresses arise from the build-up of oxygen vacancies at the metal/oxide interface which is in turn directly related to the ionic transport numbers in the film. They identify a critical value of the anionic transport number

$$t_a^o = \frac{1}{PBR} \tag{1.42}$$

such that the volume of metal consumed at the metal/oxide interface is exactly compensated by the volume of oxide formed at that interface, thus leading to zero-stress growth. The sign of the stress is therefore a direct consequence of the anionic transport number being larger or smaller than t_a^o, leading respectively to compressive stresses or free-volume build-up and therefore tensile stresses.

Within the framework of their model, transitions in the sign of the growth stress can easily be accounted for, in relation to changes in the ionic transport numbers, as illustrated on Fig.1.39. In addition to the compressive-to-tensile transitions as a function of the current density observed by Bradhurst and Nelson (on Al), Kim et al. [111] observe a similar compressive-to-tensile transition (on W) taking place for a given thickness. They interpret this observation based on the model of Nelson and Oriani as well as based on the theory proposed by

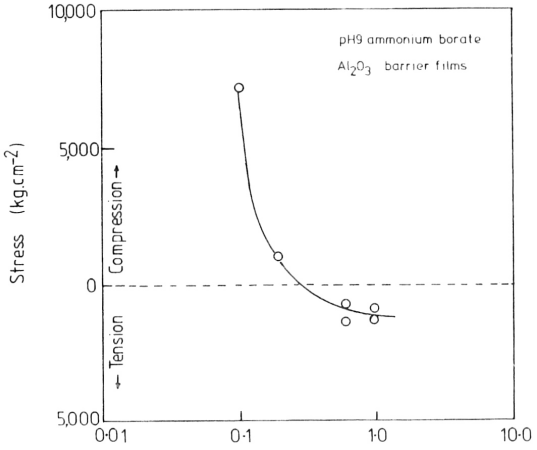

Figure 1.40: Influence of the anodisation current density on the growth stress in anodic alumina films, reproduced from Leach et al. [133].

Sato and Cohen [204] stating that the diffusion of oxygen vacancies becomes more and more difficult with increasing thickness of the oxide film. After a given thickness is reached, the diffusion of oxygen vacancies becomes too slow and vacancies progressively build-up at the metal/oxide interface, thus leading to the observed compressive-to-tensile transition. Based on the latter observations as well as on their own stress-measurements on anodic Al_2O_3 films, Moon and Pyun [159] claim that the stress in anodic oxide films is determined by the rate of creation and annihilation of both metal and oxygen vacancies in the first three atomic layers adjacent to the metal/oxide interface. Their theory can be seen as the microscopic version of the Nelson and Oriani model. The main criticism regarding the model of Nelson and Oriani is that, from a mechanical point of view, it seems unlikely that a film can grow for long with free volume being accumulated at the metal/oxide interface. This would be expected to rapidly lead to the formation of large cavities and eventually film delamination.

As to the dependence of the average stress on oxide thickness, there does not seem to be a clear trend. Archibald observes that the stress in ZrO_2 film is independent of oxide thickness in the wide range of 10 to 200 V [12], while in the same voltage range, the average stress in TiO_2 films decreases progressively with increasing thickness [13]. Constant growth stresses have been reported as well, over a much reduced V-range, for TiO_2 (Butler [33], Nelson [164], Ueno[239]) and Al_2O_3 (Wüthrich [257]). Kim et al. [111], in contrast, observe a marked thickness dependence of the stress on their WO_3 films, illustrated on

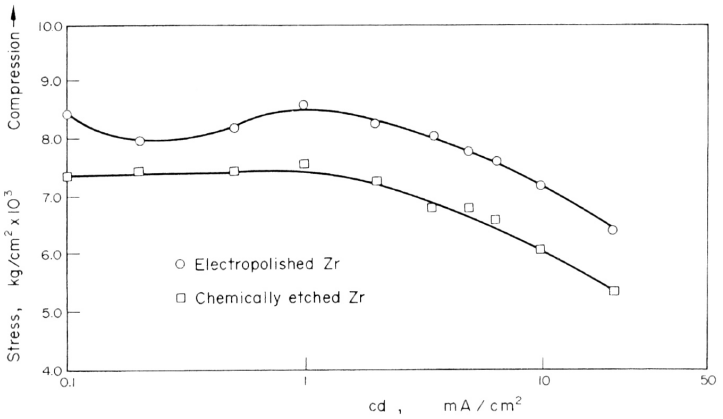

Figure 1.41: Influence of the anodisation current density on the growth stress in ZrO_2 films, reproduced from Archibald [12].

Fig.1.42.

As to the influence of the electrolyte concentration, two studies are available, which have been carried out by Moon and Pyun [159] and Benjamin et al. [21] on Al_2O_3 films[3]. The former authors observed a very significant increase of the compressive character of the stress upon increasing the concentration of their H_2SO_4 electrolyte between 0.5 M to 3.0 M. They interpret this observation as being due to a direct influence of the pH on the creation of Al^{3+} vacancies at the oxide/electrolyte interface, as a result of the dissolution of the oxide film at the oxide/electrolyte interface. Benjamin et al. [21] report the same trends. In addition to the influence of the electrolyte concentration, the influence of specific anions in the electrolyte has been investigated as well. Archibald reports that F^- additions to the electrolyte modify profoundly the stress evolution of ZrO_2 and TiO_2 films. On TiO_2 films, additions of fluorine increase the tensile character of the stresses. Therefore, he proposes that F^- ions could stimulate the cationic transport. The specific influence of F^- ions on the stress evolution may rather be related with their ability to migrate in the TiO_2 film faster than O^{2-} ions (owing to the smaller ionic radius of F^- anions) and to accumulate at the metal/film interface [82]. Their tendency to dissolve the portion of the oxide film formed at the film/electrolyte interface [82] and to favour crystallisation to rutile [127] may also play a role. A similar

[3]Surprisingly, some of the figures presented by Benjamin et al. are exactly the same as those found in the paper by Moon and Pyun (apart from a slight re-scaling), although the latter paper is not even cited in the reference list. Therefore, it is doubtful that the two papers can be considered as two independent studies.

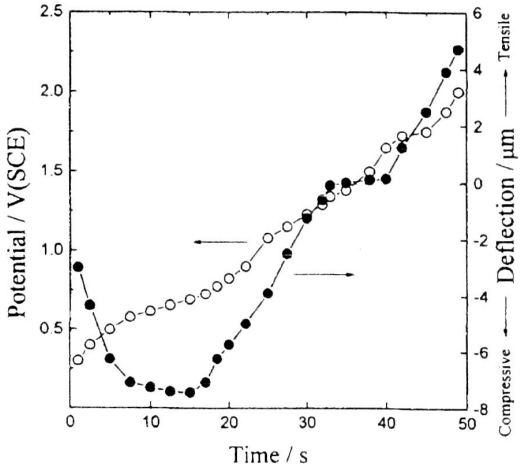

Figure 1.42: Time-evolution of the cell voltage and of the curvature (presented in terms of electrode deflection) during the anodisation of a tungsten film, reproduced from Kim et al. [111]. A compressive-to-tensile transition is observed in the course of the growth.

influence was also reported by Pyun [193, 194], with chlorine additions to the electrolyte leading to a significant increase of the compressive stresses in growing WO_3 films. This effect was more marked in electrolytes containing higher Cl^- concentrations and when the film was grown at lower current densities. Pyun suggests that Cl^- anions are incorporated in the growing film and can occupy oxygen vacancy sites in the oxide, the larger compressive stresses being attributable to the larger ionic radius of Cl^- as compared to O^{2-} anions.

Butler and Ginley [33] provide insightful information on the reversible part of the growth stress. They observe a cyclic variation of the reversible component of the stress when their electrode is submitted to a slow cyclic (triangular) polarisation (see Fig.1.43). They confirm that the reversible stress increases proportionally with the square of the electric field, as expected for electrostriction stresses. When they increased the scan rate during their cyclic polarisation experiment, they observed an irregular behaviour, with much noise, probably due to interference with other effects. Indeed, according to Wüthrich [258], the reversible stress can comprise other contributions than the electrostriction stress. He has measured internal stresses in growing anodic Al_2O_3 films using a membrane deflection technique. He points out that thermal stresses account for a significant part of the observed stress, as well as another, unidentified

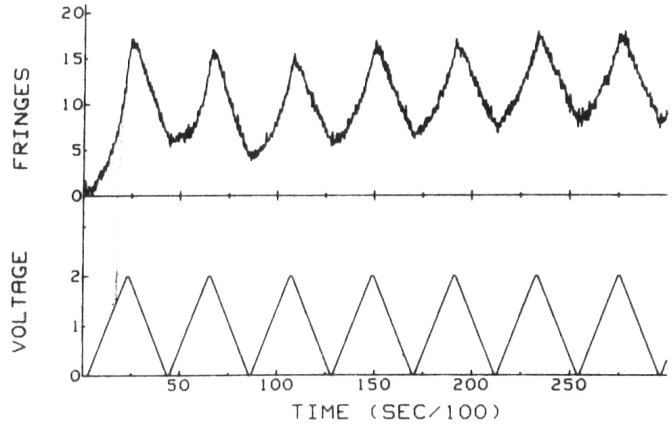

Figure 1.43: Evolution of the anode curvature accompanying potential cycling of a Ti electrode between 0 and 2V, reproduced from Butler et al. [33].

stress contribution related to the current flow.

In conclusion, stresses in anodic oxide films comprise a reversible and an irreversible part. The reversible part is composed of the respective contributions from electrostriction, thermal effects and probably electrocapillarity effects. The irreversible part represents intrinsic stresses resulting from the growth process. Although, by considering only the relative molar volumes of the metal and metal oxide, compressive intrinsic stresses would be expected, tensile stresses are usually observed in valve-metal oxides in which both cationic and anionic transport contribute to the growth. Compressive stresses are sometimes observed as well under specific conditions or in specific voltage ranges, as well as compressive-to-tensile transitions. Compressive stresses are observed in ZrO_2 and HfO_2 in which the transport is essentially provided by anions [133]. Tensile stresses have been proposed to arise from dehydration of the initially hydrated oxide [245] or from the accumulation of vacancies at the metal/oxide interface [164]. According to one or the other model, more tensile stresses would be generated at higher growth rate because of a higher degree of hydration or because of an increased contribution of cationic transport. The electrolyte can influence the stress evolution directly through ion incorporation in the oxide film [12, 13, 111] and ion adsorption on the oxide surface [205]. The electrolyte pH may influence the stress evolution through dissolution effects affecting the concentration of metal vacancies [21, 159].

1.3.2 State-of-the-art of stress measurements in TiO_2 films

In this paragraph, the main experimental observations relative to stress measurements in anodic TiO_2 films are presented. As will be discussed, comparison of the different studies is not straightforward because of major differences in the experimental conditions and thickness range investigated.

The first study dealing with this topic was carried out by Archibald [13]. He studied stresses in films grown galvanostatically on bulk Ti substrates up to 200V in ammonium borate electrolyte with and without fluorine additions. He observed only tensile stresses throughout the growth (or at least from 20V on because no stress measurements are available below that value), with the average stress decreasing from about 150 MPa down to about 40 MPa with increasing film thickness (see Fig.1.44).

Butler and Ginley [33] tackled the same problem but focused on a narrower voltage range of 0 to 2V. Films were grown potentiodynamically in 0.2 M Na_2SO_4 on sputtered Ti films with scan rates of 1 and 10 mV/s. Within that voltage range, they report the average growth stress to be compressive, independent of oxide thickness and of the order of -70 MPa (after subtraction of the reversible contribution) (see Fig.1.45). Nelson and Oriani [164] have studied oxide growth in the same potential range of 0 to 2V in order to avoid interference with the oxygen evolution reaction. They performed both potential steps and galvanostatic experiments on bulk Ti substrates in 0.1 M H_2SO_4. In both cases, they observe an immediate compressive surge at the beginning of anodisation (associated with electrostriction), followed by a tensile evolution, as illustrated on Fig.1.46. The latter observation is in contrast with that of Butler and Ginley, who observed compressive intrinsic growth stresses in the same V-range. In the study by Nelson and Oriani, under galvanostatic conditions, the tensile evolution is characterised by a constant slope, which increases proportionally with the current density, thus suggesting that the oxide film grows under constant efficiency and constant instantaneous stress conditions. These authors present all their results in terms of 'rate of deflection', so that quantitative assessment of their stress data is not straightforward.

Sahu et al. [199] devoted their study to potentiodynamic growth on sputtered Ti substrates in 1% H_2SO_4 electrolyte and in the range of 0 to 10V. They observe tensile intrinsic growth stress, as shown on Fig.1.47. They report a value of 190 MPa for the electrostriction stress.

The group of Masahiro Seo [239] provided a second study on TiO_2 films grown potentiostatically. Their oxide films were grown on sputtered Ti films for one hour at a constant potential in the range of 1 to 10V (hence the same

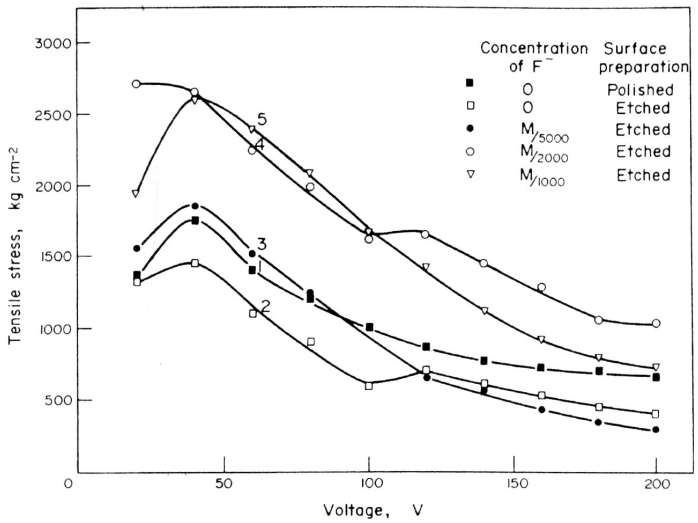

Figure 1.44: Evolution of the growth stress in anodic TiO_2 films, as a function of the final anodisation voltage, showing a decrease of the average growth stress with increasing V. This figure is reproduced from Archibald et al. [13].

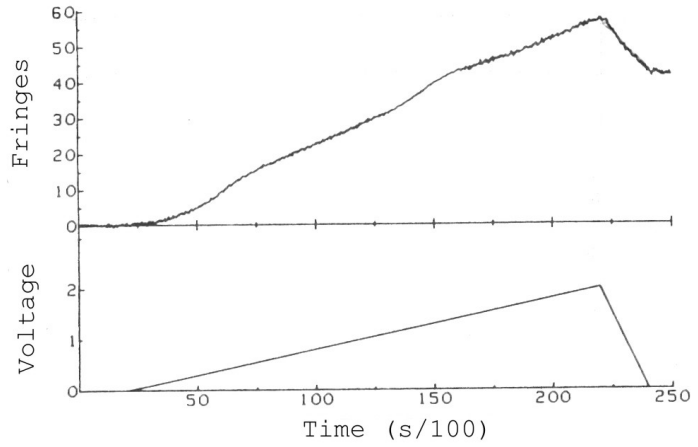

Figure 1.45: Evolution of the curvature of a Ti anode submitted to a potential cycling between 0 and 2V, reproduced from Butler et al. [33]. The residual growth stress at the end of the cycle is observed to be compressive.

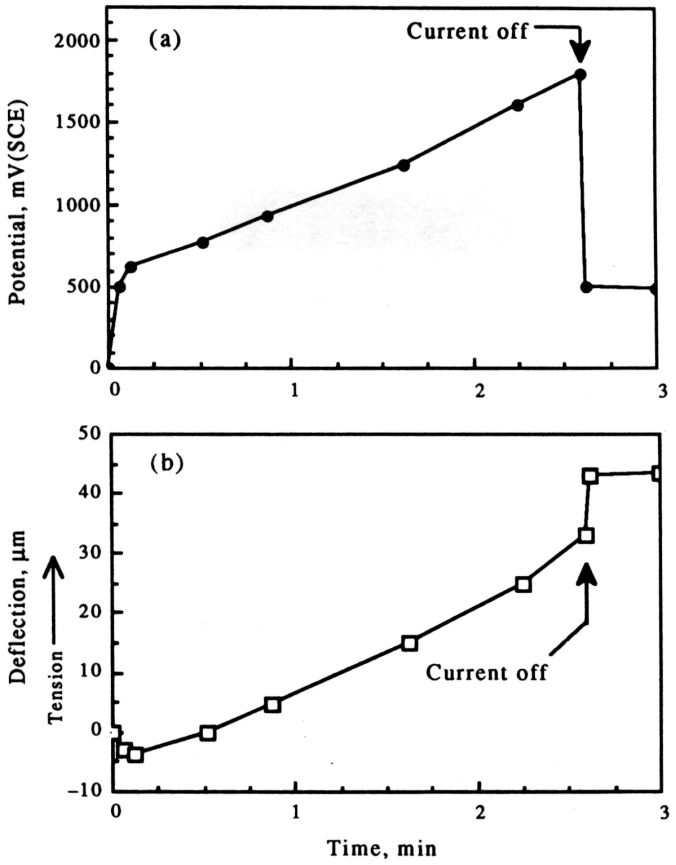

Figure 1.46: Time-evolution of the anode potential and of the anode curvature during a galvanostatic anodisation experiment, reproduced from Nelson et al. [164]. The residual growth stress when the current is turned off at the end of the experiment is observed to be tensile.

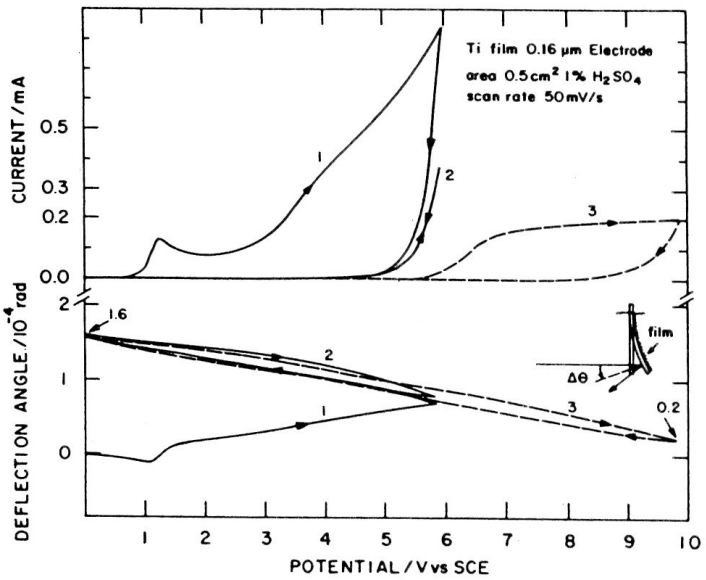

Figure 1.47: Evolution of the cell current and of the anode curvature (presented in terms of deflection angle) during potentiodynamic anodisation of a Ti electrode, reproduced from Sahu et al. [199]. The residual growth stress at the end of the first cycle is observed to be tensile.

potential range as Sahu et al.) in buffered borate solution. The growth stresses were always compressive, of the order of -500 MPa and essentially independent of oxide thickness (see Fig.1.48). In contrast to Butler et al, they report very weak electrostriction stresses of about 20 MPa.

Finally, we should mention one last study by Hong et al. [89], who have studied the stresses in passivating TiO_2 films formed under open circuit conditions on Ti substrates in 1.0 M H_2SO_4. However, stress values reported in this study appear doubtful since their reported values for the thickness of the spontaneously formed passivating film (150 nm) are, at least, one order of magnitude larger than the expected values under open-circuit conditions and are therefore very unlikely.

In the light of these experimental observations we can conclude that:

- in most cases, the films grow under constant stress conditions or, at least, the stress in the film varies slowly with film thickness, the stress variation being only visible when the anodisation process is studied over a large thickness range.

- there does not seem to be a straightforward relationship between the growth rate and the sign of the stress, since the faster and slower growth rates (potentiostatic growth and potentiodynamic growth at 10 mV/s respectively) lead to compressive stresses while all intermediate growth rates were observed to correspond to tensile stresses. Furthermore, there is no agreement between the two studies carried out under potentiostatic conditions since Nelson et al. report tensile stress evolution while Ueno et al observe a compressive stress evolution.

- tensile stresses were observed in all studies where bulk Ti was used as a substrate while both compressive and tensile stresses were reported for studies on sputtered Ti thin films.

- there is no obvious correlation between the nature of the electrolyte and the stress behaviour. Both compressive and tensile stresses were reported in both borate and sulphate electrolytes. The presence of F^- ions in the electrolyte does however strongly influence the stress evolution, leading to a less-compressive behaviour.

- as to the magnitude of the stresses, reported values range from -500 MPa (Ueno [239]) to 250 MPa (Archibald [12]), with an intermediate value of -70 MPa being reported as well (Butler [33]).

Considering the poor apparent agreement between the various experimental results and the complete absence of clear trends, we can hardly draw any firm

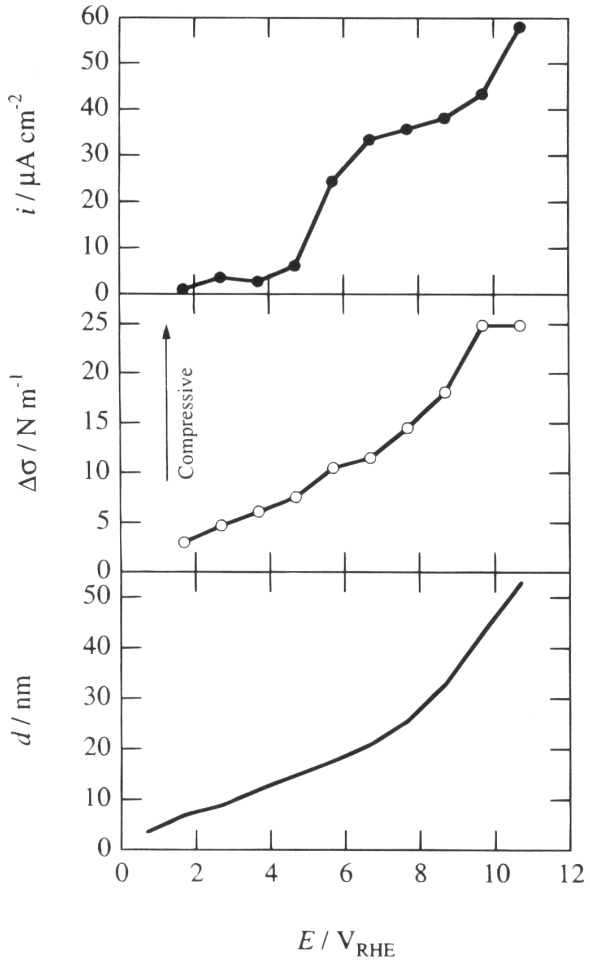

Figure 1.48: Evolution of the final cell current i, of the stress·thickness product $\Delta\sigma$ and of the oxide thickness d with the anodisation potential for a potentiostatic anodisation experiment, reproduced from Ueno et al. [239].

conclusion as to the 'typical' stress evolution behaviour of anodic TiO_2 films, neither quantitatively nor qualitatively. This is probably due to the interfering influence of yet-unidentified and/or uncontrolled experimental parameters. Within this framework, supplementary experimental data seems necessary for bringing more insight into the complex influence of the various experimental parameters.

1.4 Characterisation of anodic oxide films

1.4.1 Thickness measurements

In the field of thin films and coatings technology, measuring the thickness of a film is a very 'vital' need. While this seems to be a trivial operation for relatively thick coatings, it can turn out to be rather challenging in the case of ultrathin films, with thicknesses in the range of a few to a few hundred nanometers. A whole set of methods has been used in the literature, which are well-adapted to the thickness range of anodic films. The latter include ellipsometry [186, 105, 131, 57, 15, 259, 168, 169, 170, 171, 172], reflectometry [105, 186, 131, 189], profilometry [266], interferometry [148, 51], Auger depth profiling [48, 119, 175], RBS [213, 256, 187, 73, 74, 77, 78, 79], capacitance measurements [110, 235, 1], resistivity measurements, electron microscopy or mass gain measurements using an electrochemical quartz crystal microbalance [30, 175]. During this doctoral research, ellipsometry, electron microscopy, RBS and resistance measurements have been used and are therefore briefly presented below.

ellipsometry

Ellipsometry is an optical thickness-measurements technique. Thickness values are extracted by fitting the recorded Stokes parameters (Ψ and Δ, characterising the amplitude ratio of the incident and reflected beam and its polarisation shift) to an optical model of the sample. Ellipsometry is extremely sensitive to slight changes in the surface condition and is therefore very well-adapted for measuring very small thicknesses and thickness changes. It is also particularly adapted for measuring dielectric films (for which the imaginary part k of the refractive index is zero, hence allowing for a simplification of the optical model). It is also completely nondestructive and suitable for in-situ measurements during anodisation, which are significant advantages. The sensitivity of the technique can however turn out to be a drawback in the case of materials which are very sensitive to the preparation conditions, or which exhibit complex morphologies (multi-layered structure, partial crystallisation, incorporation of gas bubbles, blistering,...). As a result, application of ellipsometry to measuring the thickness of anodic TiO_2 films is sometimes challenging. Another drawback of ellipsometry is that the interpretation of the spectra is not very intuitive and

fitting the spectra to an erroneous optical model can lead to 'apparently correct' results which in fact are far from reality.

Cross-sectional SEM

The main advantage of microscopies for measuring thicknesses is that they provide a direct, readily interpretable, imaging of the sample, hence allowing for measuring an average thickness and to detect local deviations from the average value. In contrast, SEM offers a limited resolution, of the order of 50 nm for FEG-SEM and films thinner than 100 nm can hardly be measured with sufficient accuracy. Thinner films can be measured by transmission microscopy but the sample preparation requires a long and complicated procedure. SEM is also a semi-destructive technique, as a portion of the sample needs to be cut in order to expose a fresh cross-section.

Resistivity measurements

This method is specific to the anodic films grown on thin film metal substrates. It is an indirect measurement since it is not the thickness of the oxide film which is measured but the thickness of the underlying metal substrate. The thickness of the oxide film (h_f) can be evaluated from the amount of metal consumed (Δh_m), which in turn is assessed from the change in the resistance of the metal layer, as measured from a four-points probe. This method is extremely simple, fast, provides for an average thickness value and can offer a very high-resolution provided that the measurement is carried out under optimal condition. In fact, owing to the relative character of this measurement, the resolution depends directly on the thickness of the metal substrate prior to anodisation. The thinner the metal film, the higher the resolution. For instance, starting from a 100 nm thick Ti substrate, the resolution on the thickness of the anodic TiO_2 film will be of the order of 2 nm. However, sources of errors are numerous. Firstly, conversion of Δh_m into h_f requires a value for the density of the oxide film, which is not necessarily known. Δh_m needs to be corrected as well for any metal dissolution in the electrolyte during anodisation and the latter should therefore be accurately quantified as well. Finally, it is crucial that the resistivity of the metal film is homogeneous over the whole thickness. This is not very easy to guarantee, especially in the case of Ti, as oxygen concentration gradients are frequently observed in the film.

Rutherford backscattering spectrometry

Samples can be analysed by RBS without any specific preparation and the measurement is non-destructive. RBS provides for a composition depth-profile, hence providing at the same time readily interpretable information of the thickness and chemical composition of the various layers composing the sample. The resolution of the technique in terms of thickness is of the order of 10 to 20 nm. The main drawback of this technique is the specific, sophisticated facility re-

quired for such measurements and the relatively long acquisition time required. Similar to the case of resistivity measurements, conversion of the measured density into h_f requires a value for the density of the oxide film, which is not necessarily known.

1.4.2 Morphological and functional characterisation

A wide variety of techniques is available for characterising the chemistry, microstructure and functional properties of anodic oxide films, the description of which is beyond the scope of this thesis. The reader will find in Table 1.2 a list of the most widely used characterisation techniques. For each technique, a list of references is included, providing exemples of the application of the technique to the characterisation of anodic TiO_2 films.

1.5 Conclusion

In this first chapter, we review the current understanding of the Ti anodisation process. Kinetics and breakdown models are presented and a discussion of the specific features of anodic TiO_2 in terms of conductivity and crystallisation behaviour is provided. The influence of the main processing parameters on the characteristics of the films is discussed, as well as literature results from internal stress measurements on anodic TiO_2 films. The last section deals with the characterisation of the films. The wide variety of techniques available for the characterisation of anodic films is listed and relevant references are given.

Morphology and structure	
Optical microscopy	[57, 243]
Scanning electron microscopy (SEM)	[105, 216, 106, 133, 48, 50, 267, 141, 234, 55, 127, 154]
Transmission microscopy (TEM)	[261, 51, 133, 48, 50, 256, 146, 73, 265, 70, 77, 78, 79, 154]
Tunnelling microscopy (STM)	[259]
X-rays diffraction (XRD)	[48, 43, 187, 189, 91, 55, 163, 259, 127]
Electrons Back-Scattering Diffraction (EBSD)	[118, 212, 154]
Raman spectroscopy	[94, 168, 48, 59, 16, 192, 189, 143, 127]
Anisotropy Micro-Ellipsometry (AME)	[124]
Atomic Force Microscopy (AFM)	[187, 20, 30, 259, 154]
Chemical composition	
X-rays Photoelectrons Spectroscopy (XPS)	[177, 214, 187, 149, 126, 174, 259]
Nuclear Reaction Analysis (NRA)	[45, 220, 110, 267]
Rutherford Backscattering Spectrometry (RBS)	[213, 256, 187, 73, 74, 77, 78, 79]
Auger Electron Spectroscopy (AES)	[48, 49, 177, 50, 231, 175, 189, 126]
Glow-Discharge Optical Emission Spectroscopy	[73, 74, 77, 78, 79, 82]
Neutron Reflectometry	[253, 236, 237]
Mass Spectrometry (SIMS)	[266, 267]
X-rays Absorption Spectroscopy (XAS)	[43]
Electrical properties	
Electron Transfer Reactions (ETR)	[124, 30]
Electrochemical Impedance Spectroscopy (EIS)	[51, 136, 124, 146, 171, 185, 25, 17, 20, 91, 143, 174, 197]
Photoelectrochemical Spectroscopy (PCS)	[137, 182, 24, 83, 146, 185, 189, 113, 174, 127, 202]
Scanning Electrochemical Microscopy (SECM)	[251, 64]

Table 1.2: List of the main techniques used for characterising anodic oxide films and selected references providing examples of application to the case of anodic TiO_2.

Chapter 2

Experimental aspects of in situ stress measurements in anodic oxide films

Contents

This chapter is divided into three sections. The first one aims at providing the reader with a short overview of the various stress-measurements techniques and their respective advantages and drawbacks. In particular, the multi-beam curvature-based technique, which has been used in this study, is described more extensively. The second section deals with practical aspects of the use of the multi-beam curvature sensor; the calibration of the sensor and its resolution are discussed. Finally, the last section is devoted to a discussion of the specific experimental involvements of applying stress-measurements to the in situ monitoring of an anodising process. Details on our experimental set-up are provided, specifically on the design of the electrochemical cell and the sample preparation procedure.

2.1 Stress measurements in thin films

Two main approaches exist for measuring strains in a thin film [155]. The first one relies on measuring changes in the lattice constants of the material from the shifting of diffraction peaks of X-rays or electrons diffraction patterns. This method is highly accurate but its application to in situ studies is not straightforward, especially in the case of processes in aqueous environment. In the case of thin films a few nm thick, time-resolved stress measurements require grazing angle conditions and a high-power X-rays source (from a synchrotron) in order to achieve sufficient resolution. Hence, the expense and complexity of the tooling is a major drawback of the diffraction approach. In addition, it should be borne in mind that diffraction-based techniques are intrinsically limited to the analysis of crystalline films, which is also a significant limitation. An extensive review on the application of XRD to the study of stresses in thin films can be found in [252]. An alternative approach for thin films relies on measuring the stress-induced changes in the curvature of a sample composed of the film to be studied on an elastic substrate. Indeed, biaxial stresses in a film will induce a biaxial bending of the whole sample, which can be easily captured using a high-resolution curvature measurement tool. In this work, the latter approach has been selected. In the next sub-section 2.1.1, the Stoney equation is presented, which is the fundamental equation linking the curvature of the sample to the biaxial stress in a film. In sub-section 2.1.2, techniques for measuring the curvature are presented and discussed. In particular, the multi-beam optical sensor used in this work is described in details.

2.1.1 The Stoney equation

In this sub-section, a first paragraph is devoted to a simple intuitive derivation of the Stoney equation. The latter was presented by Stoney in 1909 [229] and has been since then the most fundamental equation in the field of thin film

mechanics. In a second paragraph, the hypotheses underlying the derivation are discussed.

Intuitive derivation of the Stoney equation

In his textbook on thin films mechanics, W. Nix proposes the following, very intuitive, derivation of the Stoney equation. A more detailed derivation can be found, for instance, in papers by Hoffman [88] or Flinn [60]. Let us consider a thin film of thickness h_f bonded to an elastic substrate of thickness $h_s >> h_f$. We also consider the typical case in which the length L of the sample is much larger than the substrate thickness ($L >> h_s$) so that the substrate behaves like a plate. We would like to find out how the whole sample behaves when the film is strained. Let us assume that the film expands relative to the substrate, for example due to an increase of the temperature and a mismatch in the coefficients of thermal expansion of the two materials. In order to understand the stress, strains and bending of the sample, let us first imagine that the film is free from the substrate so that it can freely expand. Then, in order to fit the film and substrate back together, a compression force per unit length F needs to be applied along the edge of the film and an equal and opposite force F has to be applied to the edge of the substrate. This will result in a biaxial compressive stresses in the film. Let us assume that a biaxial compression stress $\sigma_{xx} = \sigma_{yy} = \sigma_f$, uniform to a good approximation over the thickness of the film, exists as a result of the above process. We can write

$$F = \sigma_f \cdot h_f \tag{2.1}$$

As F is applied to the upper edge of the substrate, it will induce both a biaxial tension stress and a biaxial bending moment M in the substrate.

$$M = -F\frac{h_s}{2} \tag{2.2}$$

This is illustrated on Fig.2.1. Using a general result from classical plate's mechanics, the bending κ of the substrate resulting from this moment is equal to

$$\kappa = \frac{1}{R} = \left(\frac{1-\nu}{Y}\right)_s \frac{12}{h_s^3} M \tag{2.3}$$

where R is the radius of curvature of the sample, Y is the Young's modulus of the substrate and ν its Poisson ratio. The ratio $Y_s/(1-\nu)_s$ is the biaxial modulus of the substrate. Taking into account Eq.2.1 and Eq.2.2, Eq.2.3 can be equivalently written as:

$$\sigma_f = \left(\frac{Y}{1-\nu}\right)_s \frac{h_s^2}{6h_f} \kappa \tag{2.4}$$

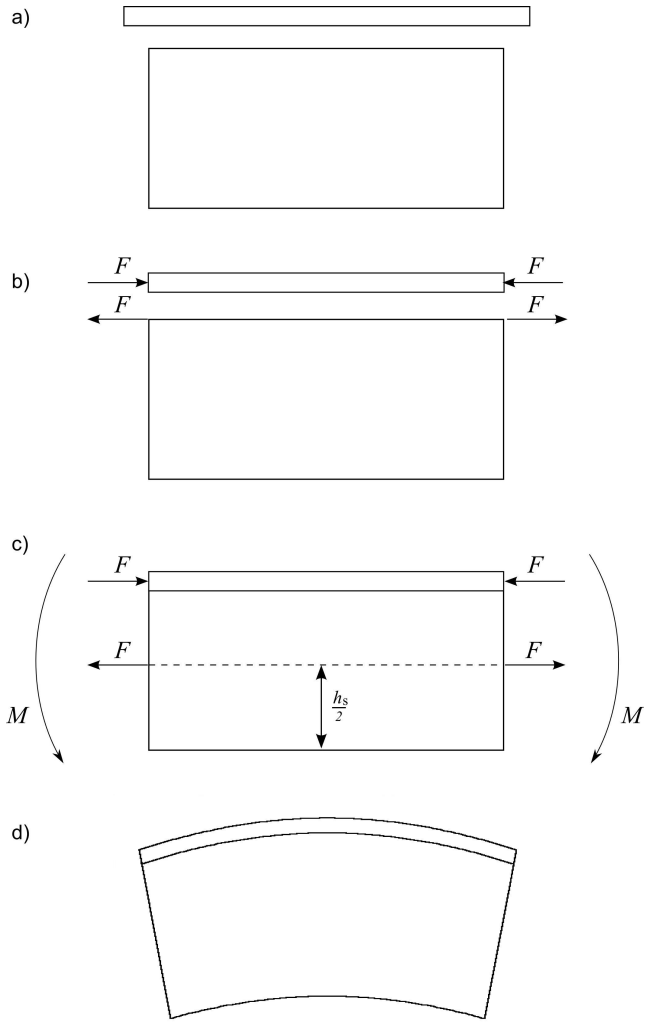

Figure 2.1: Schematic view of stress-induced curvature: a) hypothetic configuration in which the film is free from the substrate so that it can freely expand; b) in order to fit the film and substrate back together, an external compression force per unit length F needs to be applied along the edge of the film and an equal and opposite force F has to be applied to the edge of the substrate. This configuration is equivalent to the configuration c); d) As a result of the bending moment M, the sample curves.

Equation 2.4 is the so-called **Stoney equation** which is the most important equation of thin films mechanics. It links the biaxial curvature of a sample composed of a thin film on a substrate to the stresses in the film. Interestingly, it depends only on the mechanical properties of the substrate so that the biaxial modulus of the film does not need to be known, which, in many practical situations, is a significant advantage. In the next paragraph, the validity of the Stoney equation is discussed.

The hypotheses behind the Stoney equation

In the previous derivation of the Stoney equation, several assumptions were implicitly made. In this paragraph, the validity of each hypothesis is discussed. First, the Stoney equation applies to thin films only. Indeed, in the above derivation, it was assumed that the thickness h_s of the substrate is much larger than the thickness h_f of the stressed film, so that the stress and strain gradients within the film can be neglected. Furthermore, the flexural rigidity of the whole sample was tacitly assumed to be equal to that of the substrate. It can be shown that this is a good approximation as long as[1]:

$$h_s \left(\frac{Y}{1-\nu}\right)_s >> 4h_f \left(\frac{Y}{1-\nu}\right)_f \tag{2.6}$$

In this study, we have been working with silicon (100) substrates having a biaxial modulus of 180 GPa [191] and a thickness of 380 ± 25 μm. We have measured stresses in oxide films with a variable thickness in the range of 10 to 150 nm and a biaxial modulus of about 150 GPa [224]. Considering these values, the h_s/h_f ratio is thus larger than 2000 and $h_s \left(\frac{Y}{1-\nu}\right)_s$ is at least 700 times larger than $4h_f \left(\frac{Y}{1-\nu}\right)_f$ in the least favourable case. These values indicate that the thin film approximation is fully justified in our case.

In the derivation of the Stoney equation, it was also assumed that the substrate deforms isotropically and elastically. Considering the very low stresses (of at most a few MPa) experienced by our Si substrates since

$$\overline{\sigma_s} = \overline{\sigma_f}\frac{h_f}{h_s} \tag{2.7}$$

the condition of elastic deformation is obviously fulfilled. It should be noted that, as far as the film concerns, elasticity is not required since the Stoney

[1]Indeed, a more complete expression for the Stoney equation Eq.2.4 is given by [155]:

$$\sigma_f = \left(\frac{Y}{1-\nu}\right)_s \frac{h_s^2}{6h_f}\kappa\left[1 + \left(4\frac{Y_f(1-\nu_s)}{Y_s(1-\nu_f)} - 1\right)\frac{h_f}{h_s}\right] \tag{2.5}$$

The latter equation indeed reduces to Eq.2.4 when the condition given by Eq.2.6 is fulfilled.

equation remains valid for films deformed plastically. As to the isotropy of the deformation, according to Mezin [155], the validity of the Stoney equation can be limited rather rapidly by geometrical nonlinear effects. Indeed, beyond a certain level of stress (which depends on the sample dimensions), the curvature is no longer identical in all directions, the deformed shape then becoming ellipsoidal ("bifurcation effect"). This results in a modification of the flexural moment of inertia of the sample according to [155]:

$$I = \frac{bh_s^3}{12}\left(1 + 1/60\left(\frac{b^2}{h_s R}\right)^2\right) \tag{2.8}$$

where $bh_s^3/12$ is the flexural moment of inertia of an infinite non-deformed sample of width b (as considered in the derivation of the Stoney equation) while the second factor corresponds to an increase of the stiffness due to the curvature. For our own experimental set-up, the width b of the samples was around 5 mm and typical values for the measured radius of curvature amounted to 5 km. Taking those values into account, the contribution from the second factor in Eq.2.8 is of the order of 10^{-12}, thus indicating that the isotropy of deformations is definitely not a concern in our case.

Finally, it should be noted that the curvature-stress relationship can differ from the Stoney equation on the edges of the sample where non-zero shear stresses exist. However, it is usually considered that the latter shear stresses affect a region of width $5 \cdot h_f$ only along the edges of the sample [56] so that, for most samples geometries, this effect is not a real limitation. Hence, the Stoney equation can be used with confidence for converting the experimental curvature values into stress values.

The Stoney-Chu equation

In 1998, Chu has claimed that the Stoney equation was incorrect [38]. He derived his own equation linking curvature and stresses, which differs from the classical Stoney equation by a factor of two on the denominator. This causes some confusion in the literature in the field of electrochemistry, with some authors using the Stoney equation and other using the Stoney-Chu equation without any certainty as to which one is correct. Considering the fact that the Stoney equation has been used for 100 years and that its derivation has been confirmed by several authors, it seems very unlikely that the Stoney-Chu is more accurate than the original one. The approach followed by Chu might be wrong in that he postulates that the overall bending moment acting on the sample (substrate + film) is non-zero in the case of a bending due to internal stresses. However, a non-zero bending moment would mean that the sample is not at equilibrium. To the best of our knowledge, no paper provides either a confirmation that the Stoney-Chu equation is correct nor a definite confirmation

that it is wrong. Therefore, so far, it seems wiser to use the well-established Stoney equation and care must be taken, when comparing stress values from the literature as to whether they are based on the Stoney equation or on its modified version.

2.1.2 Methods for measuring curvatures

A wide variety of methods exist for measuring the curvature of a sample. The main ones are profilometry, differential capacitance, interferometry and the laser-deflection method [63].

Profilometry

In this first technique, a stylus is scanned through the sample surface, which provides for direct imaging and a quantitative measurement of the curvature. Nowadays, the best profilometers offer sub-nm vertical resolution and corresponding curvature resolution of about 50 km^{-1}. The main drawback of the method is that it requires direct contact with the sample, which involves a risk of damaging it. It is also very sensitive to the surface quality of the sample. This method is intrinsically not suitable for in-situ observation of dynamic processes, as profilometers cannot be mounted easily in a reactor or a deposition chamber. In addition, its application to the monitoring of processes in aqueous media is totally precluded. In order to illustrate this first technique, Fig.2.2 shows the profilometry scans measured on a silicon wafer, respectively before and after deposition of a 300 nm thick Ti film on one of its faces. Subtracting the initial curvature profile from the final one yields the curvature increment induced by the Ti film. From this result, an average stress of 40 MPa was calculated in the Ti film. However, no information is provided on whether this stress is uniformly distributed over the layer thickness.

Interferometry

Interferometry allows measuring deflections or displacements from relative variations of the optical path of a laser beam. With an interferometer, the curvature-induced deflection of a single point of the sample is measured. The curvature value can then be extracted from the displacement for a given experimental geometry. As compared to profilometry, this kind of technique is a non-contact one and allows for in situ follow-up of processes, even in aqueous media. Examples of the use of interferometry for in situ stress measurements can be found in the work of Butler and Ginley [33] and Wuthrich [257]. The main disadvantage of this technique is that it requires a very accurate sample positioning.

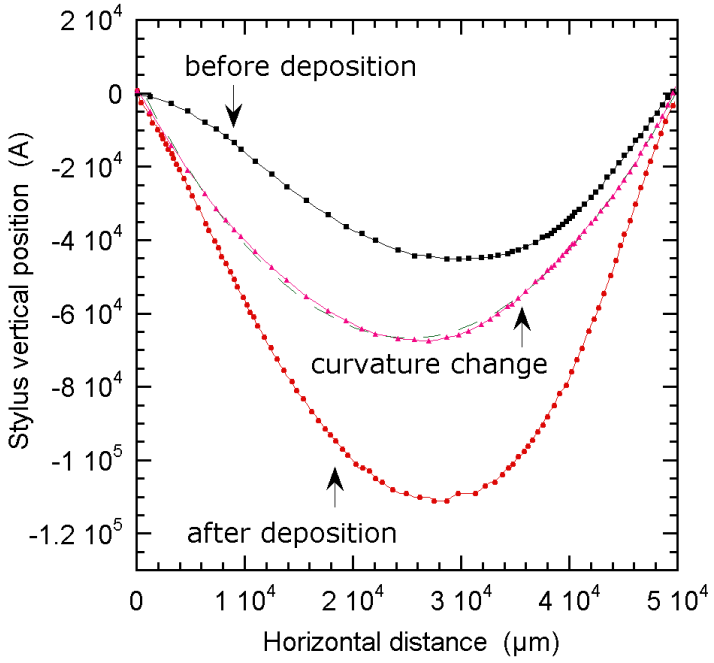

Figure 2.2: Evolution of the curvature of a Si wafer induced by the deposition of a thin Ti film, as measured by profilometry

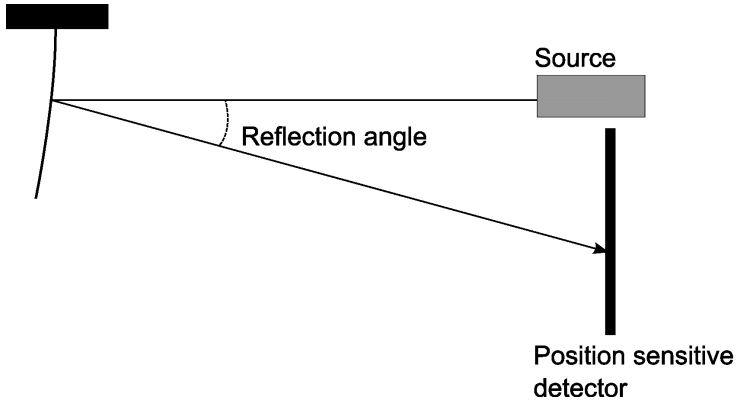

Figure 2.3: Schematic representation of the classical laser-deflection curvature-measurement technique.

Differential capacitance

The curvature of a sample can be measured very accurately by measuring relative capacitance changes of a capacitor in which the sample acts as one of the plates. This technique has a very high sensitivity (see for instance [200]) but its integration for use in an electrochemical environment is not straightforward.

Laser-deflection techniques

This class of curvature measurement techniques relies on measuring the deflection of a laser beam reflected off a curved surface. In the case of the classical laser-deflection technique, the curvature is deduced directly from the angle of reflection of the beam measured using a position-sensitive detector, as illustrated on Fig.2.3. This technique is the most widely used one, probably owing to its simplicity and versatility. The curvature measurement requires only a laser source and a position-sensitive detector (PSD), which can be easily adapted on various kinds of experimental facilities in order to achieve in situ monitoring. Examples of the use of laser-deflection techniques can be found in the work of Armyanov [225], Sahu [199], Nelson [164], Seo [238, 239, 112], Decker [46] or Stafford [227]. The resolution of the technique in terms of curvature depends on the geometry of the experimental setup, more specifically on the length of the optical path between the sample and the detector. Typical values in air and water are, respectively 0.5 [191] and 0.1 km [46]. Some authors [60, 250] have used a scanning beam technique which allows for minimising the sensitivity to displacements of the whole sample [226]. In contrast, the scanning beam reduces the time-resolution of the measurement and increases the sensitivity towards vibration noise.

The multi-beam optical sensor

A further improvement of the laser deflection technique came with the multi-beam optical sensor introduced in 1996 by Floro et al. [62, 63] and based on the two-beams technique proposed by Kobeda and Irene [116]. In contrast to the classical beam deflection technique, this technique relies on the monitoring of the spacings between an array of laser beams reflected off the sample surface. Fig.2.5 below shows a schematic representation of the experimental set-up. As compared to the single-beam technique, an optical etalon has been added in order to divide the incident laser beam into a 1D array of parallel laser beams. Using a second etalon, rotated by 90° relative to the first one, allows for further dividing the 1D array into a 2D array of beams in order to measure the curvature evolution simultaneously in two directions perpendicular to one another. In the multi-beam configuration, the position-sensitive detector has also been replaced by a CCD camera. The camera is connected to a computer via a frame grabber[2]. Each laser beam appears as a spot on the detector of the CCD camera, as illustrated on Fig.2.4. A data analysis software determines and records the position of the centroid of each laser spot on the CCD as a function of time and calculates the time-evolution of the beams spacing. This set-up allows for real-time measuring of the evolution of the spacings between each pair of laser beams. The main advantage of using a multi-beam configuration instead of a single-beam one is a reduced sensitivity towards vibrations [201], while maintaining a high time-resolution (in contrast to the scanning beam technique). Indeed, vibrations of the sample, laser source or detector are expected to affect every laser beam in the same manner so that the instantaneous spacings are expected to be virtually unaffected by this important source of noise.

The multi-beam technique has already proven successful for in-situ monitoring of the stresses generated in metal or ceramic films deposited in vacuum by CVD [85], PVD [191] or MBE [61]. The present study aims at further demonstrating its utility for in-situ monitoring of processes in aqueous media. The latter technique was selected as it was the most suitable one, allowing for real-time curvature measurements, being compatible with the constraints imposed by the electrochemical environment, being a non-contact and relatively straightforward technique, and probing a significant area at one time, thus providing directly for an average stress measurement. In the next section, practical aspects of the use of the multi-beam sensor are discussed.

[2]A frame grabber is an electronic device that captures individual, digital still frames from an analog video signal or a digital video stream. (definition from www.wikipedia.org)

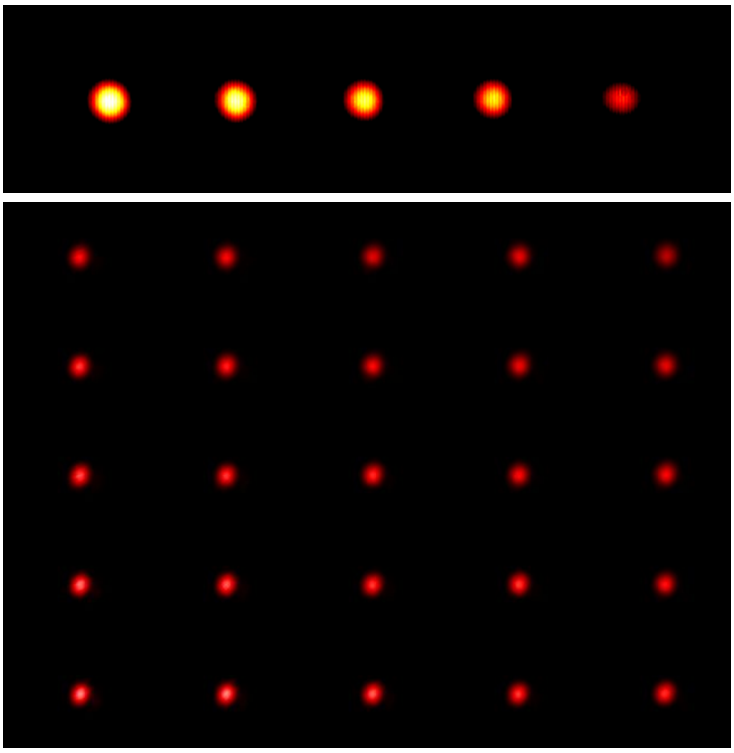

Figure 2.4: Laser spots, as observed on the CCD detector for a) a 1D and b) a 2D curvature measurement.

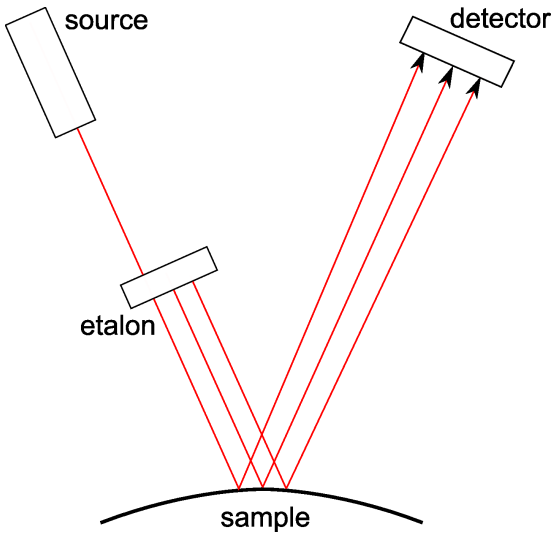

Figure 2.5: Schematic illustration of a multi-beam curvature measurement set-up.

2.2 Practical aspects of the use of the multi-beam sensor

In this section, practical issues in relation to the use of the multi-beam sensor are discussed. In particular, the calibration equations are derived in the first sub-section 2.2.1 for the case of a measurement carried out in air (or in vacuum). In the second sub-section 2.2.2, it is shown how the equation needs to be modified for measurements carried out in a liquid environment. Our calibration procedure is then described in subsection 2.2.3. Finally, the theoretical and effective resolutions of the sensor are discussed in sub-section 2.2.4.

2.2.1 Calibration equation for measurements in air

Derivation of the calibration equation for the case of uniaxial bending

We will first consider the reference case of a measurement carried out in air (or in vacuum). For the sake of simplicity, we will also consider the specific geometry in which:

- the sample bends along one single direction (uniaxial bending)
- the plane containing the incident beams is normal to the sample surface in the flat reference state and parallel to the direction of bending of the

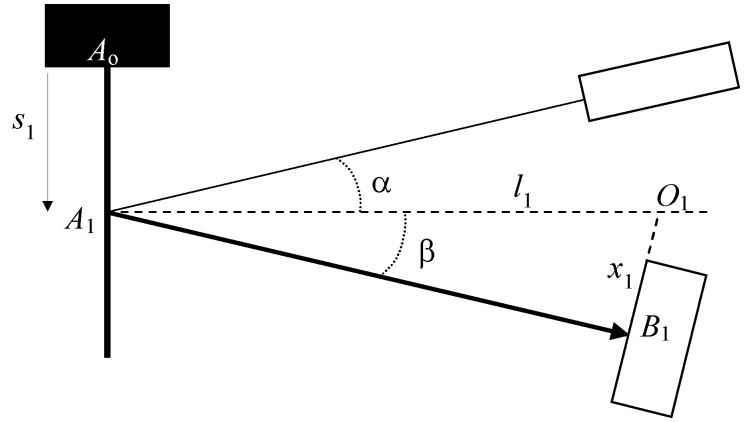

Figure 2.6: Illustration of the lengths and angles characterising the set-up geometry in the case of a single beam reflected on a flat surface.

sample.

Equivalently, this means that all the beams (incident and reflected ones) are coplanar, which authorises 2D approach of the problem. The extension of the calibration equation to other geometries is discussed later on in this sub-section. The curvature is measured using two parallel laser beams. The whole development can be extended to any number of beams by grouping the beams in pairs.

As a first step, we will consider the reference state in which the two beams are reflected on a flat surface. As illustrated on Fig.2.6, we will call A_1 the point of incidence of the first beam on the surface. The distance between the point of anchoring of the sample A_o and A_1 is equal to s_1. The first beam is reflected off the sample and reaches the detector at B_1. The reflected beam is normal to the detector surface. We also need to define the normal to the sample surface at A_1. The latter axis will be used as a reference axis for expressing all angles and dimensions. We will call O_1 the geometrical intersection of the reference axis with the plane of the detector. The length of A_1O_1 is equal to l_1 and the length of O_1B_1 is x_1. Finally, the incident beam is characterised by an angle of incidence α and a reflection angle β. In this case, as the surface is flat, $\alpha = \beta$. Considering the $A_1O_1B_1$ triangle, we can write

$$x_1 = l_1 \sin\beta \tag{2.9}$$

Similarly, for the second beam, we can define the characteristic points A_2, B_2 and O_2. We also need to define a supplementary point C_2 which is the geometrical intersection point of beam 2 with the reference axis A_1O_1. We can

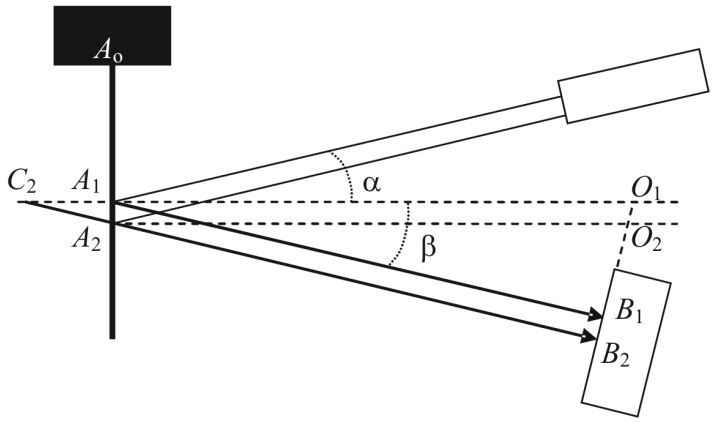

Figure 2.7: Illustration of the lengths and angles characterising the set-up geometry in the case of a pair of beams reflected on a flat surface.

now define the characteristic lengths s_2, l_2 and x_2, which are equal to the length of, respectively, A_0A_2, C_2O_1 and O_1B_2. Note that the two incident beams are parallel to one another so that the incidence angles are equal for both beams. As illustrated on Fig.2.8, considering the triangle $C_2O_1B_2$, we can write:

$$x_2 = l_2 \sin\beta \tag{2.10}$$

Furthermore, considering the triangle $A_1A_2C_2$, the length of A_1C_2 is equal to:

$$A_1C_2 = \frac{A_1A_2}{\tan\beta} \tag{2.11}$$

As illustrated on Fig.2.8:

$$A_1A_2 = (s_2 - s_1) = \frac{d_o}{\cos\alpha^*} \tag{2.12}$$

where d_o is the spacing between the two incident beams. It should be noted that, for the specific geometry of consideration, α^* is equal to the incidence angle α. However, generally speaking, for more complex geometries, it is not necessarily the case.

Therefore, taking into account the fact that $\alpha^* = \alpha = \beta$ in the flat reference state:

$$l_2 = l_1 + A_1C_2 = l_1 + \frac{d_o}{\cos\alpha\tan\beta} = l_1 + \frac{d_o}{\sin\alpha} \tag{2.13}$$

The spacing between the two reflected beams on the detector is given by:

$$d = x_2 - x_1 = \left(l_1 + \frac{d_o}{\sin\alpha}\right)\sin\alpha - l_1\sin\alpha = d_o \tag{2.14}$$

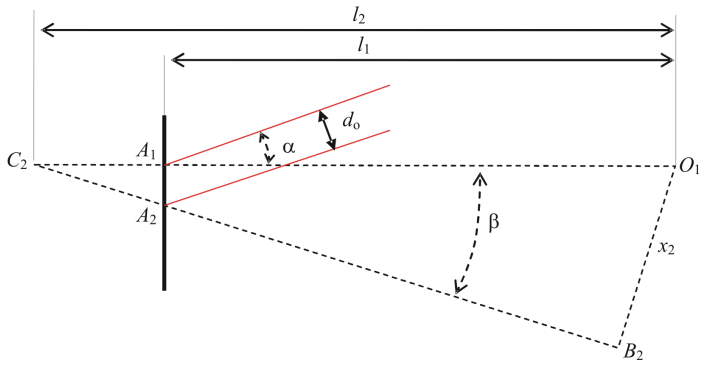

Figure 2.8: Illustration of the relationships between the parameters l_1, l_2, d_o, α and β characteristic for the geometry of the experimental set-up.

This result was of course expected for the case of a planar reference surface as the spacing between the beams is not modified after reflection on such a flat surface.
Now, let us assume that the sample becomes curved, characterised a radius of curvature R. We will make a first hypothesis which is that the curvature-induced deflection of the sample is sufficiently small to assume that the points of incidence of the beams on the sample A_1 and A_2 are the same as in the flat reference state. Due to the curvature, the normal to the sample surface at both A_1 and A_2 will be tilted by a small angle $\delta\alpha_1$ and $\delta\alpha_2$ respectively relative to the A_1O_1 axis as defined for the flat reference state. As illustrated on Fig.2.9 for the first beam, the reflection angles of the two beams (β_1 and β_2) will be modified by, respectively, $2\delta\alpha_1$ and $2\delta\alpha_2$ so that the beams will reach the detector at points B_1' and B_2'. Let us call x_1' and x_2' the length of O_1B_1' and O_1B_2'. In order to calculate x_1' and x_2', we need to make a second hypothesis. We will assume that $\delta\alpha_1$ and $\delta\alpha_2$ are small enough so that the reflected beams are almost normal to the detector surface, i.e. that $A_1O_1B_1'$ is a right triangle. Under these assumptions, from $A_1O_1B_1'$ we get:

$$x_1' = l_1 \sin\beta_1 = l_1 \sin\left(\alpha + 2\delta\alpha_1\right) \tag{2.15}$$

Similarly, for the second beam, we can write:

$$x_2' = l_2 \sin\beta_2 = \left(l_1 + \frac{d_o}{\cos\alpha^* \tan\left(\alpha + 2\delta\alpha_2\right)}\right) \sin\left(\alpha + 2\delta\alpha_2\right) \tag{2.16}$$

Again, for the geometry of consideration here, $\alpha^* = \alpha$. Now, we need to introduce a third hypothesis, the "small angle approximation" which consists

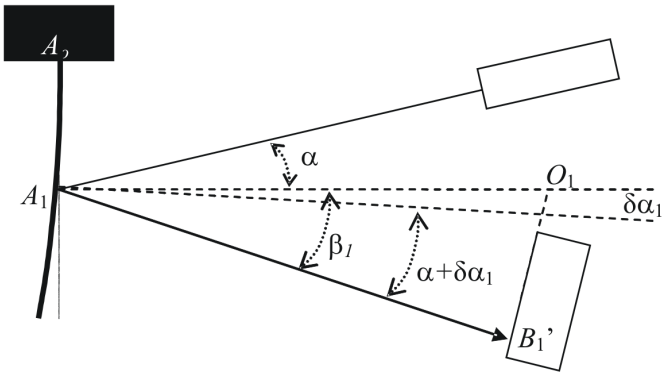

Figure 2.9: Illustration of the characteristic lengths and angles determining the geometry of the experimental set-up in the case of a single beam reflected on a curved surface

in a linearization of trigonometric functions at small angles so that:

$$\sin\alpha \approx \alpha \approx \tan\alpha \tag{2.17}$$

and

$$\cos\alpha \approx 1 \tag{2.18}$$

where the angle values are expressed in radians. Under the small angle approximation, by combining equations Eq.2.15 and Eq.2.16, we can link the spacing d between the beams to $\delta\alpha_1$ and $\delta\alpha_2$:

$$d = x_2' - x_1' = l_1\left(\alpha + 2\delta\alpha_2\right) + d_o - l_1\left(\alpha + 2\delta\alpha_1\right) \tag{2.19}$$

or, equivalently:

$$d - d_o = 2l_1\left(\delta\alpha_2 - \delta\alpha_1\right) \tag{2.20}$$

Now, as a last step we need to link the increments of the reflection angles $\delta\alpha_1$ and $\delta\alpha_2$ to the curvature of the sample. As illustrated on Fig.2.10, s_1 is related to $\delta\alpha_1$ by:

$$R\tan\delta\alpha_1 = s_1 \tag{2.21}$$

Similarly,

$$R\tan\delta\alpha_2 = s_2 \tag{2.22}$$

so that, using again the small angle approximation:

$$\delta\alpha_2 - \delta\alpha_1 = \left(\frac{s_2}{R} - \frac{s_1}{R}\right) \tag{2.23}$$

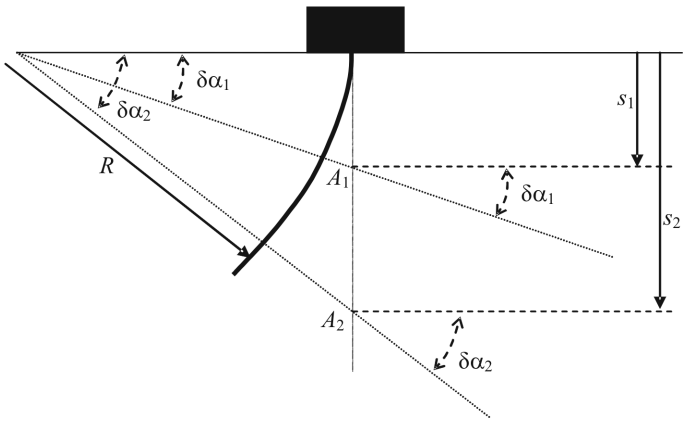

Figure 2.10: Illustration of the relationship between the increments of the reflexion angle $\delta\alpha_1$ and $\delta\alpha_2$ and the radius of curvature of the sample.

If we now combine Eq.2.20, Eq.2.23 and Eq.2.12, the change in the beams spacing due to the curvature is given by:

$$d - d_o = 2l_1 \left(\frac{s_2}{R} - \frac{s_1}{R} \right) = \frac{2l_1}{R} \frac{d_o}{\cos\alpha} \tag{2.24}$$

The latter expression can be equivalently expressed as

$$\kappa \equiv \frac{1}{R} = \frac{d - d_o}{d_o} \frac{\cos\alpha}{2l_1} \tag{2.25}$$

Equation 2.25 is the fundamental calibration equation of the multi-beam technique for measurements carried out in air. It links the curvature of the sample to the measured relative change in the spacing of the beams on the detector. The proportionality factor $\cos\alpha/2l_1$ is the length of the optical path of the beams between the sample and the detector. In the next paragraph, we discuss how the calibration equation can be extended to more complex geometries. In the last paragraph, the validity of the hypotheses made for deriving the calibration equation is assessed for our specific experimental set-up

Extension of the calibration equation to more complex geometries

In the previous derivation of the calibration equation, a specific geometry had been considered, characterised by a uniaxial bending of the sample and by the fact that the plane of incidence of the beams was normal to the sample surface in the flat reference state and parallel to the direction of bending. As a first step, we will keep this second hypothesis and show how a biaxial bending would

influence the derivation of the calibration equation. Let us have a look at Fig.2.7 again. With respect to the previous geometry, the major difference is that now, the sample is also bent in the out-of plane direction so that the reflected beams no longer lay within the same plane as A_1, A_2, O_1 and the incident beams. Let us call "horizontal" the direction defined by A_1A_2 and "vertical" the out-of plane direction perpendicular to the horizontal axis. As a result of the 3D curvature, the normal to the surface at point A_1 is rotated by a small angle $\delta\alpha_{1V}$ around the vertical axis and by a small angle $\delta\alpha_{1H}$ around the horizontal one, relative to its orientation for a flat reference sample. If we now define the horizontal plane as the one containing $A_1A_2O_1$, the whole development made in the previous paragraph for the simplified geometry remains valid if we consider the orthogonal projection of the beams on the horizontal plane. The image of B'_1 and B'_2 on the horizontal plane will be referred to as B'_{1H} and B'_{2H}. The length of $O_1B'_{1H}$ and $O_1B'_{2H}$ is noted x'_{1H} and x'_{2H} and the horizontal spacing between the beams will be given by:

$$d_H = x'_{2H} - x'_{1H} = l_1\left(\alpha + 2\delta\alpha_{2V}\right) + d_o - l_1\left(\alpha + 2\delta\alpha_{1V}\right) \tag{2.26}$$

It should be noted that the horizontal spacing is fully independent of $\delta\alpha_{1H}$ and $\delta\alpha_{2H}$. When a 2D array of laser beams is used for monitoring the curvature, two (possibly different) radii of curvature R_V and R_H will be extracted from the differential beams spacing in the horizontal and vertical directions respectively. In that case, the vertical plane will be defined as the plane orthogonal to the horizontal plane and including A_1. The orthogonal projection of the beams on the vertical plane will allow measuring the vertical spacing d_V, which will depend only on $\delta\alpha_{1H}$ and $\delta\alpha_{2H}$. It should be noted that we have defined the horizontal and vertical directions relative to the directions of the array of beams on the sample surface. However, in practice, the data analysis software defines the vertical and horizontal axes with respect to the main two directions of the CCD detector. In order to make these two orientations correspond to one another, it is therefore important to optimise the inclination of the incident laser beams so that the spots on the detector are aligned along the vertical and horizontal directions of the detector.

We will now discuss the second assumption that the plane of incidence of the beams is orthogonal to the sample surface in the flat reference state. If it is not the case, even in the flat reference state, the optical paths for all the beams are no longer coplanar but are located in parallel planes. In that case, we can, for instance, define the horizontal plane as the plane of incidence of the first beam in the flat reference state. The vertical plane is orthogonal to the horizontal one and includes A_1. The same reasoning as before can be applied to the orthogonal projection of the beams on the horizontal and vertical axes. Fig.2.7 can be thought of as the projection of beams 1 and 2 on the plane containing the optical path of the first beam. The horizontal spacing between

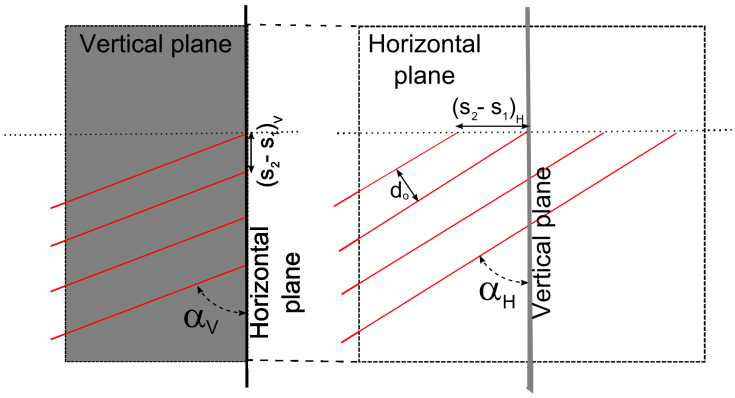

Figure 2.11: Illustration of the definition of $\alpha*$ for the vertical and horizontal spacing

the beams will be measured within this plane while the vertical spacing will be obtained from the projection on the vertical plane. Another consequence of this geometry is that we need to clarify the definition of the angle α^* in equation Eq.2.12. As illustrated on Fig.2.11, α^* takes different values for the horizontal and vertical spacing. Indeed, α^* is equal to the angle of incidence α for the vertical spacing, while, in the case of the horizontal spacing, it is equal to the angle between the horizontal direction and the incident beam in the plane of incidence. In general, the radius of curvature of a sample along the two main directions might have different values (R_V and R_H) and will be given by, respectively:

$$\kappa_V = \frac{1}{R_V} = \frac{d_V - d_o}{d_o} \frac{\cos \alpha_V}{2L} \tag{2.27}$$

and

$$\kappa_H = \frac{1}{R_H} = \frac{d_H - d_o}{d_o} \frac{\cos \alpha_H}{2L} \tag{2.28}$$

Hence, the calibration equation Eq.2.25 derived for a simplfied geometry extends to more complex geometries as well, provided that the corresponding length and angles are defined adequately.

Hypotheses underlying the derivation of the calibration equation

As mentioned in the previous paragraph, several hypotheses were made in the derivation of the calibration equation. In order to discuss their validity in the case of our specific experimental set-up, we must consider typical values of the

L_1	s	α	R	δ
1 m	2 to 4 cm	5°	100 m	0.01°

Table 2.1: Typical values of the characteristic parameters describing the experimental set-up.

different characteristic variables. Such values are summarised in Table 2.1.

As a first hypothesis, it was assumed that the curvature-induced lateral shifting of the points of incidence of the beams is negligible so that we can assume that the beams reach the sample on the same points A_1 and A_2 in the flat reference and curved states. As illustrated on Fig.2.12, the lateral shifting u of the beam on the sample surface is given by:

$$u = f \tan \alpha \tag{2.29}$$

where α is the angle of incidence of the beam with respect to the flat reference surface and f is the deflection of the sample at a distance s from the anchoring point. The latter is related to the radius of curvature by:

$$f = \frac{s^2}{2R} \tag{2.30}$$

By combining Eq.2.29 and Eq.2.30 and taking into account our specific experimental values for R and α, the lateral shifting u is expected to amount to 0.7μm (for $s = 4$ cm). As compared to the average diameter of the beams, which is of the order of 500μm, this lateral displacement appears to be very limited and therefore negligible to a good approximation.

We should also discuss the validity of the small angle approximation which was used to simplify Eq.2.15 and Eq.2.16 into Eq.2.19, and Eq.2.21 and Eq.2.22 into Eq.2.23. The ratio of α, expressed in radians, to its sine has been plotted as a function of α on Fig.2.13. As evident from this figure, the error associated with the small angle approximation is below 1% for incidence angles inferior to 14°, which is the case for our experimental set-up. For larger values of the incidence angle, this approximation breaks down and can lead to significant errors.

Our last hypothesis was to consider that the $A_1O_1B_1'$ triangle on Fig.2.9 is a right triangle. It can be shown that the latter hypothesis is valid as well as long as the small angle approximation is valid. On Fig.2.14, a schematic representation of the experimental set-up is presented. In the flat reference state, the configuration is described by the right triangle $A_1O_1B_1$ while, in the curved state, it corresponds to the scalene triangle $A_1O_1B_1'$. In practice,

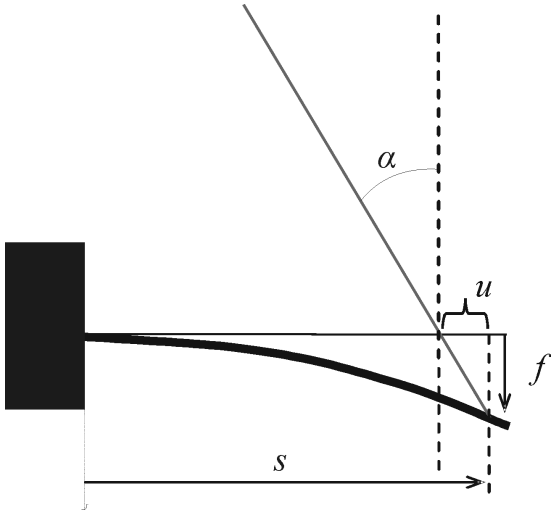

Figure 2.12: Illustration of the relationship between the lateral displacement u of the point of incidence of the beams on the sample surface and the sample curvature.

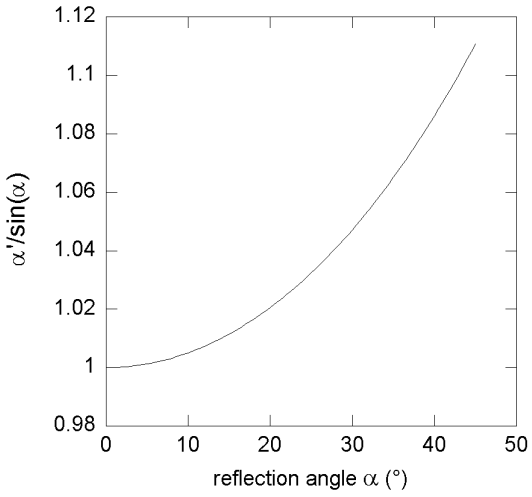

Figure 2.13: Accuracy of the small angle approximation as a function of the value of the incidence angle α.

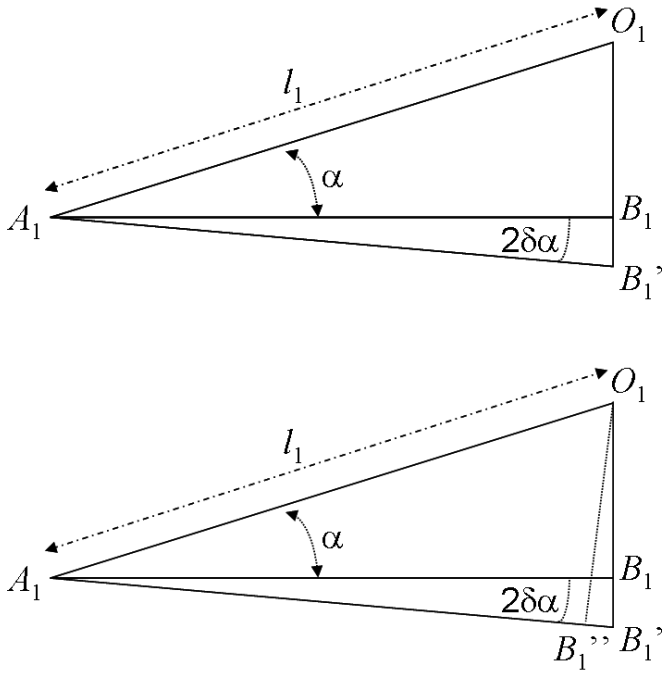

Figure 2.14: Illustration of the influence of assuming that the reflected beams are normal to the detector surface independent of the sample curvature.

we need to determine the length of O_1B_1'. In the derivation of the calibration equation, we have calculated O_1B_1' as if it was equal to O_1B_1'', where B_1'' is defined as the orthogonal projection of O_1 on A_1B_1', as shown on Fig.2.14. Formally:

$$O_1B_1' = O_1B_1 + B_1B_1' = l_1 \sin\alpha + l_1 \cos\alpha \cdot \tan 2\delta\alpha \tag{2.31}$$

while

$$O_1B_1'' = l_1 \sin(\alpha + 2\delta\alpha) \tag{2.32}$$

Obviously, provided that the small angle approximation is valid, Eq.2.31 and Eq.2.32 both simplify to:

$$O_1B_1' = l_1(\alpha + 2\delta\alpha) = O_1B_1'' \tag{2.33}$$

As a conclusion, in our case, all the assumptions made in the derivation of the calibration equation appear to be fully justified. In the ideal case where all the parameters in Eq.2.25 would be known with infinite accuracy, the error on the curvature values calculated from Eq.2.25 would be expected to be lower than 1%. It is also worth noticing that, in contrast, the use of Eq.2.25 leads to significant errors of several percents on the calculated curvature values when the experimental configuration is characterised by a large angle of incidence (larger than 10° typically). This should be borne in mind when designing new experimental facilities.

Remark on the relative character of the curvature measurements

As previously mentioned in paragraph 2.1, the multi-beam deflection technique allows quantifying curvature changes relative to a reference state. So, in practice, before any experiment, the mean differential beams spacing (MDS) is measured in a reference state defined as the condition of the sample before the experiment is performed. Then, the experiment is started and the evolution of the curvature of the sample is deduced from the measured changes in the MDS according to Eq.2.25, using the measured MDS in the reference state as d_o. However, by doing so, we implicitly assume that the sample is flat before the experiment, which, in general, is not necessarily the case. As an example, let us consider the deposition of a thin film on an initially curved substrate. The mean beam spacing corresponding to this reference state is measured to be d_o^* and the final beams spacing reaches a value d after layer deposition. The curvature change resulting from the deposition will be calculated from the difference between the beam spacing values measured in the post-deposition and the reference states:

$$\Delta\kappa' = \frac{d - d_o^*}{d_o^*} G \tag{2.34}$$

where

$$G = \frac{\cos\alpha}{2l_1} \tag{2.35}$$

In contrast, if the curvature of the sample both before and after the deposition could have been measured relative to a flat surface, the curvature change resulting from the deposition would be calculated as:

$$\Delta\kappa = \frac{d - d_o}{d_o}G - \frac{d_o^* - d_o}{d_o}G = \frac{d - d_o^*}{d_o}G \tag{2.36}$$

By comparing equations Eq.2.34 and Eq.2.36, it is evident that the relative error induced by using a curved reference instead of a flat one is equal to the ratio of the respective mean beam spacings:

$$\frac{\Delta\kappa'}{\Delta\kappa} = \frac{d_o}{d_o^*} \tag{2.37}$$

Using the expression for the absolute curvature κ_s of the substrate, equation Eq.2.37 can be rewritten as:

$$\frac{\Delta\kappa'}{\Delta\kappa} = \frac{G}{\kappa_s + G} \tag{2.38}$$

where κ_s is the absolute curvature of the substrate. Generally speaking, the error induced by using a curved reference instead of a flat one can be huge if the curvature is very large and also depends on the geometry of the experimental set-up (through the G factor). For instance, taking into account the G factor corresponding to our experimental set-up, a substrate having a concave curvature equal to $0.06m^{-1}$ would induce an overestimation of the curvature changes by 10%. It is therefore important to ensure that the curvature of our supposedly flat substrate is much below that level. In our case, a net curvature of the substrate can result either directly from the dicing process of the silicon rod or later on due to internal stresses associated with the deposition of the metal film. Measurements were carried out in which the mean beams spacing of the samples were compared to the one measured for a flat mirror. Typical values for their ratio were in the range of 0.97 to 1.03. So, a 3% error is typically associated with this type of uncertainty.

2.2.2 Calibration equation for measurements in a liquid

Derivation of the calibration equation in the case of uniaxial bending

When the sample of which the curvature has to be monitored is placed in a liquid, like in the case of an electrochemical cell, equation Eq.2.25 needs to be further modified to take into account the refraction of the reflected beams

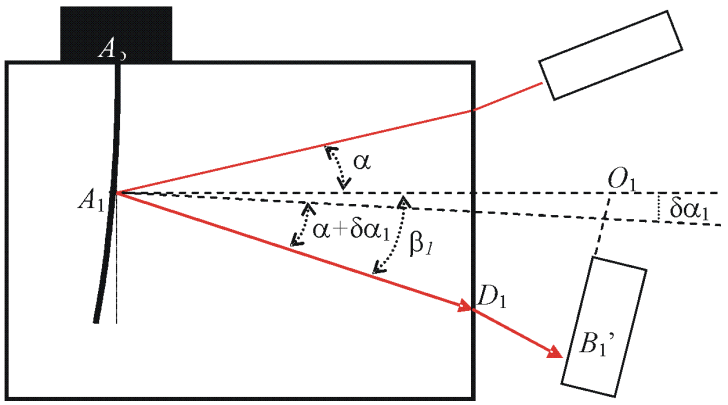

Figure 2.15: Illustration of the experimental set-up for the case of a measurement carried out in a liquid.

at the electrolyte/air interface[3]. This problem has been studied by Lang and Seo [130] and Rokob and Lang [198] for the single beam technique. In this paragraph, we derive the calibration equation for the case of the multi-beam technique. Again, for simplicity, we will consider the simplified geometry in which the sample experiences uniaxial bending and all the beams are coplanar with the direction of bending. For more complex geometries, the same reasoning is valid for the horizontal and vertical components of the beam deflection, as discussed in section 2.2.1. We will also, at first, consider the case in which the cell wall is perpendicular to the sample surface.

As illustrated on Fig.2.15 and Fig.2.16, one portion of the optical path of the laser beams lays inside the cell, filled with a liquid of refractive index n_{sol}, and one portion lays outside the cell. Similar to the previous derivation, we will define A_o, the point of anchoring of the cantilevered sample, A_1 and A_2, the points of incidence of the two beams on the surface and O_1 which is the geometrical intersection of the normal to the sample surface in the flat reference state with the plane of the detector. The effective angle of incidence of the beams on the sample is α (which, due to the refraction, differs from the angle of incidence of the beams on the cell wall) and their respective reflection angles β_1 and β_2 (measured inside the cell, prior to refraction on the cell wall)

[3]Note that the incident beams are also refracted when penetrating the cell, but as parallel beams remain parallel after refraction, this will not affect the spacing between the beams but only their angle of incidence on the sample surface. In fact, this will bring the factor $\cos\alpha$ in Eq.2.25 even closer to 1, so that we can safely assume conditions very close to normal incidence.

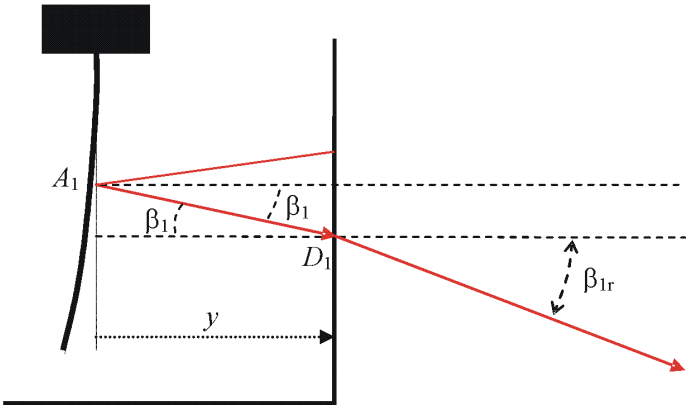

Figure 2.16: Illustration of the refraction of the reflected beams on the cell wall. The reflection and refraction angles are, respectively, noted as β_1 and $\beta_1 r$.

are such that:

$$\beta_1 = \alpha + 2\delta\alpha_1 \tag{2.39}$$

$$\beta_2 = \alpha + 2\delta\alpha_2 \tag{2.40}$$

Furthermore, similar to the previous derivation, the relationship between the radius of curvature and $\delta\alpha_1$ and $\delta\alpha_2$ is given by equation Eq.2.23. However, in this case, after reflection, the beams reach the cell wall on D_1 and D_2, are refracted and exit the cell with an angle $\beta_1 r$ and $\beta_2 r$ relative to the $A_1 O_1$ reference axis, as illustrated on Fig.2.16.

The Snell law of refraction links β_1 to β_{1r} and β_2 to β_{2r} according to:

$$\frac{\sin\beta_{ir}}{\sin\beta_i} = n_{sol} \tag{2.41}$$

for i = 1 or 2. The overall curvature-induced variation of the beams spacing can be decomposed into two parts:

$$\Delta d = \Delta d'' + \Delta d' \tag{2.42}$$

where $\Delta d''$ is the variation of the beam spacing corresponding to the portion of the optical path of the reflected beams within the cell and $\Delta d'$ is the variation of the spacing of the beams which corresponds to the portion of the optical path of the reflected beams in air, between the cell wall and the detector. As in practice, for classical set-ups, the length of the optical path outside the cell is much larger than the portion of the optical path within the cell, we will assume that $\Delta d \approx \Delta d'$. This assumption is equivalent to considering that the incident beams are reflected off the sample surface directly with an effective reflection

angle given by β_{1r} and β_{2r} instead of β_1 and β_2. Under this assumption, the derivation of the calibration equation for the case of the measurement in a liquid becomes equivalent to the derivation for the case of a measurement in air, provided that the effective reflection angles are taken into account. Therefore:

$$x_1 = l_1 \sin\beta_{1r} = l_1 n_{sol} \sin\left(\alpha + 2\delta\alpha_1\right) \tag{2.43}$$

and

$$x_2 = l_2 \sin\beta_{2r} = \left(l_1 + \frac{d_o}{\cos\alpha \cdot \tan\beta_{2r}}\right) n_{sol} \sin\left(\alpha + 2\delta\alpha_2\right) \tag{2.44}$$

Again, provided that the geometry of the experimental set-up is compatible with the small angle approximation, one can assume that $\cos\alpha \approx 1$ and $\tan\beta_{2r} \approx \sin\beta_{2r} \approx n_{sol}\sin(\alpha + 2\delta\alpha_2) \approx n_{sol}\left(\alpha + 2\delta\alpha_2\right)$ Then, by combining equations Eq.2.43, Eq.2.44 and Eq.2.23, we obtain:

$$\kappa = \frac{1}{R} = \frac{d - d_o}{d_o} \frac{\cos\alpha}{2 l_1 n_{sol}} \tag{2.45}$$

This equation links the curvature of the sample to the measured differential beams spacing for the case of a measurement carried out on a sample placed in a liquid of refractive index n_{sol}. As evident from this equation, provided that some requirements on the geometry of the experimental set-up are fulfilled, the calibration equation to be used is formally similar to the one for open-air measurements but includes a multiplicative correction factor equal to $1/n_{sol}$. This correction factor is the same as the one found by Lang and Seo for the single-beam technique. In practice this means that, for a given curvature change of the sample, the resulting measured change in the beams spacing will be amplified by a factor n_{sol}, which in fact is beneficial to the sensitivity of the sensor.

Discussion of the assumptions made in the derivation

We should now discuss the geometrical requirements associated with the calibration equation Eq.2.45. First, the length of the optical path of the beams in the cell must be very small as compared to the length of the optical path outside the cell. If it is not, a more complex calibration equation must be applied which takes into account the distance between the sample surface and the cell wall. It can be shown, based on simple geometry that the correct equation in this case is:

$$\kappa = \frac{d - d_o}{d_o} \frac{\cos\alpha}{2 l_1 n_{sol} + 2y\left(1 - n_{sol}\right)} \tag{2.46}$$

where y is the distance between the sample and the cell wall, as illustrated on Fig.2.16. The relative error $\delta\kappa$ associated with assuming $y = 0$ increases

linearly with the y/l_1 ratio according to:

$$\delta\kappa = \frac{y}{l_1}\left(\frac{1}{n_{sol}} - 1\right) \tag{2.47}$$

As expected, when y/l_1 approaches 0, the error becomes zero while, when y/l_1 approaches 1, the maximal error is equal to 25% for an aqueous solution having a refractive index equal to 1.33. In our specific experimental set-up, y is about 4 cm while l_1 is approximately 1 m. Under these conditions the expected error induced by neglecting y is around 1%.

Secondly, in the previous derivation, it was postulated that the cell wall was parallel to the sample surface. When it is not, the reflection angle β_{1r} depends explicitly on the disorientation of the cell, characterised by a misalignment angle γ, as defined on Fig.2.17. Indeed, if the cell wall is rotated by an angle γ relative to the sample surface, the effective angle of incidence of the reflected beam on the cell wall is not equal to β_1 but to $(\beta_1 + \gamma)$ (see Fig.2.17). According to the Snell law, after refraction, the reflection angle β'_{1r}, measured relative to the normal to the cell wall on D_1 will be such that

$$\frac{\sin\beta'_{1r}}{\sin\left(\beta_1 + \gamma\right)} = n_{sol} \tag{2.48}$$

and the reflection angle β_{1r}, measured relative to the normal to the flat sample surface is given by:

$$\beta_{1r} = \beta'_{1r} - \gamma \tag{2.49}$$

so that:

$$\beta_{1r} = \arcsin\left(n_{sol}\sin\left(\beta_1 + \gamma\right)\right) - \gamma \tag{2.50}$$

Further simplification of equation Eq.2.50 requires that both $(\beta_1 + \gamma)$ and β'_{1r} are compatible with the small angle approximation. Provided that it is the case:

$$\beta_{1r} \approx n_{sol}\beta_1 + \left(n_{sol} - 1\right)\gamma \tag{2.51}$$

As evident from equation Eq.2.51, when the cell wall is not parallel to the sample surface, the reflected angle after refraction by the cell wall explicitly depends on γ, even for small values of the misalignment angle. Note that, when $n_{sol} = 1$ (the cell contains air), Eq.2.51 predicts, as expected, $\beta_1 = \beta_{1r}$. Interestingly, β_{1r} is also equal to β_1 if $\gamma = -\beta_1$. This corresponds to the situation in which the misalignment angle exactly compensates for the reflection angle so that the reflected beam exhibits normal incidence on the cell wall and is therefore not refracted. For small angles, we can define an apparent refractive index n^*_{sol} which is such that

$$n^*_{sol} = \frac{\beta_{1r}}{\beta_1} \tag{2.52}$$

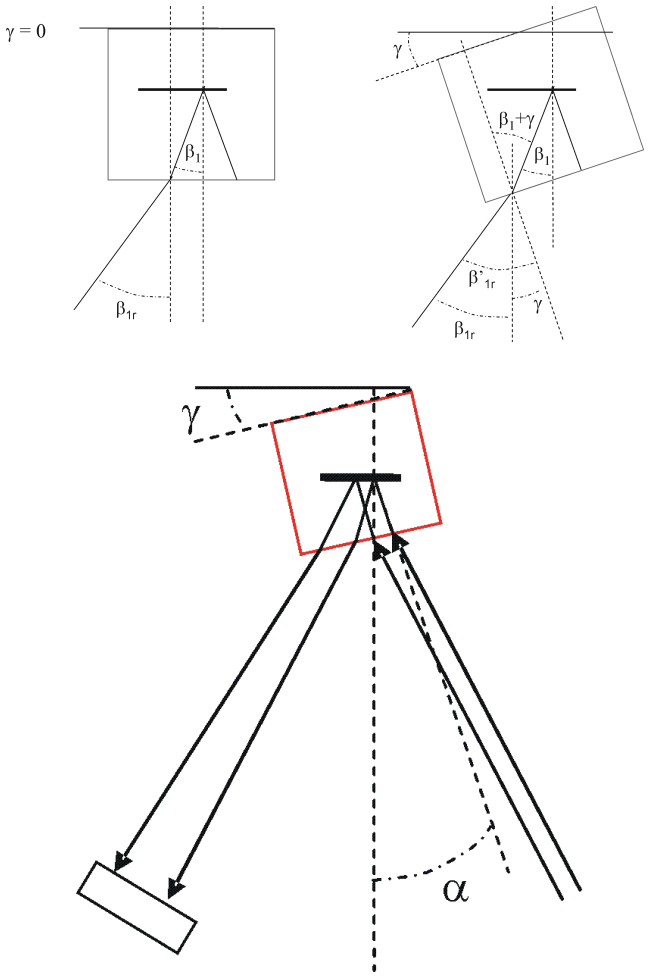

Figure 2.17: Definition of the misalignment angle γ characterising the disorientation of the cell with respect to the sample surface. By convention, $\gamma = 0$ when the cell wall is parallel to the sample surface.

Fig.2.18 shows the simulated evolution of n^*_{sol} with the misalignment angle γ for different values of α, which can be considered to be equal to β_1 as a first approximation. As expected, the apparent refractive index is equal to n_{sol} when the misalignment angle is 0, whatever the value of the incidence angle. As the misalignment angle takes positive values, i.e. as the misalignment of the cell results in an increase of the angle of incidence of the reflected beam on the cell wall, the apparent refractive index increases significantly. Interestingly, the smaller the incidence angle α, the larger the influence of the misalignment angle. For an incidence angle of 1°, it can be seen that a misalignment of the cell by only 5° would increase n^*_{sol} to a value above 3. The relative error on n_{sol} associated with the disorientation of the cell can be assessed, based on equations Eq.2.51 and Eq.2.52. It is given by:

$$\frac{n^*_{sol} - n_{sol}}{n_{sol}} = \frac{\gamma}{\beta_1}\frac{n_{sol} - 1}{n_{sol}} \approx \frac{\gamma}{\alpha}\frac{n_{sol} - 1}{n_{sol}} \tag{2.53}$$

The relative error on the refractive index is predicted to increase linearly with the γ/α ratio, with a slope equal to $(n_{sol} - 1)/n_{sol}$, i.e. about 25% for aqueous solutions. This means that, if the disorientation of the cell is of the same order of magnitude as the angle of incidence, the apparent refractive index of the solution will be overestimated by 25%.

Hence, it has been shown that the value of the reflection angle, after refraction on the cell wall, depends explicitly on the disorientation of the cell and that the associated error can be rather large. This can be problematic mainly during the calibration step, during which the proportionality between curvature and reflection angle is established. However, it can be shown as well that, provided that $(\beta + \gamma)$ and β'_r for all beams are compatible with the small angle approximation, the contributions of the misalignment angle cancel each other out in the case of a multi-beam technique. This is a supplementary advantage of the multi-beam technique which, to the best of our knowledge, has never been pointed out before. While techniques based on the deflection of a single beam are prone to inaccurate calibration arising from a disorientation of the sample relative to the cell wall, the multi-beam technique is insensitive to this type of error.

In practice, the exact value of the apparent refractive index does not need to be explicitly determined as long as the relationship between curvature and mean differential spacing is calibrated accurately using mirrors of known radii of curvature, as will be described in sub-section 2.2.3. However, if the orientation of the samples on which the measure is carried out differs slightly from that of the calibration mirrors, significant errors can arise. Therefore, in order to perform accurate measurements, it is crucial to design the experimental cell such that the source and detector of the multi-beam sensor are fixed, the cell

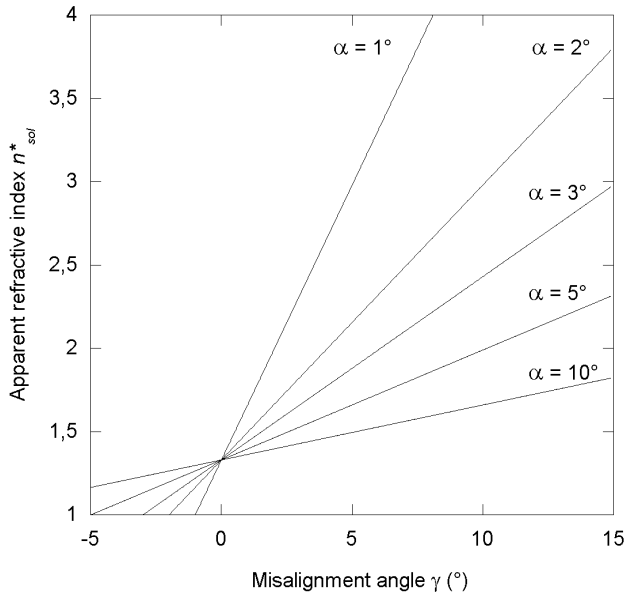

Figure 2.18: Influence of the disorientation of the cell relative to the sample surface, characterised by the misalignment angle γ, on the apparent value of the refractive index n^*_{sol}. This effect is illustrated for different values of the incidence angle α.

wall has a constant orientation with respect to the source and detector and the samples can be positioned accurately and reproducibly, both in terms of position and orientation.

Comparison with other equations from the literature

Rokob and Lang [198] have derived an equation linking the deflection of a single beam to the curvature for a measurement carried out in a liquid, in the specific case of non-normal incidence (but with the cell wall parallel to the sample surface). It is interesting to compare this equation (derived for a single-beam technique) with our equation Eq.2.45 which was derived for the multi-beam technique. Actually, both equations are found to be formally very similar, with the exception of the $\cos\alpha$ factor in our equation which is replaced by

$$\frac{\left(1 - n_{sol}^{-2}\sin^2\gamma\right)^{1/2}}{\left(1 - \sin^2\gamma\right)^{3/2}} \tag{2.54}$$

in Rokob and Lang's work. So, only the way of taking into account the non-normal incidence differs between the two works. In this work, α was defined as the angle of incidence of the laser beams on the sample surface, while γ in the paper of Rokob and Lang is the angle of incidence of the beam on the cell wall (which is supposed to be parallel to the sample surface in both cases). Taking into account the Snell's law of refraction for the incident beam crossing the cell wall, our $\cos\alpha$ factor can be expressed, using the notations from Rokob and Lang, as

$$\cos\alpha = \left(1 - n_{sol}^{-2}\sin^2\gamma\right)^{1/2} \tag{2.55}$$

Therefore, the two equations differ only by a factor $\left(1 - \sin^2\gamma\right)^{3/2}$ only. So far, it is not clear which equation is more accurate. However, it can be shown that the difference between the two expression scales with the value of the incidence angle. The evolution of the ratio of the two correction factors, which is equal to $\left(1 - \sin^2\gamma\right)^{3/2}$, was plotted on Fig.2.19 as a function of the incidence angle. As evident from this figure, the difference between the values predicted by the two equations remains below 2% for incidence angles smaller than 6°, which is the case of our experimental set-up. Only with increasing values of the incidence angle above 10° does the error increase rapidly due to the fact that the small angle approximation is no longer valid.

2.2.3 Calibration procedure

Calibrating the technique actually means determining the G factor defined on Eq.2.35 for a given experimental set-up, characterised by the length l_1 between the sample and the detector and the incidence angle α. Both parameters can be

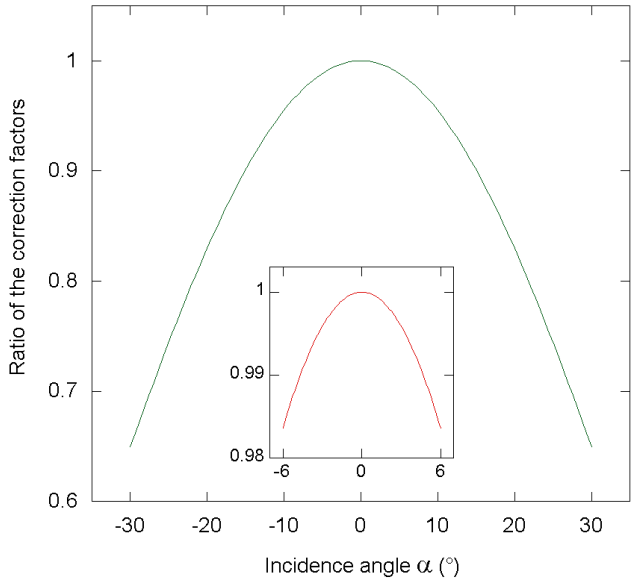

Figure 2.19: Evolution of the ratio of the correction factor in the equation of Rokob and Lang [198] to our own correction factor, plotted as a function of the incidence angle α.

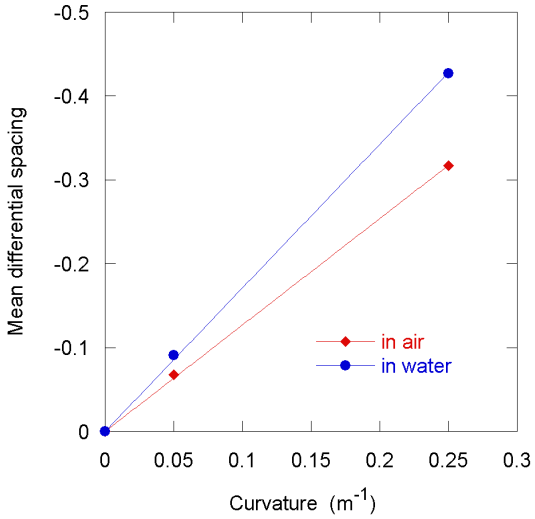

Figure 2.20: Typical example of calibration data measured both in air and in water on mirrors having a known radius of curvature.

assessed using a protractor and a tape-measure. However, a more accurate way of calibrating the multi-beam optical sensor is to use mirrors of known radii of curvature and to measure the mean differential spacing corresponding to each of those mirrors, taking a flat mirror as a reference. Plotting the MDS as a function of $1/R$ then yields a straight line from which the calibration factor can be deduced. Using this procedure, the error on the calibration factor is usually limited by the accuracy on the radius of curvature of the mirror (reported by the manufacturer to be around 10%) or on the positioning of the mirrors. Care must be taken as well not to modify anything to the experimental set-up between the different MDS measurements as this would of course lead to inaccurate calibration. Fig.2.20 shows typical calibration data recorded in air and in water using mirrors having a radius of curvature of 20 m and 4 m and a flat mirror as a reference. Slopes values of, respectively, 0.787 ± 0.007 m^{-1} and 0.584 ± 0.005 m^{-1} were obtained in air and in water. It can be noted that the ratio of the slopes is 1.34 ± 0.17, which is indeed in agreement with the expected value for the refractive index of water.

It should be noted that, although most of our anodising experiments have been carried out in 1.0 M H_2SO_4, our calibration procedure has been performed in deionised water in order to avoid corrosion of the mirrors. Since the refraction index of pure water and 1.0 M H_2SO_4 solution at 20°C are, respectively, 1.3324 and 1.3445 [41], this approximation is expected to lead to an overestimation

of the curvature by only a factor 1.3445/1.3324 = 1.009. The resulting error on the curvature is thus below 1%, which was considered to be an acceptable level.

2.2.4 Resolution of the sensor and optical perturbations

In this section, the theoretical resolution of the curvature measurement technique used in this work is discussed. In addition, several sources of perturbations and experimental artefacts associated with the optical curvature measurements are discussed and illustrated. The latter perturbations were encountered during this work and had to be overcome in order to progressively improve the accuracy of the curvature measurements by increasing the signal-to-noise ratio. Several guidelines are proposed to avoid such perturbations.

Resolution of the multi-beam sensor

With our experimental set-up, a curvature resolution of 0.18 km^{-1} (or, equivalently, 5.5 km) could be attained. The latter value was calculated as 3 times the experimental standard deviation for the curvature signal during baseline recording, which was typically of the order of 0.012%, as illustrated on Fig.2.21. It is important to note that, according to the Stoney equation (Eq.2.4), the resolution of a given curvature measurement set-up in terms of stress is determined not only by the curvature resolution but also by the characteristics of the substrate used. Indeed, if we consider a curvature measurement tool having a resolution of 5.5 km, the smallest stress variation that can be measured in a film of thickness h_f will depend strongly on the thickness of the substrate (to the power 2) as well as on its biaxial modulus. In our case, taking into account the thickness and biaxial modulus of our Si substrates, the 5.5 km curvature resolution corresponds to a resolution of 0.78 Pa·m in terms of the stress·thickness product. This means that the detection level in terms of stress is about 780 MPa for a 1 nm thick films or to 7.8 MPa in a 100 nm film. Increasing the overall resolution can be achieved either by increasing the distance between the sample and the detector (thus improving the curvature resolution) or by decreasing the thickness of the silicon substrate. As will be evident from our stress measurements presented in chapter 3, the resolution and dynamic range of the multi-beam technique were found to be very well adapted for investigating the stresses developing in anodic oxide films. It should be noted that, in practice, the effective curvature resolution is not always limited by the theoretical resolution calculated from the signal/statistical noise ratio but can be limited by the presence of optical perturbations. Such perturbations differ from the statistical noise in that they usually appear as punctual events and are therefore more difficult to distinguish from the 'real' signal. Some of these perturbations are discussed in the following paragraph.

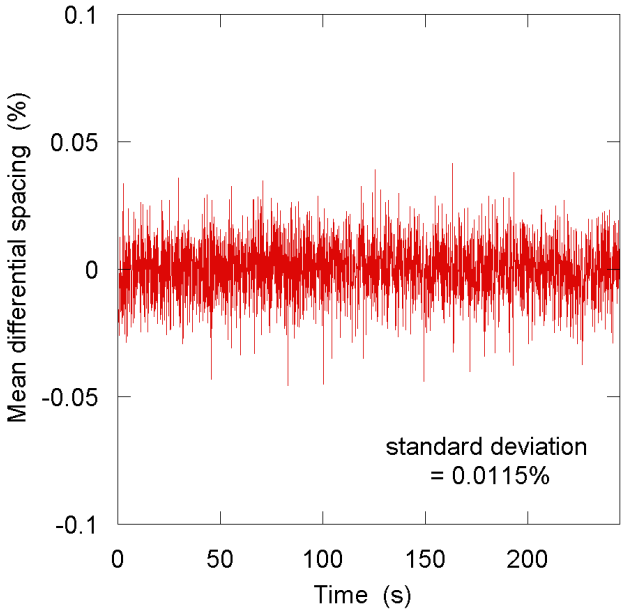

Figure 2.21: Typical example of baseline recording of the mean differential spacing showing a noise level of 0.0115% (assimilated to the standard deviation of the MDS signal).

Optical perturbations

Generally speaking, all optical perturbations, i.e. local perturbations of the laser beams, are highly detrimental to the quality of the measurement. Possible sources of perturbations may include:

- scattering of the beams on a dirt or scratch present on the cell wall or on the detector filters[4]
- scattering of the beams on the sample surface due to roughening or due to a specific reaction taking place
- convection effects.

If one of the beams is scattered or deflected by a dirt or a scratch present on the cell wall, on the sample surface or on the filters at the entrance of the detector, this may cause an artificial modification of the MDS. In fact, this will perturb the measurement only if the first or the last spot from a 1D array of spots are scattered since, due to the averaging, the contributions of the other spots cancel each other out. Indeed, for a series of 5 aligned spots, the mean vertical differential spacing will be calculated as:

$$MDS = \frac{(x_1 - x_2) + (x_2 - x_3) + (x_3 - x_4) + (x_4 - x_5)}{4} = \frac{x_1 - x_5}{4} \qquad (2.56)$$

where x_i is the vertical position of the i^{th} spot on the detector. In addition, the advantage of monitoring a series of spot at the same time is that a perturbation of the first or last spot can be easily detected by comparing the time-evolution of its position with the one for the other spots. Therefore, the multi-beam technique is relatively robust toward this kind of perturbations. Of course the cleanliness of all the components of the experimental set-up is crucial and great care must be taken not to scratch or damage the optical cell or the filters during the cleaning procedure.

Another experimental perturbation which was observed manifested itself as an increase followed by a decrease of the differential spacing. This perturbation was observed to propagate progressively from one pair of beams to the other, as illustrated on Fig.2.22. For this reason, it was at first attributed to the formation of small gas bubbles somewhere on the sample surface which would then evolve upward to the electrolyte surface. On their way to the surface, the bubbles would successively cross the path of each of the laser beams, hence causing the observed behaviour. A closer observation of the data revealed that the perturbation was in fact propagating downward from the first beam to the

[4]Such filters allow for filtering out the ambient light in order to prevent saturation of the CCD detector.

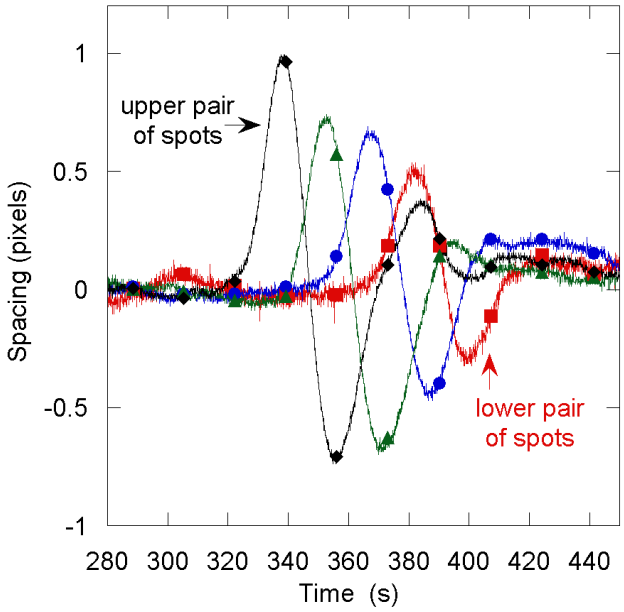

Figure 2.22: Time-evolution of the spacing between each pair of spots, supposedly corresponding to a particle-induced optical perturbation of the laser-beams.

last one. As gas bubbles could hardly 'fall' to the bottom of the cell, it is more likely that this effect would be due to a solid particle, of microscopic size, crossing the path of the laser beams. During our experiments, it was found that this kind of perturbation could be almost completely avoided by cleaning the samples in an ultrasonic bath prior to the experiment, in a solution having the same composition as the one used for the experiment. This procedure is intended to accelerate the dissolution of the contaminants present on the sample or sample holder so that no further dissolution takes place during the experiment.

As to the convection effects, they can be very easily visualised by, for instance, speaking of shuffling close to the region located between the MOS detector and the experimental cell. This reproducibly leads to a series of marked peak in the recorded MDS signal, as illustrated on Fig.2.23. This kind of effect is not encountered when the MOS device is connected directly to a vacuum deposition chamber for the monitoring of a vacuum deposition process but appears to be more problematic when the laser beams must cross open-air or an

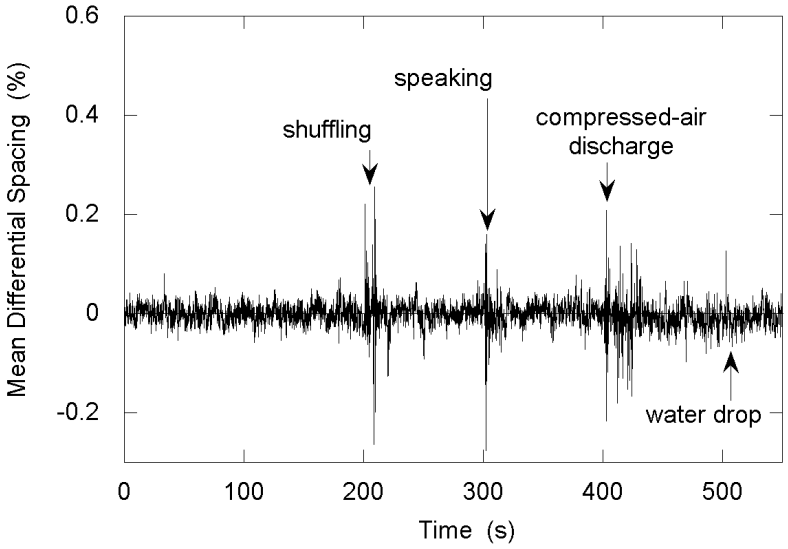

Figure 2.23: Illustration of the influence of convection effects on the MDS baseline. A very clear increase of the noise level is observed when convection effects are induced in the region between the detector and the cell by shuffling, speaking or discharging compressed air.

electrolyte. Although the origin of this effect has not been studied extensively, it is likely that convection fluxes (natural or forced) induce local changes of the density of the medium (electrolyte or air) and therefore locally modifies its refractive index. As a result of the modification of the refractive index, the laser beams are deflected which of course is observed on the MDS evolution. Such perturbations can be easily avoided by insulating the whole optical path of the laser beams from the environment. In our experimental set-up, the experimental cell and the space between the cell and the sensor box was enclosed in a PMMA box in order to limit the influence of convection fluxes to natural convection which is not expected to be significant in our case, owing to the reduced size of the box and the absence of temperature or pressure gradients.

2.3 On the application of in-situ curvature measurements to the monitoring of anodising processes

In the previous sections, general experimental aspects of stress measurements in thin films have been discussed. This third section focuses specifically on the application of the multi-beam curvature-measurement technique to the in situ monitoring of anodisation processes. The first sub-section is devoted to the description of our experimental set-up, and to the preparation and characterisation procedures of our Ti electrodes. In a second sub-section, a modified relationship between curvature changes and stress·thickness changes in the oxide film is derived for the specific case of anodisation, taking explicitly into account the consumption of the Ti substrate.

2.3.1 Description of the experimental cell and of the sample preparation procedure

Design of the electrochemical cell

Several constraints had to be taken into account when designing an experimental cell adapted for in situ stress measurements during anodising. Some constraints are related to the anodising process itself (electrochemical requirements) and are discussed in the first paragraph, while some others, imposed by the curvature measurement technique (physical requirements), are discussed in a second paragraph.

Electrochemical requirements: The electrochemical cell must consist of the sample to be anodised and a cathode, immersed in a suitable electrolyte and connected to an external power source. The cathode must be inert in the selected electrolyte. The external power source should allow for accurate control of the current flowing through the circuit (under galvanostatic conditions) or the cell voltage (under potentiostatic or potentiodynamic conditions). Both electrodes must be connected to the external circuit through low-resistance leads and the electrical contacts on the anode and cathode must be insulated from the electrolyte. It should be noted that, for most of our experiments, a simple 2-electrodes set-up was selected instead of the classical 3-electrodes configuration generally preferred for accurate electrochemical experiments. The reason for this choice was that, owing to the geometry of our optical cell for the curvature measurements, it was not straightforward to add a reference electrode close enough from the anode surface. By assimilating the anode potential to the cell voltage, one neglects the contribution of the ohmic drop within the electrolyte and the interfacial potential difference at both electrodes. As the

latter are not necessarily negligible, we verified this explicitly by comparing the evolution of the cell voltage with that of the anode potential for a series of experiments. The difference between the two measurements was almost constant for galvanostatic conditions and amounted to 50 mV, which was considered negligible as compared to usual anodising voltages.

Physical requirements: The experimental cell must allow for optical access to the anode and the anode must exhibit sufficient reflectivity. In order for the anodising to result in a curvature change of the anode, the latter must have one single active surface only. The biaxial modulus and thickness of the substrate material must also be known accurately (see the Stoney equation Eq.2.4). As anodising is intrinsically an irreversible process, the anode samples are single-use. Therefore, the experimental cell must allow for easy replacement and reproducible positioning of the anode. The latter must also be clamped at one end in order to achieve the cantilevered beam configuration and be entirely immersed in the electrolyte up to the clamping point during anodising. Finally, the whole experimental set-up must be massive enough to ensure mechanical stability.

Selected set-up

Considering all these requirements, the following configuration was selected. The anode samples consist of small cantilevered Si-beams with a thin Ti film deposited on one side and are prepared in the following way.

- Silicon wafers (380 μm thick) are used as substrate for the Ti thin film anodes. Prior to the metallization step, a 400 nm thick SiO_2 layer is grown on both sides of the Si wafer by a wet oxidation process. This layer is intended to insulate the silicon from the electrolyte and to insulate the silicon substrate from the Ti layer in order to prevent leakage currents through the substrate during the anodising.

- A thin Ti film (100 to 700 nm thick) is deposited on one face of the Si wafers. Metallization is carried out either by sputtering or by e-gun evaporation.

- The metallised wafers are then diced to make rectangular samples, approximately 5x30 mm^2 (See Fig.2.24a). A small aluminium block (4x5x6 mm^3) is glued on the Ti layer on one end of the electrode using silver paste in order to provide electrical contact to the Ti layer (See Fig.2.24b, c and d).

- The end of the electrode provided with the Al contact is then clamped in Epofix resin cast in a Teflon mould. This is illustrated step-by-step on Fig.2.24e and f and Fig.2.25a, b and c. Specific two-parts moulds

were designed and fabricated, which allow for easy sample preparation, reproducible sample positioning and complete insulation of the electrical contact.

- When the resin has dried, the two parts of the mould are separated (See Fig.2.25d and e), the cantilevered sample being attached to the upper part. A small hole is drilled in the Al block from the back of the sample to allow for connection to the power source using a banana plug (See Fig.2.25f).

- The upper part of the Teflon mould containing the cantilevered anode is attached to a stainless steel sample holder using nylon screws as illustrated on Fig.2.26a and b.

It should be noted that, after the experiment, the anode sample is cleaved at the point of anchoring in order to detach the sample from the resin block and save it for further characterisation. The resin block can be withdrawn from the mould so that the moulds are completely re-usable. The Al contacts can be recovered easily as well by fracturing the resin block.

The anodising was carried out in a cell made from optical glass (photometry cell manufactured by Hellma) with a stainless steel foil or a Ti plate as a cathode and the anode samples as described above. Weak acidic electrolytes (1.0 M or 0.1 M H_2SO_4, HNO_3 or H_3PO_4) were used for most experiments. The volume of electrolyte in the cell was 600 ml. All the curvature measurements have been carried out with a multi-beam optical sensor (MOS) fabricated by *k*-Space Associates. We have been using the version 4.4 of their data analysis software. At the beginning of each measurement, the reference state for the curvature evolution is measured by averaging over 60s the MDS corresponding to the sample prior to the experiment. The MDS is then recorded for, at least, 200s prior to starting the anodising process in order to ensure that no drift is observed and that the baseline is flat in the absence of any reaction or process taking place. The geometry of the whole experimental set-up is illustrated on Fig.2.27. An horizontal configuration was selected, with the MOS box and the sample holder being attached to a steel plate. The approximate optical distance between the sample and the detector was in the range of 75 cm to 1 m. As discussed in sub-section 2.2.4, a PMMA box shield was used in order to reduce convection-induced perturbations of the measurements. The sample holder, the electrochemical cell and the sample placement into the cell are shown on Fig.2.26c, d, e and f.

The reflection of the laser beams on the sample surface was further complicated by scattering issues in the case of Ti anodising. Indeed, as discussed in section 1.2.1, the anode potentials required for growing thick anodic oxide films are far beyond the domain of electrochemical stability of aqueous electrolytes.

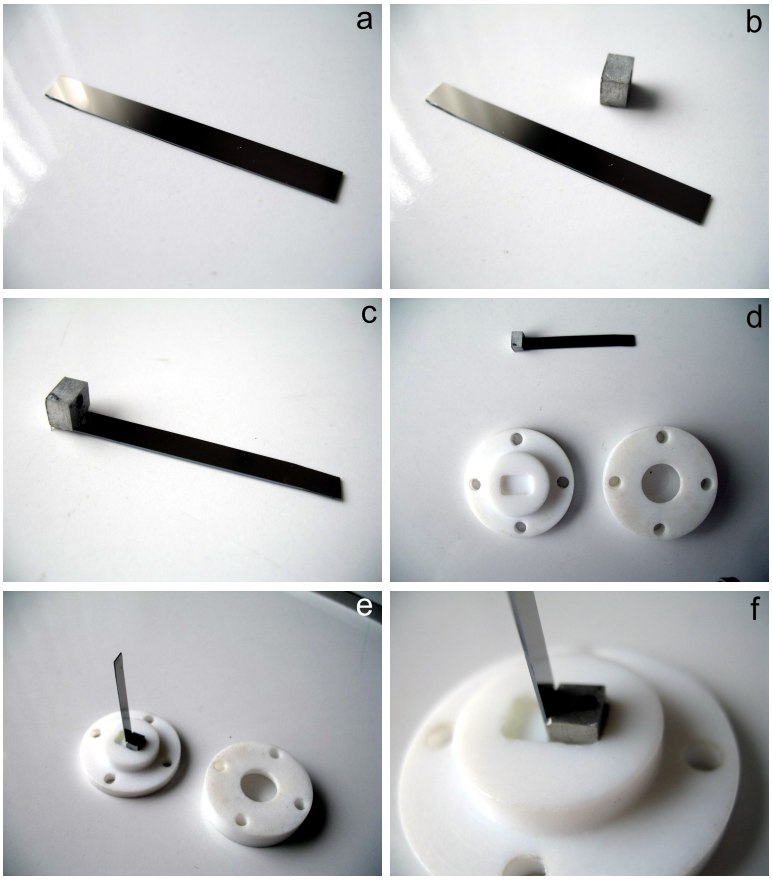

Figure 2.24: Illustration of the sample preparation procedure. Images a to d show the placement of the electrical contact on the sample. Images e and f show the placement of the sample in the Teflon moulds.

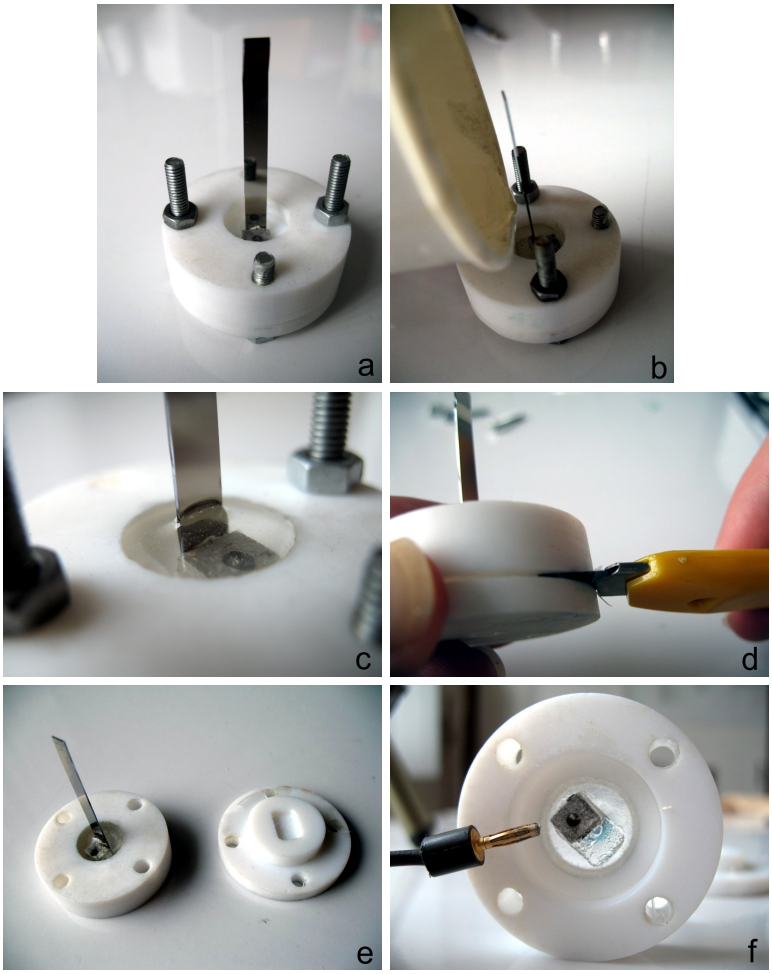

Figure 2.25: Illustration of the sample preparation procedure. Images a to e show the clamping of the lower end of the sample in epoxy resin. Image f shows the banana plug used to connect the sample to the power source.

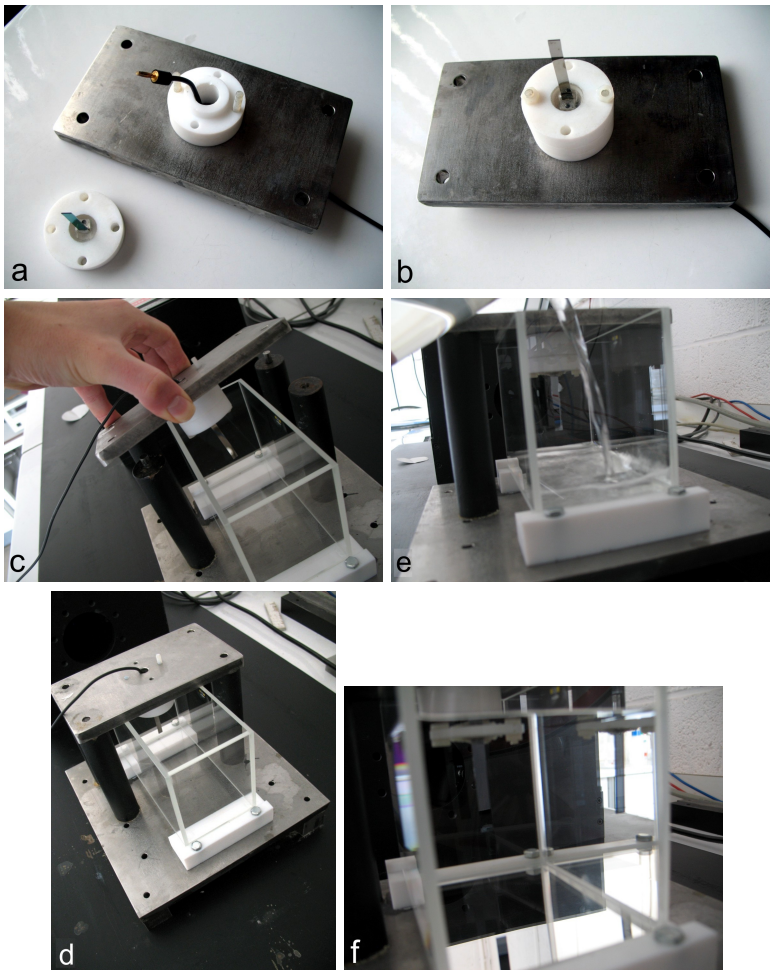

Figure 2.26: Illustration of the sample placement in the electrochemical cell. The sample is at first attached to a stainless-steel sample holder (pictures a and b). The latter is then secured to a fixed structure allowing for reproducible positioning with respect to the cell (pictures c and d). When the cell is filled with electrolyte, the sample is completely immersed up to the anchoring point (pictures e and f).

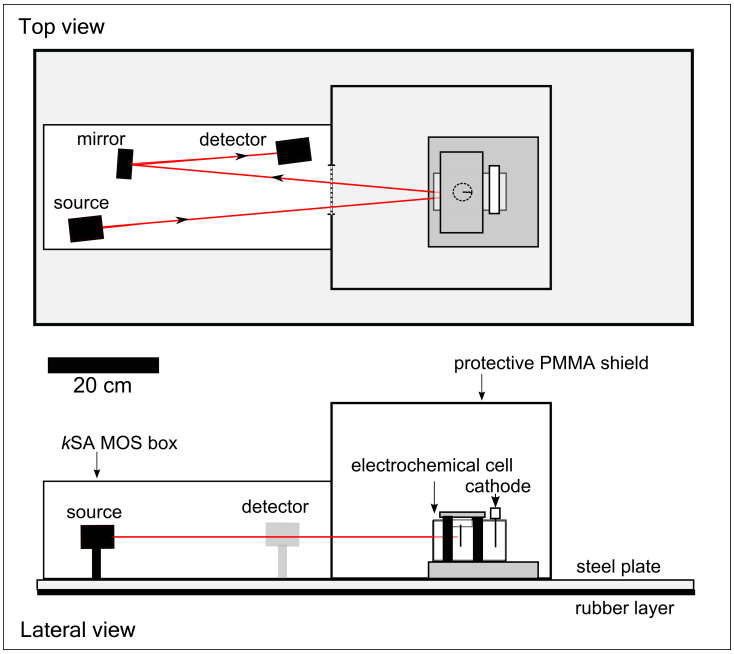

Figure 2.27: Schematic representation of the experimental set-up

Above a given potential threshold, the water decomposition reaction (or oxygen evolution reaction) takes place on the oxide surface. As a result, oxygen bubbles are formed on the sample surface which scatter the incident laser beams and prevent any measurement. In order to address this problem, the curvature of the anode was always measured from the back (non metallized) side of sample where no reaction takes place during the experiment. Double-side polished Si wafers were used in order to ensure a good reflectivity of the anode.

2.3.2 Characterisation of the Ti thin film anodes

observations

Different batches of Ti-deposits have been used for preparing the Ti electrodes for this study. Each batch of deposits has been characterised using SEM, RBS, XRD, chemical analysis (ICP) and resistivity measurements. The RBS analysis has been carried out at the Laboratoire d'Analyses par Ractions Nucléaires (LARN) from the Facultés Universitaires Notre-Dame de la Paix in Namur, with the help of Prof. Stéphane Lucas. The main results are presented in this sub-section.

Batch 'ETi'
The Ti-deposits from this batch have been prepared by e-beam evaporation. SEM micrographs reveals an average grain size of about 100 nm, essentially independent of the thickness of the deposit. In contrast, the roughness of the surface is observed to increase with increasing thickness of the deposit (see the two micrographs on Fig.2.28a and b, corresponding, respectively, to a 360 nm thick and a 700 nm thick deposit. Those films exhibit a very marked [0002] texture, as evident from the diffractogram on Fig.2.28d. RBS analysis reveals a dramatic contamination of the inner region of the Ti layer with carbon. Oxygen is found to be incorporated as well in the whole Ti deposit but in a smaller quantity (about 10 at%). No other detectable element could be found in a significant concentration from the ICP analysis. The large resistivity measured for those Ti deposits (ρ=187$\mu\Omega$·cm) is believed to be a direct consequence of this contamination.

Batch 'STi'
The Ti-deposits from this batch have been prepared by magnetron sputtering. The deposits have been made on thick Si substrates, and were therefore inappropriate for curvature measurements. Samples from this batch were used for the anodisation experiments described in chapter 5. SEM micrographs reveal a grain size slightly larger and less uniform than for the ETi batch, with grains ranging from 100 to 400 nm. Those films exhibit a marked [0002] texture, with

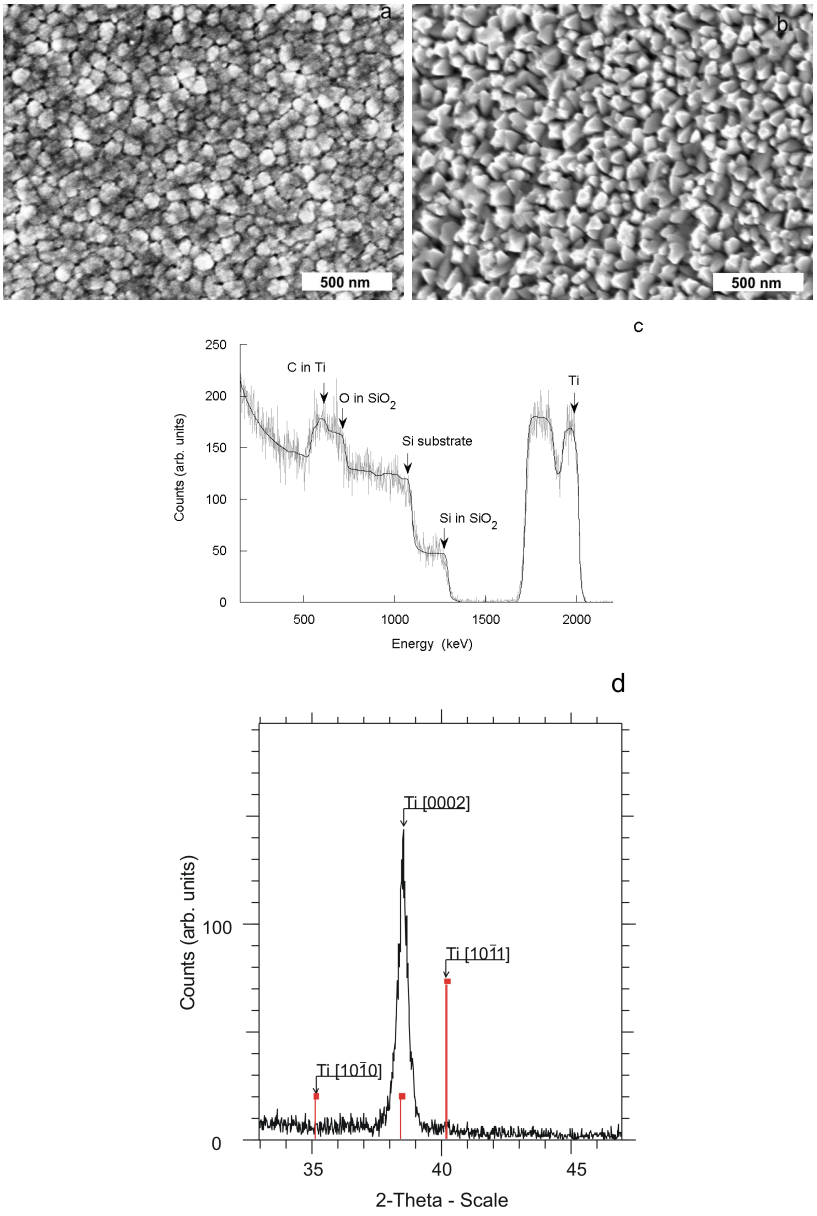

Figure 2.28: Results from the characterisation of the 'ETi' Titanium batch showing (a) and (b) the metal grain size as observed by SEM for films respectively 360 and 700 nm thick, (c) the composition depth profile obtained by RBS and (d) the crystallographic texture, as measured by XRD.

some [10$\bar{1}$1] grains being present as well, as observed from the diffractogram on Fig.2.29c. RBS analysis indicates a rather clean deposit, with only a small amount of incorporated oxygen. This was confirmed by the chemical analysis as well as by the low resistivity value (46$\mu\Omega$·cm), which is very close to the expected value for (pure) bulk Ti.

Batch 'PTi'
The Ti-deposits from this batch have been prepared by magnetron sputtering. SEM micrographs reveal an average grain size of 100 nm, similar to that observed for samples from the ETi batch. The deposits are also observed to be very rough, as illustrated on Fig.2.30a and b. Those films exhibit a marked [0002] texture, as evident from the diffractogram on Fig.2.30d. RBS analysis indicates that the Ti film contains a significant amount of oxygen (evaluated to 20%) mainly in the region adjacent to the surface. No other contaminants were detected upon chemical analysis of the Ti film. Owing to the large amount of oxygen, the films are observed to be about 5 times more resistive than expected for clean Ti deposits (ρ was measured to be 267$\mu\Omega$·cm). For this specific batch, supplementary AFM analysis was carried out and reveals a RMS roughness of 17 nm.

Batch 'ITi' The Ti-deposits from this batch have been prepared by magnetron sputtering. The SEM micrograph on Fig.2.31a reveals a grain size of 80 nm and a rather smooth surface. The films exhibit a marked [0002] texture, as evident from the diffractogram on Fig.2.31c. According to RBS analysis, the deposits are clean but contain a small quantity of incorporated oxygen. Chemical analysis confirmed that no other contaminants are present in the film.

Batch 'FTi' The Ti-deposits from this batch have been prepared by e-beam evaporation. The results from the characterisation procedure are shown on Fig.2.32. The SEM micrograph reveals an average grain size of 60 nm and a rather smooth surface. The films exhibit a marked [0002] texture, as observed from the diffractogram on Fig.2.32. RBS analysis indicates that the films are clean but contain a small quantity of incorporated oxygen. Chemical analysis confirmed that no other contaminants are present in the film.

Bulk Ti vs. Ti thin films

In the light of the discussion presented in chapter 1 on the influence of grain orientation and oxygen content of the Ti substrate, some significant differences between bulk Ti substrates and thin film Ti substrates deposited by PVD techniques are pointed out in this paragraph, as they can be expected to influence considerably the anodisation process. Firstly, thin films produced by sputter-

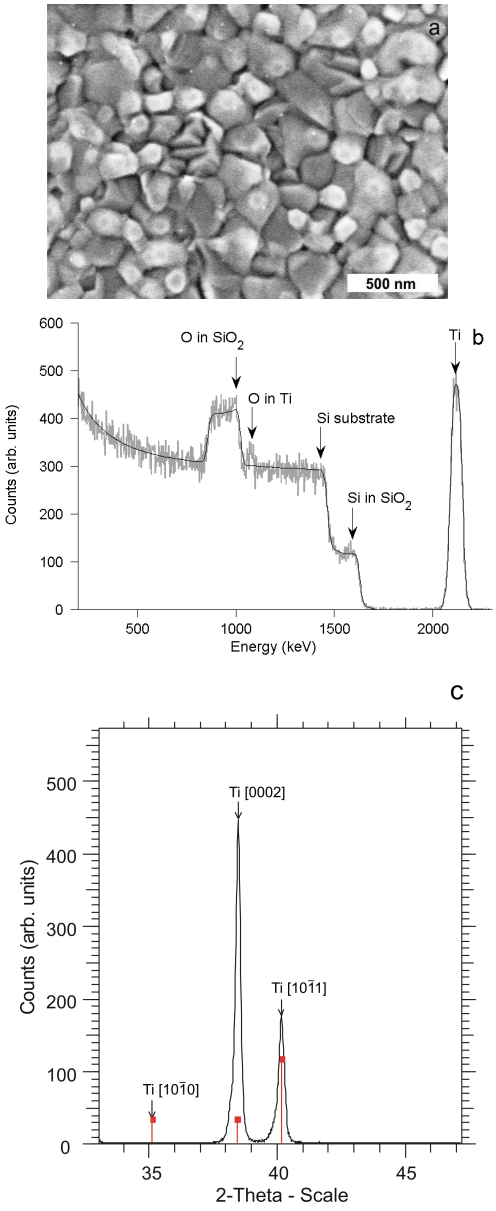

Figure 2.29: Results from the characterisation of the 'STi' Titanium batch showing (a) the metal grain size as observed in a SEM, (b) the composition depth profile obtained by RBS and (c) the crystallographic texture, as measured by XRD.

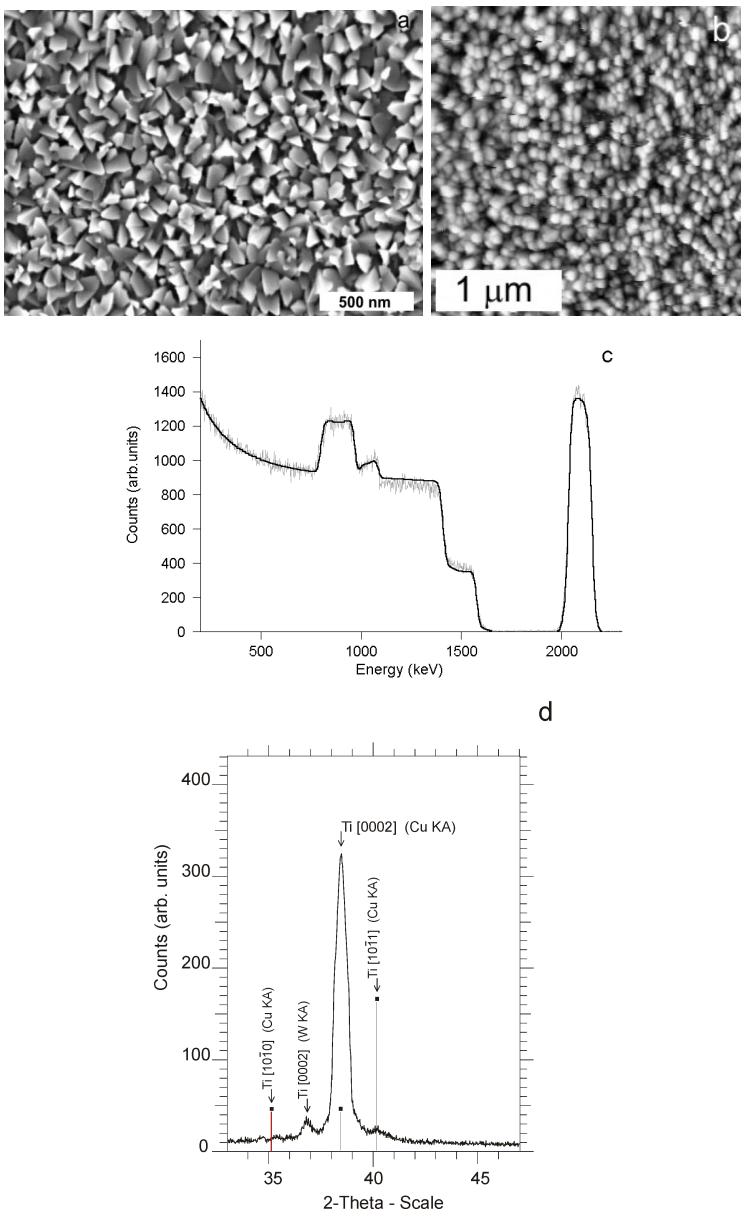

Figure 2.30: Results from the characterisation of the 'PTi' Titanium batch showing the surface of the Ti films as observed (a) in a SEM and (b) by AFM (3 μm by 3 μm scan, (c) the composition depth profile obtained by RBS and (d) the crystallographic texture, as measured by XRD.

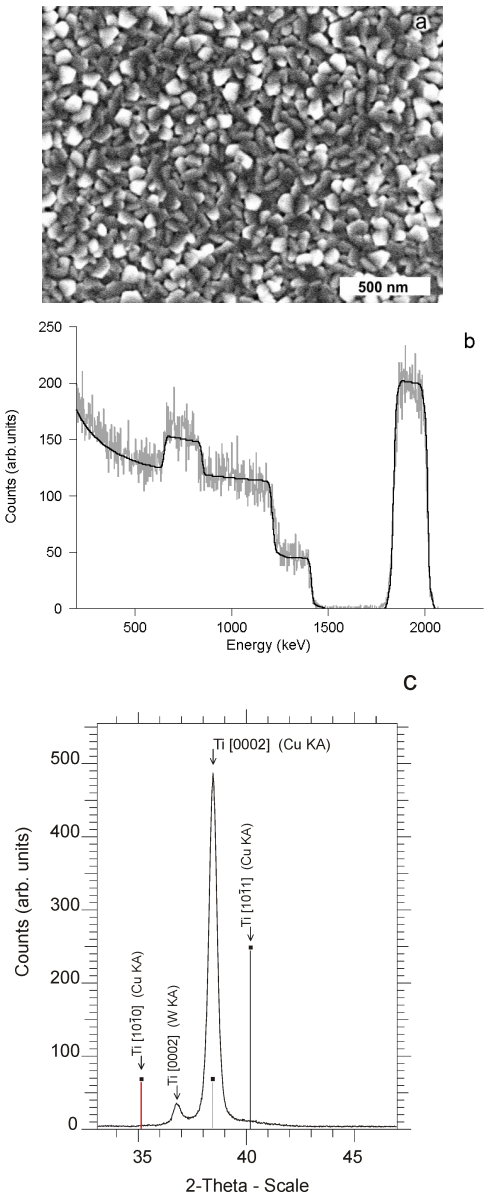

Figure 2.31: Results from the characterisation of the 'ITi' Titanium batch showing (a) the metal grain size as observed in a SEM, (b) the composition depth profile obtained by RBS and (c) the crystallographic texture, as measured by XRD.

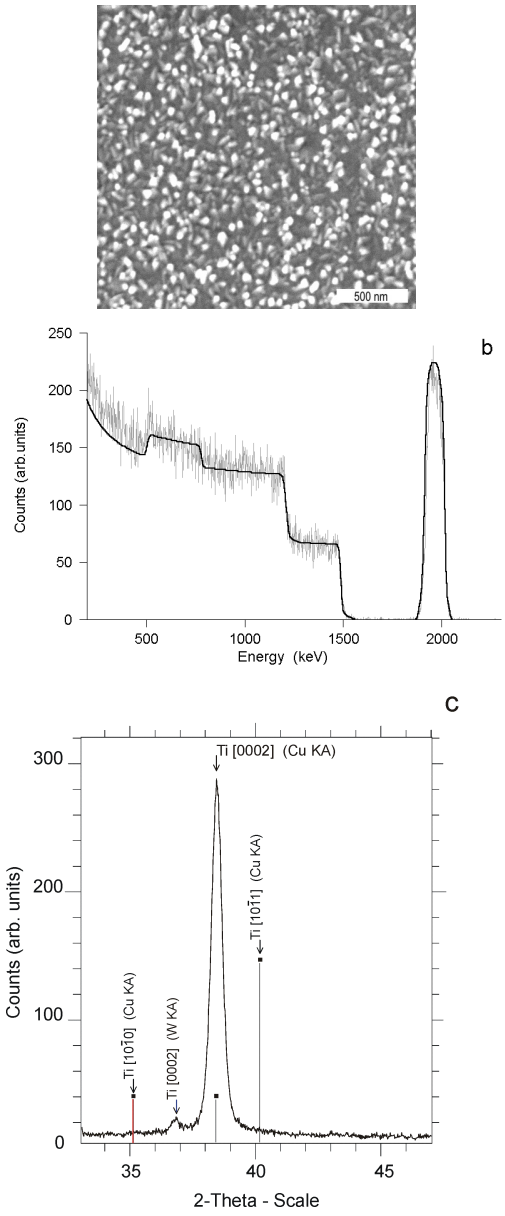

Figure 2.32: Results from the characterisation of the 'FTi' Titanium batch showing (a) the metal grain size as observed in a SEM, (b) the composition depth profile obtained by RBS and (c) the crystallographic texture, as measured by XRD.

ing or e-beam evaporation usually grow with a highly characteristic columnar morphology, as they grow with their basal plane parallel to the film surface, which allows for minimising the surface energy. As a result, typical PVD thin films are highly textured, exhibiting one main grain orientation, as confirmed by the diffractograms presented on Fig.2.28 to 2.32. This contrasts with bulk Ti substrates in which the grains are usually more or less randomly oriented. As discussed in section 1.2.4 dealing with the influence of the Ti grain orientation on the growth of the anodic oxide film, a very uniform behaviour is anticipated for anodic films grown on the thin film substrates, as the growth of the oxide film on each grain is expected to be comparable. This higher uniformity of TiO_2 films grown on thin film substrates is expected to lead to sharper transitions than in the case of bulk Ti because transitions would take place at the same time all over the sample. It should be noted that, with respect to the texture, an influence of the deposition technique and of the thickness of the deposit can be observed. By comparing Fig.2.28 with Fig.2.29, which both correspond to Ti films of comparable thickness, it appears that e-beam evaporation leads to more textured films, probably as a result of a much lower deposition rate as compared to sputtering. Furthermore, at least for the sputtered films from the STi batch, the texture was observed to be more marked for thicker films, as illustrated on Fig.2.33. Indeed, for the thinnest films (100 nm), the peaks corresponding to [0002] and $[10\bar{1}0]$ orientations are observed to have a comparable intensity while, as the films becomes thicker, the $[10\bar{1}1]$ peak vanishes and only [0002] orientation is observed.

Secondly, in the case of Ti, PVD films grow with the dense-packed Ti [0002] planes parallel to the film surface. Therefore, as confirmed by XRD analysis, the growth of the oxide film takes place on the [0002] planes, which have been demonstrated to lead to intense oxygen evolution within the film, blistering and rupture of the oxide film [154]. Therefore, thin film Ti substrates are not the most suitable ones for growing thick smooth and homogeneous TiO_2 films and the growth process can be expected to be strongly affected by the physical consequences of the oxygen evolution reaction.

Thirdly, the grain size of PVD films is usually much smaller than in the case of bulk material. The grain size of our sputtered and evaporated films was observed to range between 40 and 400nm. A direct consequence of the small grain size is the high density of grain boundaries per unit area. Grain boundaries constitute flaws in the metal surface, which can act as preferential sites for nucleation of weak, e^- conductive, spots in the oxide film [216]. Therefore, the density of grain boundaries in thin films, larger than that of bulk substrates, is anticipated to affect the growth as well.

A fourth specific feature associated with PVD Ti films is the incorporation

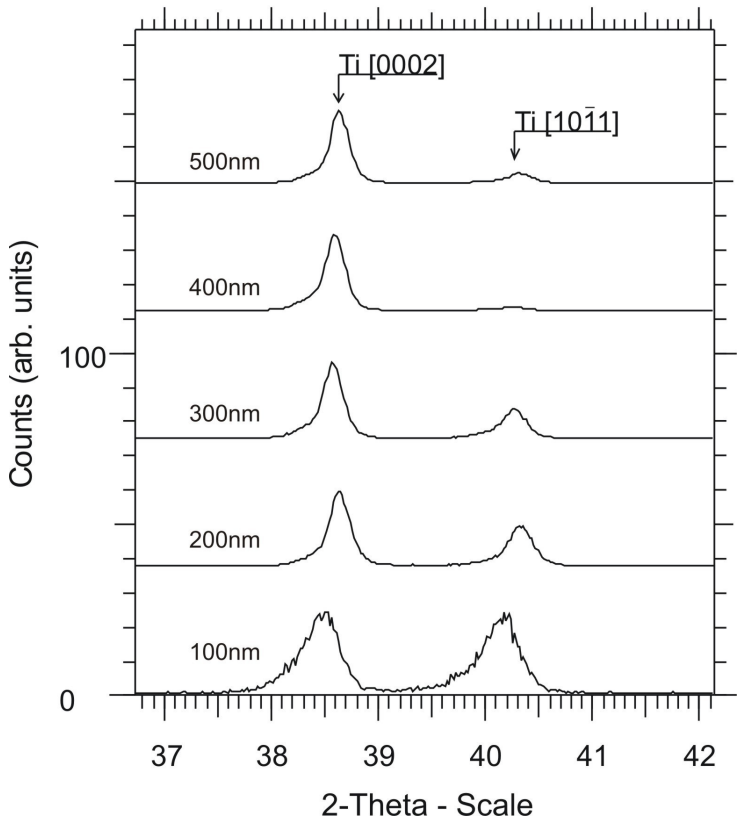

Figure 2.33: Diffractograms recorded on deposits from the STi batch having different thicknesses. Comparison of the diffractograms reveals an evolution of the texture of the Ti substrate with its thickness.

of oxygen in the film during the deposition process. The ability of Ti to capture oxygen species from the environment is well-known. Therefore, high-vacuum conditions are usually not sufficient to deposit Ti films free of oxygen. Unless they are prepared in a ultra-high vacuum facility, Ti deposits typically contain 10 to 20 at% of oxygen. Massive oxygen incorporation is indeed observed for the PTi batch, as shown on Fig.2.30c and oxygen is observed as well, although in smaller quantities, in the other Ti batches. According to the observations discussed in section 1.2.4 on the effect of incorporated oxygen on the growth of anodic oxide films, the anodisation process as a whole should not be modified significantly by the presence of oxygen in the metal. However, the rate of growth and therefore the apparent growth efficiency is expected to be affected. Therefore, if O-gradients are present in the Ti film, the interpretation of the V-t data during galvanostatic conditions will be more complicated, as slope changes in the V-t curves can result not only from a change in the AR or in the current associated with the side-reactions, but also from a change in the local oxygen concentration in the Ti film at the metal/oxide interface.

Finally, the last characteristic of the PVD Ti films is a low roughness, much lower than that of typical bulk substrates. The surface of thin films of course does not require further polishing steps and thin films should therefore provide for a more reproducible surface condition than the bulk substrates. The RMS roughness of our Ti films, as measured by AFM for the PTi batch, was typically of the order of 20 nm, which is a low value as compared to bulk samples, even after careful polishing.

Batch-to-batch reproducibility

As evident from the results of the characterisation step, some differences are observed between the different Ti batches. This is not particularly surprising considering the fact that the 5 batches have been ordered from different laboratories, hence being prepared using different deposition chambers, which leaded to a poor control on the deposition process. As, in addition, Ti is well known as a getter material, the quality of the deposit is extremely sensitive to the presence of impurities in the deposition chamber. As will be illustrated in chapter 3, significant differences in the anodisation behaviour of the different batches were observed as well. While the STi, FTi and ITi exhibited a rather 'classical' anodisation behaviour, the anodisation of the ETi and PTi batches was characterised by the presence of low-efficiency stages. In terms of texture, no major difference was observed between the batches. All of them exhibit a marked [0002] texture. Only the thinnest deposits from the STi batches are observed to present a significant proportion of $[10\bar{1}1]$ grains. Hence, the non-classical behaviour of the ETi and PTi batches does not seem to be attributable to a texture effect. The smaller grain size was observed for the FTi and ITi

batches while the largest grains were observed on the STi batch. Since those three batches exhibited quite comparable behaviours, grain size does not either seem to be a major source of differences in our case, at least not as far as the initial stages of the anodisation concerns. Hence, the specific behaviour of the ETi and PTi batches is more likely to arise from differences in the purity of the deposit. Indeed, the ETi batch is contaminated with carbon while the PTi batch was observed to contain a particularly high quantity of incorporated oxygen. Although the mechanism through which these impurities affect the anodisation behaviour is still an open question, we can conclude that the purity of the Ti substrates is a crucial point that needs to be taken care of in order to guarantee the reproducibility of the anodisation processes.

It should be noted that the day-to-day reproducibility of the anodisation experiments for a given Ti batch is also affected by the day-to-day variations in temperature. Indeed, it is well known that the growth of anodic TiO_2 films is rather sensitive to the temperature, which directly influence the mobility of the carriers, the density of the film (see section 1.2.4), the crystallisation behaviour of the film, and therefore its conductivity. All the experiments presented in this thesis have been carried out at ambient temperature, without temperature control, and hence probably involving temperature variations of about 10°C between wintertime and summertime, with temperature always falling in the range of 16 to 26 °C. As revealed by a systematic study on the influence of the temperature, this is expected to lead to small quantitative differences, mainly in terms of the slope of the V-t curves and of the voltage thresholds at which transitions take place. Therefore, the influence of temperature should be taken into account when interpreting the experimental observations.

2.3.3 Curvature-stress·thickness relationship for the specific case of anodisation

In contrast to deposition processes, in the specific case of anodising, the substrate is progressively consumed and transformed into an oxide film. Therefore, the change in curvature experimentally observed results from the superposition of two contributions, the first one being due to the growth of the strained oxide film while the second arises from the consumption of the initially stressed metal layer. Hence, the most rigorous approach for the calculation of the stresses from curvature change measurements on Ti/TiO_2 multilayers requires taking into account the fact that one minor fraction of the measured change in curvature is not due to stress in the oxide (σ_{ox}), but to the reduction of the Ti thickness (h_{Ti}). The stress·thickness product for the multilayered cantilevered stack is equal to:

$$\Delta\left(\overline{\sigma \cdot h}\right)_{stack} = \int_{stack} \sigma\left(h\right) dh = \int \sigma_{Ti} dh_{Ti} + \int \sigma_{ox} dh_{ox} \tag{2.57}$$

If we plausibly assume that the stress in the Ti layer is homogeneous over the whole thickness, hence being noted as $\overline{\sigma_{Ti}}$, and that this stress value is not modified during the anodisation process, anodising-induced changes in Eq.2.57 can be written as

$$\Delta\left(\overline{\sigma \cdot h}\right)_{stack} = \overline{\sigma_{Ti}}\Delta h_{Ti} + \Delta\left(\sigma_{ox} \cdot h_{ox}\right) \tag{2.58}$$

The ratio of the volume of oxide formed to the volume of metal consumed is given by the Pilling-Bedworth ratio (PBR). Since the electrode surface is not modified upon anodisation,

$$\Delta h_{Ti} = -\frac{\Delta h_{ox}}{PBR} \tag{2.59}$$

Hence, Eq.2.58 transforms into:

$$\Delta\left(\overline{\sigma \cdot h}\right)_{stack} = -\frac{\overline{\sigma_{Ti}}}{PBR}\Delta h_{ox} + \Delta\left(\sigma_{ox} \cdot h_{ox}\right) \tag{2.60}$$

If we now consider, to a first approximation, the stress in the TiO_2 film to be homogeneous over the whole thickness and equal to the average value $\overline{\sigma_{ox}}$, Eq.2.60 becomes:

$$\Delta\left(\overline{\sigma \cdot h}\right)_{stack} = \left(\overline{\sigma_{ox}} - \frac{\overline{\sigma_{Ti}}}{PBR}\right)\Delta h_{ox} \tag{2.61}$$

so that

$$\sigma_{ox} = \left(\frac{Y}{1-\nu}\right)_s \frac{h_s^2}{6}\frac{\Delta\kappa}{\Delta h_{ox}} + \frac{\overline{\sigma_{Ti}}}{PBR} \tag{2.62}$$

From this equation, we can evaluate the correction to be applied for taking into account the consumption of the substrate if the average stress $\overline{\sigma_{Ti}}$ in the Ti deposit is known. The latter has been systematically measured for each Ti batch by quantifying the curvature change resulting from the dissolution of the Ti layer. Unfortunately, the chemical solution allowing for dissolving the Ti layer selectively from the substrate (1 Vol NH_4OH, 1 vol H_2O_2, 5 vol H_2O) is continuously bubbling which precludes in situ curvature measurements during the dissolution. Therefore, only the average stress in the layer is accessible from the curvature change observed between pre- and post-dissolution measurements but stress gradients in the film cannot be studied in that way. The average stress in the Ti deposits was observed to be typically in the range of 50 to 200 MPa, depending on the thickness of the film and the deposition conditions. The influence of the thickness on the average stress is illustrated for the ETi batch on Fig.2.34. The PBR for the transformation of Ti into TiO_2 is about 2.4 for amorphous TiO_2. As will be shown in chapter 3, the average stress in the oxide $\overline{\sigma_{ox}}$ can vary widely, from about 100 MPa to several GPa. Hence the error made by neglecting the consumption of the Ti layer is not necessarily negligible and the contribution from the Ti consumption should be taken into account systematically.

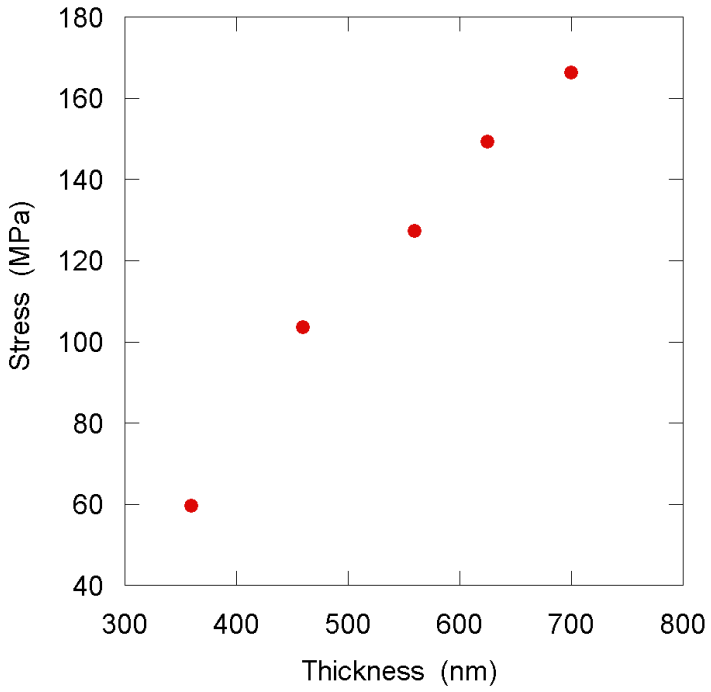

Figure 2.34: Measured average stress in Ti-deposits from the ETi batch as a function of their thickness.

2.4 Conclusion

In this second chapter, we have presented the multi-beam sensor which has been used in this study. The applicability of the constitutive equation linking our mesured curvature values to the stress in the film (the Stoney equation) has been discussed and confirmed for our specific experimental set-up. The calibration equations for the sensor have been derived for the case of a measurement carried out in air and extended to the case of a measurement in a liquid. The design of our experimental set-up has been discussed and the sample preparation procedure has been described extensively. Finally, we have pointed out the fact that the contribution from substrate consumption is not necessarily negligible in the case of anodising of Ti thin films and that it should be taken into account in order to quantify accurately the film stress. In the next chapter, experimental results on the stress evolution in anodic TiO_2 films, obtained using the multi-beam technique, are presented.

Chapter 3

Experimental investigation of the growth stress evolution in anodic TiO_2 films

Contents

As discussed in chapter 1, although the growth of anodic oxide films on Ti is relatively well-documented, very little experimental evidence is available on the mechanical aspects involved in the growth of the TiO_2 film. Furthermore, even less is known on the relationships between such mechanical aspects and the electrochemical behaviour of the film. However, as will be evidenced further in this chapter, the electrochemical and mechanical behaviour of anodic

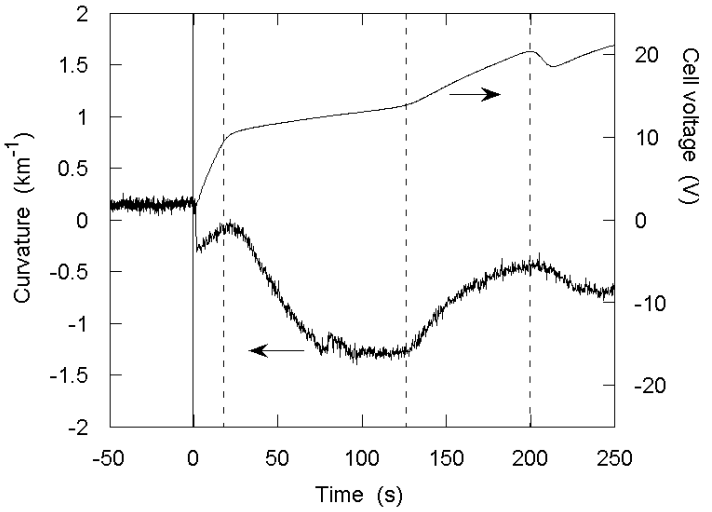

Figure 3.1: Typical example of the time evolution of the anode curvature and cell voltage during an anodisation experiment, showing a very clear correlation of the two signals. This experiment has been carried out on a sample from the ITi batch in 1.0 M H_2SO_4 at 2.4 mA/cm^2.

oxide films appear to be strongly correlated. This is illustrated on Fig.3.1, which shows a typical example of cell voltage (V) and curvature (κ) evolution recorded during the galvanostatic anodisation of a Ti thin film electrode in 1.0 M H_2SO_4 at 2.4 mA/cm^2. Remarkably, changes in the slope of the V-t curve are observed to correspond systematically to changes in the direction of the curvature evolution. Hence, the numerous events taking place in the course of the growth process which affect the electrochemical behaviour of the film (thus leading to more or less pronounced changes in the slope of the V-t curve) appear to either result from or directly affect its mechanical behaviour as well. In this chapter, we present experimental results obtained by combining the data from classical electroanalytical techniques with measurements of the stress evolution carried out in situ during the growth of the film, thus providing direct correlated information on the electrochemical and mechanical aspects involved in the growth process.

3.1 Preliminary remarks

Interpretation of the curvature data and terminology

Experimental data are obtained in the form of V-t and κ-t curves, as the ones plotted together on Fig.3.1. The curvature data can be converted into stress·thickness ($\overline{\sigma} \cdot h_f$) data using the Stoney equation (Eq.2.4 in chapter 2), where $\overline{\sigma}$ is the average stress in the film. From $\overline{\sigma} \cdot h_f$ vs. time curves, the kinetics of stress evolution can be examined and correlations between the cell voltage and stress evolution can be identified. In order to distinguish between kinetic effects and mechanical ones, the stress·thickness data can be represented as a function of oxide thickness or cell voltage, which is equivalent provided that the anodising ratio keeps a constant value over the V-range of consideration. In this form, experiments carried out at different current densities, in which case the time-scales are different, can be straightforwardly compared. Furthermore, stress values can be directly calculated from the slope of those curves. The slope of the stress·thickness vs. thickness plots is referred to as the **instantaneous stress** (σ). The slope of a straight line linking the axis origin to a given point of the curve represents the **average stress** ($\overline{\sigma}$) in the film at that time. Mathematically, this can be expressed as:

$$\overline{\sigma} = \frac{1}{h_f} \int \sigma dh_f \tag{3.1}$$

By convention, a negative sign of the instantaneous or average stress is indicative for a compressive stress while a positive sign stands for tensile stresses. Transitions from a compressive to tensile instantaneous stresses lead to a **compressive maximum** while transitions in the opposite direction are accompanied by a **tensile maximum**.

Generally speaking, the measured curvature changes encompasses three distinct contributions: a first contribution arising from the consumption of the Ti substrate (as already discussed in section 2.3.3) and two contributions corresponding to stress·thickness changes in the growing oxide film. Among the latter, the first one is a reversible, field-induced, contribution called **electrostriction stress** while the second one is an intrinsic growth-induced contribution. The reversible electrostriction stress will be discussed in detail in the next chapter. This chapter focuses more specifically on the **intrinsic growth stresses** developing in the film.

Comments on the experimental reproducibility

Before discussing the main experimental observations, it is worth commenting on the reproducibility of the stress evolution, which is of course a primary concern if trends have to be identified from series of experiments. In fact, although

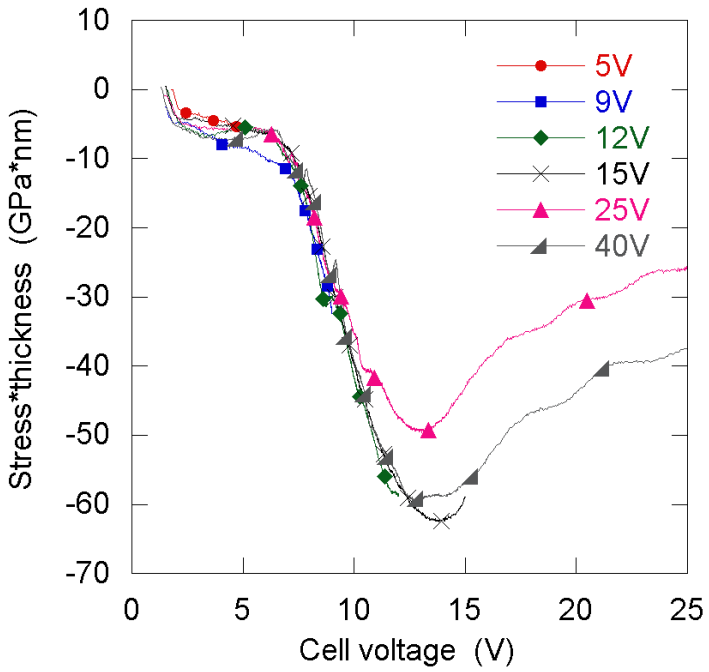

Figure 3.2: Measured evolution of the stress·thickness product with the cell voltage for a series of six samples from the PTi batch anodised at 4 mA/cm^2 in 1.0 M H_2SO_4 up to different values of the final voltage. The stress·thickness evolution exhibits a remarkable reproducibility.

the anodisation process is very sensitive towards the details of the experimental conditions, the reproducibility of the stress·thickness evolution for a given set of experimental conditions was observed to be fairly good. This is illustrated on Fig.3.2, showing the evolution of the stress·thickness product as a function of the cell voltage for 6 experiments carried out under the same conditions up to different values of the cell voltage. The six curves superpose remarkably. Only the sample anodized up to 25V shows a slightly different behaviour, with a less compressive value of the stress·thickness product at the compressive maximum.

Unfortunately, the excellent reproducibility of the stress evolution for experiments carried out under the same conditions on the same Ti substrate contrasts with the high variability observed when different Ti substrates are used. Indeed, one significant experimental obstacle encountered during this research was the fact that the anodisation behaviour was observed to be ex-

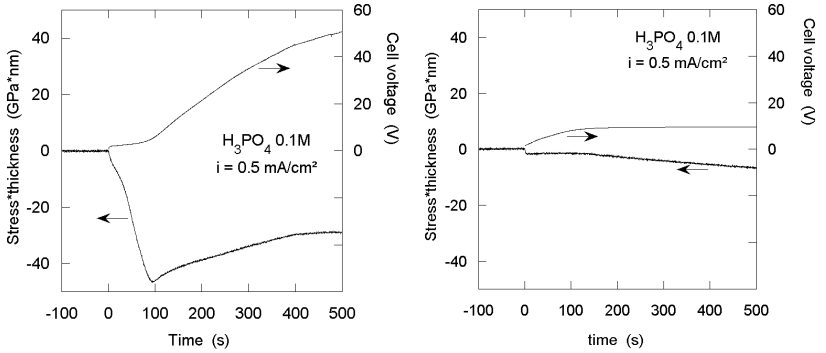

Figure 3.3: Comparison of the time-evolution of the cell voltage and of the sample curvature observed for anodisation of Ti electrodes from the ETi and ITi batches in 1.0 M H_3PO_4 with a current density of 0.5 mA/cm^2.

tremely sensitive to the characteristics of the Ti thin film substrates. As the characteristics of the latter showed poor reproducibility, a large variability of the experimental results was observed from one Ti batch to another. This is illustrated on Fig.3.3, showing the characteristic evolution of the cell voltage and the sample curvature during anodisation experiments carried out under the same conditions (1.0 M H_3PO_4, i=0.5 mA/cm^2) on Ti electrodes from two different batches (ETi and ITi batches). Obviously very different behaviours are observed, both in terms of V-evolution as of curvature evolution, with a one order of magnitude difference in the observed curvature changes. As discussed in section 1.2.4, several characteristics of the Ti substrate directly influence the anodisation process, for instance the presence of impurities in the metal or the presence of a texture. Results from the characterisation of the Ti batches have been presented on section 2.3.2. The main striking difference between the ETi and ITi batches is that the former was observed to be contaminated with carbon. The latter impurity might thus be responsible for the specific stress evolution associated with samples from that batch. In other cases however, the differences between the characteristics of the Ti batches which are reponsible for the differences in the V-t behaviour are not clearly identifiable.

Owing to this variability, conclusions can hardly be drawn as to the "typical" stress evolution in anodic TiO_2 films. The details of the V- and stress-evolution appear to be always characteristic for a given Ti batch. Nevertheless, some clear general tendencies were identified and reproducibly observed, independent of the Ti substrate. The following section is devoted to observations on TiO_2 films grown galvanostatically. In the V-range over which the film grows under high-efficiency conditions, the growth was observed to be accompanied by the

development of constant tensile stresses. In the third section, growth stress transitions are described and discussed in terms of growth instabilities.

3.2 High-efficiency growth of anodic TiO_2 films under galvanostatic conditions

As discussed in the first section, the anodisation behaviour observed on Ti thin film electrodes differs widely from one batch to another. In addition, it resembles the classical behaviour reported for galvanostatic anodisation of Ti on some batches only. The classical behaviour is characterised by a high growth efficiency and a linear V-t at the beginning of the anodisation, which then decreases above a given threshold, more or less rapidly depending on the growth rate. As a starting point for the discussion of the stress evolution in anodic TiO_2 films, we choose to present observations obtained on Ti batches which showed a behaviour close to the classical one. A very characteristic stress evolution was observed reproducibly on those samples in the V-range over which the film grows with a high efficiency, characterised by a constant tensile stress developing in the film. In addition, the stress value was observed to be independent of the current density.

Such a behaviour was observed for instance on samples from the ITi batch. The V-t curves for a series of four samples anodised in 0.1 M H_3PO_4 with current densities of 0.5, 1.4, 2.9 and 3.6 mA/cm^2 are presented on Fig.3.4a. The cell voltage is observed to increase linearly with time up to, respectively, 4, 11.5, 12 and 12.3 V for the four current densities. After that, the growth efficiency drops rapidly and a V-plateau is attained for the experiments carried out with the lowest current densities, while the cell voltage increases further in the case of the larger two current densities. The corresponding stress·thickness curves are characterised by an initial V-surge in the compressive direction, arising from electrostriction in the native oxide layer, then a tensile evolution is observed in the V-range corresponding to the high-efficiency growth. This is illustrated on Fig.3.4b showing in parallel the cell voltage and $\overline{\sigma} \cdot h_f$ evolution for the sample anodised at 1.4 mA/cm^2. After the high-efficiency region, a transition to another growth stage is observed. Such transitions will be discussed in the third section and we will focus here on the tensile stage. The stress·thickness data for the four samples are plotted altogether as a function of V on Fig.3.4c. Remarkably, the $\overline{\sigma} \cdot h_f$ curves are perfectly superposed and show a constant tensile slope in the whole V-range over which high-efficiency is observed. The almost vertical deviations of the stress·thickness curves observed at 9V and 14V for the lowest two current densities correspond to the transitions to the V-plateau. These results suggest that, under such conditions, the oxide film grows with a constant tensile stress, independent of the current density in

the range of 0.5 to 3.6 mA/cm^2.

This behaviour, with the characteristic correlation between tensile stress-evolution and high-efficiency growth was observed as well during other experiments in which it was preceded by another, low-efficiency, stage. On those samples, the tensile stage was observed to extend over a very wide V-range of more than 40V even for the lowest current density investigated, hence facilitating quantitative analysis of the data. For this reason, we decided to use this second series of experiments as a basis for the quantitative discussion of the tensile stress-evolution associated with galvanostatic high-efficiency growth. In the following sub-section, a series of four experiments carried out at different current densities, is presented and analysed in detail.

Experimental:

For this experiment, 4 samples from the same batch of evaporated Ti (batch ETi) were anodised galvanostatically with current densities of 0.5, 1.9, 2.9 and 4.1 mA/cm^2. A 0.1 M H_3PO_4 electrolyte was selected as the latter is well-known to allow growing anodic TiO_2 films up to large thicknesses [219]. For the lowest two current densities, the experiment was stopped after 1000s while, for the larger current densities, it was interrupted at 500s, after the first evidence of dielectric breakdown of the film was observed. The experimental set-up and the experimental cell were as described in chapter 2.

Results:

Fig.3.5 shows the V-t curves corresponding to the 4 experiments. The latter are characterised by:

- an initial V-surge
- a first stage characterised by a low efficiency (low $\mathrm{d}V/\mathrm{d}t$), more visible on Fig.3.5b.
- a second stage characterised by a high efficiency
- a progressive decrease of the slope
- a transition to another stage, the characteristics of which are more dependent on the current density (with large voltage fluctuations characteristic for dielectric breakdown being observed at high current density).

The values of $\mathrm{d}V/\mathrm{d}t$ for the first (low-efficiency) and second (high-efficiency) stages are listed in Table 3.1. The duration of the first stage as well as the total charge consumed during this stage are included in Table 3.1 as well. Fig.3.6 presents as a function of the current density the $\mathrm{d}V/\mathrm{d}t$ values corresponding to

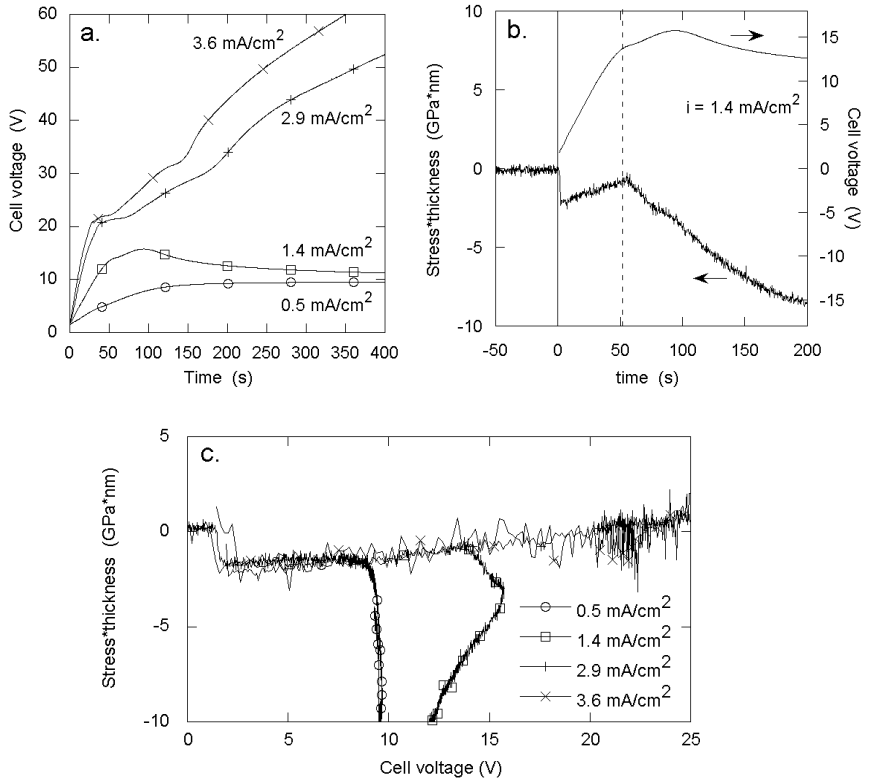

Figure 3.4: Results obtained for a series of anodisation experiments carried out on samples from the ITi batch in 0.1 M H_3PO_4, showing a) the time-evolution of the cell voltage for the 4 current densities, b) the time-evolution of the stress·thickness product for the sample anodised at 1.4 mA/cm^2 and c) the evolution of the stress·thickness product with V for the four samples.

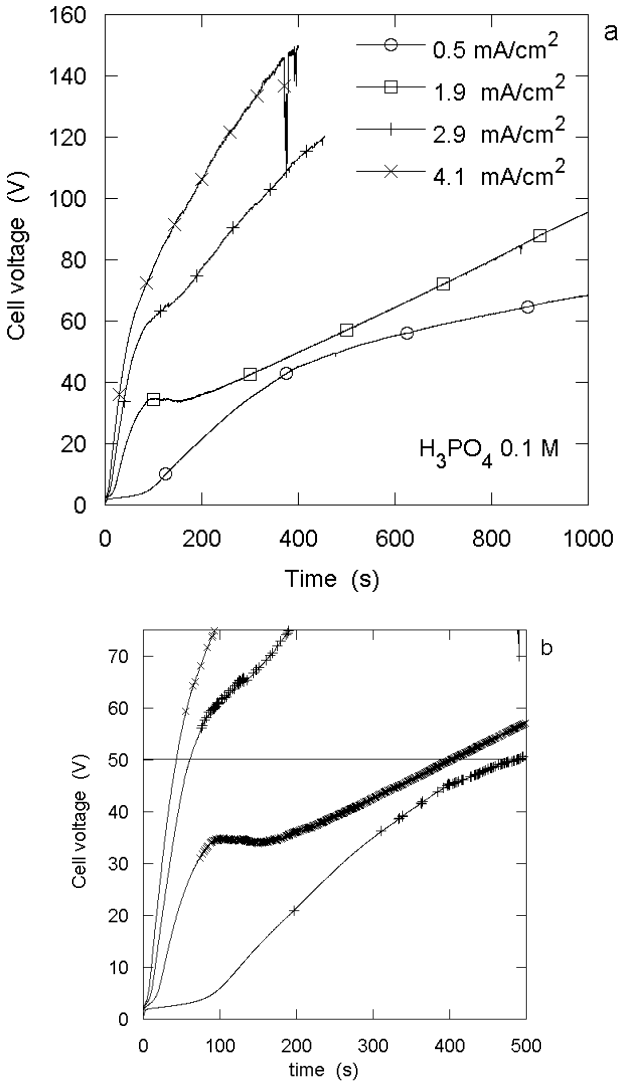

Figure 3.5: Time-evolution of the cell voltage during galvanostatic anodisation of samples from the ETi batch in 0.1 M H_3PO_4 at 4 different current densities. On figure b), markers have been added to the data points where voltage fluctuations are observed.

Current density mA/cm^2	$(dV/dt)_I$ [mV/s]	$(dV/dt)_{II}$ [mV/s]	Duration [s]	Charge [mC/cm^2]	η_I [%]
0.53	19.1±0.1	165.6±0.1	94.6	50.1	11.5
1.87	112.9±0.8	649.3±1.6	18.9	35.3	17.4
2.85	215.8±2.3	1066.1±5.8	10.6	30.1	20.2
4.06	356.7±5.7	1497.6±9.3	7.6	30.9	23.8

Table 3.1: Quantitative data extracted from the V-t anodisation curves. The efficiency values for the first stage presented in the last column have been calculated from the ratio of the dV/dt values in both stages, based on the assumption that the growth efficiency is 100% in the second stage.

the high-efficiency stage, obtained from a linear fit of the 4 V-t curves over the range of 6 to 15V. The four experimental data points are observed to fall on a straight line of slope 367±6 Vcm^{2}C^{-1} which intercepts the axes origin. The fact that dV/dt is observed to be strictly proportional to the current density suggests that the growth efficiency, the density of the film and the anodising ratio are essentially identical for the four samples[1]. Under such conditions, dV/dt is given by:

$$\frac{dV}{dt} = \frac{\eta}{AR}\frac{M_m}{zF\rho}i \tag{3.2}$$

Considering a typical value for the anodising ratio (2 nm/V) and for the density of the oxide film (3.1 g/cm^3 for amorphous anodic TiO_2 [57, 156]), the corresponding efficiency value calculated from Eq.3.2 is slightly over 100%. Hence, it is likely that, over the limited range of 6 to 15V, the four oxide films have grown with a 100% efficiency. Under that assumption and, keeping 3.1 g/cm^3 for the film density, an anodising ratio of 1.85 nm/V is calculated, which is well within the range of reported values. Using this newly calculated AR value, we can calculate the growth efficiency values for the first stage, from the corresponding dV/dt values. The latter are presented in Table 3.1.

At some stage during the growth of the film, small voltage fluctuations are observed, which might correspond to the first breakdown events on weak spots of the films. On Fig.3.5b, the V-t curves from Fig.3.5a have been reproduced, with markers added on each curve to the data points where fluctuations are ob-

[1]This might not be fully correct since, as discussed in section 1.2.4, the anodising ratio is usually observed to depend on the current density. The current density is indeed directly related to the electric field in the film though the high-field relationship [167]. Within that framework, plots of $1/i$·dV/dt vs lni allow extracting the high field coefficients i_o and β [10]. In addition, other factors come into play which have a direct influence on the effective density of the film and therefore modify the thickness-to-voltage ratio. However, in the current density range considered here, assuming a constant AR value independent of i should provide a reasonable approximation.

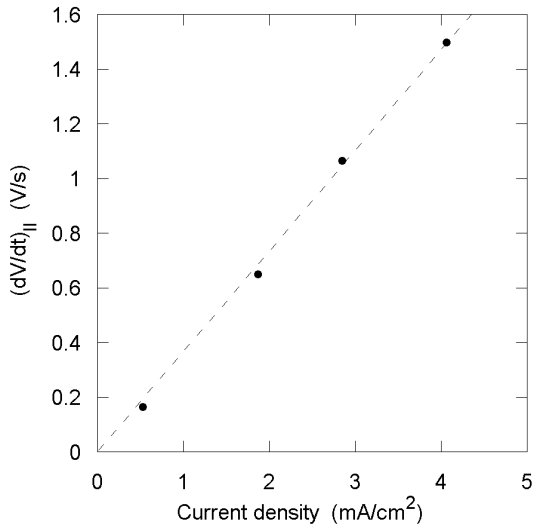

Figure 3.6: Slope of the V-t curves presented on Fig.3.5 in the range of 6 to 15V, plotted as a function of the current density.

served. As a criterion for identifying the V-fluctuations, we have considered a local decrease of the cell voltage between two consecutive data points as indicative for a fluctuation. This appeared to be an adequate criterion, excepted for the sample anodised at 1.9 mA/cm^2 for which the overall decreasing tendency of the cell voltage between 80 and 160s is interfering. The first fluctuation is observed at 21V for the sample anodised with the lowest current density, then the second is observed at 36V after which fluctuations become more abundant. For the 1.9 mA/cm^2 and 2.9 mA/cm^2 samples, fluctuations are regularly observed from, respectively, 31V and 56V on. Oscillations on the 4.1 mA/cm^2 sample start at 59V and are more abundant from 64V on. Hence, the first voltage fluctuations are observed to take place at a lower V when the anodisation is carried out at a lower current density.

As to the stress·thickness evolution, the low- and high-efficiency stages correspond to two distinct stages as well. This is illustrated on Fig.3.7 showing on the same graph the time-evolution of the cell voltage and of the stress·thickness product for the sample anodised at 2.9 mA/cm^2. The first (low-efficiency) stage is observed to correspond to the development of compressive stresses while the second (high-efficiency) stage is characterised by weakly tensile instantaneous stresses. A compressive maximum is observed at the transition between both stages. Comparing the stress·thickness vs. time traces for the 4 current den-

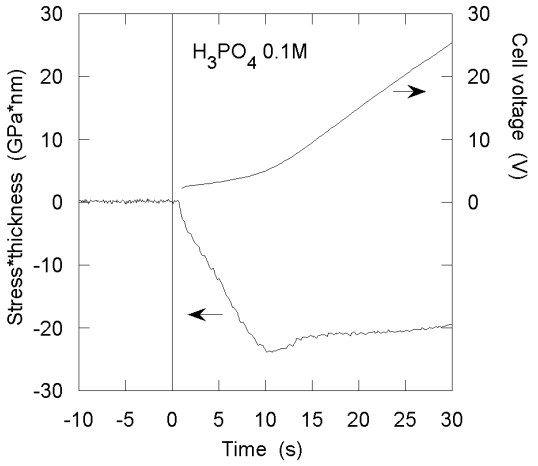

Figure 3.7: Time-evolution of the stress·thickness product and of the cell voltage at the beginning of anodisation for the sample anodised at 2.9 mA/cm^2. Two distinct stages can be identified, characterised, respectively, by a low-efficiency and large compressive stresses and by a high efficiency and weak tensile stresses.

sities (see Fig.3.8 or the tabulated values in Table 3.1 and Table 3.2), it is observed that the duration of the first stage increases with decreasing current density and that the stress·thickness value at the compressive maximum is more compressive for samples grown more slowly. As a general trend, the average stress is less compressive at higher anodisation current densities. For the sample anodised at 4.1 mA/cm^2, the average stress is even tensile from 50s on. From Fig.3.8, is can be observed as well that the stress·thickness evolution for the sample anodised with the lowest current density does not follow exactly the same trend as the other three samples in the first stage. The stress·thickness values measured at the compressive maximum as well as the slope of the stress·thickness vs. time curves in the first stage are listed in Table 3.2. Plotting the stress·thickness data for the 4 samples with V as the independent variable instead of time reveals three remarkable features, as illustrated on Fig.3.9:

- the compressive maximum is observed to take place at a given value of the cell voltage (6.0±0.7V) independent of the current density (see Fig.3.10)
- the slope of the curve in the second stage appears to be constant over the whole voltage range from 8V to 50V
- the slope value in the second stage appears to be independent of the

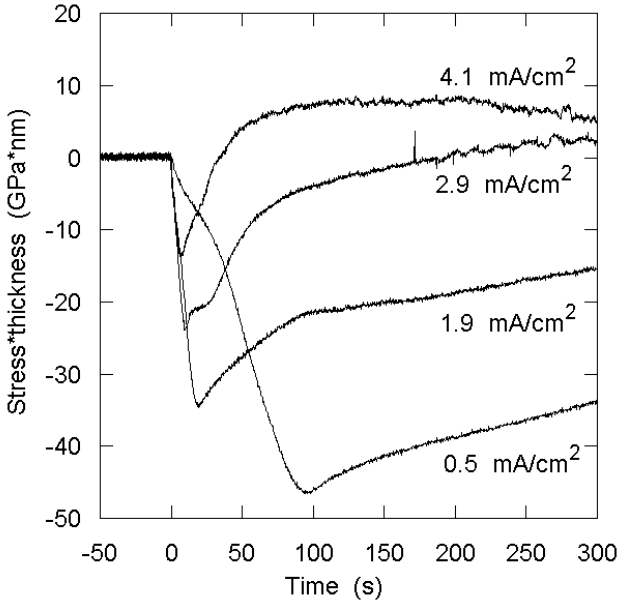

Figure 3.8: Time-evolution of the stress·thickness product accompanying the 4 anodisation experiments presented on Fig.3.5.

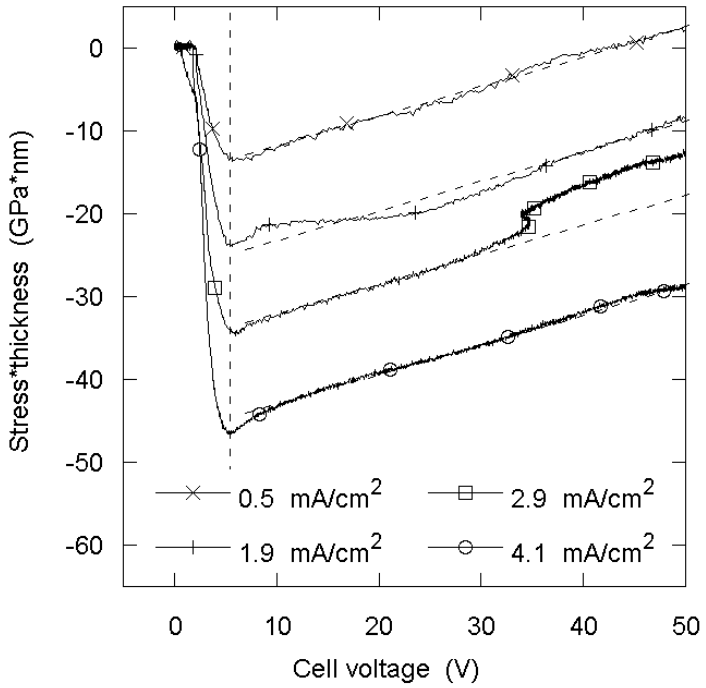

Figure 3.9: Evolution of the stress·thickness product with the cell voltage obtained from the combination of the data from Fig.3.5 and Fig.3.8.

current density.

The slope values of the stress·thickness vs. V curves, obtained by fitting the data over the range of 8 to 50V (8 to 30V in the case of the sample anodised at 1.35mA/cm^2), are listed in Table 3.3, together with the corresponding instantaneous stress values calculated using the AR value of 1.85 nm/V previously extracted from the slope of the V-t curve. The 4 stress values are statistically identical and their average value is equal to 198±5 MPa. This 'raw' stress value must be corrected for the contribution from the consumption of the Ti substrate, as discussed in section 2.3.3. As to the latter, the average stress in the Ti layer for this particular Ti batch was measured to amount to 105 MPa (tensile). Considering again a value of 3.1 g/cm^3 for the density of the oxide film, the corresponding Pilling-Bedworth ratio for the electrochemical oxidation Ti into TiO_2 is equal to 2.42. The equivalent instantaneous stress corresponding to the Ti consumption then amounts to: 42 MPa. Hence, after correction, the total stress experienced by the oxide film during the second growth stage

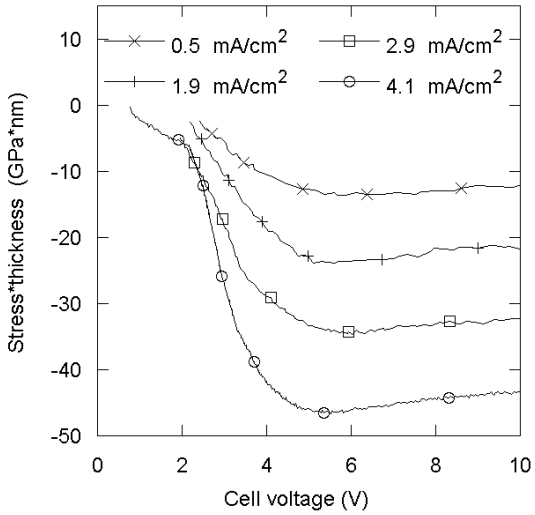

Figure 3.10: Enlarged view of Fig.3.9 in the range of 0 to 10V, showing the stress·thickness in the first stage and the transition to the second stage.

can be evaluated as 241±5 MPa. The corrected values have been added in Table 3.3. The corrected stress values still encompass two contributions, the reversible electrostriction stress and the irreversible intrinsic stress, as discussed in chapter 1. The magnitude of the reversible stress has not been quantified explicitly for this series of experiments but this will be the subject of chapter 4. According to experimental measurements from the literature, the compressive contribution from electrostriction is expected to be on the order of -200 MPa [199]. Based on this value, the magnitude of the tensile intrinsic growth stress in the film is estimated to lay around 440 MPa. It should be noted that the deviation of the stress·thickness vs thickness curve observed around 30V for the sample anodised at 2.9 mA/cm^2 is likely to be an artefact associated with the local V-maximum of the V-t curve.

Discussion:

The discussion will focus on the observations in relation to the second tensile stage. The origin of the first compressive stage is likely to reside in some unidentified side-reaction, possibly related to impurities present in the Ti substrate. From the observations described above, we can conclude that, from 6V on, the oxide film grows with a high-efficiency and a constant tensile instantaneous stress of 241±5 MPa. The tensile sign of our measured stress agrees with the observations reported by Archibald [13], Sahu et al. [199] and Nelson et al.

Current density mA/cm^2	$(\sigma \cdot h_f)_{max}$ [GPa·nm]	$\left(\frac{d\ (sigma \cdot h_f)}{dt}\right)_I$ [GPa·nm·s^{-1}]
0.53	-46.4	-0.54
1.87	-34.5	-1.95
2.85	-23.8	-2.4
4.06	-13.5	-2.04

Table 3.2: Magnitude of the stress·thickness product measured at the compressive maximum and of the slope of the stress·thickness vs. time curve in the first stage.

Current density mA/cm^2	$\left(\frac{d\sigma \cdot h_f}{dV}\right)_{II}$ [GPa·nm·V^{-1}]	σ_{II} uncorrected [MPa]	σ_{II} corrected [MPa]
0.53	0.369	199	241
1.87	0.356	203	245
2.85	0.350	189	231
4.06	0.370	200	242
average	0.361	198±5	240±5

Table 3.3: Magnitude of the slope of the stress·thickness vs. V curve in the high-efficiency stage and corresponding stress values, respectively before and after subtracting for the contribution of the metal consumption.

[164], which all correspond to galvanostatic or potentiodynamic growth. Quantitatively speaking, our stress value is in reasonable agreement with the 150 MPa reported by Archibald for anodisation in fluoride-free electrolytes. This is the only stress value available for comparison as the other two references by Sahu and Nelson do not report stress values.

The instantaneous stress developing in our TiO_2 film was observed to be remarkably independent of the current density over the range investigated (0.5 to 4 mA/cm^2). To the best of our knowledge, the influence of the current density on the instantaneous stress has never been reported before in the case of anodic TiO_2 and this study appears to be the first one dealing with that question. Such studies have been reported on Al_2O_3, studied by Bradhurst and Leach [31], and ZrO_2, studied by Archibald [12]. In both cases, a dependence of the stress on the current density was observed in some current density ranges, as illustrated on Fig.1.40 and Fig.1.41. These studies, however, have been carried out over a wider range of current densities (more than two orders of magnitude in the case of ZrO_2 and one order of magnitude in the case of Al_2O_3). For both metal oxides, the stress is indeed observed to be rather insensitive to the current density in some current density ranges, respectively at high current density in the case of Al_2O_3 and low current density on ZrO_2.

The onset of the voltage fluctuations, illustrated on Fig.3.5b does not seem to be correlated to the stress·thickness evolution. Indeed, for the lowest two current densities, abundant fluctuations are already observed in the range of 8 to 50V over which the instantaneous stress remains constant. In contrast, for the largest two current densities, the fluctuations are observed only beyond that V-range. This seems to discard any influence of the fluctuations on the overall observed stress evolution. And conversely, the voltage fluctuations do not seem to have a mechanical origin as the average stress values are very different for the four samples when the first V-fluctuation is observed. For the lowest two current densities, no noticeable features are visible on the stress·thickness vs V trace at V-values corresponding to the fluctuations. This might indicate that the fluctuations are associated with very local phenomena (isolated breakdown sparks, for instance) which do not significantly affect the macroscopic behaviour of the sample. In contrast, for the two samples anodised at 2.9 and 4.1 mA/cm^2, when the cell voltage increases over 50V, a very clear increase of the noise on the curvature signal is observed on Fig.3.8, which could indeed be indicative for the voltage fluctuations regime.

It is worth noting that the cell voltage was observed to keep a constant slope corresponding to 100% efficiency over a limited range of V. After that, the slope of the curve progressively decreases, indicating a decrease of the growth efficiency. In contrast, the slope of the stress·thickness vs. V curves was observed

to keep a constant value over a much wider V-range extending over 50V. Hence, the oxide film continues growing with the same, constant, instantaneous stress even when the growth efficiency starts decreasing. This indicates that the stress is not directly correlated with the growth efficiency and that, in contrast to the first stage, the side-reaction(s) responsible for the decrease of the efficiency do not affect noticeably the stress evolution.

According to the model proposed by Nelson and Oriani [164] introduced in section 1.3.1, the sign of the stress can be interpreted in the following way: the overall curvature of the sample is mainly influenced by the strain at the metal/film interface, the latter being determined by the respective values of the Pilling-Bedworth ratio and the transport numbers. Indeed, let us consider a metal electrode anodised with a current density i. A number of moles of metal n_m will be ionised per unit time at the metal/film interface, leading to the formation of a number of moles n_{ox} of oxide. A fraction of the oxide film will be formed at the metal/film interface while the remaining fraction (equal to t_c) is formed at the film/electrolyte interface. The corresponding volume of metal consumed and the total volume of oxide formed are given by, respectively, v_m and v_{ox}. Hence, the strain $u_{m/f}$ at the metal/film interface will be given by:

$$u_{m/f} = \frac{t_a v_{ox} - v_m}{v_m} = t_a PBR - 1 \tag{3.3}$$

Considering Eq.3.3, compressive or tensile stresses are predicted depending on whether t_a is larger or smaller than the critical value $1/PBR$. According to this model, the tensile sign of our measured stress value would require an anionic transport number smaller than 0.41, assuming that the film is amorphous with a density of 3.1 g/cm^3. Experimental values for t_a can be found in the work of Khalil et al. [110] or Habazaki et al. [74]. The former authors report a value of t_a of 0.65 for anodisation at 6 mA/cm^2, which decreases down to 0.61 when the current density is increased to 50 mA/cm^2. Habazaki et al. have measured a value of 0.61 as well for t_a for anodisation of sputter-deposited Ti films at 5 mA/cm^2. The good agreement between those values, measured at different current densities and on films grown on different Ti substrates, suggests that the value of t_a is not too sensitive to the experimental conditions. These are, however, average values measured on films with thicknesses over 40 nm, which do not provide information as to whether the transport numbers varies in the course of the growth or remains essentially constant. It should be noted that those values are far from the critical t_a^o. Hence, assuming that the t_a values in our case are similar to those measured by Khalil and Habazaki, compressive stresses would be expected, based on the criterion proposed by Nelson and Oriani. The critical threshold t_a^o becomes closer than the literature t_a values if a larger density is assumed for the oxide film. However, to predict tensile stresses in the film, a density larger than that of crystalline rutile ($\rho = 4.23$

g/cm^3) would have to be assumed. This suggests that the criterion proposed by Nelson and Oriani is not sufficient to account for the observed stress behaviour in our case. According to the model of Moon and Pyun [159], derived from that of Nelson and Oriani, in order to predict the sign of the stress, not only the proportion of the oxide film formed at the metal/film interface must be taken into account but also the amount of defects (oxygen and metal vacancies) in the film. Within the framework of their model, our tensile stress would be due to the formation of an oxide layer with a large proportion of vacancies adjacent to the metal/film interface. Their model does however not allow for quantitative predictions. As to our observed independence of the instantaneous stress on the current density, it suggests that i has a limited influence on t_a and on the defect concentration. It should be noted that, according to Moon and Pyun, the stressed region in anodic oxide films corresponds to 1 to 3 atomic layers only, hence representing a layer of sub-nm thickness. This hypothesis seems to be quantitatively incompatible with our measured stress values. Indeed, as observed on Fig.3.9, stress·thickness values of the order of several tens of GPa.nm are typically observed. While these values already appear to be quite large if the whole thickness of the film is stressed, they become completely unrealistic if they correspond to a layer of sub-nm thickness.

Conclusion

Under galvanostatic conditions, stages where the growth efficiency was close to 100% have been observed to correspond to the development of a constant tensile instantaneous stress. While the tensile sign is in agreement with previously reported trends, it cannot be accounted for by the criterion proposed by Nelson and Oriani. This suggests that either this criterion is not sufficient or that the anionic transport numbers in our case differ significantly from the literature values. The magnitude of the tensile growth stress was observed to amount to 241 MPa, which is likely to correspond to an intrinsic growth stress of about 440 MPa, assuming a reversible 200 MPa electrostriction stress. The stress value was observed to be independent of the current density in the range of 0.5 to 4.1 mA/cm^2. The stress evolution does not seem to be correlated with the appearance of V-fluctuations, which suggest that the latter do not have a mechanical origin. For the largest two current densities, the V-fluctuations regime is clearly identifiable from the stress evolution as a significant increase of the noise on the curvature signal. When the growth efficiency falls below 100%, different behaviours have been observed on Fig.3.9 as compared to Fig.3.4. For the series of experiments presented on Fig.3.9, the decrease of the growth efficiency was not observed to perturb the tensile stress evolution while, in the case of the series of experiments presented on Fig.3.4, the efficiency drop leading to a V-plateau was observed to be accompanied by a transition from

tensile to compressive stress evolution. Such transitions are discussed further in the next section.

3.3 Growth stress transitions

This section focuses on growth stress transitions. Two types of characteristic transitions are frequently observed under galvanostatic conditions. The first type corresponds to a decrease of the growth efficiency, corresponding for instance to the onset of the oxygen evolution reaction, and typically reveals itself as a transition from tensile to compressive instantaneous stress evolution. A typical example of such transition can be found in the experiment presented on Fig.3.4. The second type of transition is typically observed at the end of a low-efficiency stage and is accompanied by a compressive maximum. An example of this second type of transition was shown on Fig.3.9. In a first subsection, experimental observations on growth stress transitions are presented. The described experiment was selected as a representative example owing to the fact that the two types of transitions are observed successively. In complement to the stress measurements, TEM analysis has been carried out in order to provide insight into the microstructural evolutions accompanying the growth. In the second subsection, growth stress transitions associated with potentiostatic aging are discussed. Finally, a common discussion of growth stress transitions is provided in the third subsection.

3.3.1 Transitions observed under galvanostatic growth conditions

Experimental

This series of experiments has been carried out on samples from the PTi batch, prepared as described in section 2.3.1. The samples have been anodised at 4.0 mA/cm^2 in 1.0 M H_2SO_4. The experimental cell has been described in chapter 2.
Cross-sectional TEM Samples have been prepared by ion-milling. The samples were investigated in a Philips CM30 FEG-TEM operated at 300keV and provided with a post-column GIF200 system for energy-loss spectroscopy. This was done at the Laboratory of Electron Microscopy for Materials Science (EMAT) from the University of Antwerp, with the help of Prof. Nick Schrijvers and Dr. He Tian.

Results on the stress evolution

Two types of experiments have been carried out. The first one consisted of a series of 6 continuous galvanostatic anodising experiments carried out under

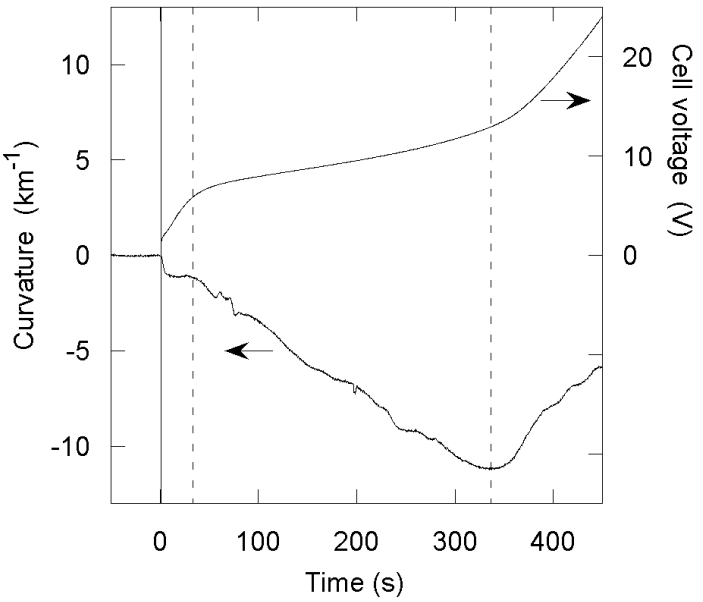

Figure 3.11: Evolution of the cell voltage and of the anode curvature during galvanostatic anodising of Ti thin film electrodes from the PTi batch in 1.0 M H_2SO_4 at 4 mA/cm^2, showing three correlated characteristic stages.

the same conditions, up to different forming voltages (5, 9, 12, 15, 25 and 40V). During each of these experiments, the evolution of the curvature of the anode was monitored continuously. For the second type of experiment, one sample was anodised to a final voltage of 40V under the same conditions as for the six continuous experiments, but the anodisation was interrupted repeatedly. The anodisation was first interrupted when the cell voltage reached 5V, after which it was left at open circuit for 80 seconds. The current was then re-applied to proceed further in the growth process. A second interruption of 80s was then carried out at 9V, then 12V, 15V and 25V. The evolution of the anode curvature was monitored continuously during galvanostatic film formation, as well as during the interruptions at open-circuit. This second type of experiment aimed at assessing the influence of interrupting the anodisation on the growth of the oxide film and therefore providing insight into the reversibility of the growth instabilities. Results from the two types of experiments are presented separately below.

A. Continuous experiments

A typical result obtained during continuous galvanostatic anodisation is presented in Fig.3.11. Superimposed on the same time scale is the evolution of both the cell voltage and the curvature signal. Three distinct stages can be observed in the evolution of the cell voltage: a first (short) stage characterised by a large growth efficiency followed by a low-efficiency plateau, then finally a return to high-efficiency conditions. Therefore, two transitions are observed between, respectively, the first and second and the second and third stages. Remarkably, these three stages correspond to three characteristic stages of the curvature evolution as well. Each stage will be described more extensively in the following paragraphs. It should be noted that the V-t curve corresponding to this experiment is completely different from the one presented on Fig.3.5 for the anodisation at 4 mA/cm^2. This is primarily attributable to the different Ti substrates used for the two experiments but also to the fact that a different electrolyte was used (1.0 M H_2SO_4 instead of 0.1 M H_3PO_4). However, as discussed previously, for a given set of experimental conditions and a given Ti batch, the V-t behaviour is observed to be highly reproducible.

First stage:
Figure 3.12a shows the evolution during the first 25 seconds of anodising of both the cell voltage and the stress·thickness product, the latter being obtained from the curvature evolution according to the Stoney equation. After an initial surge to 1.46V, attributable to the presence of a native oxide layer on the electrode surface [74], the slope of the V-t curve rapidly reaches a constant steady-state value. The cell voltage then increases at that constant rate up to a given value (V_{II}) around 4V. After V_{II}, the rate of increase of the cell voltage slows down significantly. Therefore, we have considered V_{II} as the end of the first stage. This behaviour was reproducibly observed for all 6 samples. The slope values for the V-t curve in the linear portion, as measured for each of the six experiments, are listed in Table 3.4. An average value of 170±40 mV/s was obtained.

As to the stress·thickness evolution, a rapid increase in the compressive direction is observed at the very beginning of anodisation, corresponding to the initial V-surge. At that point, the stress·thickness product has reached a value of 4.0±0.5 GPa·nm. In the region corresponding to the constant $\mathrm{d}V/\mathrm{d}t$, the stress·thickness product evolves in the compressive direction at a much reduced rate. The slope of the stress·thickness vs. V curve in this region is observed to vary significantly from one sample to the other, being in the range of -0.32 GPa·nm/V to -1.34 GPa·nm/V.

Second stage:
As illustrated on Fig.3.12b, the slope of the V-t curve in the second stage first decreases progressively, then reaches a constant steady-state value equal to 18±1 mV/s around 8V, after which the growth proceeds with that rate up

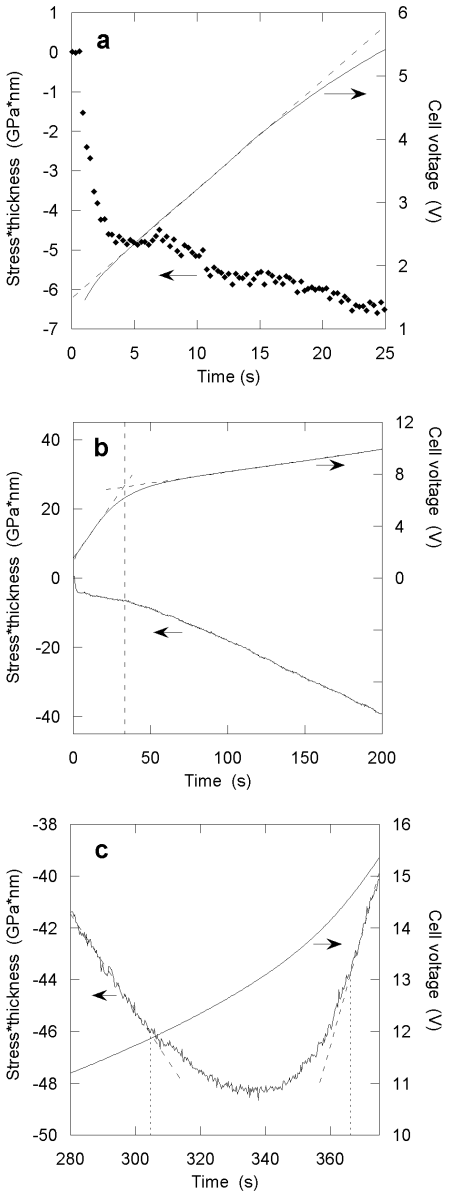

Figure 3.12: Typical evolution of the cell voltage and of the stress·thickness product during (a) the first growth stage, (b) the first and second stage and (c) the transition between the second and third stage, with the associated compressive maximum.

to 10V. The steady-state values measured for $\mathrm{d}V/\mathrm{d}t$ during the second stage for each experiment are included in Table 3.4 as well. The latter can be related to the anodising growth efficiency (η) according to Eq.3.2. Provided that AR does not change from stage I to stage II, the ratio between the $\mathrm{d}V/\mathrm{d}t$ values of stages I and II provides an estimation of the ratio of the growth efficiencies. As calculated from Table 3.4, an average efficiency ratio of 11±2% is thus obtained. This marked decrease of the growth efficiency is well-known to be attributable to a major fraction of the total current in the second stage being consumed in side-reactions, the main one being oxygen evolution [49]. If the efficiency is assumed to be close to 100% in the first stage, as usually observed before the onset of the oxygen evolution reaction [57], the growth efficiency in the second stage is around 11%, which is in agreement with literature values [49].

From the point of view of the stress·thickness product, the second stage is observed to correspond to the development of large compressive stresses. The evolution of the stress·thickness product as a function of V for the six experiments has already been presented on Fig.3.2, showing a fairly good reproducibility of the stress evolution. The corresponding constant instantaneous stress values for the 6 experiments can then be quantified from the slope of the stress·thickness vs. V curves, given in Table 3.5, and the anodising ratio. As to the latter, the AR value for the samples investigated in this study could not be determined satisfactorily, as will be discussed later on in this chapter. Therefore, all the thickness values in this section have been calculated based on the assumption of a constant AR equal to 2.7 nm/V. The latter value had been measured during a previous study on samples grown in the same electrolyte but under potentiodynamic conditions. Despite the fact that the growth modes are different, we expect this assumption to be reasonable, owing to the fact that the imposed growth rate of the potentiodynamic study (100 mV/s) was comparable to the one observed in this study. For this value of AR, the constant instantaneous stress values for the second stage are summarized in Table 3.5.

Third stage:
When anodisation is pursued over 10V, at some point, the cell voltage starts to increase more rapidly again (cf. Fig.3.11). The $\mathrm{d}V/\mathrm{d}t$ values measured for this third stage are equal to, respectively, 133.2±0.2 mV/s and 233.5±0.3 mV/s for the samples anodized to 25V and 40V. As seen in Table 3.4, these values are close to the ones measured for the first stage, which suggests that the growth efficiency returns to its initial high value in this third stage.

Remarkably, this $\mathrm{d}V/\mathrm{d}t$ transition is observed to correspond to a change from compressive to tensile instantaneous stress. As seen in more detail on Fig.3.2, the compressive maximum is observed to take place in each case at a

	$(\mathrm{d}V/\mathrm{d}t)_I$ [mV/s]	$(\mathrm{d}V/\mathrm{d}t)_{II}$ [mV/s]	η_I/η_{II} [%]	$(\mathrm{d}V/\mathrm{d}t)_{III}$ [mV/s]
5V	222.8±0.5	-	-	-
9V	174.6±0.4	17.27±0.01	9.9	-
12V	132.1±1.0	18.30±0.01	13.9	-
15V	172.4±0.3	16.85±0.01	9.8	-
25V	132.0±1.0	15.89±0.01	12.0	133.2±0.2
40V	195.4±0.4	19.97±0.02	10.2	233.5±0.3
average	172±36	18±2	11.2	-
interrupted	238.7±0.7	23.78±0.02	10.0	290.0±0.2

Table 3.4: Measured $\mathrm{d}V/\mathrm{d}t$ values for the 3 growth stages. The ratio of the growth efficiency in the second stage (η_{II}) to that in the first stage (η_I), calculated as the ratio of the $\mathrm{d}V/\mathrm{d}t$ slopes, has been included as well.

given value of the cell voltage, equal to 13.4±0.5V. The stress·thickness transition is also observed to be spread over a relatively long time-period: as seen in Fig.3.12c, it takes approximately one minute for the stress·thickness product to evolve from a constant compressive slope to a constant tensile slope. This observation suggests that the phenomenon underlying this transition is a progressive transition and not a sudden one. After the compressive maximum, the tensile slope of the stress·thickness vs. V curve decreases steadily with increasing V (cfr. Fig.3.2), from 1400 MPa directly after the compressive maximum to 480 MPa near 40V. The measured stress·thickness values at the compressive maximum are, respectively -62.4 GPa·nm, -48.3 GPa·nm and -59.3 GPa·nm for the samples anodised to 15, 25 and 40V.

B. Interrupted experiment

The time-evolution of the curvature and of the cell voltage for the interrupted experiment is presented on Fig.3.13 The curvature signal exhibits a series of discontinuities, corresponding to the successive current interruptions and re-applications. It can be observed that, after each interruption, the cell voltage does not immediately recover to its value prior to the interruption, but rather starts from a value around 4V only. A similar observation has been reported by Archibald [13] and by Di Quarto et al. [51]. According to the latter, this might indicate that electrolyte has been penetrating inside the oxide film. From 4V on, the cell voltage increases progressively at a rate which decreases with increasing number of interruptions. For instance, after the interruption at 25V, it takes about 200s before the cell voltage reaches 25V again. The cell voltage values measured when the current is re-applied, directly after each interruption, are summarized in Table 3.6. Based on Fig.3.13, we have also provided the "reconstructed" κ-t and V-t curves in Fig.3.15. The latter have been ob-

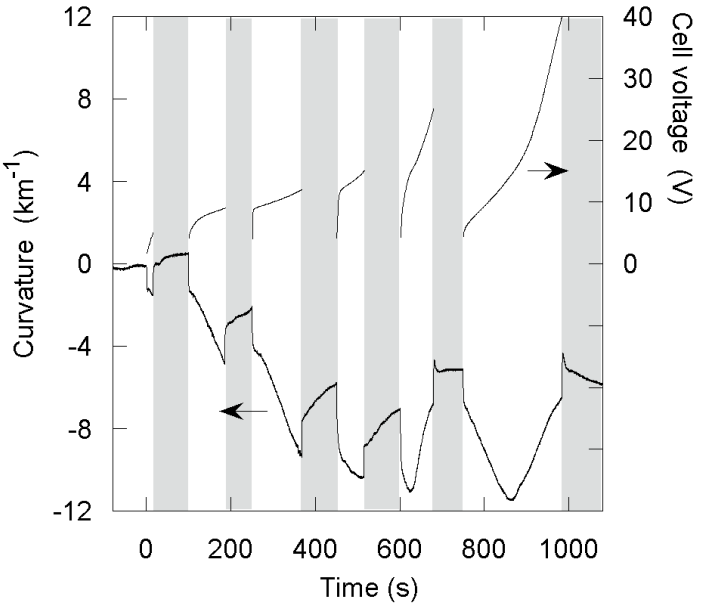

Figure 3.13: Time-evolution of the cell voltage and of the anode curvature during the interrupted anodisation experiment carried out in 1.0 M H_2SO_4 at 4.0 mA/cm^2. The shaded regions correspond to the open-circuit interruptions.

	Constant slope of the stress·thickness vs. V curve in stage II [GPa·nm/V]	$(\sigma_{ox})_{II}$ [GPa]
5V	-	-
9V	-12.00±0.07	-4.4 ± 0.4
12V	-11.05±0.05	-4.1± 0.4
15V	-12.22±0.02	-4.5 ± 0.5
25V	-8.80±0.06	-3.3 ± 0.3
40V	-12.24±0.02	-4.7 ± 0.5
interrupted	-9.07±0.01	-3.4 ± 0.3

Table 3.5: The first two columns give, respectively, the constant slope values measured in the second stage for the stress·thickness vs. V curves presented on Fig.3.2, and the corresponding constant instantaneous stress values $(\sigma_{ox})_{II}$.

interruption	5V	9V	12V	15V	25V	40V
Cell voltage directly after re-application of the current [V]	4.2	4.1	4.2	4.3	4.4	-

Table 3.6: Cell voltage values measured during the interrupted experiment directly after re-application of the current.

tained by first removing the curvature and V-data corresponding to the time intervals when the anodisation was interrupted (shaded zones in Fig.3.13), and then by removing the curvature and V-data recorded after re-application of the current and corresponding to the time interval when the cell voltage had not yet recovered to its value measured just before the interruption. In that way, a continuously increasing V-curve was obtained. The reconstructed V-t and κ-t curves are observed to be qualitatively identical to the one measured for the continuous experiments. In particular, the three distinct stages of both the cell voltage and the curvature evolution already identified for the continuous experiment are again observed. This is believed to be evidence that the repeated interruptions of the anodizing process do not significantly affect the growth of the oxide film. In other words, conclusions drawn for the interrupted experiment can be safely extended to the continuous growth process as well.

Similarly as for the continuous experiments, the steady-state $\mathrm{d}V/\mathrm{d}t$ values corresponding to the three stages of the interrupted experiment have been measured from the reconstructed V-t data and added for comparison in the last row of Table 3.4. The constant instantaneous stress value measured for the second stage was added to Table 3.5 as well. All these values are comparable to those measured for the continuous experiments. In the following paragraphs, some additional observations during the interrupted experiment are described in more details.

First stage:
Figure 3.14a shows the evolution of the cell voltage and of the stress·thickness product during the first 25s of the anodisation. The behaviour is observed to be similar to the one for the continuous experiments, shown in Fig.3.12a, with also a similar value obtained for V_{II} (-4.07V). By comparing the curvature values measured respectively under conditions of applied field and under open-circuit conditions right after the interruption at 5V, it can be concluded that the average internal stress in the film at 5V is equal to -290±50 MPa, which arises from the combination of a reversible, field-induced, compressive electrostriction stress equal to -370±50 MPa and an irreversible, growth-induced, tensile stress equal to 79±20 MPa. Interestingly, this V_{II} value is also equal to the average

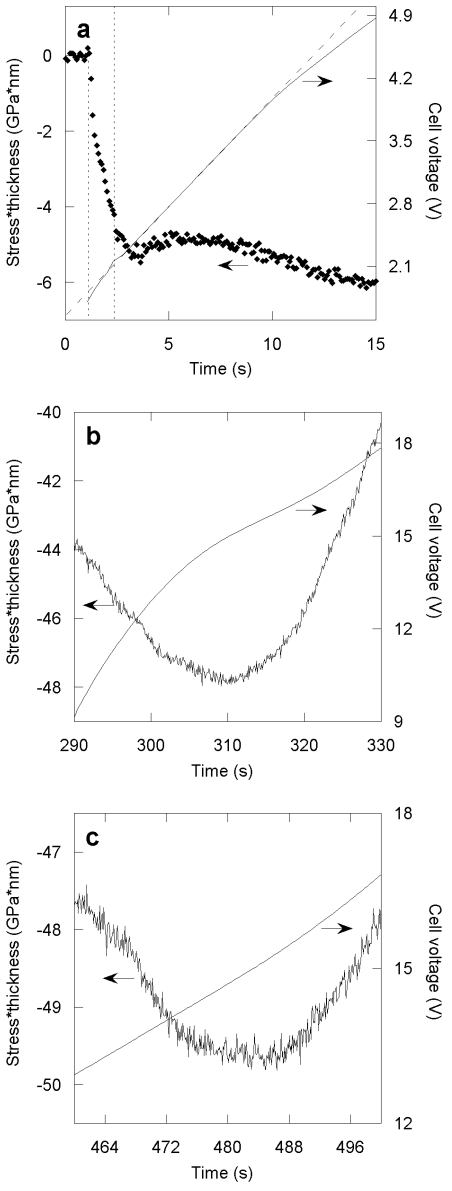

Figure 3.14: Evolution of the cell voltage and of the stress·thickness product corresponding to (a) the first growth stage and (b) and (c) the two successive compressive maxima during the interrupted experiment.

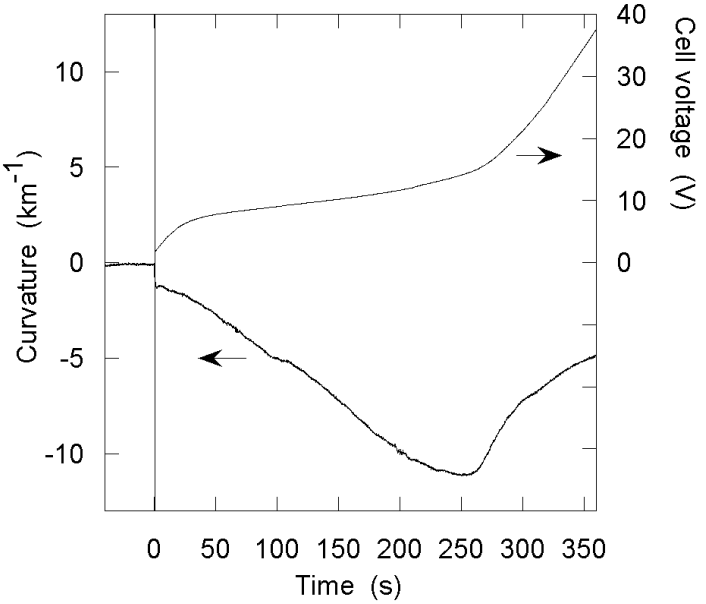

Figure 3.15: Reconstructed evolution of the cell voltage and of the anode curvature for the interrupted experiment, constructed from Fig.3.13.

value of the voltage directly after each interruption (cfr. Table 3.6), which is equal to 4.2±0.2V.

Second and third stages:
The most important observation regarding the interrupted experiment is that the compressive maximum and the corresponding transition from compressive to tensile instantaneous stress were observed twice during the interrupted experiment. Indeed, as seen in Fig.3.13, after re-applying the current after the interruption at 15V, the curvature signal changes for the first time from a compressive to a tensile evolution, while the cell voltage increases up to 25V. Then, when the current is re-applied after the interruption at 25V, the cell voltage starts to increase again from 4.4V on, and the curvature first starts evolving in the compressive direction again. As the cell voltage increases, the curvature signal passes through a second compressive maximum. The presence of two consecutive compressive maxima indicates that the growth instability responsible for the compressive maximum should be a reversible one. In both cases, the compressive maximum takes place when the cell voltage reaches 15.0V, as illustrated on Figures 3.14b and 3.14c, but this value is different from the one measured in the case of the continuous experiments (13.4±0.5V). The stress·thickness values at the compressive maximum are, respectively, -48.0 and -49.5 GPa·nm for the first and second maximum. This is comparable to the value measured for the continuous experiment carried out to 25V, but about 20% lower than the value measured for the other continuous experiments. It can be noted that the constant instantaneous stress value measured in the second stage for the interrupted experiment is also similar to the one measured for the continuous experiment carried out to 25V (cfr. Table 3.5). Finally, the tensile instantaneous growth stress in the third stage has been assessed from the slope of the reconstructed stress·thickness curve plotted as a function of V (Fig.3.16). Similarly as for the continuous experiments, the stress decreases progressively as V increases, from a value of about 1300 MPa directly after the compressive maximum to 430 MPa at 40V. These values are similar to the ones obtained for the continuous experiments.

Results from the TEM investigation

Two samples have been investigated by TEM. The first one is the sample anodised to 15V, for which anodisation was interrupted at the compressive maximum, and the second one has been anodised up to 40V, hence beyond the compressive maximum. Fig.3.17 shows a bright-field cross-sectional TEM image of the 15V sample. From this picture, a thickness of 26±5 nm has been measured. As can be observed, the surface of the sputtered Ti thin film is very rough, resulting in a roughness of oxide film of the the same order of magnitude

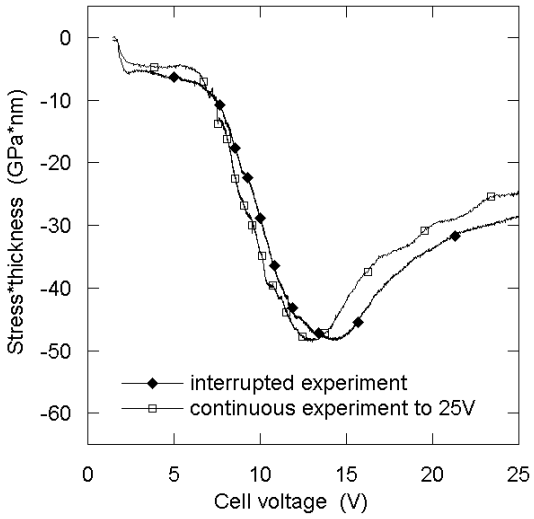

Figure 3.16: Reconstructed evolution of the stress·thickness product with cell voltage for the interrupted experiment compared to the one observed for the continuous experiment carried out up to 25V.

as the film thickness, which renders observation more complicated. From EELS measurements, it was confirmed that the oxide film is essentially composed of TiO_2. Indeed, TiO_2 can be identified clearly in ELNES by the typical splitting of the L_2 and L_3 edges of Ti, as shown on Fig.3.18. A high-resolution image of the film is shown on Fig.3.19. Small crystallites are observed, having an average diameter of about 10 nm, and dispersed in an amorphous matrix. The lattice fringes are separated by 0.35 nm, which is characteristic for anatase. The latter observation has been confirmed based on the diffraction pattern presented on Fig.3.20. The latter has been recorded on a region of the sample including both the Ti substrate and the TiO_2 film and presents diffraction rings characteristic for anatase (mainly the inner ring of diameter 0.57 $Å^{-1}$) and for hexagonal Ti (rings at 78, 89 and 160 $Å^{-1}$). Crystallites are observed over the whole thickness of the film. The metal/film interface was carefully inspected and no evidence of mechanical failure could be detected, neither in the form of a delamination nor of cracks. As discussed in section 1.2.1, Matykina et al. [154] have demonstrated that intensive oxygen evolution can take place inside anodic TiO_2 films. In addition, Habazaki et al. [76] report TEM evidence that such internal oxygen evolution results in the formation of gas bubbles embedded in the film. In our case, we haven't observed any conclusive evidence for the presence of gas bubbles inside the oxide film.

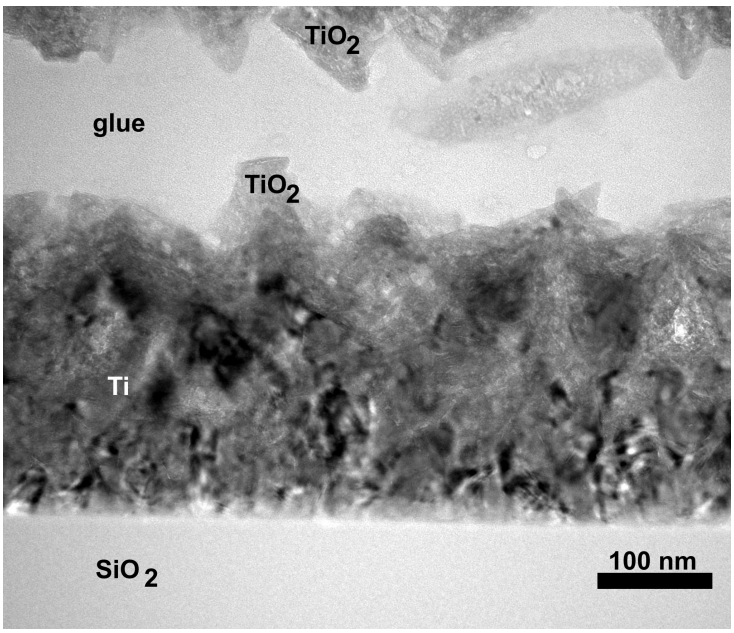

Figure 3.17: Bright-field cross-sectional image of a sample from the PTi batch anodised to 15V in 1.0 M H_2SO_4 with a current density of 4.0 mA/cm^2.

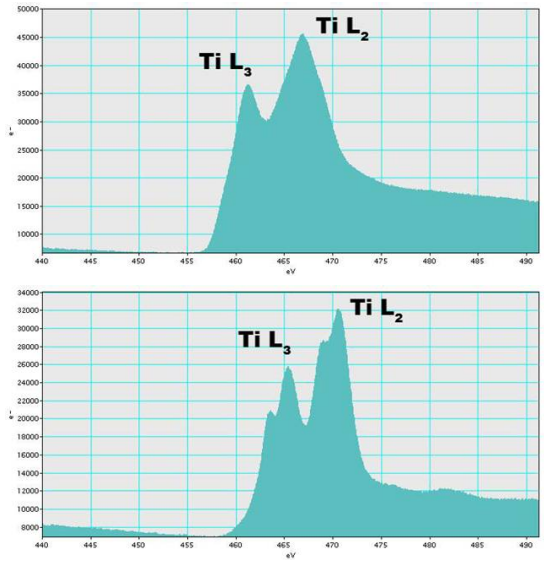

Figure 3.18: EELS spectra recorded for, respectively, the Ti substrate and the TiO_2 layer.

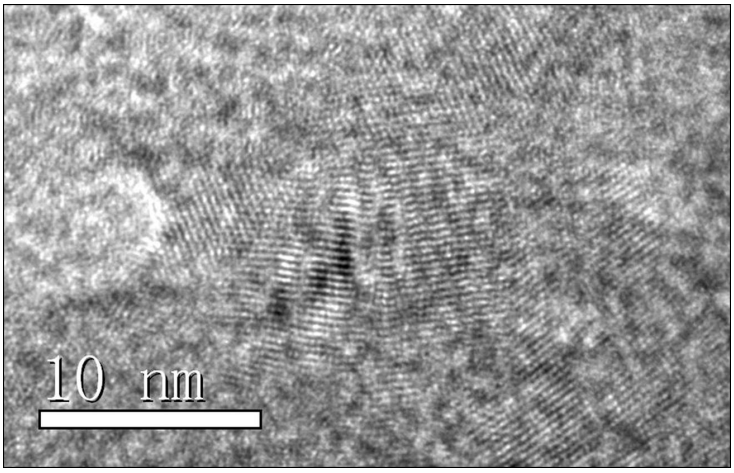

Figure 3.19: High-resolution TEM image of the sample anodised to 15V presented on Fig.3.17, showing characteristic lattice fringes corresponding to the [101] planes of anatase.

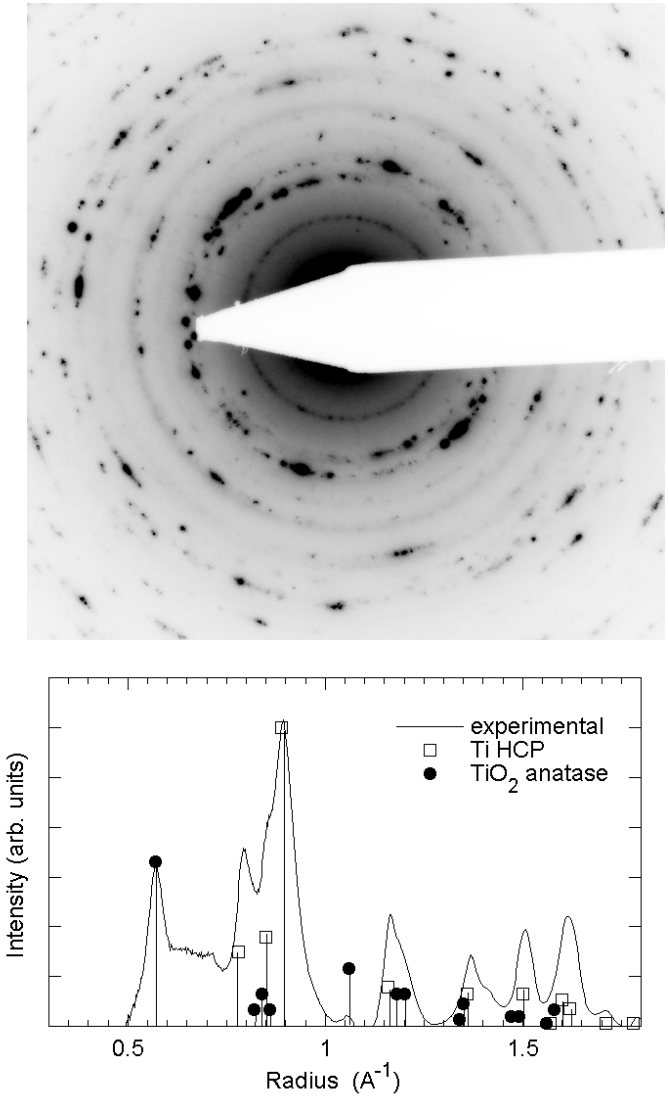

Figure 3.20: Diffraction pattern and corresponding distribution of the diffracted intensity recorded on a region encompassing both the Ti substrate and the oxide film. Rings characteristic for hexagonal Ti and for anatase are identified. This observation is more clearly illustrated on the intensity curve.

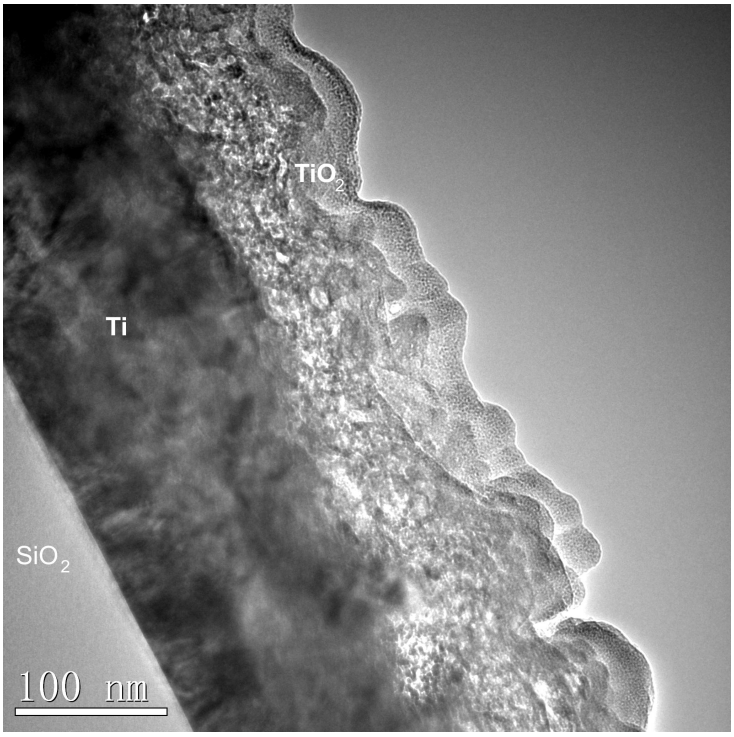

Figure 3.21: Bright-field TEM image of a sample from the PTi batch anodised to 40V in 1.0 M H_2SO_4 at 4.0 mA/cm^2.

Fig.3.21 shows a zero-loss cross-sectional TEM image of the second sample anodised to 40V. The film has a thickness of about 105±15 nm, hence corresponding to an anodising ratio of 2.6±0.4 nm/V. The average roughness of the surface is reduced as compared to the previous sample. This second sample exhibits a microstructure rather different from the one anodised to 15V. In particular, it appears to be composed of two distinct superimposed layers, one polycrystalline layer adjacent to the metal/oxide interface and an outer amorphous layer, similar to that observed on the 15V sample. The thickness ratio of the outer to the inner layers is equal to 42/58. EELS elemental mapping reveals that the two layers present a different composition, with the outer layer containing more oxygen as compared to the inner one (see Fig.3.22). This observation agrees with results reported by Serruys et al. based on RBS analysis and could be due to the outer layer being hydrated. Similar to the 15V sample, no evidence of any mechanical failure or of the presence of gas bubbles could be detected.

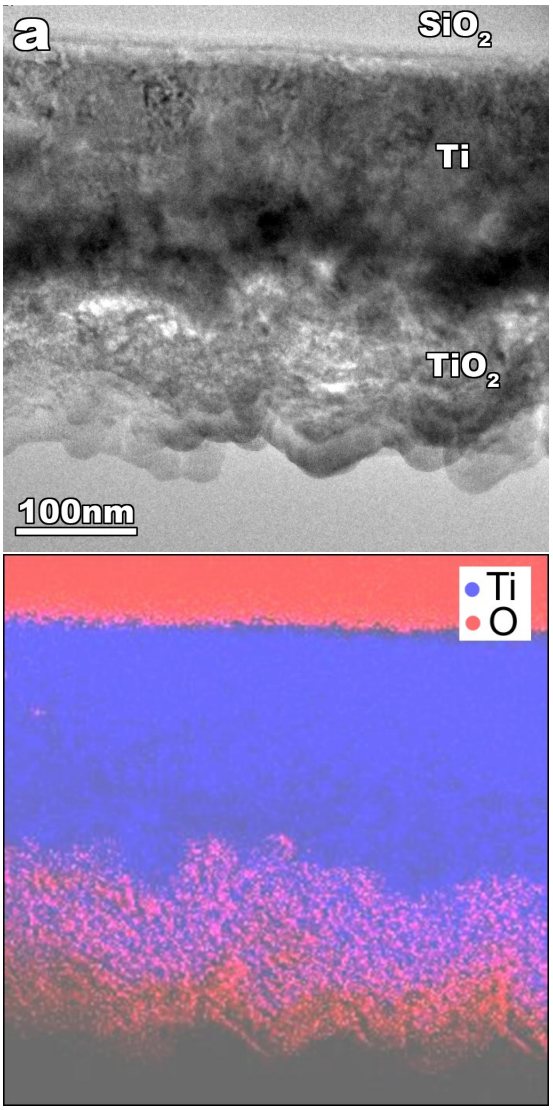

Figure 3.22: The TEM image on top reveals that the anodic oxide film anodised to 40V exhibits a characteristic 2-layer microstructure with a polycrystaline inner layer and an amorphous outer one. The EELS elemental mapping on the bottom shows that the two layers have a different composition, the outer layer being enriched in oxygen.

Discussion

In this section, the following observations have been made. In the first stage, prior to the first transition, analysis of the curvature data, both during the growth and at open-circuit, revealed that the reversible compressive stress appears to be as large as 4.6 times the tensile irreversible stress. These results confirm the already reported conclusion that electrostriction stresses can be rather large in anodic TiO_2 films [205]. In fact, neglecting their contribution can lead to a significant error in the quantification of the intrinsic, growth-induced stress component, and even to an erroneous prediction of its sign. Indeed, in the first stage, while the overall stress in the film is compressive, the intrinsic growth stress is in tension. This tensile sign is in agreement with expectations according to section 3.2.

Two types of growth stress transitions have been illustrated. The first one, observed in relation to the onset of the OER, is characterised by a marked decrease of the growth efficiency and by the development of large compressive instantaneous stresses. The second transition manifested itself as a return to high-efficiency growth and was accompanied by a transition from compressive to tensile instantaneous stress. From the interrupted experiment, it was observed that this second transition is reversible.

TEM investigations revealed that the film anodised up to 15V is composed of anatase crystallites in an amorphous TiO_2 matrix while, at 40V, the film appears to be composed of an inner microcrystalline layer and an outer amorphous layer enriched in oxygen. No evidence of cracks, delamination or cavities suggesting the presence of embedded gas bubbles could be observed.

The origin of the growth stress transitions will be discussed in subsection 3.3.3, after comparison with the stress evolution observed upon potentiostatic aging of a galvanostatically grown film.

3.3.2 Transitions observed upon potentiostatic aging

The first part of this experiment aimed at investigating the influence of performing a potentiostatic aging on the stress evolution in the film. Indeed, as mentioned in section 1.2.2, Ohtsuka et al. [172], Marsh et al. [146] and da Fonseca et al. [43] have provided direct evidence that, when submitted to a potentiostatic aging, anodic TiO_2 films undergo a 'reordering'. According to Ohtsuka, this reordering is accompanied by a decrease of the thickness of the oxide film, hence reflecting a densification. In order to investigate the influence of such a reordering on the stresses in the film, we have performed a supplementary experiment, shown on Fig.3.23, in which a TiO_2 film was grown

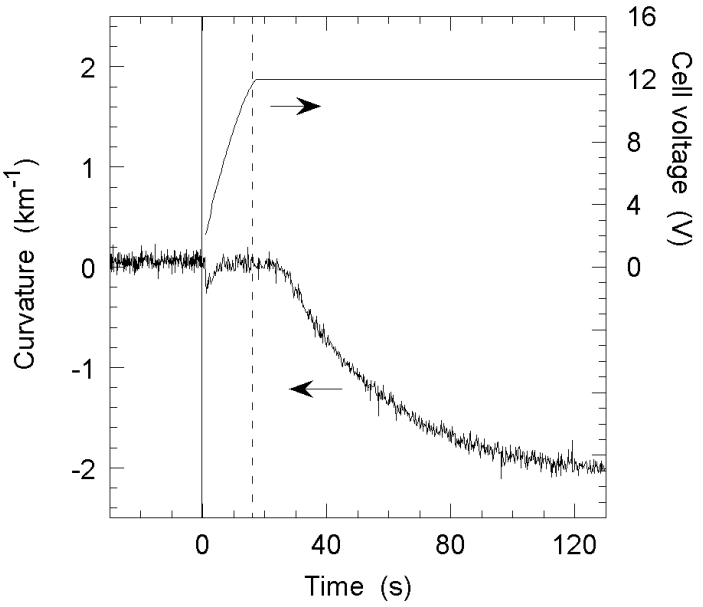

Figure 3.23: Time-evolution of the curvature and cell voltage for a galvanostatic anodisation experiment carried out in 1.0 M H_2SO_4 at 4.0 mA/cm^2, followed by a potentiostatic aging at the final voltage. This experiment has been carried out on samples from the FTi batch, as opposed to the galvanostatic experiments reported on section 3.3.1.

galvanostatically up to 12V, then aged potentiostatically at the final voltage. This experiment was carried out on Ti anodes from the FTi batch, in 1.0 M H_2SO_4 with a current density of 4 mA/cm^2. It is observed that, while during the galvanostatic growth the 'net' curvature evolution[2] in the film is almost zero, as soon as the potentiostatic regime is attained, a compressive curvature evolution is observed. This is believed to be evidence that the reordering accompanying potentiostatic aging is to be expected to lead to the development of compressive stresses. After 120s, the curvature saturates around a value of 2 km^{-1}. This corresponds to a compressive stress of -360 MPa if we consider an anodising ratio of 2 nm/V.

As a second step, the curvature evolution observed under potentiostatic aging was compared to the curvature evolution when the film is submitted to an 'uncontrolled' potentiostatic hold, i.e. in conditions when a drop of the growth efficiency is observed to occur 'naturally' and the anodisation is characterised

[2]comprising the contributions from electrostriction and metal consumption

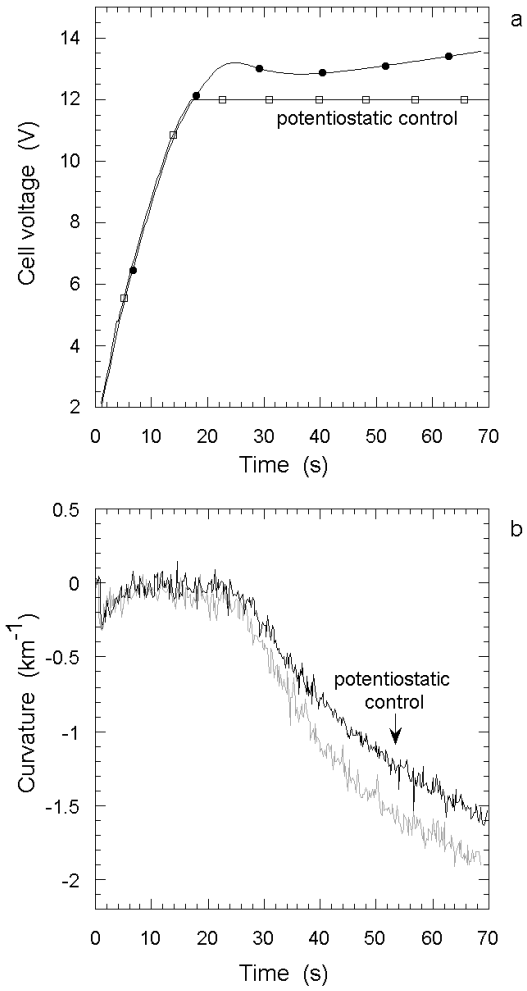

Figure 3.24: Comparison of a) the V-t evolution and b) the curvature evolution for the two experiments carried out, respectively, with and without switching to potentiostatic control at 12V.

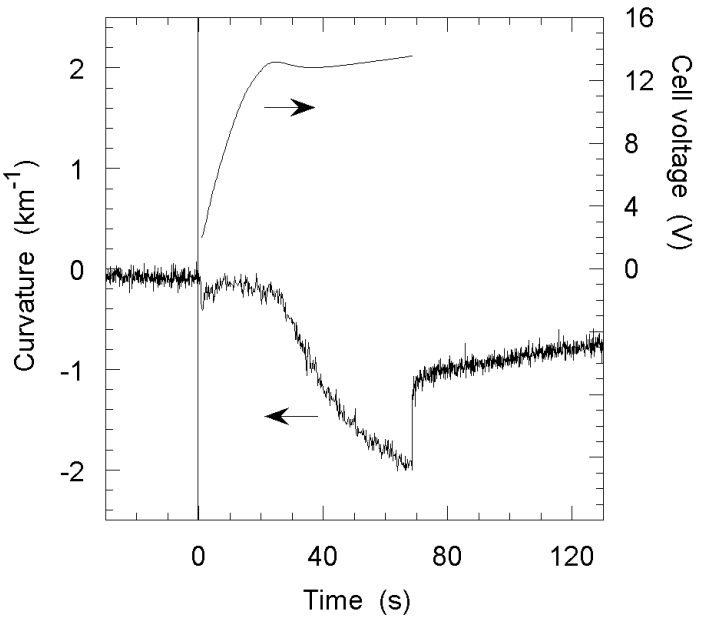

Figure 3.25: Time-evolution of the curvature and cell voltage for a galvanostatic anodisation experiment carried out in 1.0 M H_2SO_4 at 4.0 mA/cm^2 in which a V-plateau is observed at 13V.

by a voltage plateau. A Ti sample identical to the one used for the previous experiment has been anodised galvanostatically under the same conditions, but without switching to potentiostatic control at 12V. The cell voltage rose up to 13V, then saturated around that value, as shown on Fig.3.24a. It can be observed that the anodisation V-t curves for the two samples are identical up to 12V. The stress curvature for the experiment without potentiostatic control is shown on Fig.3.25. Note the large curvature discontinuity observed at the end of the experiment (70s) and corresponding to the relaxation of the electrostriction stress in the film. Remarkably, the curvature evolution in this case is almost identical to the one observed on Fig.3.23, as illustrated on Fig.3.24b. This suggests that, in terms of the stress evolution, anodisation stages where a low growth-efficiency are observed have an influence comparable to that of a potentiostatic aging, possibly inducing densification of the film and a decrease of the number of vacancies. In the framework of the high-field model, the fact that potentiostatic holds favour a reordering can be understood as follows. Under potentiostatic aging conditions, the cell current drops rapidly, and so does the rate of cations injection at the metal/oxide interface. In contrast, the electric field in the film does not decrease significantly so that the ions might retain a high mobility, hence allowing for local reorganisation of the atoms in the film.

3.3.3 Discussion of the origin of the growth stress transitions

The discussion has been divided into two paragraphs, each one corresponding to one of the growth stress transitions described previously. The first paragraph is devoted to the transition from the first to the second stage, and to the interpretation of the large compressive stresses observed in the second stage. The second paragraph deals with the interpretation of the compressive maximum.

First transition: stresses and oxygen evolution:
As to this first observation, the origin of the electrochemical transition, i.e. the decrease of the growth efficiency taking place at V_{II}, is well-documented and corresponds to the onset of the oxygen evolution reaction (OER). In contrast, the associated mechanical behaviour has never been reported so far and is somewhat unexpected. Indeed the reason why the onset of the OER would be associated with the development of large compressive stresses is not straightforward. Three possible situations have been envisioned:

- the compressive stresses could directly arise from the oxygen evolution reaction
- the compressive stresses could arise from a change in the atomistic details of oxide growth resulting from the decreased growth efficiency

- both the compressive stresses and the onset of the OER may have another common origin.

Three possible scenarios, corresponding to those three situations have been investigated and are presented and discussed below, starting from the third possibility.

Experimental evidence can be found in the literature that the onset of the OER is associated with the crystallisation of the film [133, 76]. Crystallisation could then act as the triggering phenomenon, responsible for both the change in the electronic conductivity of the film and the transition in the stress evolution. If it is the case, the crystallisation of the oxide film appears to take place at a rather low voltage in our case, which is consistent with observations by Yahalom [261] and Shibata [214] but contradicts with results from Habazaki et al. [76] or Arsov [16]. One possible explanation for this observation is that our Ti films present a marked (0001) texture. The fact that oxygen evolution takes place in our case at voltages as low as 4V is therefore also in agreement with the observations reported by Kudelka [124] on the influence of the microtexture of Ti substrates on the onset of the oxygen evolution reaction. In the case of the experiment presented on Fig.3.4, the onset of the oxygen evolution reaction is observed to take place at a voltage which depends on the growth rate and which is in fair agreement with literature. However, as evident from the TEM investigation, the films at the end of the compressive stage do not yet contain a continuous polycrystalline layer but consist of isolated crystallites in an amorphous matrix. In addition, as to the internal stress evolution, crystallisation will result in a densification of the oxide film as a result of the transformation of amorphous TiO_2 into a denser anatase or rutile phase. Hence, crystallisation would a priori be expected to induce tensile stresses in the film. This strongly contradicts with our own observation that very large compressive stresses accompany the efficiency drop in the second stage. It seems therefore unlikely that crystallisation would be the origin of the compressive stresses observed in the second stage.

A second possibility would be that the compressive stresses directly result from the oxygen evolution reaction. Indeed, as discussed in section 1.2.1, the TEM analysis carried out by Habazaki et al. on partly crystallised TiO_2 films reveals the presence of small gas bubbles within the oxide film, surrounding crystalline (anatase) nuclei [76]. This provides direct evidence that, at some stage during the growth process, oxygen gas is evolving not only on the surface of the oxide film but also within the film. This observation was recently confirmed by Matykina et al. who demonstrated that more intensive gas evolution takes place inside anodic TiO_2 films grown on the [0002] Ti planes, as it is the case for our films. We have indeed obtained direct SEM evidence of

gas-induced blistering of TiO_2 films grown to large thicknesses. However, such behaviour was not observed on the samples from this study. The exact mechanism of oxygen evolution within the film remains so far an open question. For instance, it is still unclear whether the formation of gas bubbles inside the oxide film requires electrolyte penetration in the film through cracks or if it proceeds as a purely solid-state reaction, as suggested by Zhuravlyova et al. [265] However, independent of the exact mechanism, such a process of gas evolution within a thin film is expected to lead the development of large compressive stresses [221, 265]. Our observed internal stress behaviour during the second stage might thus result from the oxygen evolution reaction. In addition, the observation that the growth efficiency recovers to its initial high value at the beginning of the third stage suggests that for some reason oxygen evolution ceases at that point. Since, at the same time, the instantaneous internal stress becomes tensile, this is supplementary evidence in favour of attributing the observed instantaneous compressive stress to the oxygen evolution reaction. In order to provide experimental evidence supporting this scenario, we have examined cross-sections of the samples anodised to 15V and 40V by TEM, as reported in section 3.3.1. No clear evidence of the presence of gas bubbles could be identified. From our observations, the presence of bubbles with a diameter larger than 20 nm, similar to the larger ones reported in the paper by Habazaki et al. [76] can be definitely excluded. Smaller bubbles might however be present in our films and not being clearly identifiable owing to their small size. Indeed, small cavities in the film cannot be readily distinguished from defects arising during the sample preparation procedure, inherent to the ion milling step. Hence, although this scenario appears as a very reasonable one, supported by evidence from the literature, no direct experimental confirmation could be obtained.

A third scenario would be that the stress evolution arises from a change in the atomistic details of the growth, resulting from the decreased growth efficiency. Indeed, although the -4.07±0.59 GPa average stress measured in the second stage appears to be very large, it is not necessarily unrealistic for the growth of anodic oxide films. A compressive 4 GPa stress can be rationalised, considering the typical values of t_a and the PBR for the growth of anodic TiO_2. According to Gere and Timoschenko [66], the in-plane stress σ that would result from a relative volume change $\Delta v/v_o$ is given by:

$$\frac{\Delta v}{v_o} = \frac{1-2\nu}{Y} 2\sigma \tag{3.4}$$

Taking into account a value of 103 GPa for the Young's modulus of the TiO_2 film and 0.28 for its Poisson's ratio [203], the relative volume change ($\Delta v/v_o$) that would correspond to an in-plane biaxial stress of -4.07 GPa is equal to 3.47%. As $\Delta v/v_o$ is also equal to $t_a PBR - 1$, according to the model of Nelson

and Oriani [164], considering a value of 0.61 for t_a [77] the measured stress value also corresponds to a PBR of 1.69, which is comparable to (and even slightly smaller than) the expected value for transformation of Ti into rutile TiO_2 (PBR=1.78). This is only a first order calculation, involving a large uncertainty on the values of the mechanical properties of the film. So, considering the very reasonable value calculated for the PBR, we can not discard the possibility that the observed compressive stresses would result merely from the transformation of Ti into dense Ti-oxide. As to the transition from tensile to compressive stresses, it can be interpreted in the framework of the model of Nelson and Oriani [164] as an increased contribution of the anionic transport in the film. This hypothesis is difficult to ascertain, as changes in the transport properties are difficult to investigate experimentally. Indeed, measurements of transport numbers require marker studies which can hardly be performed on very thin films. From a kinetic point of view, as the OER consumes oxygen ions at the film surface, it would therefore be expected to be in competition with the incorporation of oxygen ions in the oxide film. Hence, oxygen evolution does not seem favourable to an increased anionic transport. According to the model proposed by Moon and Pyun [159], the compressive stresses can arise from a change in the vacancy concentration. This can be brought in relation to our potentiostatic aging experiment presented on Fig.3.23 and Fig.3.25, which demonstrate that low-efficiency growth has a similar effect on the stress evolution in the film as potentiostatic aging and leads to compressive stresses, probably as a result of a reordering of the film leading to a decreased vacancy concentration.

Second transition: the compressive maximum

Different scenarios have also been investigated to account for the compressive maximum. Owing to the fact that this transition always appears as a relaxation of a large compressive stress, it was envisioned at first that the compressive maximum could be the result of some sort of mechanical failure, allowing for relaxation of the internal stresses. The failure would take place for a given value of oxide thickness, corresponding to a critical threshold of the elastic energy stored in the film and manifest itself either as a delamination of the film from its Ti substrate or as a cracking of the film surface. Evidence of cracking of TiO_2 films, has indeed been provided by Di Quarto [51] or Shibata [214]. From our own observations, crack nucleation could not be convincingly identified from the curvature evolution pattern. Indeed, although some small perturbations are systematically present on the curvature signal from some of the continuous experiments (cfr. Fig.3.11 and Fig.3.2), they seem to be absent during the curvature evolution for the interrupted experiments (cfr. Fig.3.13 and Fig.3.15). The increase of the growth efficiency observed at the end of the second stage seems to contradict as well with the hypothesis of a mechanical failure, since rupture of the anodic film would be expected to lead to a sharp drop of the

cell voltage as fresh Ti metal is brought into contact with the electrolyte. In addition, the observation that the transition from compressive to tensile instantaneous stress is spread over a time scale of about 1 minute, without any visible discontinuity in the curvature evolution, suggests that the phenomenon underlying this transition is not an instantaneous mechanical failure. Our third observation, provided by the interrupted experiment, that the transition is reversible seems to contradict as well with the idea of a mechanical failure. It is also incompatible with any scenario involving a direct dependence on thickness or field as neither the thickness of the film nor the field (assumed to be equal to V/h_f) have the same value at the two successive compressive maxima of the interrupted experiment. Finally, no single evidence of mechanical failure could be found upon TEM examination. Considering the whole set of our experimental observations, it seems unlikely that our compressive maximum results from a mechanical failure.

The fact that the growth efficiency progressively increases and returns to a value close to that measured in the first stage indicates that the oxygen evolution reaction ceases. Hence, if the stresses in the second stage directly result from oxygen gas evolution within the film, the source of the compressive internal stress development disappears in the third stage. In this respect, it is reassuring that the return to high efficiency growth is observed to be accompanied by a marked transition from compressive to tensile instantaneous stress. If, in contrast, the compressive stress in the second stage resulted from a densification process, the transition to the third stage would be associated with a return to the growth of a less-dense oxide.

The main open question relative to the compressive maximum is the origin of the transition from the second to the third stage, i.e. why does the growth efficiency increase again. During similar anodising experiments carried out on bulk Ti, Delplancke et al. also observed an increase of the growth efficiency after a (much longer) low efficiency plateau [48]. Bourdet et al. reported V-t curves on sputtered Ti films very similar to our own ones as well, but they do not provide any interpretation for the increase of the efficiency following the plateau [30]. From our own experiments, the fact that the transition was observed to be reversible seems to be in contradiction with the idea of a direct dependence of the compressive maximum on thickness or field. Both the gradual, progressive nature of the transition and its reversibility therefore rather point to a kinetic effect. The fact that the oxygen evolution ceases could result from a decrease in the number of charge carriers in the film, the film thus becoming more insulating. The latter explanation would be in good agreement with the hypothesis that the compressive stage is associated with an aging of the film, leading to a decrease of the vacancy concentration.

On the other hand, the large tensile stress values measured directly after the compressive maximum suggest that, besides oxide growth, further crystallisation of the oxide film takes place as well, relaxing some of the compressive stresses developed during the second stage through densification. The TEM results also reveal that, at the end of the third stage at 40V, the TiO_2 film consists of an inner polycrystalline layer and an outer amorphous one. Such a 2-layer structure was not observed on the 15V sample, so it seems that the polycrystalline layer develops in the third stage. This provides another possible scenario for accounting for the compressive-to-tensile evolution. Indeed, crystallisation would be compatible with the tensile sign of the stresses in the third stage, allowing for stress relaxation. In contrast, all other experimental observations, in particular the increase in the growth efficiency and the reversibility of the compressive maximum, are not readily interpretable based on the crystallisation scenario. Indeed, a well-crystallised TiO_2 would be expected to exhibit a larger electronic conductivity than amorphous oxide, and therefore a reduced growth efficiency.

It can finally be noted that attempts to measure the thickness of our anodic oxide films by spectroscopic ellipsometry have been unsuccessful. In fact, the ellipsometry data could not be fitted using a simple optical model consisting of a dielectric layer on a Ti substrate. Kudelka [125] had come to the same conclusions that a two-layer model was no longer sufficient to fit the ellipsometry data for their anodic TiO_2 films when they were grown above 5V. In our case, in the light of the previous discussion, more complex models would be necessary to account for the optically rather complex structure of a partly crystallised film which possibly includes gas bubbles as well. Furthermore, as the already complex morphology of the film further evolves during oxide growth as revealed by the TEM investigation, this would have required using a different optical model for each sample thickness. Finally, the large roughness of the film further complicates ellipsometric measurements.

3.4 Conclusions

In this chapter, direct experimental evidence of the correlations existing between the cell voltage and internal stress evolution has been provided. Under galvanostatic conditions, in regions where the film grows with a high efficiency, a constant tensile instantaneous stress, independent of the current density, has been observed. This observation has been discussed in the framework of the models of Nelson and Oriani and Moon and Pyun. It was shown as well that the onset of voltage fluctuations during the growth process, possibly indicative for early breakdown events, is not stress-induced. In the second part of this chapter, growth stress transitions have been discussed. A compressive stage,

corresponding to a low-efficiency V-plateau, was reproducibly observed. Two possible scenarios have been proposed to account for this observation. The compressive stresses might arise either from oxygen gas evolution within the film or be related to an aging of the film under the quasi-potentiostatic conditions, leading to a decrease in the concentration of defects in the film. At the end of the low-efficiency plateau, a return to efficient growth was observed. The latter was accompanied by a compressive maximum and a return to tensile stresses. Evidence has been shown that this transition is not associated with a mechanical failure. The return to efficient growth is believed to be associated with a more insulating character of the film resulting from the aging stage. Finally, crystallisation of the inner part of the film, revealed by TEM to take place during the stage following the compressive maximum, might contribute as well to the tensile stress evolution.

Chapter 4

Electrostriction stresses in anodic TiO_2 films

Contents

In the previous chapter, a general discussion of the growth stress evolution in anodic TiO_2 films was provided. In particular, the development of irreversible intrinsic growth stresses was discussed. The present chapter is focused on the reversible, field-induced stress contribution accompanying the growth of anodic oxide films. The first section includes a short presentation of 'electrostriction', 'dielectrostriction' and of the field-induced 'electrostriction stress'. In the second section, the adequacy of the currently available theoretical models for predicting the magnitude of the electrostriction stresses in anodic oxide films is discussed. A modified equation, linking the electrostriction stress to the electric field and the dielectric constant of the film is derived. The latter equation is experimentally validated in the third section, by comparing the theoretical

predictions with experimental values measured using high-resolution curvature measurements. Finally, in the fourth section, the use of in situ electrostriction stress measurements for monitoring the dielectric properties of anodic oxide films during their growth is discussed.

4.1 General introduction to electrostriction, dielectrostriction and electrostriction stresses

Electrostriction: Several definitions of '**electrostriction**' can be found in the literature. Grindlay defines electrostriction very generally as a nonlinear coupling of the elastic and dielectric properties of an insulator [68]. According to Stratton, electrostriction can be defined, more practically, as the deformation of a dielectric under forces exerted by an electrostatic field [230]. This deformation is a result of the tendency of the dipoles composing the dielectric material to re-orient parallel to the direction of the applied electrostatic field. It should be noted that electrostriction is distinct from reverse piezoelectricity. Indeed, the latter effect is also a coupling between elastic and dielectric properties of specific dielectric materials. However, piezoelectricity is observed in anisotropic crystals meeting certain symmetry conditions, in contrast to electrostriction which is observed in any dielectric material. Furthermore, the amplitude of the piezoelectric deformation is usually much larger than for those induced by electrostriction.
A direct consequence of the electrostrictive deformations is to induce a change in the dielectric properties of the material, in accordance with the classical Clausius-Mosotti theory. In this chapter, the variations of the dielectric properties of a material with deformations will be referred to as '**dielectrostriction**', as proposed by Lee [135]. The Clausius-Mosotti theory considers dielectrics as composed of an ensemble of non-polar but polarisable molecules. The constitutive equation links the dielectric constant ϵ of a material to the number density of polarisable molecules n and their polarisabiity ψ according to [218]:

$$\epsilon = \frac{3\epsilon_o + 2\psi n}{3\epsilon_o - \psi n} \tag{4.1}$$

where ϵ_o is the vacuum permittivity. The relationship linking dielectric constant to deformations depends on how both n and ψ vary when the material is strained, which in turn depends on the symmetry of the material lattice and on the geometrical boundary conditions.

Electrostriction stress: When a dielectric is submitted to an electric field, it experiences an electrostatic stress which encompasses two distinct, though interlinked contributions. The first stress contribution, usually referred to as the **Maxwell stress**, results from the Coulombic attraction between the bound

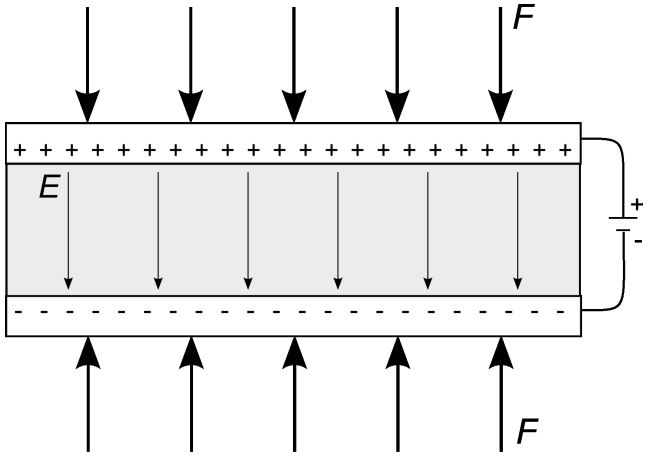

Figure 4.1: Schematic illustration of a dielectric film submitted to an homogeneous electric field E. The Coulombic attraction between the charges of opposite sign located on the two electrodes results in a compressive force F.

charges of opposite sign located on both sides of the dielectric. The second stress contribution arises from dielectrostriction itself, i.e. from the change of the dielectric properties of the material as a result of dipole reorientation when the material is deformed under the action of the Maxwell stress. The two stress components are coupled and cannot be treated independently. It should be noted that electrochemists usually refer to the overall electrostatic stress, including both contributions, as the '**electrostriction stress**'. In this chapter, we will adopt the latter convention.

Let us now consider the case of a dielectric film of uniform thickness placed between two parallel electrodes (See Fig.4.1). The film is attached to the electrodes, which prevents any lateral deformation. This geometry is analogous to the case of an anodic oxide film on a metal substrate in an electrolytic solution. When a potential difference is applied between the two electrodes, the Maxwell stress acting on a dielectric film can be described by a simple parallel plate capacitor model and varies with the electric field according to:

$$\sigma_{ES} = -\frac{\epsilon_o \epsilon}{2} E^2 \tag{4.2}$$

The minus-sign in Eq.4.2 indicates that the in-plane stress resulting from the Maxwell stress is compressive, independent of the direction of the applied field. Due to the fact that the dielectric film is attached to the electrode and cannot deform laterally, the corresponding in-plane stress experienced by the film is

given by:

$$\sigma^*_{ES} = -\frac{\nu}{1-\nu}\frac{\epsilon_o \epsilon}{2}E^2 \tag{4.3}$$

where ν is the Poisson coefficient of the oxide film. The in-plane stress σ_{ES} given by Eq.4.3 is the electrostriction stress (which would be measurable from the sample curvature) in the absence of dielectrostriction. As long as the field to which the dielectric is submitted is low to moderate, the Maxwell stress has a low, barely measurable value. However, owing to the second order dependence towards the electric field, its magnitude scales up rapidly when the magnitude of the applied field is increased.

The importance of electrostriction as a source of (reversible) stress accompanying the growth of anodic oxide films has been known for long. Indeed, the very intense electric fields associated with the high-field ion migration, typically of the order of 10^7 V/cm [164], induce rather large electrostriction stresses in growing anodic films. As previously discussed in section 1.3.1, even the first pioneering studies on stress development in anodic oxide films include a discussion of the role of electrostriction on the total measured internal stress. In particular, Butler et al. [33] demonstrated the quadratic dependence of the electrostriction stress towards the electric field.

In the second section, it is discussed how Eq.4.3 needs to be corrected to take into account dielectrostriction.

4.2 Derivation of a modified constitutive equation for the electrostriction stresses

In many studies devoted to internal stresses developing in anodic oxide films, the electrostriction stress is assessed taking into account the contribution of the Maxwell stresses only, i.e. based on Eq.4.2. However, as already pointed out by Wüthrich [257], by doing so, the second, major, contribution which arises from dielectrostriction is missed. This second contribution to the overall field-induced electrostriction stress is far from being negligible: dielectrostriction stress would even exceed the Maxwell stress contribution for values of the dielectric constant larger than 4 [135]. Experimental observations, including our own experimental results presented in Section 4.3, confirm the inadequacy of the simplified equation, based on the Maxwell stress only, for predicting the magnitude of the actual electrostriction stress in anodic oxide films.
Sato, in 1971 derived a model for the electrostriction stress based on thermodynamics [205]. He predicts the following dependence of the electrostriction-induced pressure (p) in the film:

$$p - p_o = \frac{\epsilon(\epsilon - 1)}{8\pi}E^2 \tag{4.4}$$

where p_o is the atmospheric pressure. However, his model does not take into account dielectrostriction either, since it is explicitly based on the assumption that the number density of dipoles in the dielectric remains constant. Another model, taking into account the effect of dielectrostriction, has been proposed by Wüthrich [257]. However, his model predicts the additional stress contribution of dielectrostriction to be a tensile one, which is in disagreement with the experimental observation that the measured electrostriction stresses are more compressive than expected values based on the Maxwell stress only [199].

The development presented in this section is based on an alternative model, developed originally for linear isotropic dielectrics, as is the case for the most common anodic valve metal oxides. In that case, the effect of dielectrostriction can be taken into account through the use of the two electrostriction parameters α_1 and α_2. A detailed treatment can be found in the work of Lee [135] or McMeeking [150], which are both based on the original work of Landau and Lifshitz [129]. Generally speaking, the electrostriction stress in a dielectric material can be expressed as [135]:

$$\sigma_{ES,ik} = \frac{E \cdot D}{2}\delta_{ik} + \frac{E_i D_k + E_k D_i}{2} - \frac{1}{2}\left[\frac{\partial D_i}{\partial u_{ik}}\right]_{T,E} E_i \tag{4.5}$$

where D is the electric displacement vector, E is the electric field vector, u_{ij} is the strain tensor and δ_{ij} is the Kronecker delta. The first two terms in the right-hand side of the Eq.4.5 correspond to the Maxwell stress while the third term corresponds to dielectrostriction. Now, we need to introduce a constitutive equation for the dependence of the dielectric properties on the strains u_{ik}. Let us consider the case of an isotropic linear solid dielectric having a dielectric constant ϵ^u. This should be an adequate model for most anodic oxide films. When strained, under the action of the electrostatic field, the dielectric does not necessarily remain isotropic, so that the dielectric constant in the unstrained state ϵ^u must be replaced by a dielectric tensor ϵ_{ij}. According to Landau and Lifshitz [129], under the assumption of infinitesimal strains, the variation of the dielectric tensor ϵ_{ij} with strains can be described by a linear function, using two electrostriction coefficients α_1 and α_2:

$$\epsilon_{ij} = \epsilon^u + \alpha_1 u_{ij} + \alpha_2 u_{kk}\delta_{ij} \tag{4.6}$$

Adopting the model of Landau and Lifshitz, Eq.4.5 becomes [135]:

$$\sigma_{ES,ij} = \frac{\epsilon_o}{2}\left(2\epsilon - \alpha_1\right) E_i E_j - \frac{\epsilon_o}{2}\left(\epsilon + \alpha_2\right) E^2 \delta_{ij} \tag{4.7}$$

In the particular case of a dielectric film attached to two parallel electrodes, which ensures conditions of uniform, unidirectional field ($E_x = E_y = 0, E_z \neq 0$)

and no lateral displacement, Eq.4.7 simplifies. The stress experienced by the dielectric film in the direction normal to the film plane is given by [217]:

$$\sigma_{zz} = \frac{\epsilon_o}{2} \left[\epsilon - (\alpha_1 + \alpha_2)\right] E^2 \tag{4.8}$$

and the resulting in-plane stress ($\sigma_{xx} = \sigma_{yy} \equiv \sigma_{ES}$) is given by:

$$\sigma_{ES} = -\frac{\nu}{1-\nu} \frac{\epsilon_o}{2} \left[\epsilon - (\alpha_1 + \alpha_2)\right] E^2 \tag{4.9}$$

This modified equation, which is formally equivalent to the simplified Eq.4.3 for the Maxwell stress, takes explicitly into account the contribution from di-electrostriction through the use of the two electrostriction parameters α_1 and α_2. It is valid for small strains and the values of α_1 and α_2 must be adapted to the symmetry of the material. In order to predict numerical values for the electrostriction stress, one needs to know the values for the two electrostriction parameters. These parameters are not easy to determine experimentally and, to the best of our knowledge, their values for anodic TiO_2 films have never been reported so far. However, Shkel and Klingenberg have established a theoretical framework which allows expressing the electrostriction parameters α_1 and α_2 as a function of the dielectric constant ϵ [218]. Their derivation is based on the original Clausius-Mosotti equation and on the specific relationship between strain and polarisation for the specific case of amorphous materials. They found:

$$\alpha_1 = -\frac{2}{5} (\epsilon - 1)^2 \tag{4.10}$$

$$\alpha_2 = -\frac{1}{3} (\epsilon - 1)(\epsilon + 2) + \frac{2}{15} (\epsilon - 1)^2 \tag{4.11}$$

Using their expressions, our previous Eq.4.9 for the in-plane electrostriction stress can be further expressed as:

$$\sigma_{ES} = -\frac{\nu}{1-\nu} \frac{\epsilon_o}{2} \left[0.6\epsilon^2 + 0.8\epsilon - 0.4\right] E^2 \tag{4.12}$$

Eq.4.12 is the central equation in this chapter. It provides a new relationship for predicting the magnitude of the electrostriction stress in a material of dielectric constant ϵ submitted to a uniform field E. Most interestingly, a quadratic dependence of the electrostriction stress on the dielectric constant of anodic oxide films is predicted. This is fundamentally different from the linear dependence predicted by the simplified Eq.4.3, based on the Maxwell stress contribution only. In contrast, it agrees with the tendency predicted by the Sato model [205]. As TiO_2 has one of the largest permittivities of all anodic oxides, this quadratic relation is also the reason for the large magnitude of the electrostriction stresses measured in these films as compared to other metal

oxides. Inversely, the disagreement between electrostriction stress values predicted by the simplified Eq.4.5 and the modified Eq.4.12 can be expected to be significantly smaller in the case of lower permittivity oxides, like anodic Al_2O_3 ($\epsilon \cong 9$ [32]) and Ta_2O_5 ($\epsilon \cong 27$ [109]).

In the next section, experimental observations on the magnitude of electrostriction stresses in anodic TiO_2 films are presented. As will be evidenced, the large magnitude of the measured σ_{ES}-values cannot be accounted for by using the simplified Eq.4.3, which takes into account the Maxwell stress contribution only. This led us to reconsider the problem of electrostriction stresses and to derive the modified equation Eq.4.12. The latter are coherent with our experimental observations, both in absolute magnitude, field- and permittivity dependence, as will be demonstrated in the next section.

4.3 Experimental observations on the magnitude and field dependence of electrostriction stresses

In this section, experimental results on the magnitude and field-dependence of the electrostriction stresses in anodic TiO_2 are presented. A new experimental methodology, inspired by that of Sahu et al. [199] and Butler et al. [33] is proposed, which consists in repeatedly varying the electric field applied to the oxide film after the growth.

Experimental

The experimental set-up and sample preparation procedure for these measurements were as described in chapter 2. Anodising of the Ti thin film (Ti from the 'PTi' batch) and the subsequent study of the electrostriction stresses in the oxide film were carried out by repeatedly scanning the cell voltage between 1 and 9 V at a rate of 0.1 V/s in a 1.0 M H_2SO_4 electrolyte.

Results

Figure 4.2 shows the measured curvature evolution during six consecutive potentiodynamic cycles. During the first cycle, a thin TiO_2 film is formed. After this initial oxide formation step, in order to determine the magnitude and field-dependence of the electrostriction stress, the electrostatic field in the oxide film is systematically changed by repeatedly cycling the cell voltage again up to the forming voltage. A very clear curvature evolution is observed during cycling, which provides a remarkable and direct evidence of the large magnitude of the

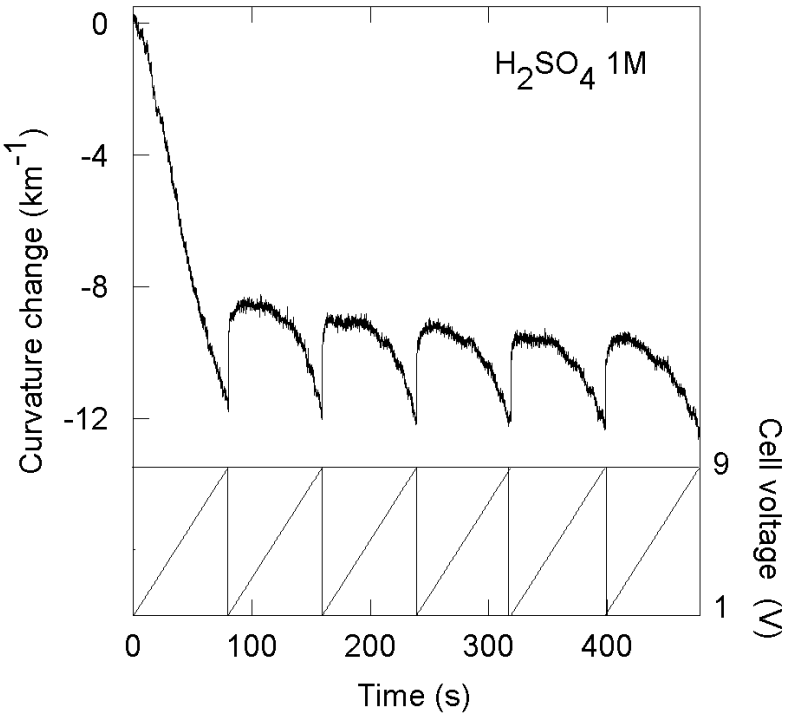

Figure 4.2: Time evolution of the applied cell voltage and of the resulting anode curvature for six identical potential scans. This experiment was performed on samples from the PTi batch in a 1.0 M H_2SO_4 electrolyte with a scan rate of 0.1 V/s.

reversible field-induced stress contribution to the overall stress. The in-situ curvature results shown in Fig.4.2 for the first and subsequent cycles will now be further analysed and discussed in the following paragraphs.

First cycle

During the first cycle, a thin oxide film grows on the Ti anode. The thickness h_f of this oxide film increases proportionally with the applied cell voltage V, with an anodising ratio of 2.7±0.1 nm/V, as determined by ex-situ ellipsometry. The electrostatic field in the oxide film ($E \equiv V/h_f$) was therefore assumed to retain a constant value throughout the growth process, equal to $3.7{\cdot}10^8$ V/m. At the end of the first cycle, the thickness of the oxide film has reached 24 nm. During oxide growth, the curvature of the anode is observed to increase

fairly linearly in the compressive direction. The measured curvature change $\Delta\kappa$, being the sum of contributions from electrostriction ($\Delta\kappa_{ES}$) and intrinsic growth stresses ($\Delta\kappa_{gr}$), can be expressed, based on Eq.4.9 and on the Stoney equation (Eq.2.4), as:

$$\Delta\kappa = \frac{6}{M_s h_s^2}\left(-\frac{\nu}{1-\nu}\frac{\epsilon_o}{2}\left[\epsilon-(\alpha_1+\alpha_2)\right]\right)\frac{V^2}{h_f} + \frac{6}{M_s h_s^2}\Delta\left(\sigma_{gr}h_f\right) \qquad (4.13)$$

As the thickness of the growing film is proportional to the applied voltage, the contribution from electrostriction is expected to increase linearly with time in the case of a potentiodynamic experiment. Moreover, the slope of the curvature vs. time curve in Fig.4.2 corresponding to the first cycle is observed to be constant to a good approximation. Therefore, according to Eq.4.13, this indicates that the oxide film forms with a constant growth stress σ_{gr}. At the end of the first scan, the cell voltage is switched back to 1V. At the same time, the curvature is observed to decrease instantaneously as a consequence of the relaxation of the reversible electrostriction stresses in the oxide film. The magnitude of the latter after the first cycle can therefore already be assessed by quantifying this curvature discontinuity. A compressive value of -360±60 MPa is measured. The growth stress obtained after subtracting the electrostriction stress contribution then amounts to -1.52±0.06 GPa (see Fig.4.3). The evolution of the cell current during the first stage is shown as well on Fig.4.3. It can be observed that the current evolution does not exhibit the characteristic current plateau, as would be expected for the growth of an insulating barrier layer. This behaviour, however, it not surprising in the case of TiO_2 grown on dense-packed Ti planes, as discussed by Kudelka et al. [124]. The decrease of the cell current observed from 22s on suggests that the film becomes more insulating in the course of the growth. It can be observed as well that the voltage range investigated seems to be below the voltage value marking the onset of the oxygen evolution reaction, as suggested by the absence of large current peaks.

Cycles 2 to 6

The above-mentioned way of quantifying electrostriction stresses offers limited precision, as evidenced by the large relative error. This can be fully attributed to the inaccuracies in the determination of the precise starting and ending points of the curvature discontinuity. Therefore, the anodised film obtained after the 1^{st} cycle was subjected again to a varying electrostatic field during five, identical cycles. From Fig.4.2, after the immediate discontinuity at the beginning of each cycle, a curvature relaxation in the tensile direction is first observed. As will be evidenced later, this initial stage corresponds to a discharge of the oxide film, which is beyond the scope of this chapter. The curvature is then observed to increase again in the compressive direction. If we assume that the thickness of the pre-formed oxide film remains constant after the first cycle

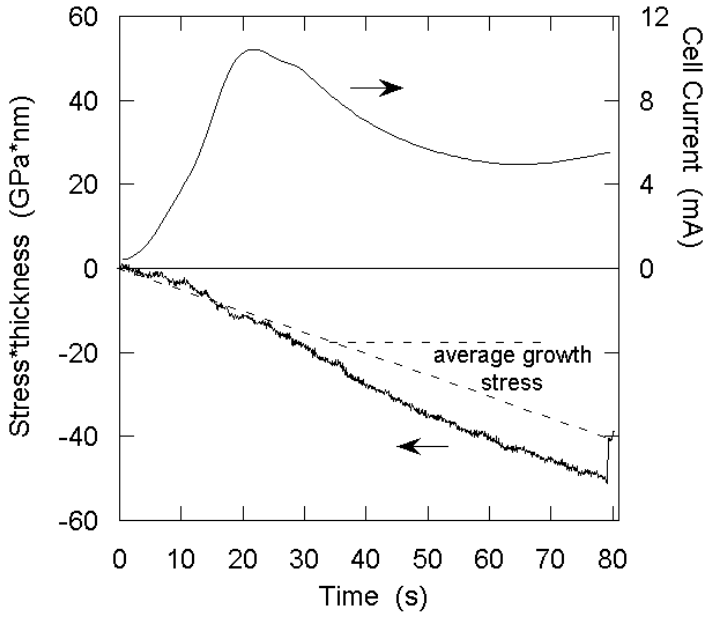

Figure 4.3: Illustration of the evaluation of the growth stress σ_{gr} from the slope of the curvature trace and the curvature discontinuity at the end of the first cycle.

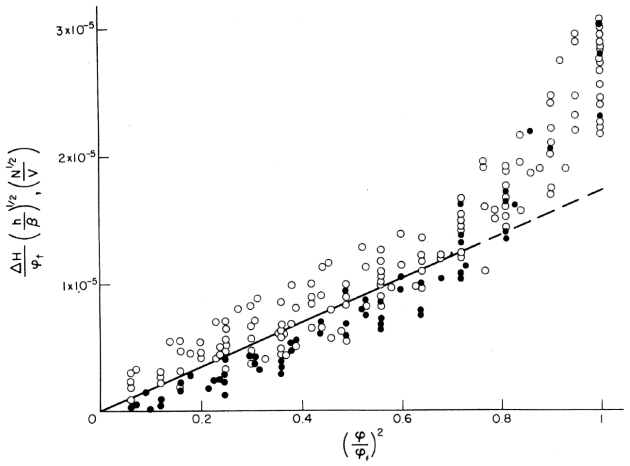

Figure 4.4: Evolution of a stress-proportional measured quantity with the square of the ratio of the applied cell voltage ϕ to the formation voltage ϕ_f, as measured by Wüthrich on Al_2O_3 films (reproduced from [257]).

($\Delta h_f = 0$), a plot of the curvature data vs. V^2 is expected to show a linear dependence, characteristic of electrostriction. Indeed, the second, growth-related term in Eq.4.13 vanishes in that case. Such a plot is presented in Fig.4.5 for the third cycle. It is seen that the dependence of the measured curvature data after the transition stage is not simply proportional to V^2. Hence, this result suggests that the thickness of the oxide film is still further increasing during cycles 2 to 6. A similar deviation from linearity of deflection vs. V^2 curves has been observed by Wüthrich on barrier anodic Al_2O_3 films (See Fig.4.4), and was attributed to ionic currents flowing through the film [257]. We believe these currents to be responsible for the further growth of the oxide film. Our measured current data have therefore been included in Fig.4.5 as well. Note how the initially negative current (see inset of Fig.4.5) confirms the transition stage to be due to oxide discharging.

In order to be able to calculate accurate values for the electrostriction stress during cycles 2 to 6, the contribution of oxide growth must at first be subtracted from the measured curvature data. While the general equation Eq.4.13 still applies, its interpretation during cycles 2 to 6 is different from the first cycle. Indeed, during these subsequent cycles, the oxide thickness is no longer proportional to the cell voltage, nor is $E \equiv V/h_f$ constant anymore. The anticipated increase in film thickness Δh_f during each cycle must therefore be

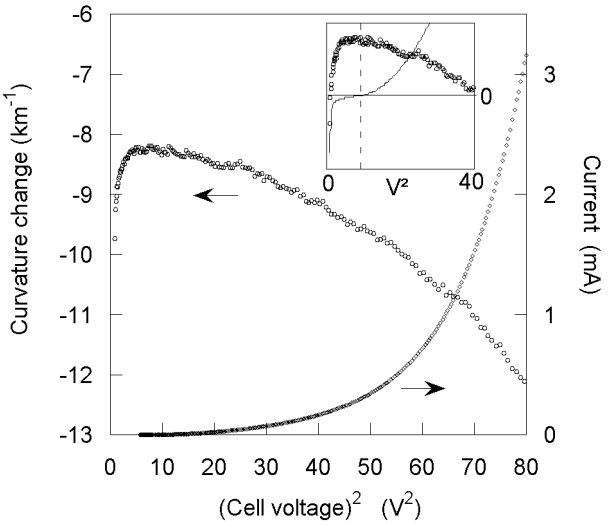

Figure 4.5: Evolution of the anode curvature and of the cell current with the square of the applied cell voltage for the third cycle. The inset shows the initial stage of the cycle, characterised by a transition from negative to positive cell current.

assessed based on the amount of (positive) charge passing during that cycle:

$$\Delta h_f = \frac{v_m}{4FS} \int \eta\,(t) \cdot I(t) dt \tag{4.14}$$

where v_m is the molar volume of the TiO_2 formed, S the anode surface, F Faraday's constant, η the growth efficiency and I the positive cell current. If we consider a constant, average growth efficiency during a given cycle, the above equation simplifies to:

$$\Delta h_f = \frac{v_m}{4FS} \eta Q \tag{4.15}$$

Q being the total positive charge consumed during the cycle. Combining Eq.4.13 and Eq.4.15 then yields, for a given cycle j :

$$\Delta \kappa = A \frac{V^2}{h_{f,j} + \Delta h_{f,j}} + \sigma_{gr} B \eta Q \tag{4.16}$$

where

$$A = \frac{6}{M_s h_s^2} \left(\frac{-\nu}{1-\nu} \frac{\epsilon_o}{2} \left[\epsilon - (\alpha_1 + \alpha_2) \right] \right) \tag{4.17}$$

and

$$B = \frac{6}{M_s h_s^2} \frac{V_m}{4FS} \tag{4.18}$$

In Eq.4.16, $h_{f,j}$ represents the oxide thickness at the very beginning of cycle j. In the above derivation, a constant value for the growth stress σ_{gr} has been assumed in the fraction of the film growing during cycle j. This hypothesis is based on the observation that the initial oxide film during the first cycle also grew with a fairly constant growth stress. Its magnitude has therefore been fixed at the previously determined value of -1.52 GPa. The influence of the latter assumption on the accuracy of the electrostriction stress values was found to be very limited, as will be discussed in the next paragraph. The molar volume of the oxide film was measured by Rutherford Backscattering Spectroscopy (RBS) to be 26.6 cm^3/mol, so that the factor B defined on Eq.4.18 takes a constant value of 0.11 $(GPa.m.C)^{-1}$. In order to further facilitate the data analysis, one final approximation was made by considering the thickness increments $\Delta h_{f,j}$ during each cycle to be sufficiently small as compared to the initial oxide thickness $h_{f,j}$. In that case, Eq.4.16 simplifies to:

$$\Delta \kappa \cong A \frac{V^2}{h_{f,j}} + \sigma_{gr} B \eta Q \tag{4.19}$$

The validity of the latter assumption will be confirmed in the discussion part, based on quantitative results for the thickness increments $\Delta h_{f,j}$.

Cycle	2	3	4	5	6
A [10^{-13} V^{-2}]	-4.9±0.1	-6.4±0.1	-6.8±0.1	-6.8±0.1	-6.7±0.1
η	0.78±0.15	0.66±0.13	0.69±0.13	0.68±0.13	0.64±0.12
Δh_f [nm]	5.8±0.9	3.5±0.6	3.2±0.5	2.8±0.5	1.7±0.3

Table 4.1: Values of the regression parameters A and η and the thickness increments Δh_f for each of the cycles 2 to 6, as obtained from a multivariate regression of the curvature data to Eq.4.19.

It is obvious that the above equations only apply to the analysis of charge-induced stresses, either electrostriction- or growth-related. As a result, only the curvature data corresponding to the charging of the oxide film should be considered. Therefore, prior to fitting the curvature measurements to Eq.4.19, the data corresponding to the transition region, where a negative current was measured, were first eliminated. A multivariate linear regression of the remaining curvature vs. V^2 data for each of the cycles 2 to 6 then yielded the values for the regression parameters A, which contain the electrostriction parameters, and η, the average growth efficiency. Their values, as well as the ones for the thickness increments of each cycle calculated from Eq.4.15, are shown in Table 4.1. They will be further discussed in the next section. To illustrate the data analysis procedure, Fig.4.6 represents the same experimental curvature data as in Fig.4.5, together with the corrected values obtained after subtraction of the estimated contribution of oxide growth according to Eq.4.19. The corrected data, which are now fully attributable to the electrostriction effect only, are observed to indeed vary linearly with V^2.

Discussion

Before discussing the results on the magnitude of the electrostriction stresses, we first examine the validity of one of the hypothesis made in arriving at equation Eq.4.19. Indeed, in order to simplify Eq.4.16, it was assumed that the thickness increments during each cycle were small as compared to the thickness of the oxide film at the beginning of the cycle. Considering the thickness increments presented in Table 4.1, this hypothesis is indeed very reasonable, as their final values are, except for the 2^{nd} cycle, only about 10% of the initial oxide thickness. Moreover, as can be seen from the current signal in Fig.4.5, the thickness increment takes place during a relatively short final stage of each cycle, so that the approximation only affects the final data at each stage. The data obtained from the mulivariate linear regression to Eq.4.19 can therefore be considered as sufficiently accurate. As to the growth efficiency values η in Table 4.1, their values are within the range of 50-100% reported by Dyer and Leach for slowly grown anodic TiO_2 films below 10V [57] . Therefore, in addi-

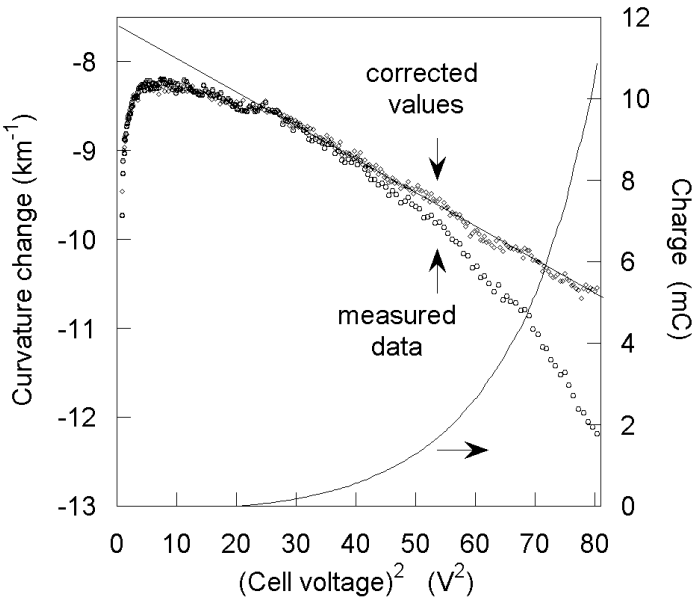

Figure 4.6: Evolution of the anode curvature and of the consumed charge with the square of the applied cell voltage for the same cycle as in Fig.4.5. The corrected curvature values, obtained after subtraction of the contribution of oxide growth, are superimposed on the rough data.

tion to resulting in reasonable values for the thickness increments, these growth efficiency values are believed to be another reliable indication of the coherence of the proposed data analysis procedure.
As to the values of the electrostriction stresses, the value obtained after the first cycle from the curvature discontinuity was -360±60 MPa. For the subsequent cycles 2 to 6, their magnitude at the end of each cycle can be calculated from Eq.4.16 and the Stoney equation, using the values of A and Δh_f in Table 4.1. Results are shown in Table 4.2, and seen to be in the range of -140 to -240 MPa. The measured electrostriction stress is observed to decrease steadily from one cycle to the other as a result of the increase of the oxide thickness. Indeed, the latter induces, at the same final cell voltage, a decrease of the magnitude of the electrostatic field. The same argument holds as well for explaining the decrease between the values obtained after the first (-360±60 MPa) and second cycle (-236±39 MPa): their ratio (1.53±0.36) is equal to the square of the corresponding inverse thickness ratio (1.56±0.08), as expected from the quadratic dependence of σ_{ES} on E.

Our measured values are also in fair agreement with the measured electrostriction stresses of, respectively, -190 MPa and -200 MPa reported on TiO_2 thin films by Sahu et al. [199] and Panagopoulos [184]. In contrast, they are about one order of magnitude larger than the ones predicted by Vermilyea [245], predictions which were based on the simplified Eq.4.3. The latter disagreement points to an important, more generic conclusion: neglecting the effect of dielectrostriction can lead to a systematic underestimation of the contribution of electrostriction to the overall internal stress in anodic oxides. Inversely, the relatively large electrostriction stresses reported for TiO_2 in this and other publications cannot be accounted for by the current, simplified models, which take only the Maxwell stress contribution into account. Indeed, when using the simplified equation 4.3, the dielectric constant of our oxide films would have to be as large as 988 for an imposed electrostatic field of $3.7{\cdot}10^8$ V/m to result in the measured electrostriction stress on the order of -200 MPa. Obviously, this is an unrealistic permittivity value.

In order to judge whether the modified equation 4.12 proposed in Section 4.2 predicts more realistic values, one needs to calculate the permittivity values corresponding to the measured A coefficients for each cycle. Using Eq.4.10 and Eq.4.11 for α_1 and α_2, our previous Eq.4.17 for the regression parameter A can be further expressed as:

$$A = -\frac{\nu}{1-\nu}\frac{3\epsilon_o}{M_s h_s^2}\left[0.6\epsilon^2 + 0.8\epsilon - 0.4\right] \tag{4.20}$$

This expression allows calculating, from the A-values in Table 4.1, the permittivity of the TiO_2 film in each cycle (a value of 0.25 was used for the Poisson

Cycle	2	3	4	5	6
σ_{ES} [MPa]	-236±39	-223±37	-192±31	-163±27	-141±23
ϵ	48±6	55±6	57±6	57±6	56±6

Table 4.2: Electrostriction stress values obtained from the data in Table 4.1 at the end of each cycle. The corresponding dielectric constant for each cycle, calculated from Eq.4.20, is included as well.

coefficient of TiO_2 [164]). These values have been presented in Table 4.2 as well, resulting in a constant average permittivity of 54±4, statistically equal for all cycles.

Of course, the above permittivity calculation is based explicitly on Eq.4.10 and Eq.4.11 for the electrostriction parameters α_1 and α_2, the validity of which has so far not been confirmed experimentally for TiO_2. Therefore, the dielectric constant of the oxide film was measured independently as well by ex-situ impedance measurements performed on metal/oxide/metal structures, after deposition of Al contacts on the surface of the TiO_2 films. In order to minimise the parasitic influence of ionic currents on the impedance measurement, measurements were carried out at a rather high frequency of 100 kHz. A value of 55±6 was obtained, statistically equal to the one calculated using Eq.4.20 and well in the range of published permittivity values for anodic TiO_2 thin films [131, 23]. The latter established agreement also confirms the validity of the above equations 4.10 and 4.11 for obtaining the electrostriction parameters α_1 and α_2 of amorphous TiO_2 thin films simply from their permittivity value.

As pointed out earlier, in the derivation of Eq.4.16, a constant growth stress was assumed for cycles 2 to 6, having the same value as for the first growth stage. This hypothesis may be somewhat open to criticism, as its validity has not been explicitly confirmed. However, it turns out that the values presented in Table 2 for the electrostriction stress and for the dielectric constant are very robust towards the value postulated for the growth stress. For instance, an over- or underestimation of the growth stress by 0.5 GPa (33%) will induce, respectively, an overestimation by 5% and an underestimation by 9% of the electrostriction stress. Similarly, it should be noted that our electrostriction stress values have been extracted by fitting the curvature data as a function of the cell voltage while, more rigorously, only the part of the cell voltage corresponding to the voltage drop through the oxide film (ϕ_f) should have been considered. The difference between V and ϕ_f can be split into two main contributions. The first one corresponds to the ohmic drop within the electrolyte and at the cathode while the second one arises from the voltage drop on the anode at the metal/oxide and oxide/electrolyte interface. We quantified the first con-

tribution explicitly by measuring simultaneously the cell voltage and the anode potential using a 3-electrodes set-up. The ohmic drop within the electrolyte and at the cathode was observed to amount to 50 mV at the forming voltage, which corresponds to the maximum of current flowing through the cell. In contrast, the contribution of the potential drop at the oxide/electrolyte interface, which is usually neglected in studies devoted to anodising, is not readily accessible to the experiment and was therefore assessed based on theoretical values from the literature. Values up to 250 mV have been reported for aluminium oxide films at pH zero [39]. Again, it turns out that the values presented in Table 2 for the electrostriction stress and for the dielectric constant are very robust towards the approximation of ϕ_f being equal to V. For instance, an unrealistically excessive overestimation of ϕ_f by 500 mV will induce an underestimation by 10% of the electrostriction stress and an underestimation by 5% of the dielectric constant. The latter values fall within the reported experimental error.

Another question may arise as to whether our repeated potentiodynamic cycling could alter the characteristics of the oxide film. Indeed, if the potentiodynamic scans used to measure the electrostrictive stresses in our study would induce an aging of the oxide films, this should indeed be taken into account in the interpretation of our data. As discussed in section 1.2.4, only a few studies have been devoted to the aging behaviour of anodic TiO_2 films. The work of Ohtsuka and Otsuki [171, 172], which deals with the aging of anodic TiO_2 films under potentiostatic conditions, shows how potentiostatic aging at the formation potential can lead to a relaxation of the film. This relaxation manifests itself as an increase of the refractive index of the oxide, which the authors attribute to the dehydration of the oxide film, which originally grows with a $TiO_2.xH_2O$ stoechiometry. The question then arises as to what extent potentiodynamic cycling leads to a similar relaxation as potentiostatic one. If relaxation occurs under potentiostatic conditions, there is indeed no obvious reason why no relaxation at all would occur for potentiodynamic regime. However, if the aging relies on a field-driven migration, relaxation might occur to a significantly lower extent or more slowly under potentiodynamic conditions as compared to potentiostatic ones owing to the lower average value of the electrostatic field through the film. According to Azumi and Seo [17], during potentiodynamic aging of anodic TiO_2 films, the dissociation of the bound water in the hydrated oxide takes place reversibly. The latter effect could induce an intricate relationship between aging and apparent dielectric constant, involving a reversible potential dependence. In our study, however, we did not observe an evolution of the value of the dielectric constant during the cycles. The value of the electrostriction stress at the end of the growth cycle was assessed, based on the discontinuity, to be 360±60 MPa. The latter value corresponds to a dielectric constant of 54±10 which is not statistically different from the values measured for the following cycles. This suggests that, under

our experimental conditions, not much relaxation occurs or that the relaxation has a limited influence on the dielectric constant of the oxide film, which falls within our experimental error.

Conclusions

In this section, a new experimental procedure has been proposed for investigating electrostriction stresses developing during the growth of anodic oxide thin films. This procedure was applied to potentiodynamically grown TiO_2 films and compressive electrostriction stresses as large as -240 MPa have been measured in such films. The inadequacy of simplified electrostriction models neglecting the contribution of dielectrostriction for the assessment of the electrostriction stress is quantitatively demonstrated. Our measured electrostriction stress values are in good agreement with the modified theory presented in Section 4.2, both in absolute magnitude, field- and permittivity dependence. The next section provides a discussion on how electrostriction stresses can be used as a diagnostic tool for studying the evolution of the characteristics of the oxide films.

4.4 Electrostriction stress measurements as a way of monitoring the evolution of the dielectric properties of anodic oxide films

As discussed in Section 4.2, electrostriction stresses exhibit a quadratic dependence towards the dielectric constant of the film. Therefore, the evolution of σ_{ES} in the course of the growth should a priori provide a sensitive means of monitoring the evolution of the dielectric properties of anodic oxide films. Indeed, oxide films growing anodically can undergo various morphological changes, like crystallisation, phase transitions, hydration/dehydration or porosity incorporation. All these phenomena affect the density of the oxide film and hence its dielectric properties. Monitoring the evolution of the electrostriction stresses in the film during anodisation could therefore help identify such morphological transitions. In this section, results from two series of experiments are presented, in which the evolution of σ_{ES} was used for monitoring changes in the properties of anodic TiO_2 films. The two series of experiments are presented successively, then a common discussion follows.

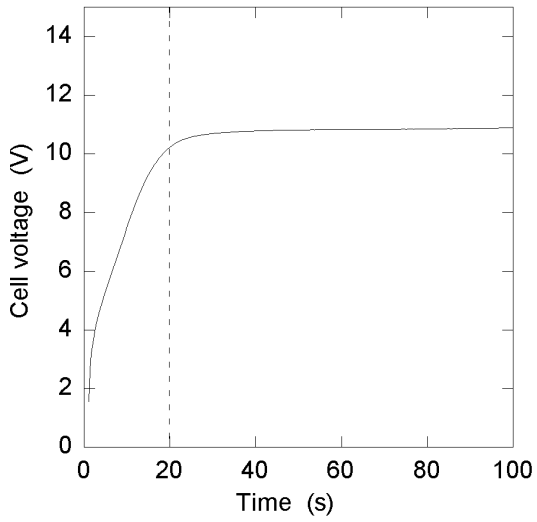

Figure 4.7: Typical evolution of the cell voltage for Ti anodisation in 1.0 M HNO_3 at 1 mA/cm^2.

4.4.1 First series of experiments

Experimental

In contrast to the experiments described in Section 4.3, in the present experiment, anodisation of the Ti electrodes has been carried out in a different, smaller, electrochemical cell. The cell was 10 x 10 mm^2 in section and 40 mm high, thus having a volume of 4 ml. The Ti electrodes, prepared as described in chapter 2, were taken from the 'ETi' batch. A 2-electrode configuration was chosen and a foil of stainless steel (8 x 35 mm^2) was used as cathode. The distance between the two parallel electrodes was 5 mm. Anodic oxide films were grown under galvanostatic conditions using three different sets of experimental parameters: 1.0 M HNO_3 with current densities of, respectively, 1 and 3 mA/cm^2, and 1.0 M H_3PO_4 with a current density of 0.5 mA/cm^2. The anodisation process was interrupted repeatedly and the dielectric properties of the anodic film were assessed from the curvature discontinuities resulting from the relaxation of the electrostriction stress under open-circuit conditions.

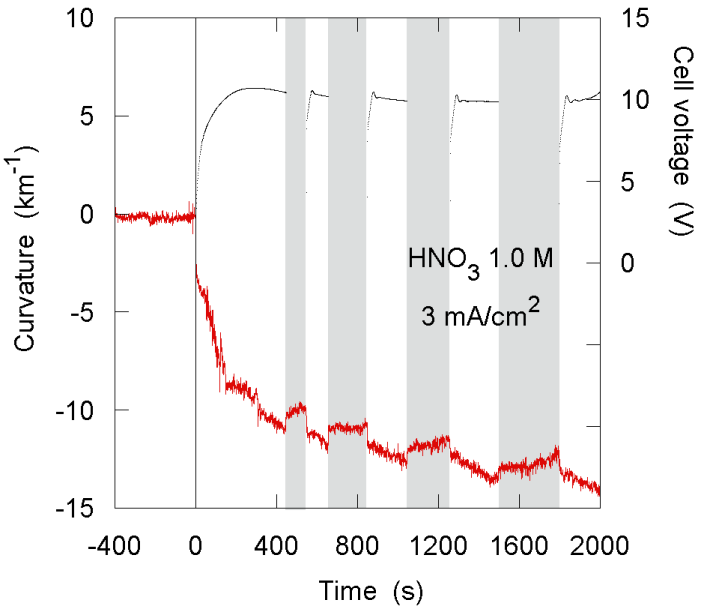

Figure 4.8: Evolution of the sample curvature and of the cell voltage during anodisation in 1.0 M HNO_3 at 3 mA/cm^2, showing the characteristic discontinuities associated with the relaxation of electrostriction stresses upon interruption of the anodisation process. The shaded regions correspond those interruptions.

Results and discussion

Figure 4.7 shows a typical evolution of the cell voltage V with time during anodisation in nitric acid at 1 mA/cm^2 (the evolution was qualitatively very similar for the other anodising conditions). The V-t curve is seen to be characterised by two distinct stages. In the first growth stage, the cell voltage increases relatively fast up to around 10 V, the exact value depending on the current density and the electrolyte used. After that, the cell voltage stabilises and reaches a plateau region. From the vanishing slope of the V-t curve in the plateau region, which is generally attributed to the onset of massive oxygen evolution, it can be assessed that the oxide film thickens at a significantly reduced rate.

Measurements of the electrostriction stress in nitric acid have only been carried out in the plateau region, while in the case of phosphoric acid, measurements were carried out in the two growth regions. Fig.4.8, showing in parallel the evolution of the cell voltage and of the sample curvature during the experi-

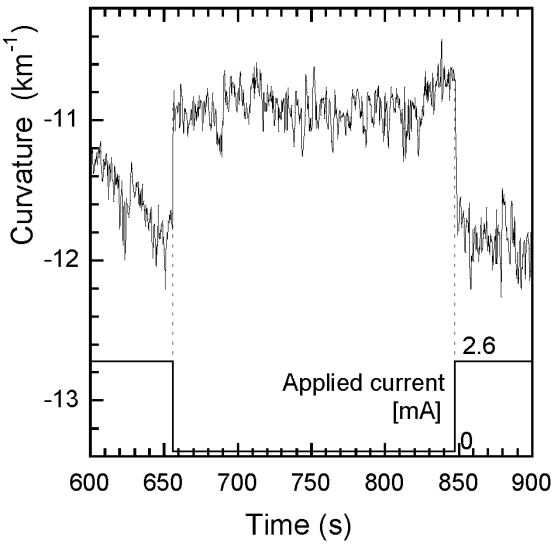

Figure 4.9: Example of discontinuities in the curvature evolution resulting from the interruption and re-application of the current in the plateau region during Ti anodisation in 1.0 M HNO_3 at 3 mA/cm^2.

		σ_{ES} initial[MPa]	σ_{ES} final[MPa]
HNO_3 3 mA/cm^2	1^l	199 ± 31	232 ± 15
	2^l	192 ± 20	217 ± 51
	3^l	163 ± 62	196 ± 16
	4^h	161 ± 33	175 ± 46
HNO_3 1 mA/cm^2	1^l	327 ± 17	327 ± 18
	2^l	314 ± 34	323 ± 47
	3^l	505 ± 83	517 ± 100
H_3PO_4 0.5 mA/cm^2	1^*	1270± 200	2280 ± 200
	2^*	772 ± 156	1230 ± 494
	3^*	619 ± 315	1065 ± 280
	4^*	260 ± 26	830 ± 83
	5^*	315 ± 40	325 ± 105
	6^*	228 ± 64	285 ± 145

Table 4.3: Measured values for the electrostriction stress σ_{ES}, based on the quantification of the initial and the final curvature jumps and on the thickness of the oxide film calculated using an AR value of 1.9 nm/V.

ment carried out in HNO_3 at 3 mA/cm^2, illustrates the experimental procedure. The shaded zones correspond to the time-intervals when anodisation was interrupted. An enlargement of the second shaded region of Fig.4.8, showing a typical curvature discontinuity, is presented on Fig.4.9. Table 4.3 summarises the σ_{ES}-values calculated from all curvature discontinuities for the three anodisation experiments, both at interrupting (σ_{ES} initial) and re-applying (σ_{ES} final) the current. These stress values have been calculated based on a value of 1.9 nm/V for the anodising ratio, as measured by ex-situ ellipsometry. For H_3PO_4, measurements 1^* to 4^* are taken in the first growth region, while 5^* and 6^* are inside the plateau region. The error values given in Table 4.3 correspond to uncertainties in quantifying the curvature discontinuities as a result of the finite curvature resolution (on the order of 0.2 km^{-1}). As the curvature jumps upon interrupting the current were always in the tensile direction, all σ_{ES}-values reported correspond to compressive electrostriction stresses. Generally, during current interruption, a continuing relaxation of the curvature in the tensile direction is observed (See Fig.4.10a). Only some of the discontinuities of the experiment carried out in HNO_3 at 3 mA/cm^2, like the one shown in Fig.4.9, did not exhibit this feature.

It can be seen from Table 4.3 that, mainly for the measurements carried out in H_3PO_4 before the plateau region (points 1^* to 4^*), the curvature discontinuities measured upon current interruption differ from the ones measured when the current is turned back on. We consider that the initial discontinuities

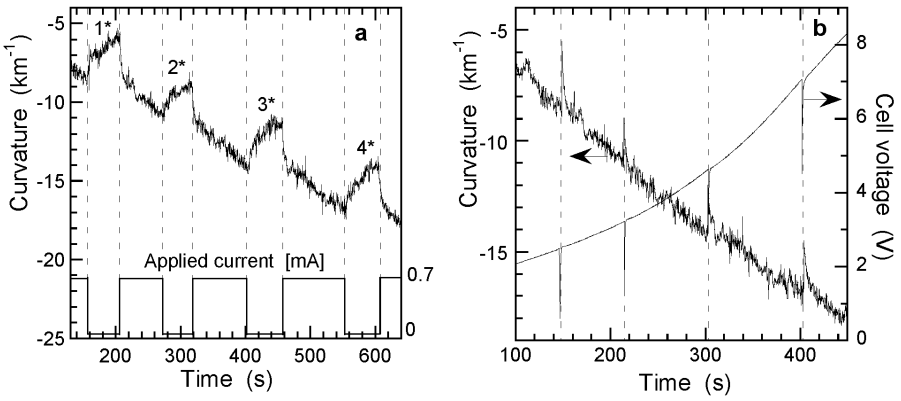

Figure 4.10: (a) Evolution of the curvature κ with time in the first growth region during interrupted anodisation in H_3PO_4. The numbers refer to the curvature jumps quantified in Table 4.3. (b) Corresponding κ-t and V-t curves, reconstructed by removing the time periods when the current was turned off.

provide more accurate measurements of the electrostriction stress than the final one. Indeed, growth of the oxide film resumes as soon as the current is switched on again. Therefore, separating the curvature change due to the electrostriction stress from the contribution of the growth stress is not straightforward for the final curvature discontinuities. Due to the reduced growth rate in the plateau region as a result of the oxygen evolution reaction, the discrepancy between the final and initial curvature jumps can be expected to be most significant before the plateau region is reached, as indeed observed. In the following discussion, we have therefore based our analysis of the permittivity evolution during anodisation on the initial curvature discontinuities only, which are believed to be more reliable.

Fig.4.12 shows the values for ϵ, calculated from Eq.4.12 and corresponding to the measured curvature jumps in, respectively, H_3PO_4 (a) and HNO_3 (b). It should be noted that these values are based on the hypothesis that the evolution of the curvature jumps is fully attributable to variations of the dielectric constant. This hypothesis is further discussed in section 4.4.3. The dielectric permittivity is observed to decrease progressively during the first growth regime (points 1^* to 4^* on Fig.4.12a), after which it tends towards a constant value when the voltage reaches the plateau regime (Fig.4.12b and points 5^* to 6^* on Fig.4.12a). Although the ϵ values should be confirmed by supplementary

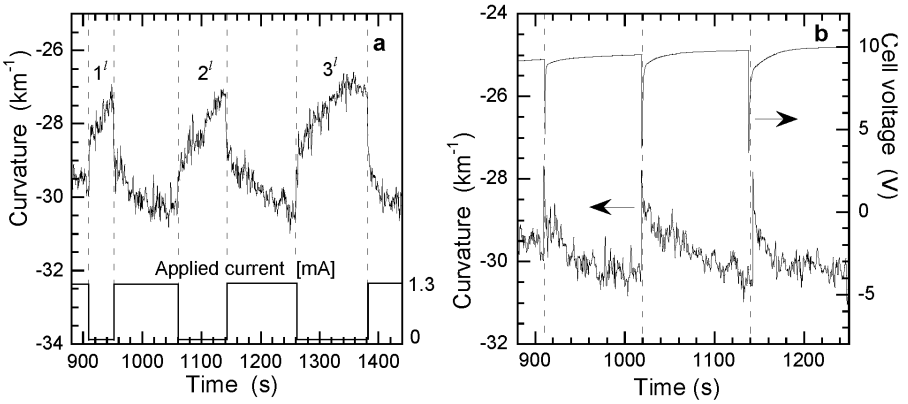

Figure 4.11: (a) Evolution of the curvature κ with time in the plateau region during interrupted anodisation at 1 mA/cm^2 in HNO_3. The numbers refer to the curvature jumps quantified in Table 4.3. (b) Corresponding κ-t and V-t curves, reconstructed by removing the time periods when the current was turned off.

capacitance measurements, the fact that the calculated values (25 to 70) lay in the range of literature values for anodic TiO_2 films is reassuring.

For the experiments carried out in HNO_3 with different current densities, the average value of the electrostriction stress and hence of the corresponding permittivity are observed to increase with decreasing applied current density (see Fig.4.12b). This result is in agreement with the (controversial) observation by Blackwood et al. that anodic oxide films grown more slowly (i.e. at lower current density) are denser and therefore have a larger permittivity than rapidly grown ones (see section 1.2.4). When considering the evolution of the dielectric constant for a given set of experimental conditions, two observations have been made. First, during the initial high-efficiency region, the electrostriction stress decreases continuously as the film thickens, which was interpreted as a decrease of the film's dielectric constant. This observation will be further discussed in section 4.4.3, after the description of the second series of experiments. In contrast, the electrostriction stress in the plateau region is observed to be essentially constant in all cases. As the thickness of the film is expected to remain almost constant during that stage, this suggests that the permittivity of the film remains constant as well, i.e. that no major structural change takes place in the film during that stage.

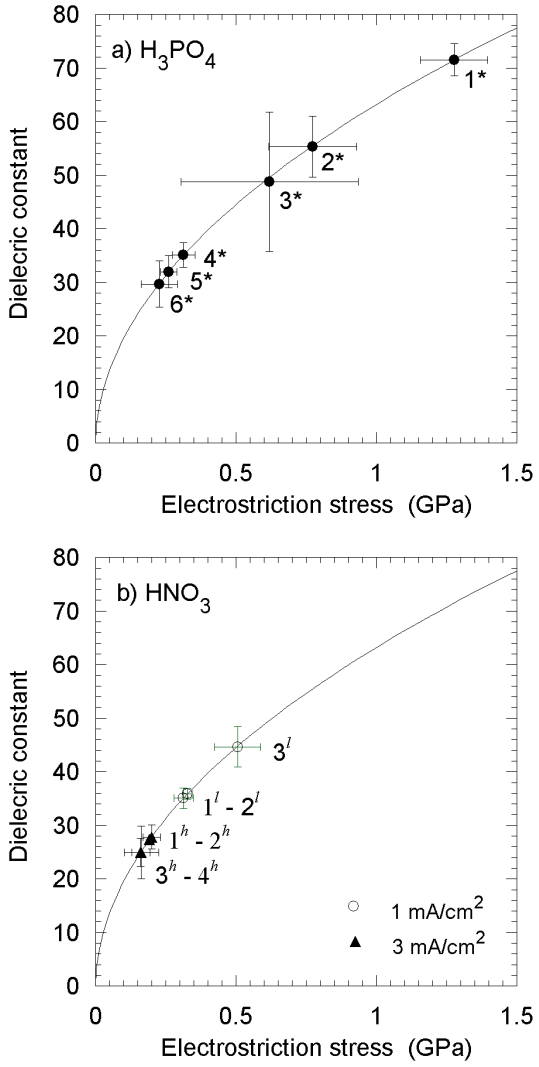

Figure 4.12: Values of the dielectric permittivity calculated from Eq.4.12 and corresponding to the measured electrostriction stresses in (a) H_3PO_4 and (b) HNO_3. The latter values have been obtained under the hypothesis that the evolution of the curvature discontinuities is fully attributable to the evolution of the dielectric constant.

4.4.2 Second series of experiments:

Experimental

The second series of data comes from the experiment already presented in chapter 3, which consisted of a series of 6 continuous anodising experiments carried out under galvanostatic conditions, with a current density of 4 mA/cm^2 in 1.0 M H_2SO_4. As previously discussed the curvature evolution accompanying this anodisation experiment was characterised by a marked compressive maximum taking place around 15V. The six samples were anodised up to forming voltages respectively below (5V, 9V and 12V) and above (15V, 25V and 40V) the voltage at which the compressive maximum was observed. At the end of each experiment, the curvature discontinuity resulting from the relaxation of the electrostriction stress was quantified. One supplementary sample was anodised to a final voltage of 40V under the same conditions as for the six continuous experiments, but the anodisation was interrupted repeatedly, similar to the procedure described for the first series of experiments in subsection 4.4.1. The anodisation was first interrupted when the cell voltage reached 5V, after which it was left at open circuit for 80 seconds. The current was then re-applied to proceed further in the growth process. A second interruption of 80s was then carried out at 9V, then 12V, 15V and 25V. The evolution of the anode curvature was monitored continuously during each interruption at open-circuit and the discontinuities in the evolution of the curvature resulting from the relaxation of the compressive stress contribution from electrostriction have been quantified. The latter have been compared to the curvature discontinuities measured at the end of each of the 6 continuous experiments. This type of experiment aimed at assessing the influence of interrupting the anodisation on the growth of the oxide film and therefore providing insight into the reversibility of the growth instabilities described in chapter 3.

Results

At the end of each experiment, when the applied current is interrupted, a characteristic discontinuity in the evolution of the curvature, resulting from the relaxation of the electrostriction stress, is observed. Fig.4.13 shows the curvature discontinuities measured at the end of each experiment. Their magnitude is presented in Table 4.4. As to the interrupted experiment, the time-evolution of the curvature and of the cell voltage are presented on Fig.4.14. The curvature signal exhibits a series of discontinuities, corresponding to the successive current interruptions and re-applications. Fig.4.15 shows the curvature discontinuities observed upon each interruption, while their magnitude is presented in Table 4.4.

It can be observed that the evolution of the electrostriction stress·thickness

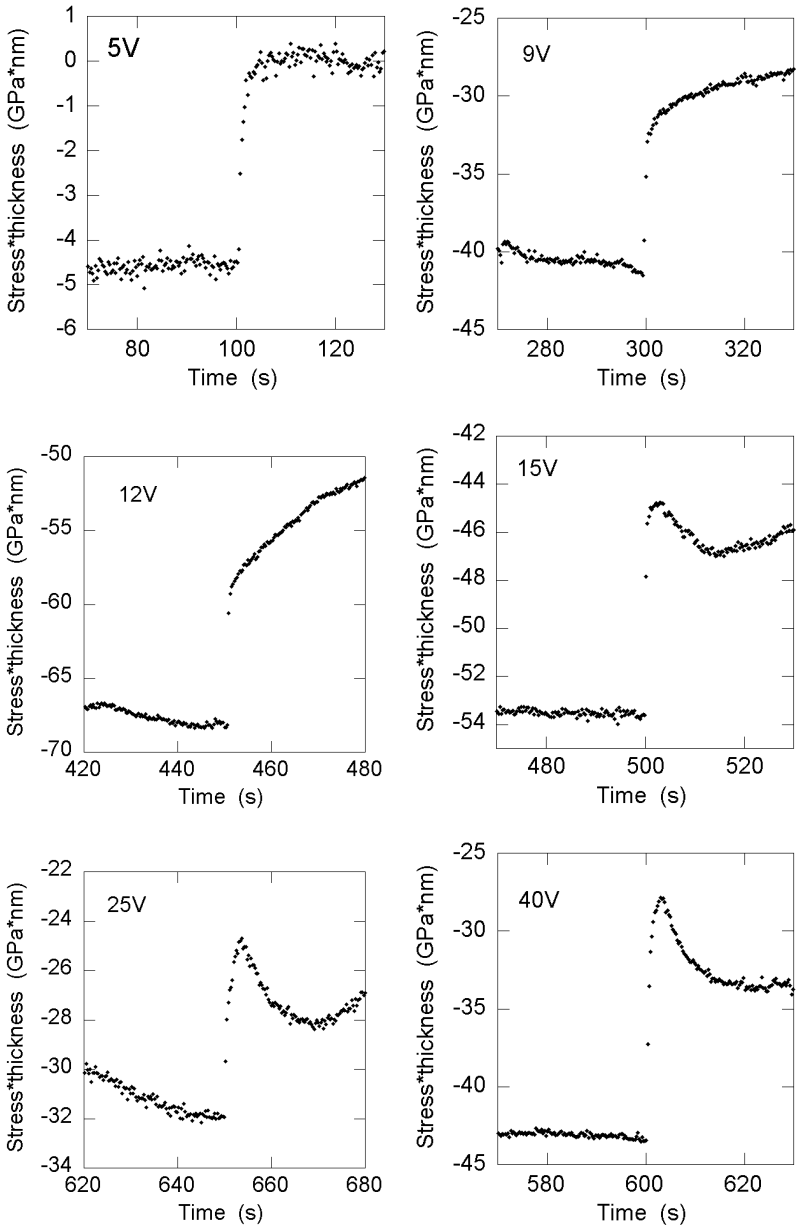

Figure 4.13: Discontinuities in the stress·thickness evolution corresponding to the relaxation of the electrostriction stress in the oxide film under open-circuit conditions at the end of the six continuous experiments.

	Magnitude of the stress·thickness discontinuity [GPa*nm]	Dielectric constant ϵ
continuous experiments		
5V	4.3±0.2	50.3±1.5
9V	9.5±1.0	56.1±3.2
12V	8.8±0.7	46.2±1.7
15V	6.9±1.1	36.7±3.0
25V	6.5±1.5	27.4±3.2
40V	12.5±3.0	30.0±3.7
interrupted experiment		
5V	5.7±0.7	58.5±3.9
9V	6.3±1.2	42.2±4.3
12V	6.5±1.3	39.7±4.0
15V	6.0±0.6	34.4±1.8
25V	7.4±1.7	29.2±3.5
40V	7.0±1.9	22.8±3.1

Table 4.4: Measured values of the discontinuities of the stress·thickness evolution and corresponding values of the dielectric constant, calculated according to Eq.4.12, for both the six continuous experiments and the interrupted one.

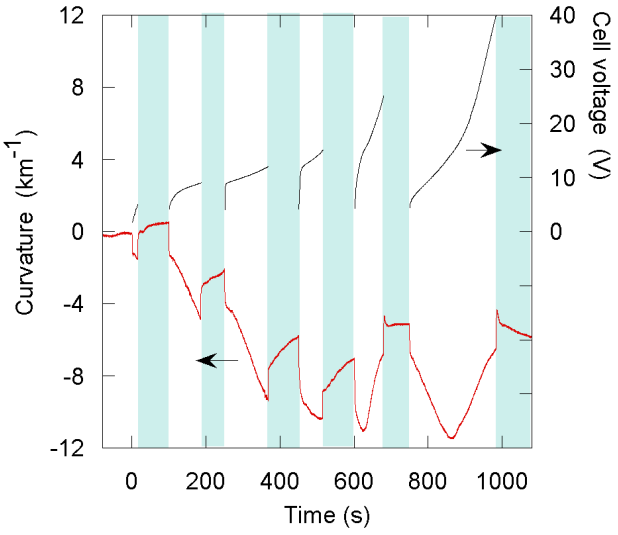

Figure 4.14: Evolution of the sample curvature and of the cell voltage for the interrupted experiment. The shaded zones correspond to the time-periods when the anodisation was interrupted. (This figure is identical to Fig.3.13 presented in the third chapter.)

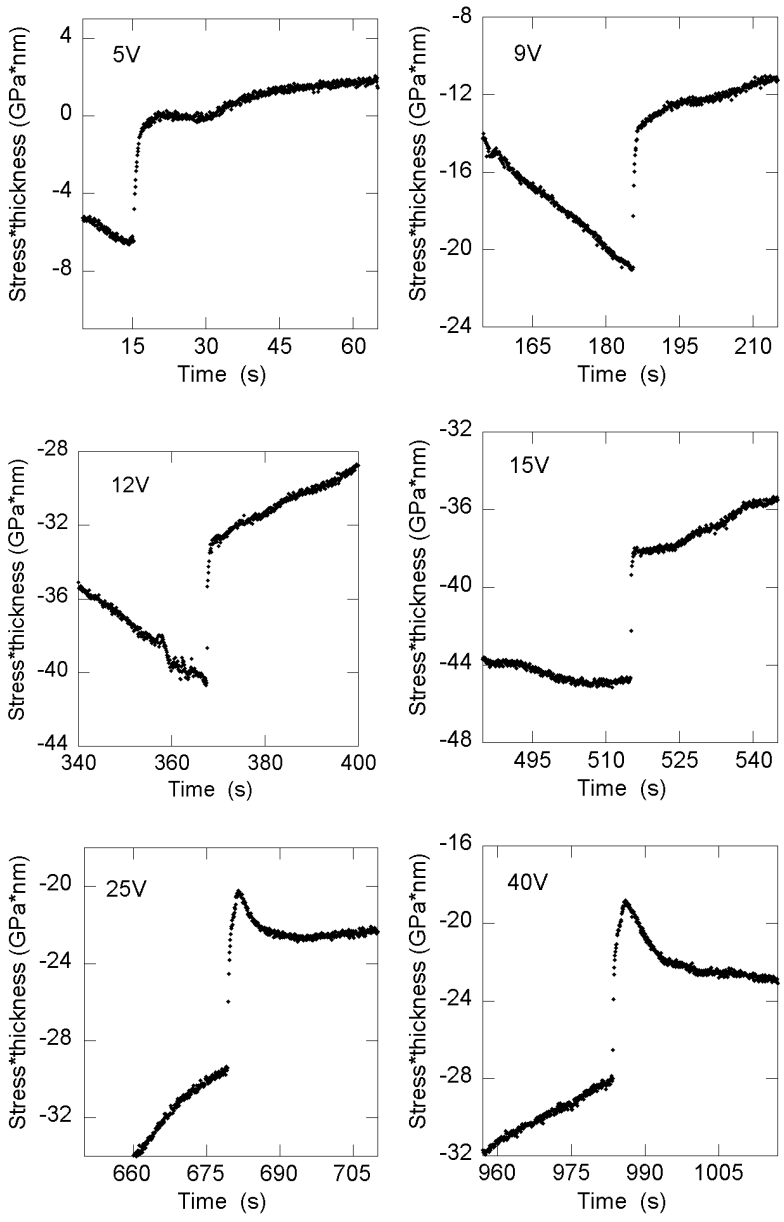

Figure 4.15: Discontinuities in the stress·thickness evolution corresponding to the relaxation of the electrostriction stress in the oxide film under open-circuit conditions at the beginning of each interruption for the interrupted experiment.

product with V for both the six continuous experiments and the interrupted one does not correspond to what would be expected for a homogeneous barrier oxide film with constant dielectric properties growing under constant electrostatic field conditions. Indeed, under such conditions, the electrostrictive stress is expected to keep a constant value, so that the contribution from electrostriction to the overall stress·thickness product would be expected to increase proportionally with the thickness of the oxide film, i.e. with the cell voltage [164]. In our case, the stress·thickness discontinuity increases with V only up to 9V, after which it is observed to remain fairly constant. This might indicate that the assumption of constant dielectric properties breaks down at some point during the growth. The ϵ values corresponding to the measured electrostriction discontinuities are presented in Table 4.4 and plotted on Fig.4.16. The latter values have been calculated according to Eq.4.12. The calculated ϵ values show a decreasing trend with increasing V. The average value measured at the beginning of anodisation (5V, $\epsilon = 54\pm6$), agrees well with literature values for dense anodic TiO_2 [131, 23], while the average value measured in the third stage at 40V ($\epsilon = 26\pm5$) is comparable with the one reported by Di Quarto et al. in the case when they observed growth instabilities [51].

The evolution of the stress·thickness product under open-circuit conditions, after the relaxation of the electrostriction stress, is also very characteristic (see Fig.4.13). At 5V, after the almost instantaneous relaxation of the compressive electrostriction stress, a steady-state stress plateau is rapidly attained, which is indicative that no further stress relaxation takes place. In the case of the samples anodized to 9V and 12V (hence into the second stage), the stress·thickness product does not reach such a plateau after the initial discontinuity and the relaxation is observed to proceed further for several minutes in the tensile direction. From 15V on (i.e. in the third stage, after the compressive maximum), a different shape is observed, characterized by a tensile peak followed by a compressive decay to a steady-state plateau. The same trend is observed for both the six continuous experiments and the interrupted one, with the only difference that, for the latter, the shape of the transient observed upon interruption at 15V is similar to that observed at 5V, 9V and 12V, while, in the case of the continuous experiments, the transient at 15V exhibits a shape similar to that observed at 25V and 40V. As, in the case of the interrupted experiment, the compressive maximum was observed to take place at a slightly higher cell voltage than for the continuous experiments (15.0V instead of 13.4V), the interruption at 15V in the interrupted experiment takes place right before (or at) the compressive maximum, while it takes place right above the compressive maximum for the continuous experiment. This, in fact, tends to confirm that the characteristic shape of the open-circuit transient is intrinsically related to the growth instability taking place at the compressive maximum. So far, the origin of this specific shape is still open question.

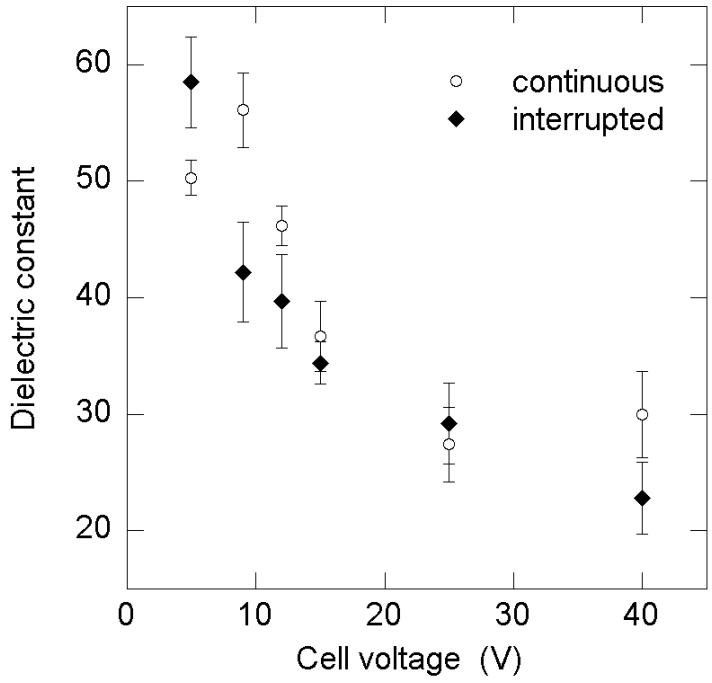

Figure 4.16: Evolution of the dielectric constant of the film for both the continuous experiments and the interrupted one, as calculated from the stress·thickness discontinuities using Eq.4.12. The latter values have been obtained under the hypothesis that the evolution of the curvature discontinuities is fully attributable to the evolution of the dielectric constant.

4.4.3 Common Discussion

Evolution of the curvature discontinuities in the course of the growth process.

The main observation common to the two series of experiments is the fact that the curvature discontinuities $\Delta\kappa_{ES}$, corresponding to the relaxation of the electrostriction stress, do not increase with the final voltage, as would be expected for barrier films of constant ϵ. For the sake of clarity, the discussion will focus on the observations from the second series of experiments, but is applicable to experiments from the first series as well.

As observed from the values tabulated in Table 4.4, the curvature discontinuities $\Delta\kappa_{ES}$, which are proportional to the product of the electrostriction stress and the film thickness, increase only slightly from the first to the last sample, while the thickness of the oxide film does increase. For the interrupted experiment, this observation is particularly striking, with $\Delta\kappa_{ES}$ increasing by 20% only between 5 and 40V, while the thickness of the oxide film is multiplied by a factor 8. This observation can be interpreted as a decrease of the electrostriction stress in the film, which itself would arise from a decrease of the dielectric constant. However, the reason why the dielectric constant of the film would decrease is not straightforward. Indeed, a decrease of the dielectric constant would correspond to a significant decrease of the density of the film, which is not very likely to occur, unless the nature of the oxide film changes dramatically in the course of the growth. Furthermore, a decrease of the density is clearly in contradiction with one of the scenarios proposed in the previous chapter, according to which the compressive stage would be related to an aging of the film leading to annihilation of free volume. In contrast, it can be seen as evidence supporting the second proposed scenario according to which oxygen gas would be evolved within the film in the compressive stage. In that case, the dielectric constant would decrease as a consequence of the presence of numerous tiny gas-filled cavities in the oxide film. However, the apparent independence of the $\Delta\kappa_{ES}$ towards the film thickness could be due to other reasons which must be considered as well.

According to the Stoney equation and our model equation for electrostriction Eq.4.12:

$$\Delta\kappa_{ES} \propto \sigma_{ES} h_{mech} \propto \epsilon^2 E^2 h_{mech} \tag{4.21}$$

where h_{mech} is defined as the thickness over which the electrostriction stress is experienced. In general, $h_{mech} = h_f$, but we cannot a priori neglect the possibility that $h_{mech} < h_f$. According to Eq.4.21, the fact that $\Delta\kappa_{ES}$ is almost constant indicates that either h_{mech} does not increase proportionally with h_f or that the electrostriction stress in the film progressively decreases

and compensates for the increase of the oxide thickness. Such a decrease of the electrostriction stress could be due to a decrease of the dielectric constant, as previously discussed, but could also arise from a decrease of the electric field to which the film is submitted.

As to the first possibility, if we assume that a region of the film of constant thickness adjacent to the metal/oxide interface would experience the stress, independent of the film thickness, this could indeed account for the observed behaviour. As discussed in chapter 1, it was proposed by Bradhurst and Leach [31] and by Nelson and Oriani [164] that the stress in the film is concentrated in the inner region of the film while the outer region, adjacent to the oxide/electrolyte interface, would grow relatively free of stresses. Moon and Pyun [159] go as far as concluding that stresses are fully determined by the first two or three atomic layers adjacent to the metal/oxide interface. This hypothesis seems plausible as far as the intrinsic growth-stresses concerns. However, in the case of the field-induced stress contribution, the stress is logically expected to be experienced by the whole region of the film to which the field is applied. Therefore, to our opinion, h_{mech} could be smaller than h_f only if the electric field is not applied to the whole film but to a fraction of it. Owing to the progressive build-up of a space charge in the film, the potential drop across the film could indeed be concentrated in a space-charge region smaller than the whole thickness of the film, as discussed by Blackwood [25] or Ueno et al. [239]. Lohrengel [140] also points out that the concentration of mobile ions in valve metal oxides is very large and can cause local distortions of the field strength. From typical values of the donor density in anodic TiO_2 films, Ueno et al. estimate the depth of the space-charge layer to be of the order of 25 nm. Hence, from about 12V on, the electric field might no longer be applied to the whole film, but to a thinner region adjacent to the oxide/electrolyte interface. In that case, the field might not be constant over the whole thickness, which will directly affect the evolution of the electrostriction stress in an intricate way.

As to the second possible origin, a decrease of the field in the film is a priori not unrealistic and would in addition be qualitatively coherent with our observed decrease of the growth efficiency, as will be further discussed in chapter 5. However, quantitatively, this scenario is unrealistic. Indeed, in order for $\Delta\kappa_{ES}$ to keep a constant value almost independent of the anodisation voltage, the effective field in the film would have to vary according to $E = 1/V$, instead of the expected constant value. This is not very likely as it would indicate that the proportionality between V and h_f does no longer hold, which is not coherent with our TEM-based thickness measurements.

Finally, it should be noted that, from 15V on, the electrostriction model given by Eq.4.12 might no longer be adapted. Indeed, the TEM investigation

demonstrated that the inner part of the film crystallises in that voltage range, hence leading to a 2-layer structure. More complex models would probably be necessary to describe adequately the mechanical and electrical behaviour of such a multi-layered sample. In addition, the electrostriction equation Eq.4.12, which was derived explicitly for amorphous materials, may no longer be applicable. Expressions linking α_1 and α_2 to the dielectric constant have been derived as well for crystalline materials with simple crystal symmetry (FCC) and differ considerably from those for amorphous films [218]. In the case of FCC materials, α_1 and α_2 have opposite signs, so that the predicted σ_{ES} will be smaller than in the case of amorphous materials. Below 15V, our samples consist of small crystallites embedded in an amorphous matrix (see chapter 3), so that the amorphous model seems to be much more adapted than a model developed for crystalline material. In the case of thicker films presenting an inner polycrystalline layer, like in the case of our sample grown up to 40V, our model is probably no longer adequate.

This question remains open and will require further investigation, including correlation of the stress measurements with capacitance measurements, in order to ascertain whether the observation of the constant $\Delta\kappa_{ES}$ reflects a change in the dielectric constant of the film or if it is due to the fact that our oxide films do not behave like ideal elastic dielectrics, which involves errors in the quantification of field or mechanical thickness. Our attempts to measure the film capacitance by ex-situ impedance measurements remained however unsuccessful, owing to the very leaky character of the oxide films which prevented any stable and reproducible measurement of the film capacitance.

Influence of the repeated interruptions

An important issue regarding our experimental methodology is the possible influence of the repeated interruptions on the growth process. Indeed, it is not easy to ascertain that interrupting the growth repeatedly does not affect the growth process too much, so that conclusions drawn from interrupted experiments also apply to continuous anodisation. In order to provide insight into that question, we have examined the 'reconstructed' V-t and κ-t curves obtained by removing from both curves the data corresponding to the time periods when the current was turned off. Figures 4.10a and 4.11a show the curvature evolution with time obtained for the first series of experiments in, respectively, H_3PO_4 in the first region and HNO_3 (at 1 mA/cm) in the plateau region. Figures 4.10b and 4.11b show the corresponding reconstructed κ-t and V-t curves. It can be seen that the curvature discontinuities measured in the first growth region show very good reversibility (Fig.4.10b): when the current is turned back on at the end of each interval, the cell voltage and the curvature return to their original values almost instantaneously. In contrast, samples

measured in the plateau region were observed to need more time to return to the initial values of V and κ obtained before the current was turned off, which could be indicative for a more marked influence of the interruptions on the growth process. As to the second series of experiments, we have compared the 'reconstructed' κ-t and V-t curves to the corresponding curves obtained for the continuous experiments. The continuous and reconstructed curves are plotted together on Fig.4.17a and b. In this case, the reconstructed V-t curve has been obtained by first removing the V-data corresponding to the time intervals when the anodisation was interrupted (shaded zones in Fig.4.14), and then by removing as well the V-data recorded after re-application of the current and corresponding to the time interval when the cell voltage had not yet recovered to its value measured just before the interruption. In that way, a continuously increasing V-t curve was obtained. The same procedure was followed for building the reconstructed curvature trace. The reconstructed V-t and κ-t curves are observed to be qualitatively identical to the one measured for the continuous experiments. In particular, the three distinct stages of both the cell voltage and the curvature evolution already identified for the continuous experiment are again observed. Although further characterisation would be required to ascertain that the interruptions do not affect the characteristics of the growing films, the observation that the reconstructed V-t and κ-t are almost identical to the ones measured for continuous experiments is believed to be evidence that the repeated interruptions of the anodizing process do not significantly affect the anodisation process. Therefore, we are confident that conclusions drawn for the interrupted experiment can be safely extended to the continuous growth process as well.

Influence of the intrinsic growth strains on the dielectric constant

It can be noted that the dielectric constant of the film was shown to be strain-dependent, as described by Eq.4.6. Hence, not only the reversible electrostriction stress but also the intrinsic growth stress is expected to have a direct influence on the film's dielectric constant. The question may arise as to whether the observed progressive decrease of ϵ could be the consequence of an increase of the average stress in the film. As pointed out in the previous paragraph, the decrease of ϵ indeed takes place in a V-region where large compressive stresses develop. McAleer and Peter [148] observed a similar decrease of the dielectric constant of their films and suggest that this could be the results of strains in the film. However, in our case, such an effect would be expected to act in the opposite direction. Indeed, the average stress in our anodic films was observed to be compressive for all experiments, thus being asociated with an increased number density n of polarisable molecules in the dielectric. According to the Clausius-Mosotti equation Eq.4.1, such an increase of n is expected to lead to

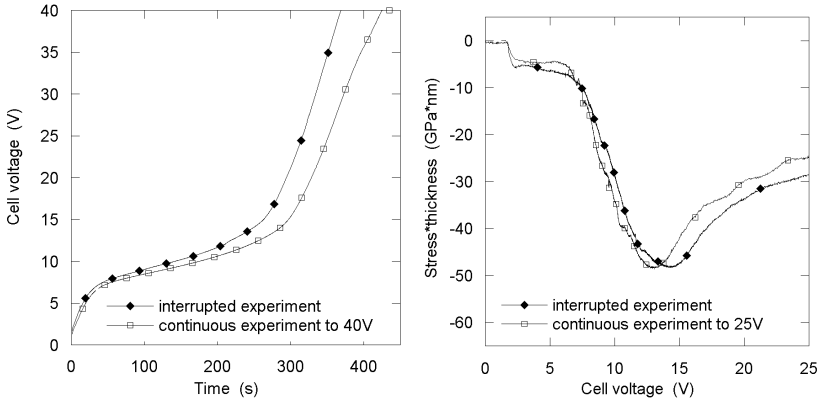

Figure 4.17: Comparison of the reconstructed κ-t and V-t evolution curves obtained for the interrupted experiment with those observed for the continuous experiments.

a larger value of the dielectric constant, in contrast with our observation. In addition, although large in-plane intrinsic stresses accompany the growth of the film, it should be noted that the intrinsic growth stress in the out-of-plane direction is much smaller, owing to the fact that the film can grow freely in the z-direction. Therefore, the intrinsic contribution to the overall stress in not expected to have a significant influence on the film's dielectric constant ϵ_{zz} in the out-of-plane direction.

4.5 Conclusion

From the experimental point of view, the interest of high-resolution curvature measurements for investigating electrostriction stresses in anodic oxide films has been demonstrated. This technique was found to be well-adapted to this kind of measurements, both in terms of curvature and time resolution. The electrostriction stress contribution could be separated from the irreversible intrinsic growth stresses and its field-dependence was investigated. Quantitative experimental data on the magnitude of electrostriction stresses in thin anodic TiO_2 films is provided as well. From the theoretical point of view, a novel equation was proposed for amorphous materials, linking the electrostriction stress to the electrostatic field and the material dielectric constant. This new equation is fundamentally different from the equation generally used in the literature in that it takes into account explicitly the dielectrostriction phenomenon. It predicts a quadratic dependence of the electrostriction stress on the dielectric constant, in contrast to the linear dependence predicted by the classical equa-

tion. A good agreement was observed between our measured electrostriction stress values and predictions from our newly-derived equation. Finally, it has been discussed how the evolution of the electrostriction stress could be used to diagnose changes in the material dielectric and/or morphological characteristics.

Chapter 5

Discussion of conductivity transitions in anodic TiO_2

Contents

As already introduced in chapter 1, the anodisation of Ti presents some peculiarities, most of them being somehow related to the semiconducting character of TiO_2. Anodisation of Ti is, for instance, typically accompanied by side-reactions, hence inducing characteristic variations of the growth efficiency. The first section of this chapter deals with a very fundamental question which, to the best of our knowledge, has never been addressed explicitly in the literature: do efficiency changes induce field variations in the film? This question is discussed in the well-established framework of the high-field model. The second section provides a discussion of the influence of such field variations on the cell voltage evolution. In particular, the origin of a local V-maximum of the V-t anodisation curves, which was reproducibly observed to accompany the efficiency changes, is discussed. Finally, in the third section, the possible microstructural origin of the transition is examined, based on TEM observations.

5.1 Growth kinetics of anodic TiO_2 films

The high-field growth model is usually considered to be applicable to the growth of anodic TiO_2 films. However, the fact that only a fraction of the total current (i_{tot}) is carried by ions (ionic current i_i), owing to the semiconducting character of TiO_2, must be taken into account when studying the growth kinetics. We can define an ionic efficiency η=i_i/i_{tot} and write the high-field equation as:

$$i_i = \eta \cdot i_{tot} = i_o exp(\beta \cdot E) \tag{5.1}$$

Keeping in mind the definition of the anodising ratio, Eq.5.1 can be written equivalently as

$$AR = \frac{\beta}{ln(\eta) + ln(i_{tot}) - ln(i_o)} \tag{5.2}$$

According to Eq.5.2, the value of the anodising ratio can only be constant during galvanostatic anodising as long as the growth efficiency η remains constant as well. This is indeed the case during anodising for most of the valve metals forming insulating oxide films. However, it is not so for semiconducting oxides such as TiO_2, for which efficiency changes are to be expected as a consequence of side-reactions accompanying the growth of the film [157]. In that case, Eq.5.2 predicts an increase of the anodising ratio when the growth efficiency decreases.

5.2 Influence of efficiency changes on the cell voltage evolution

The voltage evolution with time during galvanostatic anodising of bulk Ti has been reported in the literature to exhibit several particularities. One of them is the as yet unexplained observation of local maxima and hence the presence of a local V-decrease, followed by a change in the slope of the chronopotentiometric V-t curves. Ammar and Kamal for instance reported the presence of what they called "slight maxima" associated with slope changes on the V-t curves during bulk Ti anodising with current densities in the mA/cm^2 range [10]. Some of the anodising curves presented in the work of Delplancke et al. [47] exhibit the same characteristic features: their V-t curves also exhibit a local V-decrease associated with a slope change. Considering the definition of the anodizing ratio (AR),

$$AR(t) = \frac{h_{ox}(t)}{V(t)} \tag{5.3}$$

such a local decrease in the evolution of the anode voltage $V(t)$ can be attributed to an instantaneous increase in the anodising ratio, provided that the thickness of the oxide film h_{ox}, assumed to be homogeneous over the sample

surface, is continuously increasing with time. As discussed in the first section, such AR-changes can arise from efficiency changes. The aim of this section is to report our observation that the characteristic V-t behaviour during galvanostatic Ti anodising, in particular the local V-decrease, can be quantitatively reproduced within the framework of the classical high-field model, based on the assumption that the change in AR is entirely determined by the evolution of the growth efficiency.

Experimental

Ti anodising
This study has been carried out on Ti electrodes from the STi batch, prepared as described in chapter 2. Anodising of the Ti thin films was carried out under galvanostatic conditions in 1.0 M H_2SO_4 with a current density of 4 mA/cm^2. Six samples were anodised under the same conditions, but up to different anodising voltages of, respectively, 5, 8, 11, 15, 21 and 25V. In contrast to the experiments described in the previous chapters, the electrochemical cell consisted of a classical 3-electrodes set-up with the Ti thin film anode, a stainless steel cathode, and a calomel reference electrode. The area of the sample surface exposed to the electrolyte was 1 cm^2. It should be noted that, in our data analysis, the anode voltage V has been assimilated to the potential drop across the oxide film ϕ_{ox}. In fact, it is the latter which more rigorously should have been used in Eq.5.3 instead of V. However, the difference between V and ϕ_{ox}, which can arise from additional potential differences at the metal/oxide or oxide/electrolyte interface, has been demonstrated in the literature to be smaller than 0.1V for typical valve metals, and to remain constant under galvanostatic anodising conditions [44, 220]. Relative to the anode voltages measured in this work, this contribution can be considered to be negligible, making the anode voltage V a reliable estimation of ϕ_{ox}. It should be noted that, although the same overall V-t behaviour, characterised by the local V-decrease accompanying the slope change, was observed independent of the electrolyte temperature, the transition was much sharper when the anodisation was carried out in a cold electrolyte. In particular, the V-t curve shown on Fig.5.1, showing a very sharp transition, was obtained for an electrolyte temperature of around 7°C.

Oxide characterisation
The thickness of the oxide films was measured by ex-situ ellipsometry using a Sentech SE800 spectroscopic ellipsometer. Spectra were recorded over the wavelength range of 190 to 900 nm. The ellipsometry data were then fitted to a two-layer model consisting of a dielectric TiO_2 film (with the imaginary part of the refractive index equal to 0) on a Ti substrate. A spectrum was recorded for the Ti substrate prior to anodising and used as an optical model for the Ti layer. Both the thickness (h_{ox}) and the optical index (n) of the TiO_2

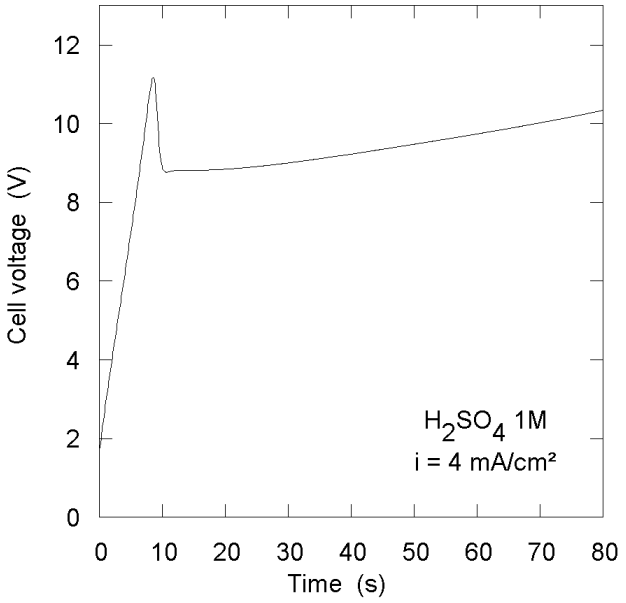

Figure 5.1: Experimental chronopotentiometric anodising curve for a sputtered Ti film from the STi batch anodised in 1.0 M H_2SO_4 at 4 mA/cm^2.

layers were free fitting parameters to the ellipsometric data. While the fitted h_{ox}-values increased with the forming voltage, a constant n-value of 2.0±0.1 (at λ=632nm) was found for all samples. The atomic density (Γ) of the TiO_2 layers was measured by Rutherford Backscattering Spectrometry (RBS). Each sample was analysed at 170° backscattering angle with 2.8 MeV He^+ ions. The samples were tilted by 6° within the beam-analyser plane. The RBS data were analysed using commercial SIMNRA software. The density ρ of the oxide film was then calculated according to

$$\rho = \frac{\Gamma}{h_{ox}} \frac{M_w}{3N_{AV}} \tag{5.4}$$

where M_w is the molar weight of TiO_2 (80 g/mol) and N_{AV} Avogadro's number.

Results and Discussion

Fig.5.1 shows a typical anodising curve reproducibly observed during galvanostatic anodising of our sputtered Ti films in 1.0 M H_2SO_4 at 4 mA/cm^2. The V-t curve is characterized by two linear stages, separated by a transition region

where a sharp, local decrease of V is observed. The constant slopes corresponding to the first and second stage have been determined as, respectively, 1.116±0.003 V/s and 0.0260±0.0001 V/s. In order to qualitatively understand the origin of this characteristic voltage evolution, Eq.5.3 can be combined with a Faraday-type expression for the oxide thickness :

$$V(t) = \frac{h_{ox}(t)}{AR(t)} = \frac{1}{AR(t)} \left(\frac{M \cdot i_{tot}}{4F\rho} \int_o^t \eta(t)dt + h_o \right) \tag{5.5}$$

where F is Faraday's constant, i_{tot} is the total applied current density and h_o is the thickness of a possible native oxide layer on the anode surface. Note that, in the above formula, we have implicitly assumed that the rate of chemical dissolution of the oxide film in the electrolyte is negligible. This is not necessarily true for all anodic oxides [223], but it can be expected to be the case for TiO_2 which is known to be chemically very stable in diluted H_2SO_4 [22]. On the other hand, any electrochemically-assisted oxide dissolution is taken into account by the growth efficiency $\eta(t)$. According to Eq.5.5, the constant slopes $\mathrm{d}V/\mathrm{d}t$ observed for the first and second stage suggest that the anodising ratio and the oxide density remain constant within each of these regions, while the transition region is indicative for a variation of at least one of these parameters. We verified this explicitly by quantifying the evolution of the oxide thickness and density during anodising.

Fig.5.2 shows the thickness evolution of the oxide film measured ex-situ by ellipsometry as a function of the final voltage. The first two points correspond to samples for which anodising was stopped before the transition region, while the last four ones correspond to samples which have been anodised into the second linear stage. From this figure, the AR calculated from the two available data points in the 1^{st} stage (1.9±0.1 nm/V) is observed to be significantly different from the one corresponding to the 2^{nd} stage (2.7±0.1 nm/V). The density of the oxide films was then assessed by combining the thickness data from ellipsometry with atomic density values measured on the same samples by RBS, shown in Fig.5.3. According to Eq.5.4, the density of the oxide films can be extracted from the slope of the linearly proportional fit in Fig.5.3. A constant density of 3.0±0.2 g/cm^3 is thus obtained, statistically equal for all samples during both stage 1 and 2. This observation is in agreement with the fact that a constant value of the refractive index was measured for all samples. Moreover, the absolute values of the density and the refractive index are indicative that our anodic oxide films are essentially amorphous [57, 172]. From the above measurements of h_{ox} and ρ, it can therefore be concluded that within each of the 2 constant slope stages, the anodising ratio AR (and, according to Eq.5.2, therefore also the growth efficiency η) and the density of the oxide film remain constant, while in the transition region, AR is observed to increase while ρ remains constant. As a result, the derivative of Eq.5.5

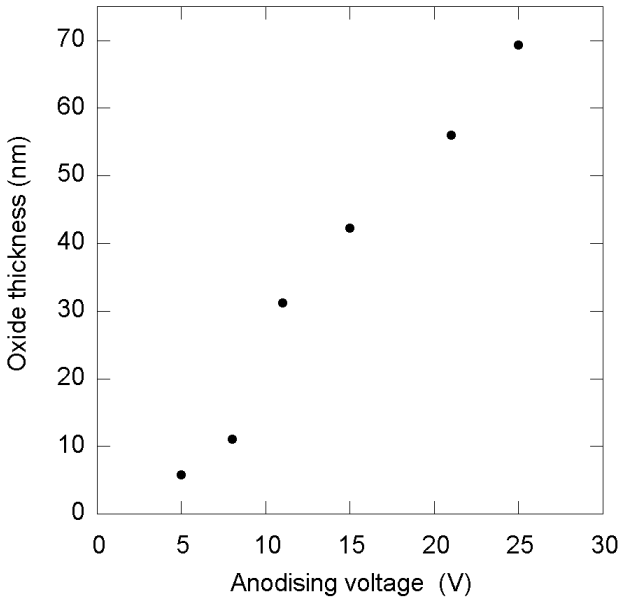

Figure 5.2: Thickness of the anodic oxide films, measured by spectroscopic ellipsometry, as a function of the final anodising voltage.

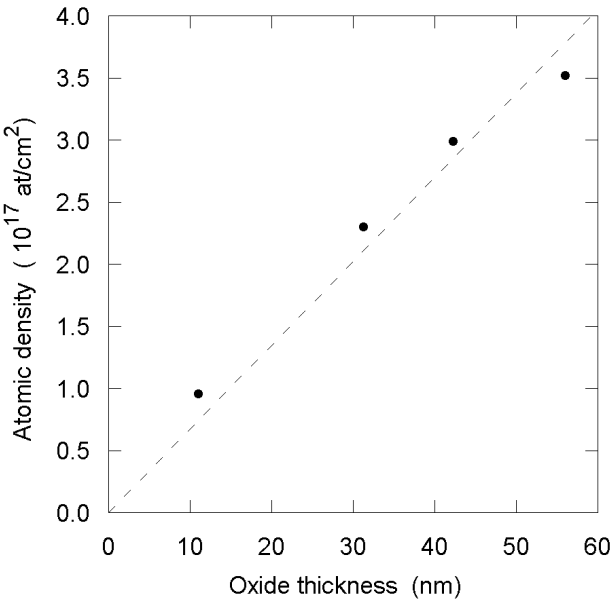

Figure 5.3: Atomic density values, as measured by RBS, as a function of oxide thickness determined by ellipsometry.

simplifies to the following expression for each of the 2 constant slope stages (i = 1,2) :

$$\left(\frac{dV}{dt}\right)_i = \frac{M \cdot i_{tot}}{4F\rho}\left(\frac{\eta}{AR}\right)_i \tag{5.6}$$

According to Eq.5.6, growth efficiency values can then be calculated for the first and second stage from the experimental dV/dt, density and AR values. The slope of the first stage corresponds to an efficiency of 78±5%, while in the second stage, the oxide film grows with a significantly reduced efficiency of only 2.5±0.2%. Such a dramatic drop in anodising efficiency has been reported by many others before and is characteristic for Ti anodising. As already introduced in chapter 1, it is a direct consequence of a major fraction of the current through the semiconducting TiO_2 film becoming electronic in nature above a certain threshold voltage. The origin of this transition in the conduction properties of the film will be discussed further in the third section.

Based on the above-determined AR- and η-values, the characteristic rate constants i_o and β of the high-field model can now be evaluated from Eq.5.2. The thus obtained values i_o = 6.6 10^{-6} mA/cm^2 and β = 25.5 nm/V are well within the range of published values for anodic TiO_2 [10, 139, 167]. It should

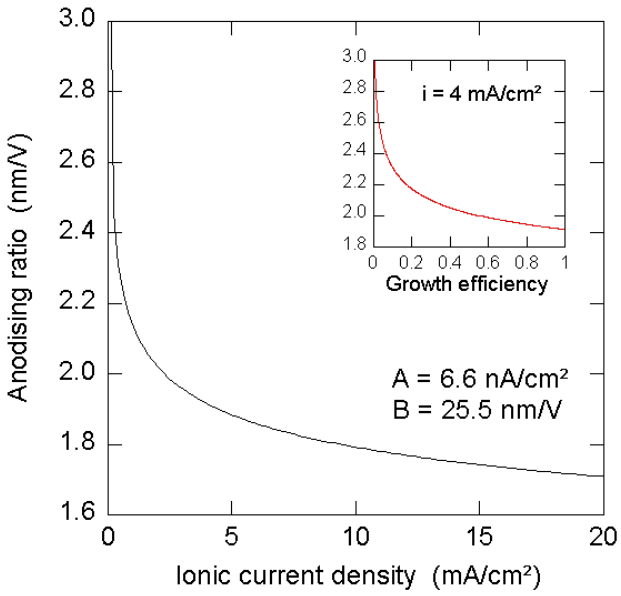

Figure 5.4: Simulated evolution of the anodising ratio with ionic current density, according to Eq.5.2. The values determined for the high-field rate constants i_o and β are characteristic for Ti anodising. The inset shows the predicted evolution of the anodising ratio with growth efficiency for the current density of 4 mA/cm^2 applied in this work.

be noted that, the previous extraction of i_o and β is implicitly based on the assumption that their values are constant for a given metal, electrolyte and temperature and are not affected by the changes in the ionic current density or the resulting change in the electric field. As previously introduced in section 1.1.2, the two parameters of the high-field model are defined as:

$$i_o = zF\nu ac_x exp\left(\frac{-W}{RT}\right) \tag{5.7}$$

and

$$\beta = \frac{\alpha azF}{RT} \tag{5.8}$$

Considering the definition of β, the latter parameter is determined by the activation distance associated with the transfer of ions to an adjacent site. It is therefore expected to be unaffected by the magnitude of the current flowing through the film. The primary current i_o depends explicitly on the concentration c_x of charge carriers in the film, which could indeed be field-dependent [114]. In our case, the oxide film right after the transition would contain an excess of charge carriers and would evolve towards an equilibrium state characterised by a lower concentration of charge carriers and hence a lower i_o. However, according to Bean et al. [19], such a field-dependence of i_o is observed only under low-field conditions. Therefore, this effect is expected to have only a limited impact on our calculated i_o-values. With the above calculated values for the rate constant i_o and β, Fig.5.4 then shows the evolution of the anodising ratio as a function of the ionic current density ($i_i = \eta i_{tot}$), as predicted by Eq.5.2. The inset shows the predicted evolution of AR as a function of the growth efficiency for an applied current density of 4 mA/cm^2, identical to the one used in this work. It is seen that the anodising ratio varies only weakly at relatively high ionic current densities. For example, a decrease in current density over one order of magnitude from 10 down to 1 mA/cm^2 will increase the AR by only 16%. This weak dependence of AR on i_i as resolved in Fig.5.4 for the mA/cm^2 range clearly justifies the tabulating in the literature of characteristic, seemingly current density independent AR values for anodic oxides (as e.g. in [211]), despite the explicit current density dependence predicted by Eq.5.2. However, when the ionic current density further decreases below the level of 0.1 mA/cm^2, the anodising ratio starts to increase much more steeply. As a result, for the galvanostatic anodising conditions in the mA/cm^2 range typically encountered in the scientific literature, a significant increase in anodising ratio can be expected when the growth efficiency falls below a few percents. Obviously, there should be some threshold value for the ionic current density below which the high-field model breaks down, and the current flowing through the film becomes diffusion-controlled. In this paper however, in view of the still meaningful values obtained for i_o and β, it seems that the high-field model remains valid in the low-efficiency region as well. In our case, the growth

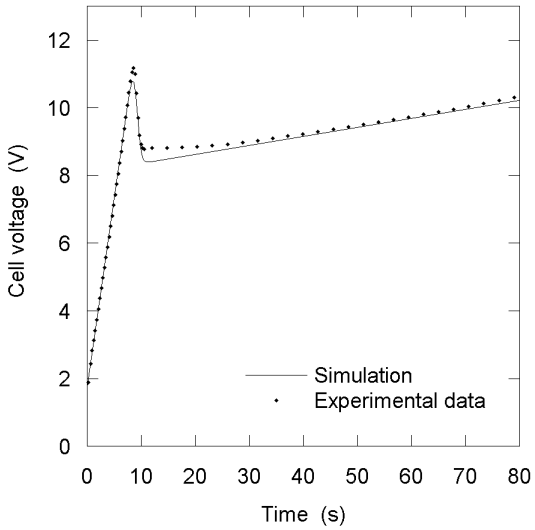

Figure 5.5: Evolution of the anode voltage with time calculated according to Eq.5.5, superimposed on the experimental curve from Fig.5.1.

efficiency was observed to drop by more than an order of magnitude, from a value close to 80% to a very low value below 3%. With $i_{tot} = 4$ mA/cm^2, this then explains the observed dramatic increase of the anodising ratio (cfr. inset of Fig.5.4). In the following paragraph, we will show that also the experimentally recorded V-t curve, including the characteristic local V-decrease, can be quantitatively accounted for by this decrease in growth efficiency.

According to Eq.5.5, after inserting Eq.5.2 for $AR(t)$ and taking into account our experimental observation that the density of the oxide film remains constant, the time evolution of the voltage signal is now seen to be fully determined by the evolution of the growth efficiency $\eta(t)$. In order to be able to use Eq.5.5 for reproducing the measured V-t curve of Fig.5.1, we must, apart from inserting the previously determined values for i_o, β and ρ, also find and integrate a realistic function for $\eta(t)$. As the latter should exhibit as a main feature a fast transition between two constant values, the following analytical function is proposed :

$$\eta(t) = \eta_2 + \frac{\eta_1 - \eta_2}{exp\left(\frac{t-t_m}{\alpha}\right) + 1} \tag{5.9}$$

In Eq.5.9, η_1 and η_2 are the constant anodising efficiency values for the first and second stage already determined earlier, and t_m is the transition time, cor-

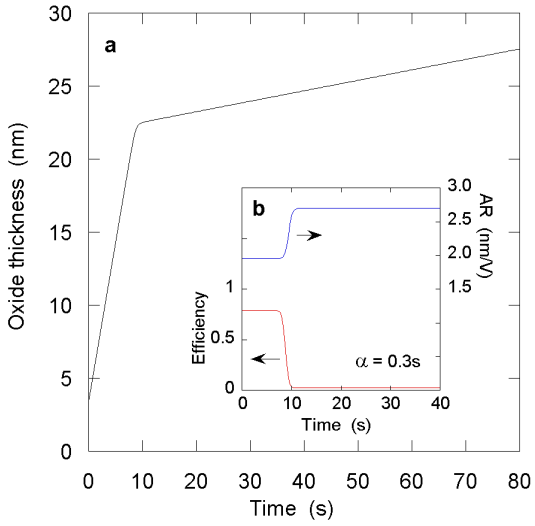

Figure 5.6: (a) Simulated evolution of the oxide thickness with time. (b, inset) Time-evolution of the growth efficiency, as described by Eq.5.9 with α= 0.3s, and related evolution of the anodising ratio (AR), as given by Eq.5.2.

responding to the maximum of the V-t curve and equal to 8.7 sec in Fig.5.1. Therefore, the only free fitting parameter is α, a characteristic for the spreading of the transition region around t_m. Its value has been optimized as $\alpha = 0.3$ sec in order to obtain the best fit to the experimental V-t data in the transition region. Fig.5.5 then shows the voltage evolution with time calculated according to Eq.5.5, superimposed on the experimental V-t curve from Fig.5.1. The value for the thickness h_o of the native oxide film in Eq.5.5 was calculated from the value of the initial potential jump at $t = 0$. A thickness of 3.4±0.2 nm was obtained, in fair agreement with reported values for the native oxide thickness on sputtered Ti films [237]. The fact that good agreement is observed between the simulated local voltage decrease and the actual experimental data is also in favour of the validity of our initial statement, namely that the increase of the anodising ratio can be entirely accounted for by the high-field theory, which essentially links the ionic current density, or, more fundamentally, the growth efficiency η, to the anodising ratio. As already discussed with Eq.5.5, the experimentally observed local V-decrease is therefore mathematically a direct result from this efficiency-induced AR-change, combined with a continuously increasing oxide thickness throughout the transition region. This is illustrated in Fig.5.6a, which shows the time evolution of the oxide thickness as reproduced by substituting into Faraday's law the previously obtained values for $\eta(t)$. The

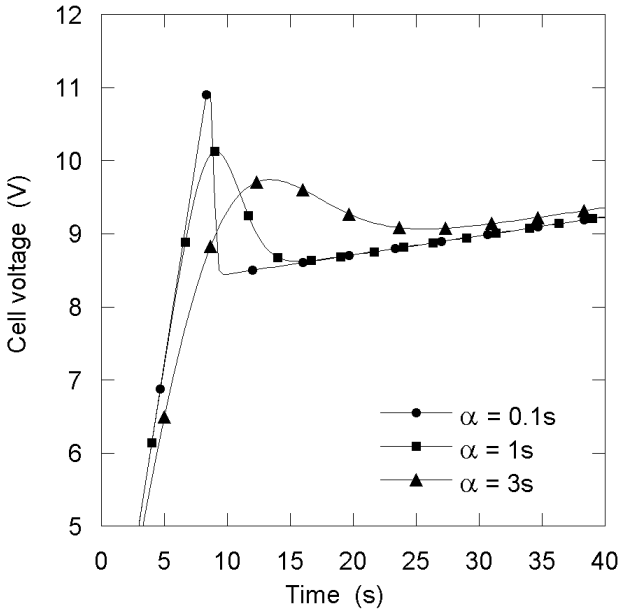

Figure 5.7: Simulated evolution of the anode voltage with time in and near the transition region for different values of the fitting parameter α.

latter are shown in turn, together with $AR(t)$, in the inset Fig.5.6b.

Finally, we must acknowledge that the actual variation of the growth efficiency in the transition region might not follow exactly the function $\eta(t)$ proposed in Eq.5.9. This is probably also the reason why the experimental V-t curve was not exactly reproduced in Fig.5.5. However, the main V-t characteristics, including the position of the local voltage maximum, the extent of the transition region and the difference between the maximum and the minimum voltage, have been correctly captured with our simple $\eta(t)$ function. Nonetheless, it is still of interest to investigate the effect of the value of the fitting parameter α in Eq.5.9 as well. Fig.5.7 shows the simulated evolution of the voltage with time in and near the transition region for different values of α. It can be seen that low values of α lead to a very sharp transition, which appears almost like a V-discontinuity. As α increases, the whole transition region is spread over a longer period in time, and the difference between the maximum and the minimum voltage is reduced. In our experimental V-t curve of Fig.5.1, the transition appears to be quite sharp, in any case sharper than the previously cited observations from the literature on bulk Ti anodising [10, 47].

A speculative explanation for such a sharp transition might be the fact that our sputtered Ti films exhibit a marked [002] texture. Indeed, as discussed in section 1.2.4 Kudelka et al. have demonstrated that the electronic properties, and hence also the potential at which the oxygen evolution sets off, of slowly anodised TiO_2 films depend strongly on the orientation of the underlying Ti substrate [124]. Therefore, in the case of TiO_2 grown on a polycrystallline bulk Ti substrate, one can expect some spreading of the threshold voltage from one grain to the other. In contrast, in our case of a highly textured Ti thin film substrate, the oxygen evolution can be expected to start more homogenously in time all over the sample, leading to the observed sharp transition.

Conclusions

In the first and second sections, the influence of efficiency changes on the cell voltage evolution has been discussed. It was shown that, according to the high-field theory for ionic migration, an increase of the anodising ratio is to be expected when the growth efficiency decreases. This effect becomes quite significant for applied current densities in the mA/cm^2 range when the anodic growth efficiency falls below a few percents. This is illustrated in the second section, based on experimental observations of the V-t and thickness evolution. Finally, it was shown that the specific shape of our anodising curves, characterised by a local V-decrease accompanying the efficiency drop, can be quantitatively reproduced based only on the evolution of the growth efficiency.

5.3 TEM investigation of the origin of the conductivity changes in anodic TiO_2.

In the first two sections, we have discussed indirect consequences of the transition in the electronic properties of TiO_2 films on their growth. In this third section, the microstructural origin of this transition is discussed, based on observations from in-plane TEM investigations. Indeed, as introduced in chapter 1, according to Habazaki et al. [76], the transition in the electronic properties of TiO_2 films and the resulting decrease of the growth efficiency would be directly related to their crystallisation to anatase. In order to gain insight into that question, we have investigated the evolution of the microstructure of our films in the course of the growth. Three samples, anodised to 5V, 8V (below V_{max}) and 11V (over V_{max}) have been examined in order to detect any structural change associated with the local V-decrease. Owing to the very small thickness of the films to be investigated, TEM appeared to be the most appropriate technique.

Experimental

In order to render them suitable for TEM investigation, the TiO_2 films were stripped from their substrate using a procedure similar to that initially proposed by Nurse and Wormwell [166], which was also successfully used by Delplancke et al. [48], Marsh et al. [146] or Shibata et al. [214]. The Ti substrate has been dissolved selectively by immersing the samples (5x5 mm^2) for 1 hour in a solution composed of 10% bromine in anhydrous methanol. The solution was then filtered on a cellulose filter paper (Schleicher & Schuell 589^2) which was subsequently rinsed with methanol. After air drying, small oxide fragments, appearing as tiny iridescent rods, are observed on the filter paper. Inspection under an optical microscope reveals that the stripped films have coiled up, hence having the appearence of small rolls approximately 50 μm wide and a few mm long, as illustrated on Fig.5.8. The oxide fragments were transferred from the filter paper to copper TEM grids by gently pressing the grid on the filter paper. Using that procedure, isolated TiO_2 films have been prepared for the samples anodised at 5V, 8V and 11V, hence corresponding to thicknesses of approximately 8, 14 and 27 nm, well-adapted for TEM observation. The TEM investigations have been carried out on a Leo 922 microscope operated at 200 keV and provided with a Köhler illuminator. The latter allows for automatically scaling the size of the region exposed to the electron beam when changing the magnification (hence preventing irradiating a region of the sample while observing an adjacent region). This is of specific importance in the case of anodic oxide films, as such films are well-known to be prone to electron-beam crystallisation in the TEM [5, 108]. In addition, care was taken to work with the smallest possible current (around 2μA) and to reduce as much as possible the time of exposure to the beam. In particular, after optimising the focus, the sample was always slightly shifted in order to record the images and diffraction patterns on a fresh region. Due to the coil-shape of the samples, TEM investigation was carried out close to the edges of the samples in regions where, apparently, the sample consisted of a single layer. The obtained diffraction patterns were post-treated using ProcessDiffraction V4.3.8 B freeware [128], in order to represent in a more quantitative way the distribution of the diffracted intensity.

Results

Identification of the crystalline phases

Figure 5.9 shows a typical electron diffraction pattern recorded for the sample anodised to 8V. The same series of diffraction rings was reproducibly observed on all three samples but the relative intensity of the rings and their appearance (continuous or spotty) varied from one sample to another. Three intense diffraction rings of diameter 0.57, 0.81 and 1.41 $Å^{-1}$ have been identified, com-

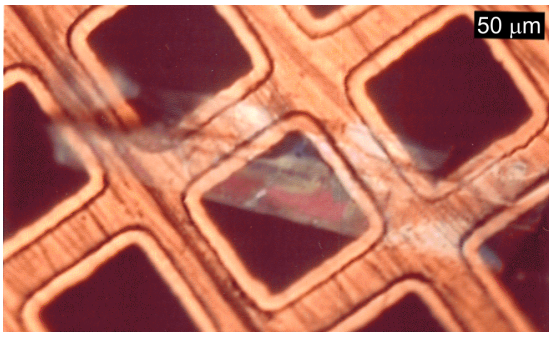

Figure 5.8: Optical microscopy image from a coiled-up 14 nm thick TiO_2 sample after its transfer on the TEM grid.

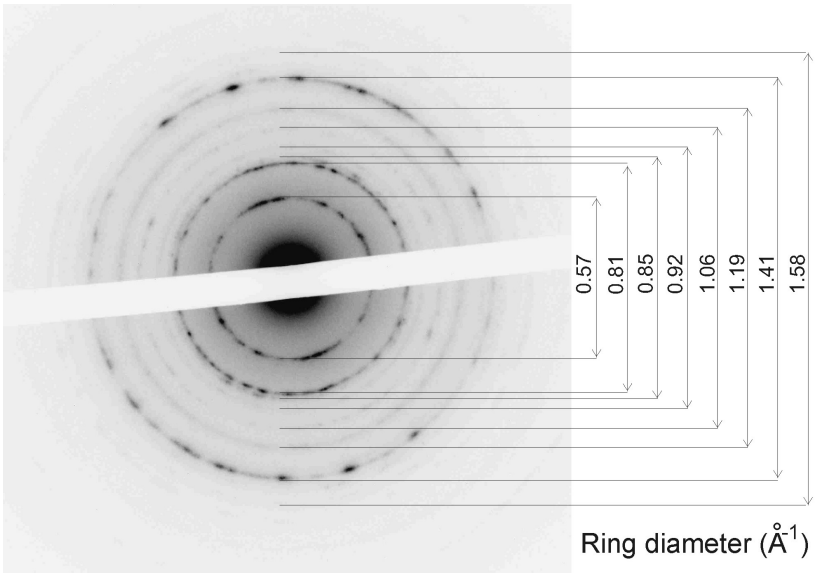

Figure 5.9: Typical diffraction pattern observed for our TiO_2 samples.

d [Å]	*intensity*	h	k	l	ring diameter [$Å^{-1}$]
3.5200	100	1	0	1	0.57
2.4310	10	1	0	3	0.82
2.3780	20	0	0	4	0.84
2.3320	10	1	1	2	0.86
1.8920	35	2	0	0	1.06
1.6999	20	1	0	5	1.18
1.6665	20	2	1	1	1.20
1.4930	4	2	1	3	1.34
1.4808	14	2	0	4	1.35
1.3641	6	1	1	6	1.47
1.3378	6	2	2	0	1.49
1.2795	2	1	0	7	1.56
1.2649	10	2	1	5	1.58

Table 5.1: CPDS data for TiO_2 anatase (ref 00-021-1272)

plemented by a series of weaker rings at 0.85, 0.92, 1.06, 1.19 and 1.58 $Å^{-1}$. The first intense ring at 0.57 $Å^{-1}$, corresponding to an interreticular distance d of 3.5 Å, is characteristic for the [101] planes of TiO_2 anatase [76]. The CPDS data for anatase (ref. 00-021-1272) is reproduced in Table 5.1. It can be observed that all the most important diffraction peaks of anatase are indeed observed on the diffraction pattern presented on Fig.5.9. In contrast, the intense ring observed at 1.41 $Å^{-1}$ and the weak one observed at 0.92 $Å^{-1}$ do clearly not belong to anatase. In addition, the large intensity of the 0.81 $Å^{-1}$ ring is not coherent with the expected relative intensities of the anatase rings. The latter observations are indicative for the presence of, at least, a second crystalline phase in addition to anatase.

In order to help identifying this second crystalline phase, the following procedure was followed. A dark-field image was recorded, using the signal corresponding to the external unidentified diffraction ring at 1.41 $Å^{-1}$. Then, by using an appropriate diaphragm, a small area of 175 nm in diameter was selected on the sample in a region containing a large proportion of the second phase. The diffraction pattern recorded on that area is reproduced on Fig.5.11a. Using the same procedure on an anatase-rich region of the sample, the selected area diffraction pattern (SADP) reproduced on Fig.5.11b was obtained. As evident from Fig.5.11a, the ring at 1.41 $Å^{-1}$ is accompanied by an inner ring at 0.80 $Å^{-1}$. Hence, it is likely that the large intensity of the 0.81 $Å^{-1}$ ring of the overall diffraction pattern arises from the superposition of the anatase ring at 0.82 $Å^{-1}$ and the 0.80 $Å^{-1}$ ring from the second phase. In

contrast, the unidentified ring observed at 0.92 $Å^{-1}$ does not seem to belong to this second phase, hence suggesting that a third phase might be present. In order to interpret the diffraction pattern from Fig.5.11a, the latter was compared to the CPDS data for the main other Ti-oxides, i.e. TiO_2 rutile, Ti_2O_3, TiO or a one of the Magnéli phases of generic formula Ti_nO_{2n-1} (with n between 4 and 10). Clearly, the presence of Ti_2O_3 or FCC TiO is incompatible with our obtained diffraction pattern (see Tables 5.3 and 5.5). The presence of randomly-oriented rutile seems to be unlikely as well, given the complete absence of the main rutile ring corresponding to the [110] planes, which would be observed at 0.62 $Å^{-1}$. Rutile showing a marked preferential orientation is however believed to account for the single unidentified diffraction ring at 0.92 $Å^{-1}$. We will come back to this point in the following paragraphs. Magnéli phases consist of ordered substoichiometric Ti oxides and are usually produced by reducing TiO_2 at high temperature (>1000°) in an hydrogen atmosphere [222]. Their presence in anodic Ti-oxide films has never been reported so far, not even in the study carried out by Pouilleau et al. [188] in which Magnéli phase are directly compared with anodic Ti-oxide films using XPS. Information on the crystallographic properties of such phases can be found in the paper by Reece and Morrell [196] and in the JCPDS database (patterns 00-51-641, 00-50-787 and 00-18-1401). Owing to the low (triclinic) symmetry of these oxides, the diffraction figures are rather complex and do not seem to correspond to our observed ones. Finally, and rather surprisingly, the ring at 80 $Å^{-1}$ on Fig.5.11a could correspond to the main ring of hexagonal TiO, both in terms of position and symmetry. As to the second (1.41 $Å^{-1}$) ring, it cannot be attributed to the [211] planes which would not be observed together with the [110] planes. We believe it might correspond to the [300] planes, if we admit a slight deviation of the lattice parameters of the order of 2%. The SADP image of Fig.5.11 would then correspond to the basal plane of hexagonal TiO. This seems to be the most likely possibility based on the available observations. It should be noted that the diffraction pattern presented on Fig.3.20, which was prepared for the TEM examination using a completely different procedure, also provides some evidence of the presence of hexagonal TiO (mainly a small peak at 1.41$Å^{-1}$). Hence, we believe that the latter phase is indeed produced during the anodisation and not during the film stripping procedure.

As the observation of crystalline TiO in our samples is rather unexpected, we have explicitly ensured that the diffraction signal does not correspond to an artefact arising from residual undissolved Ti on the TiO_2 film, from the copper grid or from a contaminant formed during the film stripping procedure (for instance $TiBr_2$ or $TiBr_4$). As evident from the crystallographic CPDS data reproduced on Table 5.2 the position of the diffraction rings of the second phase is incompatible with the hypothesis that the latter would be attributable to residual Ti. The diffraction signal could not either come from the copper grid.

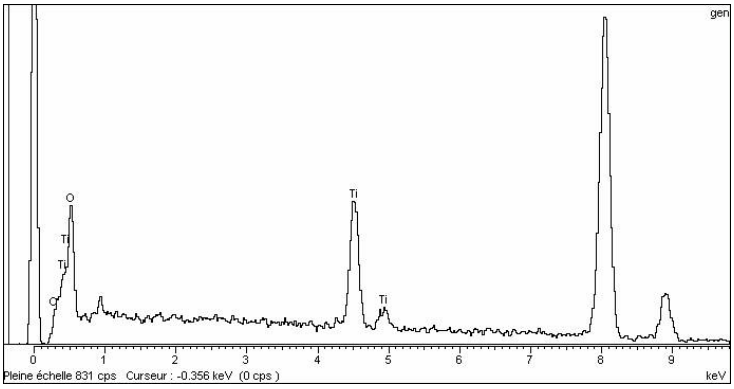

Figure 5.10: EDX spectrum recorded on the 11V sample.

As to the possibility that the diffraction signal would be attributable to a contaminant produced during the film stripping procedure, it should be noted that $TiBr_4$ has some diffraction rings very close to those of TiO_2 anatase (see Table 5.7). For instance, the bromide is characterised by rings at 0.56, 0.83, 1.06 and 1.2 $Å^{-1}$, which almost correspond to positions of anatase rings, and presents supplementary rings at 0.9 and 1.42 $Å^{-1}$, which almost correspond to the positions of the unidentified rings. This suggests that the signal attributed to anatase could be, at least partly, attributable to $TiBr_4$ which would have formed during the stripping procedure. However, some of our observations render this hypothesis doubtful. Firstly, even though $TiBr_4$ might be present in the sample, anatase is definitely present as well, as the symmetry of the SADP on Fig.5.11b unambiguously corresponds to anatase. Secondly, EDX analysis, coupled to the TEM, was carried out on the samples in order to check for the presence of possible contaminants. The EDX spectrum is reproduced on Fig.5.10. No elements other than Ti and O have been detected. The fact that no bromine was detected by EDX analysis and that all the most intense peaks of $TiBr_4$ (corresponding to diameters of 0.61, 0.71, 1 and 1.17 $Å^{-1}$) are missing in the diffraction patterns seems to discard the hypothesis that Ti bromides are formed. Furthermore, the geometry of the SADP presented on Fig.5.11a is not either compatible with that expected for a Ti bromide if the two rings correspond to the [332] and [800] planes. Finally, the fact that a clear evolution of the diffraction signal corresponding to this second phase is observed between 5V and 11V suggests that this phase is formed during the anodisation and not during the film stripping procedure. Hence, the presence of $TiBr_4$ does not seem very likely. The presence of $TiBr_2$ is even less likely, as evident from the corresponding CPDS data (see Table 5.8).

d [Å]	*intensity*	h	k	l	ring diameter [$Å^{-1}$]
2.555	25	1	0	0	0.78
2.341	30	0	0	2	0.85
2.243	100	1	0	1	0.89
1.7262	13	1	0	2	1.16
1.4753	11	1	1	0	1.36
1.332	11	1	0	3	1.50
1.2776	1	2	0	0	1.57
1.2481	9	1	1	2	1.60
1.2324	6	2	0	1	1.62
1.1707	1	0	0	4	1.71
1.1215	1	2	0	2	1.78
1.0643	1	1	0	4	1.88
0.98865	2	2	0	3	2.02
0.96578	1	2	1	0	2.07
0.94591	4	2	1	1	2.11
0.91701	3	1	1	4	2.18
0.89281	1	2	1	2	2.24

Table 5.2: CPDS data for Ti (ref 00-044-1294)

Hence, it seems that the second phase, characterised by the two intense diffraction rings at 0.81 and 1.41 $Å^{-1}$), would correspond to hexagonal TiO. The last unidentified ring at 0.92 $Å^{-1}$), which does not belong to the diffraction pattern of anatase nor of TiO is believed to correspond to (111)-oriented rutile, although final conclusions can hardly be drawn from this single ring. In the following paragraph, the microstructural evolution of the film between 5V and 11V is described in more details and discussed.

Evolution of the structure of the TiO_2 film
In the case of the sample anodised to 5V, crystalline material is clearly already present in the film. A continuous inner ring is observed at 0.57 $Å^{-1}$, characteristic for the (101) planes of anatase. This ring is accompanied by much weaker anatase rings at 1.06, 1.18-1.20 and 1.47-1.49 $Å^{-1}$. The observation of anatase crystallites at 5V is in agreement with results reported by Leach and Pearson for anodic oxide films grown on Ti at low current density [133]. The anatase crystallites are likely to be very small and randomly oriented, as suggested by the continuous appearance of the diffraction rings. Besides anatase, evidence for the presence of the second crystalline phase, identified as hexagonal TiO, is observed on the diffraction pattern. The latter is characterised by two outer

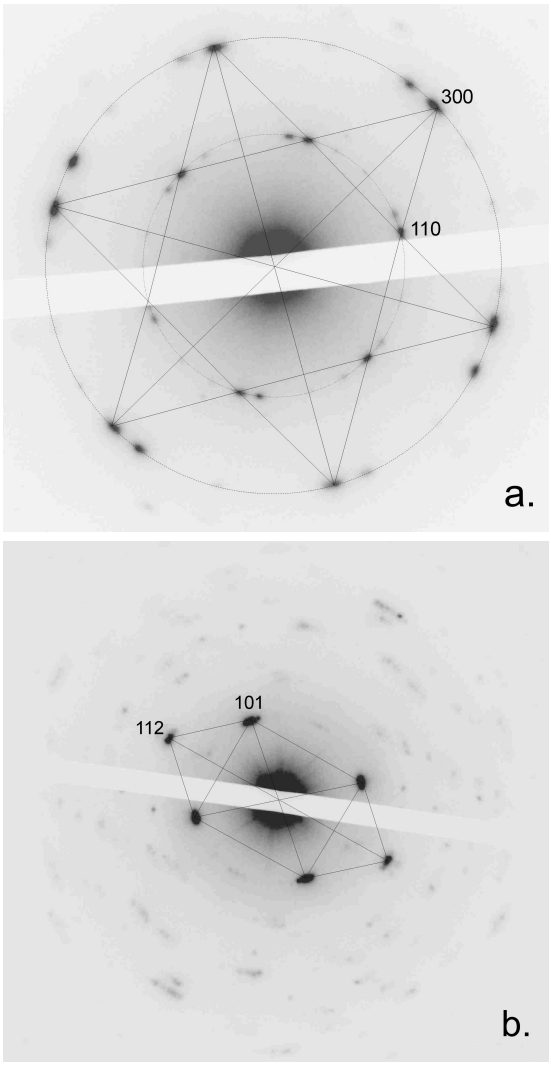

Figure 5.11: Selected area diffraction patterns (170 nm in diameter) for the two main phases present in the anodic films. The first one is believed to correspond to the basal plane of hexagonal TiO and the second one correponds to anatase.

d [Å]	*intensity*	h	k	l	ring diameter [Å^{-1}]
2.407	45	1	1	1	0.83
2.085	100	2	0	0	0.96
1.475	50	2	2	0	1.36
1.259	14	3	1	1	1.59
1.205	12	2	2	2	1.66
1.044	6	4	0	0	1.92
0.958	6	3	3	1	2.09

Table 5.3: CPDS data for TiO FCC (ref 00-008-0117)

d [Å]	*intensity*	h	k	l	ring diameter [Å^{-1}]
2.495	100	1	1	0	0.80
2.396	85	1	0	1	0.83
1.886	25	1	1	1	1.06
1.729	55	2	0	1	1.16
1.441	40	3	0	0	1.39
1.421	30	2	1	1	1.41
1.247	30	1	1	2	1.60

Table 5.4: CPDS data for hexagonal TiO (ref 00-012-0754)

d [Å]	*intensity*	h	k	l	ring diameter [Å^{-1}]
3.732	25	0	1	2	0.54
2.712	50	1	0	4	0.74
2.572	60	1	1	0	0.78
2.277	8	0	0	6	0.88
2.238	35	1	1	3	0.89
2.116	12	2	0	2	0.95
1.865	35	0	2	4	1.07
1.704	100	1	1	6	1.17
1.634	12	1	2	2	1.22
1.592	4	0	1	8	1.26
1.51	30	2	1	4	1.32
1.483	45	3	0	0	1.35
1.306	25	1	0	10	1.53
1.2849	18	2	2	0	1.56
1.2432	12	3	0	6	1.61

Table 5.5: CPDS data for Ti_2O_3 (ref 00-010-0063)

d [Å]	*intensity*	h	k	l	ring diameter [$Å^{-1}$]
3.247	100	1	1	0	0.62
2.487	50	1	0	1	0.80
2.297	8	2	0	0	0.87
2.188	25	1	1	1	0.91
2.054	10	2	1	0	0.97
1.6874	60	2	1	1	1.19
1.6237	20	2	2	0	1.23
1.4797	10	0	0	2	1.35
1.4528	10	3	1	0	1.38
1.4243	2	2	2	1	1.40
1.3598	20	3	0	1	1.47
1.3465	12	1	1	2	1.49
1.3041	2	3	1	1	1.53

Table 5.6: CPDS data for TiO_2 rutile (ref 00-021-1276)

d [Å]	*intensity*	h	k	l	ring diameter [$Å^{-1}$]
4.61	30	2	1	1	0.43
3.57	40	3	1	0	0.56
3.26	100	2	2	2	0.61
2.825	90	4	0	0	0.71
2.663	10	4	1	1	0.75
2.409	10	3	3	2	0.83
2.216	20	5	1	0	0.90
1.998	100	4	4	0	1.00
1.883	10	6	0	0	1.06
1.883	10	6	1	1	1.06
1.704	100	6	2	2	1.17
1.666	40	6	3	1	1.20
1.631	40	4	4	4	1.23
1.413	10	8	0	0	1.42
1.296	10	6	6	2	1.54

Table 5.7: CPDS data for $TiBr_4$ (ref 00-011-0064)

d [Å]	*intensity*	h	k	l	ring diameter [Å^{-1}]
6.5	60	0	0	1	0.31
3.24	80	0	0	2	0.62
3.149	10	1	0	0	0.64
2.827	100	1	0	1	0.71
2.255	80	1	0	2	0.89
2.155	10	0	0	3	0.93
1.806	80	1	1	0	1.11
1.785	80	1	0	3	1.12
1.618	60	0	0	4	1.24
1.586	40	1	1	2	1.26
1.521	40	2	0	1	1.31
1.415	30	2	0	2	1.41

Table 5.8: CPDS data for $TiBr_2$ (ref 00-014-0642)

rings at 0.81 and 1.41 Å^{-1}.

At 8V, Fig.5.13b shows that the intensity signal of the anatase rings increases relative to the TiO-ones, indicating that the latter is still observed but its relative proportion decreases as compared to the proportion of anatase. Moreover, as a general trend, the diffraction pattern at 8V is spottier than the one at 5V, which indicates that either the size of the crystallites increases or that some specific crystalline orientations disappear. Finally, it can be noted that a weak supplementary ring is observed at 0.92 Å^{-1}, which does not belong to the pattern of anatase. We will come back to this important observation as well.

The microstructural evolution follows the same trend between 8V and 11V: the relative proportion of anatase is observed to increase further. The relative intensity of the ring observed at 0.92 Å^{-1} increases significantly as well but is observed to vary significantly from one region to another on the same sample, as evident from the dispersion between the four intensity curves superposed on Fig.5.13c. It can be observed that the diffraction rings corresponding to anatase are still continuous although they present some more intense portions. In contrast, the rings corresponding to the second phase and the ring at 0.92 Å^{-1} are observed in the form of discontinuous ring segments. Besides the rings corresponding to the crystalline phases, a characteristic halo is observed on all diffraction patterns recorded on the three samples. The latter arises from the presence of the amorphous matrix [214].

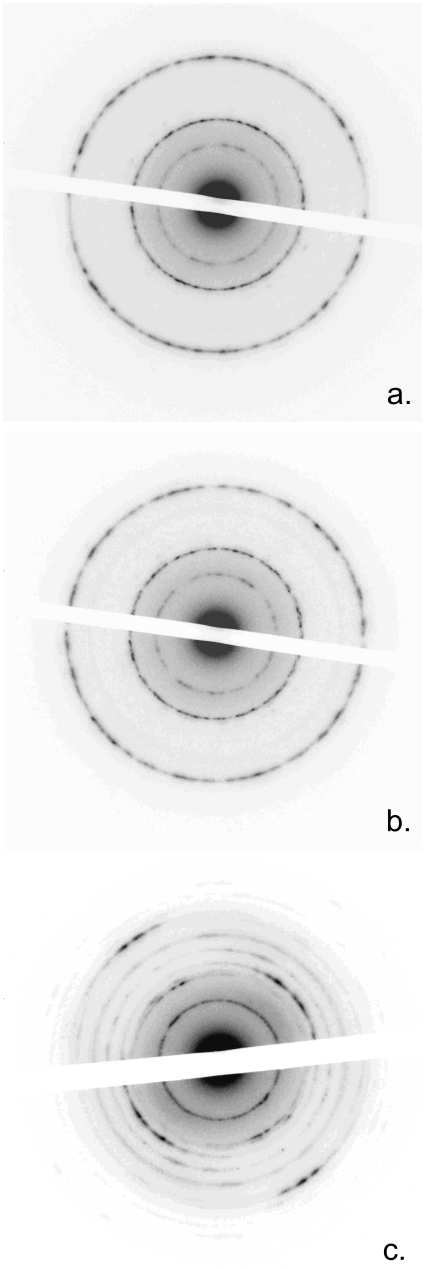

Figure 5.12: Diffraction patterns recorded for the samples anodised to (a) 5V, (b) 8V and (c) 11V.

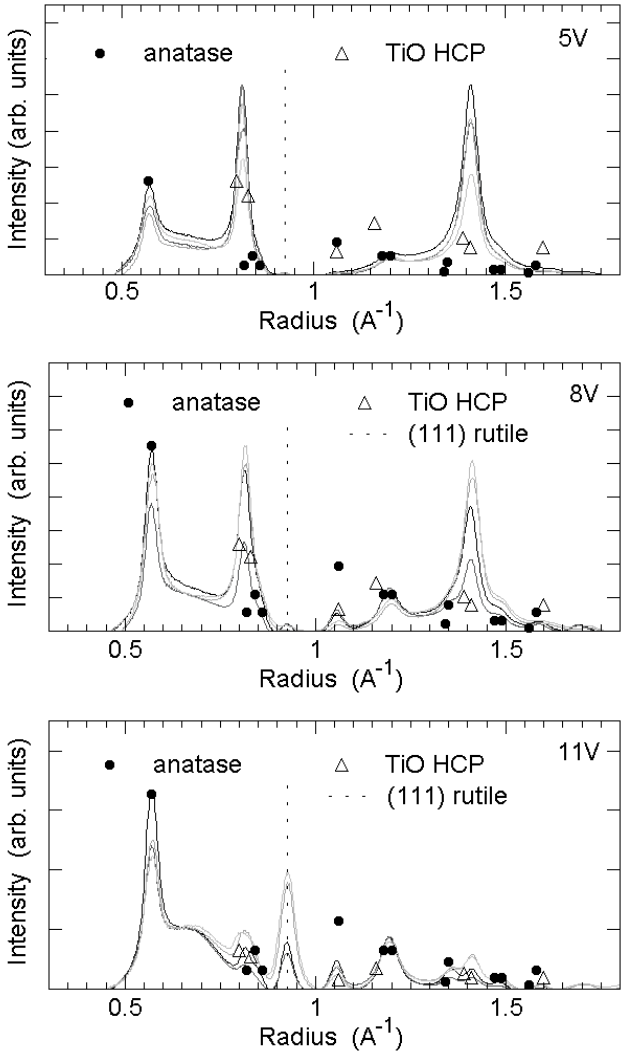

Figure 5.13: Distribution of the diffracted intensity corresponding to the diffraction patterns recorded on the samples anodised to 5V, 8V and 11V, obtained using ProcessDiffraction freeware [128]. On each graph, 4 intensity curves have been superposed corresponding to 4 diffraction patterns recorded on 4 ditinct regions of the sample. The theoretical pattern of anatase and hexagonal TiO have been included as well.

Localisation of the two phases
Fig.5.14 shows dark-field images corresponding respectively to the TiO and anatase phases. The latter appears to be finely dispersed. In contrast, the TiO phase appears to be present in the form of large clusters of small crystallites exhibiting the same orientation. Those clusters have an average diameter of 200 nm.

Discussion

From these observations, the following conclusions can be made with respect to the physical origin of the observed efficiency changes. The most important one is that crystalline anatase is already present in the film at 5V and 8V, i.e. well before the local V-decrease. Hence, in our case, the efficiency change accompanying the local V-maximum cannot be attributed to a simple, instantaneous, amorphous-to-crystalline transition, as is sometimes proposed in the literature [146, 76]. It seems that more subtle changes in the structure of the film are responsible for the change in the electronic conductivity and the related observed efficiency change. The transition could rather be related to a given threshold in terms of size of the crystallites or of volume fraction of the anatase phase, associated for instance with a percolation threshold or to a decrease of the oxide bandgap, as suggested by Santamaria [202]. The initial crystallites are likely to be very small when anodisation is interrupted at 5V, as suggested by the continuous diffraction rings observed on Fig.5.13a. The size of the crystallites can then be assumed to increase with increasing final voltage, hence giving rise to the spottier diffraction pattern of Fig.5.13c. In any case, at 11V, the crystallites are still embedded in an amorphous matrix as evident from the characteristic halo on the diffraction patterns and from the low values already reported in section 5.2 for the refractive index and the oxide density.

The presence of the third crystalline phase, identified as hexagonal TiO, was somewhat unexpected. Anodic TiO_2 films have indeed been reported previously by some authors to contain Ti-oxides with an oxidation state lower than four (TiO and Ti_2O_3) at the metal/oxide interface. However, such interfacial TiO and Ti_2O_3 layers are generally considered to represent a progressive transition between Ti and TiO_2 stoichiometries, characterised by a continuous concentration gradient, and hence not corresponding to any well-defined crystal structure. The presence of TiO/Ti_2O_3 interfacial layers was discussed in the review paper by Aladjem [6], by Armstrong et al. [14], Pouilleau et al. [187] and McCafferty et al. [149], although the latter authors conclude that the observation of TiO and Ti_2O_3 could be an artefact of the ion milling in XPS depth-profiling studies. According to Huber et al. [93], the fact that a stoichiometry close to TiO is observed at the metal/oxide interface is due to

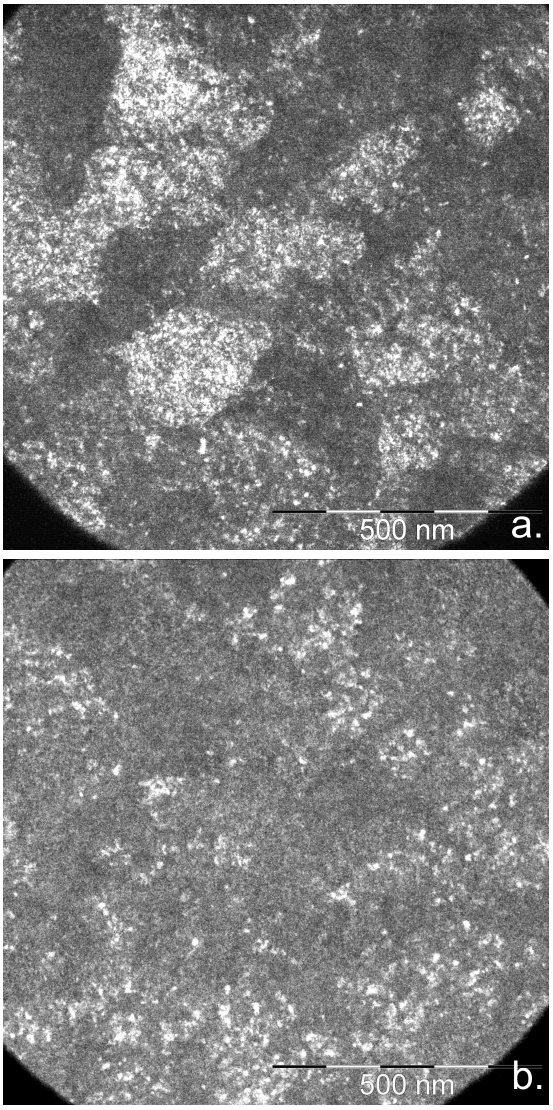

Figure 5.14: Dark-field images of the 8V sample corresponding to (a fraction of) the diffraction signal of (a) the 1.41 $Å^{-1}$ ring corresponding to the TiO phase and (b) the 0.57 $Å^{-1}$ ring corresponding to anatase.

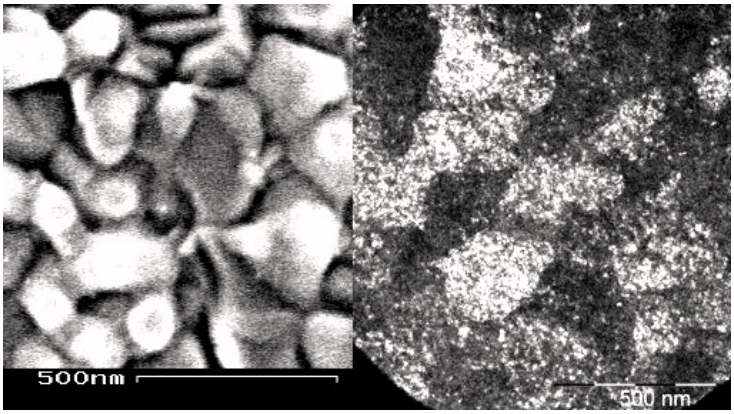

Figure 5.15: Comparison of the grain size of the Ti substrate with the size of the TiO clusters, as measured by TEM.

the migration of the Ti atoms across the metal/oxide interface, hence producing an excess of Ti in the vicinity of that interface. Similarly, Pouilleau et al. [187] report the observation of an interfacial TiO_x layer, the stoichiometry of which varies continuously between the metal substrate and the bulk TiO_2 and is therefore not detectable by X-ray diffraction. Hence, in our case, it is somewhat surprising to observe a well-crystallised TiO material. Furthermore, although no data could be found on the solubility of TiO in bromine, it would a priori be expected to dissolve in such a strong oxidising solution. The dissolution rate might however be lower than that of Ti, which would account for the fact that TiO is still present at the end of the 1 hour dissolution step. Interestingly, the size of the TiO clusters presenting the same crystal orientation is observed to be comparable to the average size of the underlying grains of the Ti substrate (see Fig.5.15). This suggests that oriented TiO might be formed preferentially on the [0002] planes of Ti owing to a favourable orientation relationship. This would also account for the fact that crystalline TiO was not reported so far for bulk Ti, while we have systematically observed this phase on our Ti thin film samples exhibiting a marked texture. At this stage however, it still needs to be confirmed whether the presence of TiO in the first stages of the anodisation process is a specific feature of our particular samples or is a more general trend. It can be noted that, from the mechanical point of view, the presence of such a TiO buffer layer at the metal/oxide interface would be highly favourable. Indeed, hexagonal TiO is denser than Ti, and the two compounds have a very similar molar volume (10.63 cm^3/mol for Ti and 12.47 cm^3/mol for TiO), which would allow for a significant reduction of the mechanical stresses as compared to the situation where TiO_2 would grow directly on Ti.

Finally, between 8V and 11V, the main observed change is a significant increase of the intensity of the ring at 0.92 $Å^{-1}$. This latter ring does not belong to the diffraction pattern of anatase neither to TiO. In contrast, it might correspond to (111)-oriented rutile, although firm conclusions can hardly be drawn from this single ring. As previously mentioned, the presence of randomly-oriented rutile in our films is unlikely, considering the absence of the main rutile ring at 0.62 $Å^{-1}$. However, rutile crystallites might form with a specific orientation relationship with either the Ti substrate or the anatase or TiO phases. Recent results from Matykina et al. suggest that rutile crystallites are formed preferentially at the metal/oxide interface on (0002) Ti grains [154]. According to these authors, such oriented rutile crystallites would play a role in the oxygen evolution reaction and hence on the conductivity of the TiO_2 films. This might be related to the lower bandgap of the rutile phase as compared to anatase (respectively 3.06 and 3.2 eV). The increase in the proportion and size of rutile crystallites could contribute to decreasing the overall bandgap of the film or lead to the establishment of preferential conduction path [146]. Hence, the fact that the intensity of the 0.92 $Å^{-1}$ ring increases significantly in the transition region supports the idea that the rutile phase plays a major role in the conductivity transitions associated with the observed efficiency change.

5.4 Conclusion

In this chapter, some aspects of conductivity transitions in anodic TiO_2 films are discussed. The starting point was the observation, upon anodising the Ti electrodes from the STi batch, of a very sharp decrease of the growth efficiency corresponding to a conductivity transition. This efficiency drop was reproducibly observed to be accompanied by a local decrease of the cell voltage. In the first two sections, it is shown that this observation can be interpreted in the framework of the high-field model, based solely on the assumption that the V-evolution is entirely determined by the evolution of the growth efficiency. In the third section, the microstructural evolution of the oxide films around the transition is investigated in order to identify whether the conduction transition can be correlated with a microstructural transition. TEM investigations convincingly demonstrate that the oxide films already contain anatase crystallites well before the efficiency transition. Besides anatase, other crystalline phases have been detected, among which one phase, already present on the 5V sample, and identified as hexagonal TiO. The latter phase seems to be formed directly on the Ti grains at the metal/oxide interface, with a direct influence of the metal substrate on the orientation of the crystallites. Diffraction signal from a third phase, identified as Rutile, is observed as well. This third phase is believed to play a major role, as a significant increase of its intensity in the electron

diffraction patterns is observed before and after the efficiency transition.

General conclusions and perspectives

As discussed in the introduction, the contributions from this thesis are essentially threefold, namely demonstrating the feasability of the experimental technique and designing an adapted experimental set-up, deriving a novel model for the electrostriction stresses and providing experimental data on the stress evolution in anodic TiO_2 films. In this section, we would like to summarise the progresses obtained for each of those three aspects, discuss possible improvements and suggest paths that could be followed for pursuing this research.

Firstly, this thesis demonstrates the suitability of the multi-beam curvature sensor as an efficient tool for following the stress evolution in anodic oxide films in situ during their growth. The resolution and dynamic range of the technique have been shown to be very well adapted to this kind of measurements and the experimental difficulties inherent to the use of optical techniques for monitoring dynamic processes in a liquid environment could be overcome. The theoretical framework for the use of the multi-beam sensor has been described extensively and a simple experimental set-up has been specifically designed for in-situ monitoring of anodisation processes. All approximations made in the derivation of the calibration equations were demonstrated to be appropriate for the case of our experimental set-up so that they can be adopted with confidence.

Our experimental cell could however be further improved. The curvature monitoring can not as yet be considered as a routine measurement, mainly owing to various optical perturbations and to the difficulty encountered in some cases to stabilise the curvature signal at the beginning of the experiment. The possible origin of several types of perturbations and the way of avoiding them were discussed in the chapter 2. Nevertheless unidentified perturbations are still observed in some cases, which constitutes the main obstacle to the success and repeatability of the measurements. More investigation of the possible source of perturbations and the way of preventing them should, to our opinion,

be a priority. Other minor improvements could also be brought to our setup. For instance, the next generation of the experimental cell should ideally allow for temperature control, as this parameter is well known to have a significant influence on anodisation processes. Another aspect of the sensor which could be improved is the calibration procedure. The calibration procedure described in section 2.2.3 requires measuring the mean spacing for three mirrors of known radii of curvature. This is a relatively simple and accurate procedure. However, it seems that the sensor itself provides a way of determining the length of the optical path. Indeed, the focus of the initial laser beam has to be tuned in order to have the laser spots focused on the detector window. So far, this is done without quantitative control. Quantification of the laser focus would provide for an accurate measurement of the length of the optical path, without requiring any additional experiment, which would constitute a valuable improvement.

Secondly, some efforts have been oriented towards developing a better knowledge of electrostriction stresses in anodic oxide films. It has been demonstrated that electrostriction stresses in TiO_2 films are large, typically of the order of 200 MPa, and that the current models for electrostriction based on the Maxwell stress contribution only cannot account for such large stresses. A novel constitutive equation has been proposed which takes into account explicitly dielectrostriction. Our experimental electrostriction stress values were in good agreement with the model. Future work should now be devoted to provide further confirmation of the model, through different means. Firstly, the adequacy of the model should be tested on metal/oxide/metal structures, in order to avoid any interfering influence of film growth. For this purpose, samples could be prepared by depositing a second metal electrode on top of anodic films. Then, by following the evolution of the curvature of the sample in air while scanning the potential difference between the two electrodes, a very straightforward observation of electrostriction should be obtained. As a second step, the electrostriction stress data should be correlated with electrochemical impedance measurements, in order to quantify the oxide dielectric constant. This should allow for a direct confirmation of the correctness of the constitutive equation linking the electrostriction stress to the dielectric constant. Finally, experimental confirmation of the model should be extended to other metal oxides. Some of our experimental observations regarding electrostriction stresses remain so far unexplained and would require further investigations. For instance, the very characteristic change of the shape of the open-circuit transients systematically observed after the compressive maximum must be indicative for some kind of transition in the film and might therefore be very insightful if this transition could be identified. The trend observed during most experiments that the electrostriction stress in the film tends to decrease in the course of the growth is intriguing as well. It seems to be attributable to a decrease of the film dielectric constant, although this would certainly require direct confirmation based

on independent capacitance measurements.

Finally, the most fundamental contribution of this thesis was to demonstrate that very clear correlations exist between the evolution of mechanical and electrochemical variables during the growth of anodic TiO_2 films under galvanostatic conditions. Most of the previous studies on this topic have been interested in depicting the stress evolution, but with little attention devoted to the correlations between the growth stress and cell voltage evolution. We have shown that the stress evolution is markedly influenced by the same phenomena responsible for the various transitions in the evolution of the cell voltage. This directly demonstrates the interest of curvature measurements as a fundamental technique for investigating the details of the growth process of anodic oxide films. With this respect, this thesis opens many perspectives for further investigations on anodic oxide films. The interpretation of our stress data was not straightforward, partly owing to the complexity of the phenomena coming into play during the growth of anodic TiO_2. In our case, it appears that the interpretation of our experimental data was further complicated by the unreliable characteristics of our Ti thin film substrates, which in some cases gave rise to an anodisation behaviour very different from the classical one reported for bulk Ti. In the future, the reproducibility of the characteristics of the Ti substrates is certainly something that should be worked on. Nevertheless, the fact that tensile stresses always accompany galvanostatic oxide growth under (near-)maximum efficiency conditions is a well established trend, observed sytematically for all experiments, and constitutes a first important result. It was further demonstrated that the instantaneous tensile stress developing in the film under such conditions is independent of the current density in the range of 0.5 to 5 mA/cm^2 and keeps a constant value over a V-range which enlarges with increasing current density. The origin of the large compressive stresses reproducibly observed over specific V-ranges on some Ti batches and always associated with low growth efficiency remains so far an open question. In this thesis, observations susceptible to help bringing insight into that questions have been reported and discussed. To our opinion, two main scenarios could reasonably account for the development of the compressive stresses. The latter could be due either to the evolution of oxygen gas within the oxide film or to a densification of the film, leading to a significant decrease of the concentration of oxygen vacancies in the film.

Final confirmation of whether the oxide film contains incorporated oxygen gas might be obtained from residual gas analysis (RGA). However, the oxygen gas might diffuse out of the film rapidly after the growth process and hence not be detected by ex-situ analysis. Electrical characterisation of the film would certainly be insightful as well. If the compressive stresses are associated with a reordering and a decrease of the vacancy concentration, this

should also correspond to a marked change in the conductivity properties of the film which should be observable using photoelectrochemical measurements or Mott-Schottky analysis. In the future, quantitative interpretation of the curvature measurements would be greatly facilitated by working with stress-free metal substrates, or at least, metal films with well-controlled internal stresses. Indeed, the fraction of the curvature change associated with the dissolution of the metal substrate remains a major source of uncertainty. In this study, the measured stress values have been corrected for this contribution. However, the best we could do was to assess the later contribution from the average stress in the metal film and consider that Ti dissolution in the electrolyte was negligible (so that the mass of metal consumed is directly related to the thickness of metal oxide formed, according to the PBR). This is likely to be an oversimplification as stress gradients might be present in the metal film and significant Ti dissolution might occur in some V-range. Working with stress-free substrates would ensure that the measured curvature changes are fully attributable to the stresses developing in the oxide film and hence facilitate accurate stress quantification.

Comparing the stress evolution accompanying Ti anodisation to that observed on Ti-Si alloys might be a promising way to gain insight into the mechanisms responsible for the stress development. Indeed, as discussed in section 1.2.4, Si species in Ti have a delaying effect on the film crystallisation and on the onset of the oxygen evolution reaction. Hence, it is expected that the efficient growth of amorphous TiO_2 films will be observed over a wider V-range on such alloys, without the interfering influence of side-reactions, so that the stress evolution attributable to homogeneous film growth will be more easily quantified. The resulting oxide films will also be thicker, which would facilitate ex situ characterisation of such amorphous films. Finally, as discussed in chapter 1, Si can be used as a marker species, hence allowing for direct quantification of the transport numbers. This would be a very insightful information for correlating the observed stresses with predictions from the Nelson model.

Bibliography

[1] M.A. Abdel Rahim, J. Appl. Electrochem. 25 (1995) 881.

[2] A. Afshar and M.R. Vaezi, Surf. Coat. Technol. 186 (2004) 394.

[3] S. Ahn, D. Kim and H. Kwon, J. Electrochem. Soc. 153 (2006) B370.

[4] A. Aladjem and D.G. Brandon, Vac. Sci. Technol. 6 (1969) 635.

[5] A. Aladjem, D.G. Brandon, J. Yahalom and J. Zahavi, Electrochim. Acta 15 (1970) 663.

[6] A. Aladjem, M. Aucouturier and P. Lacombe, J. Mater. Sci. 8 (1973) 787.

[7] A. Aladjem, J. Mater. Sci. 8 (1973) 688.

[8] J.M. Albella, J. Montero and J.M. Martinez-Duart, Electrochim. Acta 32 (1987) 255.

[9] J.M. Albella, I. Montero, J.M. Martinez-Duart and V. Parkhutik, J. Mater. Sci. 26 (1991) 3422.

[10] I.A. Ammar and I. Kammal, Electrochim. Acta 16 (1971) 1539.

[11] G. Amsel and D. Samuel, J. Phys. Chem. Solids 23 (1962) 1707.

[12] L.C. Archibald and J.S.L. Leach, Electrochim. Acta 22 (1977) 15.

[13] L. C. Archibald, Electrochim. Acta 22 (1977) 657.

[14] N.R. Armstrong and R.K. Quinn, Surf. Sci. 67 (1977) 451.

[15] Lj. D. Arsov, Electrochim. Acta 30 (1985) 1645.

[16] Lj. D. Arsov, C. Kormann and W. Plieth, J. Electrochem. Soc. 138 (1991) 2964.

[17] K. Azumi and M. Seo, Corros. Sci. 43 (2001) 533.

[18] V. Battaglia and J. Newman, J. Electrochem. Soc. 142 (1995) 1423.

[19] C.P. Bean, J.C. Fisher and D.A. Vermilyea, Phys. Rev. 101 (1956) 551.

[20] J.P. Bearinger, C.A. Orme and J.L. Gilbert, Biomaterials 24 (2003) 1837.

[21] S.E. Benjamin and F.A. Khalid, Oxidation of Metals 52 (1999) 209.

[22] D.J. Blackwood and L.M. Peter, Electrochim. Acta 33 (1988) 1143.

[23] D.J. Blackwood, R. Greef and L.M. Peter, Electrochim. Acta 34 (1989) 875.

[24] D.J. Blackwood and L.M. Peter, Electrochim. Acta 34 (1989) 1505.

[25] D.J. Blackwood, Electrochim. Acta 46 (2000) 563.

[26] G. Blondeau, M. Froelicher, M. Froment and A. Hugot-Le Goff, Thin Solid Films 42 (1977) 147.

[27] P.J. Boddy, J. Electrochem. Soc. 115 (1968) 199.

[28] M. Bojinov, Electrochim. Acta 42 (1997) 3489.

[29] S.H. Bonilla and C.F. Zinola, Electrochim. Acta 43 (1998) 423.

[30] P. Bourdet, F. Vacandio, L. Argème, S. Rossi, and Y. Massiani, Thin Solid Films 483 (2005) 205.

[31] D.H. Bradhurst and J.S.L. Leach, J. Electrochem. Soc. 113 (1966) 1245.

[32] D.A. Brevnov, G.V. Rama Rao, G.P. Lopez and P.B. Atanassov, Electrochim. Acta 49 (2004) 2487.

[33] M.A. Butler and D.S. Ginley, J.Electrochem. Soc. 135 (1988) 45.

[34] H.-J. Butt, J. Colloid Interf. Sci. 180 (1996) 251.

[35] N. Cabrera and N.F. Mott, Rep. Prog. Phys. 12 (1948-1949) 163.

[36] O.R. Camara, C.P. de Pauli and M.C. Giordano, Electrochim. Acta 29 (1984) 1111.

[37] C.Y. Chao, L.F. Lin and D.D. Macdonald, J. Electrochem. Soc. 128 (1981) 1187.

[38] S.N. Chu, J. Electrochem. Soc. 145 (1998) 3621.

[39] C. Cichos and Th. Geidel, Colloid Polym. Sci. 261 (1983) 947.

[40] F. Climent and R. Capellades, Electrochim. Acta 33 (1988) 433.

[41] CRC Handbook of Chemistry and Physics, 53^{rd} edition, 1972, p. D-219.

[42] C. da Fonseca, M. Guerreiro Ferreira and M. da Cunha Belo, Electrochim. Acta 39 (1994) 2197.

[43] C. da Fonseca, A. Traverse, A. Tadjeddine and M. de Cunha Belo, J. Electroanal. Chem. 388 (1995) 115.

[44] A.J. Davenport and G.T. Burstein, J. Electrochem. Soc. 137 (1990) 1496.

[45] J.A. Davies, B. Domeij, J.P.S. Pringle and F. Brown, J. Electrochem. Soc. 112 (1965) 675.

[46] F. Decker, E. Pantano, D. Dini, S. Cattarin, S. Maffi and G. Razzini, Electrochim. Acta 45 (2000) 4607.

[47] J.-L. Delplancke, M. Degrez, A. Fontana, and R. Winand, Surf. Technol. 16 (1982) 153.

[48] J.-L. Delplancke and R. Winand, Electrochim. Acta 33 (1988) 1539.

[49] J.-L. Delplancke and R. Winand, Electrochim. Acta 33 (1988) 1551.

[50] J.-L. Delplancke, A. Garnier, Y. Massiani and R. Winand, Electrochim. Acta 39 (1994) 1281.

[51] F. Di Quarto, K. Doblhofer and H. Gerischer, Electrochim. Acta 23 (1978) 195.

[52] F. Di Quarto, S. Piazza and C. Sunseri, J. Electrochem. Soc. 131 (1984) 2901.

[53] F. Di Quarto, S. Piazza and C. Sunseri, Electrochim. Acta 38 (1993) 29.

[54] F. Di Quarto, C. Sunseri, S. Piazza and M.C. Romano, J. Phys. Chem. B, 101 (1997) 2519.

[55] M.V. Diamanti and M.P. Pedeferri, Corros. Sci. 49 (2007) 939.

[56] M.F. Doerner and W.D. Nix, Crit. Rev. Solid St. Mater. Sci. 14 (1988) 225.

[57] C.K. Dyer and J.S.L. Leach, J. Electrochem. Soc. 125 (1978) 1032.

[58] C.K. Dyer and J.S.L. Leach, Electrochim. Acta 23 (1978) 1387.

[59] A. Felske and W. Plieth, Electrochim. Acta 34 (1989) 75.

[60] P.A. Flinn, D.S. Gardner and W.D. Nix, IEEE Trans. Elec. Dev. 34 (1987) 689.

[61] J.A. Floro and E. Chason, Appl. Phys. Lett. 69 (1996) 3830.

[62] J.A. Floro and E. Chason, Mater. Res. Soc. Symp. Proc. 428 (1996) 499.

[63] J.A. Floro and E. Chason, "Curvature-based Techniques for Real-Time Stress Measurement During Thin Film Growth", white paper available from www.k-space.com.

[64] K. Fushimi, T. Okawa, K. Azumi and M. Seo, J. Electrochem. Soc 147 (2000) 524.

[65] S.J. Garcia-Vergara, P. Skeldon, G.E. Thompson and H. Habazaki, Electrochim. Acta 52 (2006) 681.

[66] J. Gere and S. Timoshenko, Mechanics of Materials (fourth edition), PWS Publishing Company, Boston, 1997.

[67] A. Goossens, Surf. Sci. 371 (1997) 390.

[68] J. Grindlay, Phys. Rev. 160 (1967) 698.

[69] I.L. Guy, S. Muensit and E.M. Goldys, Appl. Phys. Lett. 75 (1999) 3641.

[70] J.-P. Gueneau de Mussy, G. Langelaan, J. Decerf and J.-L. Delplancke, Scripta Mater. 48 (2003) 23.

[71] H. Habazaki, K. Shimizu, P. Skeldon, G.E. Thompson and G.C. Wood, Thin Solid Films 300 (1997) 131.

[72] H. Habazaki, K. Takahiro and S. Yamaguchi, Phil. Mag. A 78 (1998) 171.

[73] H. Habazaki, K. Shimizu, S. Nagata, P. Skeldon, G.E. Thompson and G.C. Wood, J. Electrochem. Soc. 149 (2002) B70.

[74] H. Habazaki, K. Shimizu, S. Nagata, P. Skeldon, G.E. Thompson, and G.C. Wood, Corros. Sci. 44 (2002) 1047.

[75] H. Habazaki, M. Uozumi, H. Konno, K. Shimizu, S. Nagata, K. Asami, P. Skeldon and G.E. Thompson, Electrochim. Acta 47 (2002) 3837.

[76] H. Habazaki, M. Uozumi, H. Konno, K. Shimizu, P. Skeldon and G.E. Thompson, Corros. Sci. 45 (2003) 2063.

[77] H. Habazaki, M. Uozumi, H. Konno, S. Nagata and K. Shimizu, Surf. Coat. Tech. 169-170 (2003) 151.

[78] H. Habazaki, M. Uozumi, H. Konno, K. Shimizu, S. Nagata, K. Asami, K. Matsumoto, K. Takayama, Y. Oda, P. Skeldon and G. E. Thompson, Electrochim. Acta 48 (2003) 3257.

[79] H. Habazaki, M. Uozumi, H. Konno, K. Shimizu, S. Nagata, K. Takayama, Y. Oda and P. Skeldon, J. Electrochem. Soc. 152 (2005) B263.

[80] H. Habazaki, T. Ogasawara, H. Konno, K. Shimizu, K. Asami, K. Saito, S. Nagata, P. Skeldon and G.E. Thompson, Electrochim. Acta 50 (2005) 5334.

[81] H. Habazaki, K. Shimizu, S. Nagata, K. Asami, K. Takayama, Y. Oda, P. Skeldon and G.E. Thompson, Thin Solid Films 479 (2005) 144.

[82] H. Habazaki, K. Fushimi, K. Shimizu, P. Skeldon and G. Thompson, Electrochem. Commun. 9 (2007) 1222.

[83] J.W. Halley, M. Kozlowski, M. Michalewicz, W. Smyrl. and N. Tit, Surf. Sci. 256 (1991) 397.

[84] J.A. Harrisson and D.E. Williams, Electrochim. Acta 27 (1982) 891.

[85] S. Hearne, E. Chason, J. Han, J.A. Floro, J. Figiel, J. Hunter, H. Amano and I.S.T. Tsong, Appl. Phys. Lett. 74 (1999) 356.

[86] S.C. Hendy, N.J. Laycock and M.P. Ryan, J. Electrochem. Soc. 152 (2005) B271.

[87] H. Herranen and J.-O. Carlsson, Corros. Sci. 43 (2001) 365.

[88] R.W. Hoffman, Thin Solid Films 34 (1976) 185.

[89] L. Hong, G. Kewei and C. Wuyang, Scripta Mat. 37 (1997) 1387.

[90] J.E. Houser and K.R. Hebert, Phys. Stat. Sol. (a) 205 (2008) 2396.

[91] Y.Z. Huang and D.J. Blackwood, Electrochim. Acta 51 (2005) 1099.

[92] Y. Z. Huang and D. J. Blackwood, Electrochim. Acta 51 (2005) 3521.

[93] F. Huber, J. Electrochem. Soc. 110 (1963) 846.

[94] A. Hugot-Le Goff, Thin Solid Films 142 (1986) 193.

[95] T. Hurlen and W. Wilhelmsen, Electrochim. Acta 31 (1986) 1139.

[96] T. Hurlen, W. Wilhelmsen, S. Hornkjol, E. Gulbrandsen, and C. Simon, Electrochim. Acta 34 (1989) 519.

[97] T. Hurlen and S. Hornkjol, Electrochim. Acta 36 (1991) 189.

[98] T. Hurlen and E. Gulbrandsen, Electrochim. Acta 39 (1994) 2169.

[99] S. Ikonopisov, Electrochim. Acta 22 (1977) 1077.

[100] N.F. Jackson, J. Applied Electrochem. 3 (1973) 91.

[101] M. Janik-Czachor, A. Jaskiewicz, M. Dolata and Z. Werner, Mater. Chem. Phys. 92 (2005) 348.

[102] A. Jenny and W. Lewis, The anodic oxidation of aluminium and its alloys, Ed. Charles Griffin, London (1952).

[103] R. Jérisian, J.C. Marchenoir and J.P. Loup, Thin Solid Films 100 (1983) 121.

[104] J. Joseph and A. Gagnaire, Thin Solid Films 103 (1983) 257.

[105] G. Jouve, A. Politi, P. Lacombe and G. Vuye, J. Less-Common Met. 59 (1978) 175.

[106] G. Jouve and N.E. Derradji, J. Less-Common Met. 86 (1982) 161.

[107] G. Jouve and J.S.L. Leach, Thin Solid Films 110 (1983) 263.

[108] P. Kern, C. Jaeggi, I. Utke, V. Friedli and J. Michler, Appl. Phys. Lett. 89 (2006) 021902.

[109] O. Kerrec, D. Devilliers, H. Groult and M. Chemla., Electrochim. Acta 40 (1995) 719.

[110] N. Khalil and J.S.L. Leach, Electrochim. Acta 31 (1986) 1279.

[111] J.-D. Kim, S.-I. Pyun and R.A. Oriani, Electrochim. Acta 40 (1995) 1171.

[112] J.-D. Kim and M. Seo, J. Electrochem. Soc. 150 (2003) B193.

[113] D. Kim, S. Ahn and H. Kwon, Thin Solid Films 513 (2006) 212.

[114] R. Kirchheim, Electrochim. Acta 32 (1987) 1619.

[115] R. Kirchheim, Corros. Sci. 29 (1989) 183.

[116] E. Kobeda and E.A. Irene, J. Vac. Sci. Tech. B 4 (1986) 720.

[117] D.-S. Kong and J.-X. Wu, J. Electrochem. Soc. 155 (2008) C32.

[118] U. König and B. Davepon, Electrochim. Acta 47 (2001) 149.

[119] M. Kozlowski, W.H. Smyrl, L. Atanasoska and R. Atanasoski, Electrochim. Acta 34 (1989) 1763.

[120] E. Krasicka-Cydzik, Corros. Sci. 46 (2004) 2487.

[121] B. Krishnamurthy, R.E. White and H.J. Ploehn, Electrochim. Acta 46 (2001) 3387.

[122] B. Krishnamurthy, R.E. White and H.J. Ploehn, Electrochim. Acta 47 (2002) 2505.

[123] B. Krishnamurthy, R.E. White and H.J. Ploehn, Electrochim. Acta 47 (2002) 3375.

[124] S. Kudelka, A. Michaelis and J.W. Schultze, Electrochim. Acta 41 (1996) 863.

[125] S. Kudelka and J.W. Schultze, Electrochim. Acta 42 (1997) 2817.

[126] J. Kunze, A. Ghicov, H. Hildebrand, J. Macak, L. Taveira and P. Schmuki, Z. Phys. Chem. 219 (2005) 1561.

[127] J. Kunze, A. Seyeux and P. Schmuki, Electrochem. Solid St. Lett. 11 (2008) K11.

[128] J.L. Labar, Ultramicroscopy 103 (2005) 237.

[129] L.D. Landau and E.M. Lifshitz, Electrodynamics of Continuous Media, Pergamon, Oxford, 1960.

[130] G.G. Lang and M. Seo, J. Electroanal. Chem. 490 (2000) 98.

[131] D. Laser, M. Yaniv and S. Gottesfeld, J. Electrochem. Soc. 125 (1978) 358.

[132] J.S.L. Leach and B.R. Pearson, Electrochim. Acta 29 (1984) 1263.

[133] J.S.L. Leach and B.R. Pearson, Corros. Sci. 28 (1988) 43.

[134] D.J. LeClere, A. Velota, P. Skeldon, G.E. Thompson, S. Berger, J. Kunze, P. Schmuki, H. Habazaki and S. Nagata, J. Electrochem. Soc. 155 (2008) C487.

[135] H.Y. Lee, Y. Peng and Y. Shkel, J. Appl. Phys. 98 (2005) 074104.

[136] E.-J. Lee and S.-I. Pyun, J. Appl. Electrochem. 22 (1992) 156.

[137] K. Leitner, J.W. Schultze and U. Stimming, J. Electrochem. Soc. 133 (1986) 1561.

[138] E. Leiva, P. Meyer and W. Schmickler, Corros. Sci. 29 (1989) 225.

[139] M.M. Lohrengel, Mater. Sci. Eng. R11 (1993) 243.

[140] M.M. Lohrengel, Electrochim. Acta 39 (1994) 1265.

[141] J.M. Macak, K. Sirotna and P. Schmuki, Electrochim. Acta 50 (2005) 3679.

[142] D.D. Macdonald and M. Urquidi-Macdonald, J. Electrochem. Soc. 137 (1990) 2395.

[143] A.G. Mantzila and M.I. Prodromidis, Electrochim. Acta 51 (2006) 3537.

[144] J.C. Marchenoir, J.P. Loup and J. Masson, Thin Solid Films 66 (1980) 357.

[145] P. Marcus, Electrochim. Acta 43 (1998) 109.

[146] J. Marsh and D. Gorse, Electrochim. Acta 43 (1998) 659.

[147] H. Masuda and K. Fukuda, Science 268 (1995) 1466.

[148] J.F. McAleer and L.M. Peter, J. Electrochem. Soc. 129 (1982) 1252.

[149] E. McCafferty and J.P. Wightman, Appl. Surf. Sci. 143 (1999) 92.

[150] R.M. McMeeking and C.M. Landis, J. Appl. Mech. 72 (2005) 581.

[151] Y.E. Makushok, V.P. Parkhutik, J.M. Martinez-Duart and J.M. Albella, J. Phys. D: Appl. Phys. 27 (1994) 661.

[152] C.E.B. Marino, E.M. Oliveira, R.C. Rocha-Filho and S.R. Biaggio, Corros. Sci. 43 (2001) 1465.

[153] E. Matykina, G. Doucet, F. Monfort, A. Berkani, P. Skeldon, G.E. Thompson, Electrochim. Acta 51 (2006) 4709.

[154] E. Matykina, R. Arrabal, P. Skeldon, G.E. Thompson and H. Habazaki, Thin Solid Films 516 (2008) 2296.

[155] A. Mezin, Surf. Coat. Technol. 200 (2006) 5259.

[156] A. Michaelis and J.W. Schultze, Thin Solid Films 274 (1996) 82.

[157] W. Mizushima, J. Electrochem. Soc. 108 (1961) 825.

[158] I. Montero, J.M. Albella and J.M. Martinez-Duart, J. Electrochem. Soc. 132 (1985) 814.

[159] S.-M. Moon and S.-I. Pyun, Electrochim. Acta 42 (1998) 3117.

[160] G.K. Mor, O.K. Varghese, M. Paulose, N. Mukherjee and C.A. Grimes, J. Mater. Res. 18 (2003) 2588.

[161] G.K. Mor, O.K. Varghese, M. Paulose, K. Shankar and C.A. Grimes, Sol. Energy Mater. 90 (2006) 2011.

[162] A.G. Munoz, Electrochim. Acta 52 (2007) 4167.

[163] R. Narayanan and S.K. Seshadri, Corros. Sci. 49 (2007) 542.

[164] J.C. Nelson and R.A. Oriani, Corros. Sci. 34 (1993) 307.

[165] W.D. Nix, Mechanical Properties of Thin Films (class notes for a graduate class at Stanford University), available online from http://imechanica.org.

[166] T.J. Nurse and F. Wormwell, J. Appl. Chem. 2 (1952) 550.

[167] T. Ohtsuka, M. Masuda and N. Sato, J. Electrochem. Soc. 132 (1985) 787.

[168] T. Ohtsuka, J. Guo and N. Sato, J. Electrochem. Soc. 133 (1986) 2473.

[169] T. Ohtsuka, M. Masuda and N. Sato, J. Electrochem. Soc. 134 (1987) 2406.

[170] T. Ohtsuka and N. Nomura, Corros. Sci. 39 (1997) 1253.

[171] T. Ohtsuka and T. Otsuki, Corros. Sci. 40 (1998) 951.

[172] T. Ohtsuka and T. Otsuki, Corros. Sci. 45 (2003) 1793.

[173] E.M. Oliveira, C.E.B. Marino, S.R. Biaggio and R.C. Rocha-Filho, Electrochem. Commun. 2 (2000) 254.

[174] N.T.C. Oliveira, S.R. Biaggio, P.A.P. Nascente, S. Piazza, C. Sunseri and F. Di Quarto, Electrochim. Acta 51 (2006) 3506.

[175] C.-O.A. Olsson and D. Landolt, Electrochim. Acta 48 (2003) 3999.

[176] C.-O.A. Olsson, M.G. Vergé and D. Landolt, J. Electrochem. Soc. 151 (2004) B652.

[177] J.L. Ong, L.C. Lucas, G.N. Raikar and J.C. Gregory, Appl. Surf. Sci. 72 (1993) 7.

[178] J.L. Ord, J. Electrochem. Soc. 129 (1982) 2038.

[179] J.L. Ord, D.J. De Smet and D.J. Beckstead, J. Electrochem. Soc. 136 (1989) 2178.

[180] J.L. Ord, J. Electrochem. Soc. 138 (1991) 2934.

[181] J.P. O'Sullivan and G.C. Wood, Proc. Roy. Soc. Lond. A. 317 (1970) 511.

[182] C.-H. Paik, M.R. Kozlowski, P.S. Tyler and W.H. Smyrl, J. Electrochem. Soc. 135 (1988) 2395.

[183] J. Pan, D. Thierry and C. Leygraf, Electrochim. Acta 41 (1996) 1143.

[184] C.N. Panagopoulos, J. Less-Common Met. 141 (1988) 335.

[185] S. Piazza, G. Lo Biundo, M.C. Romano, C. Sunseri and F. Di Quarto, Corros. Sci. 40 (1998) 1087.

[186] A. Politi, G. Jouve and P. Lacombe, J. Less-Common Met. 56 (1977) 263.

[187] J. Pouilleau, D. Devilliers, F. Garrido, S. Durand-Vidal and E. Mahé, Mater. Sci. Eng. B47 (1997) 235.

[188] J. Pouilleau, D. Devilliers, H. Groult and P. Marcus, J. Mater. Sci. 32 (1997) 5645.

[189] S.K. Poznyak, D.V. Talapin and A.I. Kulak, J. Electroanal. Chem. 579 (2005) 299.

[190] J.P.S. Pringle, Electrochim. Acta 25 (1980) 1423.

[191] J. Proost and F. Spaepen, J. Appl. Phys. 91 (2002) 204.

[192] A. Prusi, Lj. Arsov, B. Haran and B.N. Popov, J. Electrochem. Soc. 149 (2002) B491.

[193] S.-I. Pyun and M.-H. Hong, Electrochim. Acta 37 (1992) 327.

[194] S-I Pyun, Mater. Lett. 27 (1996) 297.

[195] R.K. Quinn and N.R. Armstrong, J. Electrochem. Soc. 125 (1978) 1790.

[196] M. Reece and R. Morrell, J. Mater. Sci. 26 (1991) 5566.

[197] B. Roh and D.D. Macdonald, Russ. J. Electrochem. 43 (2007) 125.

[198] R.A. Rokob and G.G. Lang, Electrochim. Acta 51 (2005) 93.

[199] S.N. Sahu, J. Scarminio and F. Decker, J. Electrochem Soc. 137 (1990) 1150.

[200] D. Sander and H. Ibach, Phys. Rev. B 43 (1991) 4263.

[201] D. Sander, Current Opinion in Solid State and Materials Science 7 (2003) 51.

[202] M. Santamaria, F. Di Quarto and H. Habazaki, Corros. Sci. 50 (2008) 2012.

[203] E. Santos, N.K. Kuromoto and G.A. Soares, Mater. Chem. Phys. 102 (2007) 92.

[204] N. Sato and M. Cohen, J. Electrochem. Soc. 111 (1964) 512.

[205] N. Sato, Electrochim. Acta 16 (1971) 1683.

[206] N. Sato, Electrochemistry at metal and semiconductor electrodes, Elsevier Science, Amsterdam (1998).

[207] P. Schmuki, J. Solid St. Electrochem. 6 (2002) 145.

[208] J. Schoonman, K. Vos and G. Blasse, J. Electrochem. Soc. 128 (1981) 1154.

[209] J.W. Schultze and M.M. Lohrengel, Electrochim. Acta 28 (1983) 973.

[210] J.W. Schultze and L. Elfenthal, J. Electroanal. Chem. 204 (1986) 153.

[211] J.W. Schultze and M.M. Lohrengel, Electrochim. Acta 45 (2000) 2499.

[212] J.W. Schultze, M. Pilaski, M.M. Lohrengel and U. König, Faraday Discuss. 121 (2002) 211.

[213] Y. Serruys, T. Sakout and D. Gorse, Surf. Sci. 282 (1993) 279.

[214] T. Shibata and Y.-C. Zhu, Corros. Sci. 37 (1995) 133.

[215] T. Shibata and Y.-C. Zhu, Corros Sci. 37 (1995) 253.

[216] K. Shimizu, G.E. Thompson and G.C. Wood, Thin Solid Films 92 (1982) 231.

[217] Y.M. Shkel and D.J. Klingenberg, J. Appl. Phys. 80 (1996) 4566.

[218] Y.M. Shkel and D.J. Klingenberg, J. Appl. Phys. 83 (1998) 7834.

[219] M.E. Sibert, J. Electrochem. Soc. 110 (1963) 65.

[220] J. Siejka, J.P. Nadai and G. Amsel, J. Electrochem. Soc. 118 (1971) 727.

[221] P. Skeldon, G.E. Thompson, G.C. Wood and X. Zhou, Philos. Mag. 76 (1997) 729.

[222] J.R. Smith, F.C. Walsh and R.L. Clarke, J. Appl. Electrochem. 28 (1998) 1021.

[223] L.O. Snizhko, A.L. Yerokhin, N.L. Gurevina, D.O. Misnyankin, A. Pilkington, A. Leyland and A. Matthews, Electrochim. Acta 50 (2005) 5458.

[224] P. Soares, A. Mikowski, C.M. Lepienski, E. Santos, G.A. Soares, V. Swinka Filho, N.K. Kuromoto, J. Biomed. Mater. Res. B: Appl. Biomater. 84B (2007) 524.

[225] G.S. Sotirova-Chakarova and S.A. Armyanov, J. Electrochem. Soc. 137 (1990) 3551.

[226] F. Spaepen and A.L. Shull, Current Opinion in Solid State and Materials Science 1 (1996) 679.

[227] G.R. Stafford, O.E. Kongstein and G.M. Haarberg J. Electrochem. Soc. 153 (2006) C207.

[228] K. Stella and D. Diesing, J. Electrochem. Soc. 154 (2007) C663.

[229] G.G. Stoney, Proc. Roy. Soc. A82 (1909) 172.

[230] J.A. Stratton, Electromagnetic Theory, McGraw-Hill, New York, 1941.

[231] Y.-T. Sul, C.B. Johansson, Y. Jeong, and T. Albrektsson, Med. Eng. Phys. 23 (2001) 329.

[232] M.T. Tanvir, K. Fushimi, K. Shimizu, S. Nagata, P. Skeldon, G.E. Thompson, H. Habazaki, Electrochim. Acta 52 (2007) 6834.

[233] L.V. Taveira, J.M. Macak, H. Tsuchiya, L.F.P. Dick, and P. Schmuki, J. Electrochem. Soc. 152 (2005) B405.

[234] L.V. Taveira, J.M. Macak, K. Sirotna, L.F.P. Dick, and P. Schmuki, J. Electrochem. Soc. 153 (2006) B137.

[235] R.M. Torresi, O.R. Camara and C.P. De Pauli, Electrochim. Acta 32 (1987) 1291.

[236] Z. Tun, J.J. Noël and D.W. Shoesmith, Physica B 241-243 (1998) 1107.

[237] Z. Tun, J.J. Noël and D.W. Shoesmith, J. Electrochem. Soc. 146 (1999) 988.

[238] K. Ueno and M. Seo, J. Electrochem. Soc. 146 (1999) 1496.

[239] K. Ueno, S.-I. Pyun and M. Seo, J. Electrochem. Soc. 147 (2000) 4519.

[240] W.B. Utomo and S.W. Donne, Electrochim. Acta 51 (2006) 3338.

[241] P. Van Rysselberghe, J. Electrochem. Soc. 106 (1959) 355.

[242] M.-G. Vergé, P. Mettraux, C.-O. Olsson and D. Landolt, J. Electroanal. Chem. 566 (2004) 361.

[243] D.A. Vermilyea, J. Electrochem. Soc. 102 (1955) 207.

[244] D.A. Vermilyea, J. Electrochem. Soc. 104 (1957) 542.

[245] D.A. Vermilyea, J. Electrochem. Soc. 110 (1963) 345.

[246] E.J.W. Verwey, Physica 2 (1935) 1059.

[247] K.J. Vetter, Electrochim. Acta 16 (1971) 1923.

[248] K.J. Vetter and F. Gorn, Electrochim. Acta 18 (1973) 321.

[249] A.K. Vijh, Oxidation of Metals 4 (1972) 63.

[250] C.A. Volkert, J. Appl. Phys. 70 (1991) 3521.

[251] C. Wei and A.J. Bard, J. Electrochem. Soc. 142 (1995) 2523.

[252] U. Welzel, J. Ligot, P. Lamparter, A.C. Vermeulen and E.J. Mittemeijer, Journal of Applied Crystallography 38 (2005) 1.

[253] D.G. Wiesler and C.F. Majkrzak, Physica B 198 (1994) 181.

[254] W. Wilhelmsen and T. Hurlen, Electrochim. Acta 32 (1987) 85.

[255] G.C. Wood and C. Pearson, Corros. Sci. 7 (1967) 119.

[256] G.C. Wood, P. Skeldon, G.E. Thompson and K. Shimizu, J. Electrochem. Soc. 143 (1996) 74.

[257] N. Wüthrich, Electrochimica Acta 25 (1980) 819.

[258] N. Wüthrich, Electrochimica Acta 26 (1981) 1617.

[259] Z. Xia, H. Nanjo, H. Tetsuka, T. Ebina, M. Izumisawa, M. Fujimura and J. Onagawa, Electrochem. Commun. 9 (2007) 850.

[260] J. Yahalom and T. P. Hoar, Electrochim. Acta 15 (1970) 877.

[261] J. Yahalom and J. Zahavi, Electrochim. Acta 15 (1970) 1429.

[262] A.L. Yerokhin, X. Nie, A. Leyland, A. Matthews and S.J. Dowey, Surf. Coat. Technol. 122 (1999) 73.

[263] L. Young, Proc. Roy. Soc. Lond. A 263 (1961) 395.

[264] L. Young and D.J. Smith, J. Electrochem. Soc. 126 (1979) 765.

[265] E. Zhuravlyova, L. Iglesias-Rubianes, A. Pakes, P. Skeldon, G.E. Thompson, X. Zhou, T. Quance, M.J. Graham, H. Habazaki and K. Shimizu, Corros. Sci. 44 (2002) 2153.

[266] V. Zwilling, M. Aucouturier and E. Darque-Ceretti, Electrochim. Acta 45 (1999) 921.

[267] V. Zwilling, E. Darque-Ceretti, A. Boutry-Forveille, D. David, M.Y. Perrin and M. Aucouturier, Surf. Interf. Anal. 27 (1999) 629.